DESIGN OF AN INTEGRITY SUPPORT MESSAGE FOR OFFLINE ADVANCED RAIM

von der Fakultät für Elektrotechnik und Informationstechnik der Rheinisch-Westfälischen Technischen Hochschule Aachen zur Erlangung des akademischen Grades eines

Doktors der Ingenieurwissenschaften

genehmigte Dissertation vorgelegt von

Santiago Perea Díaz, M.Sc.

aus Bollullos del Condado, Spanien.

Berichter:

1. Univ.-Prof. Dr.-Ing. habil. Michael Meurer
2. Prof. Boris Pervan, Ph.D., Illinois Institute of Technology, USA
3. Univ.-Prof. Dr.-Ing. Jens-Rainer Ohm

Tag der mündlichen Prüfung 13.05.2019

Abstract

The modernization of GPS along with the emergence of new GNSS constellations opens new opportunities to redesign traditional Receiver Autonomous Integrity Monitoring (RAIM) in order to target more demanding navigation requirements. The evolution from legacy to Advanced RAIM will became a reality within the next years thanks to measurement redundancy that will guarantee navigation integrity, continuity, and accuracy on a global scale. In order for ARAIM users to evaluate these performance metrics, inputs from ground must be encapsulated within the Integrity Support Message (ISM). The first set of parameters broadcast through this message defines the individual satellite and constellation fault rates which reflect GNSS operational commitments. The second set provides the necessary parameters to create an integrity and accuracy bound for satellite unfaulted ranging errors which need to be assessed through GNSS performance characterization. In response to this need, this research focuses on the design of an ISM covering GNSS performance monitoring, error correlation analysis, sample independence, and overbounding theory.

This dissertation presents a methodology to make use of the currently deployed Multi-GNSS EXperiment (MGEX) ground infrastructures to emulate the architecture of a future Air Navigation Service Provider (ANSP) ground network. The main scope of this technique is the establishment of a security layer between orbit and clock products and ISM generation. It guarantees that no fabricated errors are introduced at the same time that no integrity events are overlooked due to data unavailability. Using this monitor, GPS and Galileo service history are analyzed providing a comprehensive ephemeris and clock error characterization. A novelty introduced in this work is the time-dependent analysis which exposes the high correlation that inherently affects GNSS Signal-in-Space Range Error (SISRE). Based on an estimation variance study, this dissertation presents an analytical methodology to determine the time between effective independent samples. Results show that GPS and Galileo exhibit significantly different correlation behavior in that the European constellation is less affected by it. Based on Bayesian inference, this work proves that an analytical expression of the error Cumulative Distribution Function (CDF) as a function of the number of independent samples can be derived. In order to account for the impact of sample correlation on the error bounds, this work determines the factor by which the overbounding distribution needs to be inflated. This factor is inversely proportional to the number of independent samples representing the higher confidence that can be placed in the estimation as more independent data are collected. The fact Galileo range error is less correlated in time than GPS implies that shorter monitoring periods are needed to characterize the nominal performance of the European GNSS.

This dissertation presents a modification of the error accuracy and integrity models

in order to create more efficient and equally safe bounds. Based on empirical evidence, this work proposes the partition of error distributions in two sections; a quasi-Gaussian core and a flat tail distribution with large error magnitudes. Both distributions are individually bounded by Gaussian functions which are combined to create a weighted Multi Gaussian (MG) overbound. Unlike the current Single Gaussian (SG) bound, results show that the MG methodology provides the flexibility to bound large tail errors without sacrificing the narrow core. In order to incorporate the MG bound in the current ARAIM architecture, this dissertation modifies the currently used pair-bound theory proving that it still is a safe overbound in the position domain after convolution.

This thesis carries out a modification of the current Multiple Hypothesis Solution Separation (MHSS) baseline algorithm defined by the US-EU Working Group C (WGC). ARAIM simulations show that a significant enhancement on service availability can be achieved with the inclusion of MG bounding within the user algorithm. Finally, this work presents three different ISM designs for incorporating the necessary parameters for the users to perform MG overbounds. Out of these three dissemination options, an optimal design is recommended allowing the ISM generator full flexibility to exploit core-tail partition.

Acknowledgment

There has been a large group of people who have accompanied me through this journey and I would like to thank them all. First, I would like to express my deepest gratitude to my PhD advisor, Prof. Michael Meurer, who offered me the opportunity to pursue my doctoral studies at RWTH Aachen. His expertise and counseling have steered my research into the right direction over the past years. I also owe great debt of gratitude to my PhD co-advisor, Prof. Boris Pervan, who first introduced me to the fascinating world of satellite navigation during my master studies at IIT. His wise advice and guidance, along with his hospitality, made every visit to his lab a milestone in my research journey. The coordination and mutual understanding between them have taken this dissertation to a successful destination. To both of them, muchas gracias.

I sincerely thank the Institute of Communication and Navigation at the German Aerospace Center (DLR) for my time there. Those four and a half years certainly contributed to make me the researcher that I am today. I could never thank enough Dr. Oliver Montenbruck for the innumerable times that he has answered my questions. His priceless knowledge on ground monitoring has greatly influenced my work. I keep special memories from my former officemates Markus Rippl and Dr. Ilaria Martini from DLR's ARAIM team. As a young graduate, being able to learn from them every day was a gift. I would also like to thank my former managers at DLR, Dr. Boubeker Belabbas, Dr. Johann Furthner (also Prof. Meurer) and Prof. Christoph Günther for allowing me to combine my research with project work always fostering my exchanges with IIT. I could not forget my fellow PhD student and friend Simona Circiu who has been with me through all the ups and downs that grad students face. To the rest my colleagues at DLR, Anja Grosh, Dr. Okuary Osechas, María Caamaño, Omar García, Emilio Pérez, Dr. Michael Felux, Steffen Thölert, Daniel Gerbeth, Friederike Fohlmeister, Dr. Andrey Konovaltsev, etc, thanks for being part of my journey.

I would like to thank Prof. Mathieu Joerger for his dedication and patience during my masters studies at IIT. Making a newbie understand the ARAIM concept is not an easy task. I also need to thank Dr. Todd Walter and Dr. Juan Blanch from Stanford University GPS Lab. They were always happy to discuss new ideas and provide valuable feedback. To the three of them, muchas gracias. I also would like to thank my fellow researchers from IIT Navigation Lab, Dr. Çağatay Tanil, Dr. Samer Khanafseh, Dr. Yawei Zhai and Jaymin Patel. They always made my visits to Chicago a wonderful time.

I could have not done this without the support of my friends in Munich. Marion, Andreas, Sam, Bethany and Alberto, you always cheered me up when I was down. To my friends Elena, Javi, Alex, Jesús, Carlitos, María José and Julia because despite the

distance, they were always one call away to make me laugh in gray days. Por tantas llamadas interminables compartiendo venturas y desventuras, muchas gracias amigos.

But above all, I owe this achievement to my family. A pesar de estar a miles de kilómetros de distancia, me han acompañado en cada paso para llegar hasta aquí. Mi padre, Santiago, hombre de negocios que me enseñó que el trabajo duro, el esfuerzo y la dedicación siempre tienen una recompensa. Gracias a su ejemplo, invertir vacaciones y días de fiesta en terminar esta tesis ha sido más liviano. Mi hermana, Rocío, que siguiendo los pasos de mi padre cada día me sorprende por su fortaleza y espíritu incansable. Sus llamadas y mensajes de ánimo han sido una constante durante estos años. Pero sobre todo este logro se lo debo a mi madre, Maribel, quien desde pequeño me enseñó a amar la ciencia y la cultura. Ella ha sido mi gran apoyo en la travesía que me ha llevado hasta aquí, creyendo en mí esos días en los que ni yo creía en mí mismo. Por todo eso y por mucho más, Mamá, esta tesis te la dedico a ti.

Contents

List of Figures

List of Tables

Acronyms

AAIM	Aircraft Autonomous Integrity Monitoring
ABAS	Aircraft Based Augmentation Systems
AC	Analysis Center
AL	Alert Limit
ANSP	Air Navigation Service Provider
ANTEX	ANTenna EXchage
APC	Antenna Phase Center
APV	Approach Procedure with Vertical guidance
ARAIM	Advanced Receiver Autonomous Integrity Monitoring
ARMA	AutoRegressive–Moving-Average
ARNS	Aeronautical Radio Navigation Service
ATS	ARAIM Technical Subgroup
BCE	BroadCast Ephemeris
BF	Body-Fixed
BKG	Bundesamt für Kartographie und Geodäsie
C/A	Coarse/Acquisition
CDF	Cumulative Distribution Function
CLT	Central Limit Theorem
CNES	Centre National d'Études Spatiales
CODE	Center for Orbit Determination in Europe
CSP	Constellation Service Provider
CoM	Center of Mass
Cs	Cesium
DAL	Design Assurance Level
DCB	Differential Code Bias

DF	Dual Frequency
DLR	German Aerospace Center
DME	Distance Measuring Equipment
DOC	Degree of Coverage
DOP	Dilution Of Precision
ECEF	Earth-Centered Earth-Fixed
EC	European Commission
EGNOS	European Geostationary Navigation Overlay Service
EMT	Effective Monitor Threshold
ESA	European Space Agency
EU	European Union
EVT	Extreme Value Theory
FAA	Federal Aviation Administration
FA	False Alarm
FCDF	Folded Cumulative Distribution Function
FOC	Full Operational Capability
GBAS	Ground Based Augmentation System
GFZ	GeoForschungsZentrum
GIS	Galileo Initial Services
GLONASS	GLobalnaya NAvigatsionnaya Sputnikovaya Sistema
GNSS	Global Navigation Satellite System
GPS-SPS-PS	GPS Standard Positioning Service Performance Standard
GPS	Global Positioning System
GSA	European GNSS Agency
H-ARAIM	Horizontal ARAIM
HAL	Horizontal Alert Limit
HPL	Horizontal Protection Level
ICAO	International Civil Aviation Organization
IFB	Inter-Frequency Bias
IFGF	Ionosphere Free Geometry Free
IF	Ionosphere Free

IGS	International GNSS Service
IIT	Illinois Institute of Technology
ILS	Instrumental Landing System
IODC	Issue of Data Clock
IOV	In Orbit Validation
ISM	Integrity Support Message
IUP	Instantenoeus User Projection
IURE	Instantaneous User Range Error
LOS	Line-Of-Sight
LPV	Localizer Performance with Vertical guidance
LSE	Least Square Estimator
MAAST	MatLab Algorithm Availability Simulation Tool
MFMC	Multi-Frequency Multi-Constellation
MGEX	Multi-GNSS EXperiment
MG	Multi Gaussian
MHSS	Multiple Hypothesis Solution Separation
MOPS	Minimum Operational Performance Standards
NAGU	Notice Advisory to Galileo Users
NANU	Notice Advisory to Navstar Users
NGA	National Geospatial-Intelligence Agency
OCS	Operational Control Segment
ODTS	Orbit Determination and Time Synchronization
OS	Open Service
PDF	Probability Density Function
PHMI	Probability of Hazardous Misleading Information
PHM	Passive Hydrogen Maser
PL	Protection Level
PPP	Precise Point Positioning
PRO	Precise Reference Orbit
PVT	Position Velocity and Time
QQ	Quantile-Quantile

QZSS	Quasi-Zenith Satellite System
RAC	Radial, Along-Track, Cross-Track
RAFS	Rubidium Atomic Frequency Standard
RAIM	Receiver Autonomous Integrity Monitoring
RFH	Relative Frequency Histogram
RINEX	Receiver INdependent EXchange
RMC	Radial-Minus-Clock
RMS	Root Mean Square
RNP	Required Navigation Performance
RTCA	Radio Technical Commission for Aeronautics
Rb	Rubidium
SARPS	Standards and Recommended Practices
SBAS	Space Based Augmentation Systems
SFSC	Single-Frequency Single-Constellation
SF	Single Frequency
SG	Single Gaussian
SINEX	Solution INdependent EXchange
SISA	Signal-in-Space Accuracy
SISE	Signal-in-Space Error
SISRE	Signal-in-Space Range Error
SIS	Signal-in-Space
SQM	Signal Quality Monitoring
SSAS	Singled-Sided Amplitude Spectrum
SS	Solution Separation
SVS	Service Volume Simulation
SoL	Safety-of-Life
TEC	Total Electron Content
TTA	Time To Alert
TTOM	Time of Transmission of the Message
TUM	Technical University of Munich
ToC	Time of Clock

URA	User Range Accuracy
URE	User Range Error
USNO	US Naval Observatory
V-ARAIM	Vertical ARAIM
VAL	Vertical Alert Limit
VDB	Very High Frequency Data Broadcast
VOR	Very High Frequency Omni-Directional Range
VPL	Vertical Protection Level
WAAS	Wide Area Augmentation System
WGC	US-EU Working Group C
WLSE	Weighted Least-Squares Estimator
WUL	Worst User Location
ZPD	Zenith Path Delay

Nomenclature

Measurements

ρ	code measurement
φ	phase measurement
R	geometric range
δ	satellite clock bias
τ	receiver clock bias
T_d	tropospheric delay
I_d	ionospheric delay
ν_ρ	code measurement error
ν_φ	phase measurement error
θ	elevation
B_ρ	code measurement bias
B_φ	phase measurements bias
η	carrier phase integer ambiguity
N_ϕ	carrier phase cycles integer ambiguity
γ	signal travel time
c	speed of light in vacuum
f	carrier frequency
λ	carrier wavelength

For a given measurement $\rho_{j,f}^{i,k}$, indexes refer to satellite i, recorded by receiver j in frequency f at an epoch k. In case of iono-free linear combination IF is indicated.

Position, Velocity and Timing

Bold lowercase variables refer to vectors whereas bold uppercase variables refer to matrices. All vectors are columns. Variables denoted by *hat* indicate estimations of the true variable. For example, $\hat{\mathbf{x}}^k$ is an estimated solution of the state vector $\mathbf{x}$ at epoch k.

$\boldsymbol{x}$	position vector
x_l	position coordinate l
$\boldsymbol{v}$	velocity vector
$\mathbf{x}$	state vector
x_l	state vector element l

$\boldsymbol{z}$	range measurement vector
$\boldsymbol{\nu}$	range error vector
$\boldsymbol{f}$	range fault vector
$\boldsymbol{e}_s$	line-of-sight vector
$\boldsymbol{G}$	geometry matrix
$\boldsymbol{C}$	covariance matrix
$\boldsymbol{W}$	weighting matrix
$\boldsymbol{S}$	least square estimator matrix
$\boldsymbol{P}$	least square estimator covariance matrix
$\boldsymbol{s}_l$	least square estimator vector for coordinate l
$\boldsymbol{\alpha}_l$	coordinate selection vector l
$\boldsymbol{\varepsilon}$	estimate error vector
ε_l	estimate error for coordinate l

Satellite Ephemeris and Clock Errors

We express satellite position vector as $\boldsymbol{x}^{i,k,\mathrm{BCE}}_{\mathrm{CoM,ECEF}}$. Indexes i and k refer to satellite and epoch, respectively. CoM indicates to which point of the satellite the position is referred (alternatively APC); ECEF expresses the reference frame for the vector (alternatively RAC or BF); BCE indicates the data source from which the vector is obtained (alternatively PRO). For satellite user-dependent variables, the nomenclature adds subindex j to account for the user as $\Delta^{i,k}_{\mathrm{relpath},j}$.

$\boldsymbol{\varepsilon}_{\mathrm{orb}}$	satellite orbit error vector
$\tilde{\varepsilon}_{\mathrm{clk}}$	satellite broadcast clock error (individual) x
$\varepsilon_{\mathrm{clk}}$	satellite broadcast clock error (remove constellation average) x
$\Delta_{\mathrm{relpath}}$	relativistic path correction
δ_{rel}	relativistic clock correction
$\boldsymbol{R}$	coordinate transformation matrix x
$\boldsymbol{\Delta}$APC	satellite CoM-APC offset vector
$\boldsymbol{e}$	unit vector
$IURE$	instantaneous user range error
$SISRE_{GA}$	SISRE global average
$SISRE_{WUL}$	SISRE worst user location
$SISRE_{WUL,\mathrm{orb}}$	SISRE worst user location orbit component
$SISRE_{IUP}$	SISRE individual user projection
rad	radial coordinate index
aln	along-track coordinate index
crs	cross-track coordinate index
clk	clock state index
rmc	radial-minus-clock state index

Estimation and Inference

x	random variable
X	population sample (dataset) of the random variable x
μ_{x}	mean of the random variable x
$\hat{\mu}_{\mathrm{x}}$	estimated mean of the random variable x (also $\bar{\mathrm{x}}$)
m_{x}	median of the random variable x
$\hat{m}_{\mathrm{x}}$	estimated median of the random variable x
σ_{x}	standard deviation of the random variable x
$\hat{\sigma}_{\mathrm{x}}$	estimated standard deviation of the random variable x (also s)
ψ^2_{x}	mean square value of the random variable x
$\hat{\psi}^2_{\mathrm{x}}$	estimated mean square value of the random variable x
f_{x}	probability density function of the random variable x
F_{x}	cumulative density function of the random variable x
R_{xx}	autocorrelation function of the random variable x
$\hat{R}_{\mathrm{xx}}$	estimated autocorrelation function of the random variable x
C_{xx}	autocovariance function of the random variable x
$\hat{C}_{\mathrm{xx}}$	estimated autocovariance function of the random variable x
$\bar{C}_{\mathrm{xx}}$	normalized autocovariance function of the random variable x
S_{xx}	power spectral density function of the random variable x
ΔT_{ind}	time between effective independent samples
N_{A}	total number of samples of set A
$N_{\mathrm{A}*}$	total number of effectively independent samples of set A
$\frac{N^*}{N}\Big\vert_{\hat{\mu}_{\mathrm{x}}}$	fraction of effectively independent samples determined by $\hat{\mu}_{\mathrm{x}}$
$\frac{N^*}{N}\Big\vert_{\hat{\psi}^2_{\mathrm{x}}}$	fraction of effectively independent samples determined by $\hat{\psi}^2_{\mathrm{x}}$
Γ	Gamma function
${}_2F_1$	Gaussian hypergeometric function

Range Error Model

This variables follows similar nomenclature to measurements. For a given error $\sigma^{i,k}_{error,j,f}$, indexes refers to satellite i, recorded by receiver j in frequency f at an epoch k. If one of the indexes is missing, it indicates that the model is not a function of that particular one. For example σ^{i}_{URE} is only satellite-dependent for all receivers for all frequencies. If an error model is different for code and phase measurements, the corresponding index ρ or φ is indicated. In case none is included, it indicates that code and phase shall use the same model, for example, residual tropospheric error.

σ_{tropo}	residual tropospheric uncertainty model
σ_{user}	user range error contribution model
σ_{noise}	signal noise range error contribution model
σ_{mp}	signal multipath range error contribution model
$\sigma_{\mathrm{orb,clk}}$	ephemeris and clock range error contribution model
$K_{\mathrm{user,IF}}$	dual frequency user multipath and noise inflation factor

ISM Parameters

σ_{URA}	1-sigma integrity bound for GPS ephemeris and clock error
σ_{SISA}	1-sigma integrity bound for Galileo ephemeris and clock error
σ_{URE}	1-sigma accuracy bound for GPS ephemeris and clock error
σ_{SISE}	1-sigma accuracy bound for Galileo ephemeris and clock error
b_{nom}	maximum nominal bias for integrity
P_{sat}	prior probability of satellite fault per approach
P_{const}	prior probability of constellation fault per approach
w_c	weighting factor for core distribution
w_t	weighting factor for tail distribution
σ^c_{ob}	1-sigma integrity bound for ephemeris and clock core error
σ^t_{ob}	1-sigma integrity bound for ephemeris and clock tail error
K^c_{uncer}	sample correlation inflation factor for core bounding
K^t_{uncer}	sample correlation inflation factor for tail bounding
O^c_{SG}	single Gaussian overbounding of core error distribution
O^t_{SG}	single Gaussian overbounding of tail error distribution
O_{MG}	multi Gaussian overbounding distribution

MHSS and Navigation Requirements

P_{HMI}	probability of hazardous misleading information
I_{REQ}	navigation integrity requirement
C_{REQ}	navigation continuity requirement
$^{(0)}$	all-in-view solution
$^{(k)}$	fault-tolerant solution
VPL	vertical protection level
HPL	horizontal protection level
σ_{acc}	fault-free accuracy
EMT	effective monitor threshold
AL	position error alert limit
T	test statistic threshold
Q	tail probability function
$\bar{Q}$	modified tail probability function
K_{fa}	sigma multiplier for continuity
N_f	number of fault hypotheses
$p_{f,k}$	prior probability of occurrence of fault hypothesis k

For the Multi Gaussian MHSS algorithm, subindexes C and T refer to *core* and *tail* bounds correspondingly.

1 Introduction

1.1 GNSS for Aviation

The Global Navigation Satellite System (GNSS) has supported aviation navigation for decades. In particular, the US Global Positioning System (GPS) has provided lateral guidance for single frequency L1 users since 1995 complementing terrestrial radio navigation systems. The inclusion of new constellations like European Galileo and the constant enhancement of GPS will add new navigation signals and frequencies which will improve the performance of GNSS-based systems. A modernized GNSS scenario will provide continuous, accurate and reliable positioning service for end-to-end navigation including en route, terminal area flight, and vertical guidance during precision approach. The GNSS ambition is to support navigation capabilities for global users potentially reducing ground infrastructures for systems like Very High Frequency Omni-Directional Range (VOR), Distance Measuring Equipment (DME), and Instrumental Landing System (ILS).

The currently in use radio navigation systems (VOR, DME, and ILS) have demonstrated their reliability and integrity throughout the past sixty years. However in a globalized world with rapidly expanding air traffic, legacy navaids might become obsolete and inefficient in the next few years. GNSS navigation provides accurate, safe, flexible and fuel efficient guidance reducing airport congestion and contributing to a cleaner sky. The most demanding requirement that satellite navigation must face is the guarantee of Safety-of-Life (SoL) during vertical guidance for precision landing operations. In this context, GNSS needs to be augmented in order to fulfill the integrity and accuracy requirements that the International Civil Aviation Organization (ICAO) demands. Augmentation systems are independent of the core constellation and based on how performance is monitored, three different systems can be listed: Ground Based Augmentation System (GBAS), Space Based Augmentation Systems (SBAS), and Aircraft Based Augmentation Systems (ABAS). The first two systems are based on differential GNSS where fault detection capability does not reside within the aviation user itself but in the provider of the augmentation. Conversely, ABAS users are fully responsible for detecting and excluding potentially faulty measurements. Figure 1.1 illustrates the application of each GNSS-based navigation attending to the requirements of each flight phase (information taken from [5]).

GBAS is a local area differential GNSS that supports precision approach service for aircrafts in the proximity of the host airport. The first task of the GBAS ground segment is the real-time computation of range corrections by collecting code and phase measurements through a set of redundant reference receivers [6]. These corrections

are broadcast to the users through Very High Frequency Data Broadcast (VDB) antennas located in the proximity of the runways. The second task of the GBAS ground segment is the detection of faults or anomalies in the ranging measurements that can lead to large positioning errors. It must monitor against four types of faults: erroneous navigation message (including ephemeris and clock errors induced by the GNSS ground segment), erroneous satellite payload behavior (including signal deformation and on-board clock anomalies), signal propagation anomalies (including tropospheric and ionospheric gradients), and faults within augmentation system equipment (including failures in the local GNSS receivers). In case of a faulty event, it is the duty of the GBAS ground segment to notify aviation users within the six seconds Time To Alert (TTA) for Category I approaches and two seconds for Category II and III [1]. The currently certified GBAS only augments GPS L1 service supporting Category I precision approach operations. Thanks to the modernization of GNSSs, future Multi-Frequency Multi-Constellation (MFMC) GBAS aims to provide Category II and III approaches including zero-visibility landings [7].

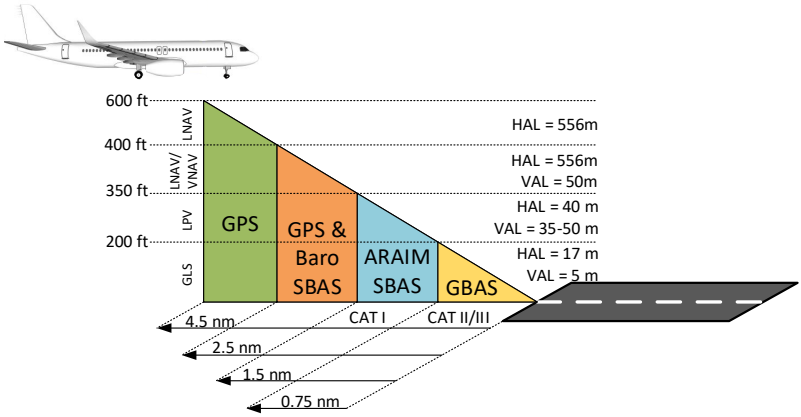

Figure 1.1: Aircraft approach procedures based on GNSS augmented systems

SBAS is a wide area differential GNSS that supports precision approach service for aircraft without the need of local infrastructures at the host airport. The principle of SBAS is not significantly different from GBAS. On top of the real-time computation of differential corrections and the integrity monitoring, SBAS adds ranging capability. The SBAS signals are similar to GPS L1 Coarse/Acquisition (C/A) so that SBAS-enabled users can track them and incorporate additional ranging measurements in the position fixed determination. One of the major advantages of SBAS is that no local augmentation infrastructure is required at the airport (unlike GBAS). SBAS uses a network of ground reference stations in charge of collecting code and phase measurements in real time. As with GBAS, redundancy and diversification in the stations are required to ensure backup hardware and avoid common fault modes. The collected data is then transferred to the processing facilities which are in charge of

computing differential corrections, determining the confidence bounds, and encoding the SBAS message. Finally this message is uploaded to the geostationary satellites and transmitted to the users. Analogous to the GBAS concept, it is the duty of the SBAS ground segment to assure the integrity of the system and to guarantee that in case of a faulty event users will be notified before 6 seconds. The first deployed SBAS was the American Wide Area Augmentation System (WAAS), certified for SoL operations since July 2003 and providing CAT I service for airports located in the continental US, Canada, and Alaska. Then, the European Geostationary Navigation Overlay Service (EGNOS) was declared operational on 1 October 2009 and was certified on 2 March 2011 for SoL services. Further information regarding SBAS architecture and operational details can be found in Chapter 12 of [8].

Aircraft Based Augmentation Systems (ABAS) is the last type of augmentation system. Unlike GBAS and SBAS, the GNSS augmentation is fully performed onboard the aircraft so that users are fully responsible for their integrity monitoring. Typically, the augmentation is achieved by two methods: the inclusion of additional sensors and the leverage of redundant GNSS measurements. The first type of ABAS combines GNSS signals with additional measurements coming from altimetry systems or inertial sensors forming the so-called Aircraft Autonomous Integrity Monitoring (AAIM). As shown in Figure 1.1, the combination of GPS measurements and barometer can provide horizontal and vertical navigation down to 350 ft.

The second type of ABAS is the most extended augmentation system within civil aviation, the Receiver Autonomous Integrity Monitoring (RAIM). By leveraging the GNSS measurement redundancy, users perform consistency checks that enable onboard integrity monitoring. In traditional RAIM, if more than four satellites are visible, users are able to identified faulted ranging measurements without the need for range corrections through a real-time data link. When more than five satellites are in view, RAIM not only identifies but also excludes potentially faulted ranges. However, current GPS-based RAIM only supports lateral navigation since it is still very brittle to satellite availability and geometry. The work developed through this thesis focuses on the evolution of traditional Single-Frequency Single-Constellation (SFSC) RAIM to Advanced RAIM in order to support vertical guidance for precision approach. Section 1.4 presents background work performed in the Advanced Receiver Autonomous Integrity Monitoring (ARAIM) field and sets the motivation for the activities conducted within this work. In addition, Chapter 2 thoroughly defines the ARAIM system and segments.

1.2 Safety of Life Operations: Integrity, Continuity, Accuracy and Availability

ARAIM is meant to provide vertical guidance for safety critical operations such as aircraft precision approach. In particular, the target operational level for ARAIM is Localizer Performance with Vertical guidance (LPV) with a decision height of 200 ft which conforms to CAT I approaches. In order to assess navigation system per-

formance, four metrics are evaluated: accuracy, integrity, continuity, and availability. The ICAO Standards and Recommended Practices (SARPS) [1] and GNSS Manual [9] define them as follows:

Integrity:"A measure of the trust that can be placed in the correctness of the information supplied by the total system." Integrity includes the ability of a system to provide timely and valid warnings to the user within the required TTA. Integrity risk or Probability of Hazardous Misleading Information (PHMI) is the probability that the true position lays outside the error bound. This error bound, also called Protection Level (PL), needs to be supplied by the navigation system (onboard algorithm in case of ARAIM) and checked against the corresponding Alert Limit (AL). Depending on the operational level, the PHMI must be below a certain probability which can range between 10^{-7} and 10^{-9}.

Continuity: "It is the capability of the system to perform its function without unscheduled interruptions during the intended operation, expressed as a probability. For example, there should be a high probability that guidance will remain available throughout an entire instrument approach procedure." As it occurs for integrity, the continuity requirement depends on the operational level. In case of Approach Procedure with Vertical guidance (APV) and CAT I approaches, missed approaches due to the lack of visual reference below the decision altitude are considered nominal operation. The continuity requirement for these operations applies to the average risk (over time) of loss of service, normalized to a 15-second exposure time.

Accuracy: "GNSS position accuracy is defined as the difference between a computed and a true position." For an estimated position at a specific location, the probability should be at least 95% that the position error is within the accuracy requirement. Since GNSS errors can change over time due to satellite motion, the accuracy is specified as a probability for each and every sample.

Availability: The availability of a service is the fraction of time during which the system is simultaneously meeting the required accuracy, integrity, and continuity. Aviation demands availability figures above 99% depending on the operational level. In the case of an augmentation system, availability is the parameter that ultimately measures the operational performance of a given navigation system.

1.3 Navigation Requirements

The navigation requirements are tied to the target operation which ultimately depends on the phase of flight. As indicated in Figure 1.1, as the decision altitude decreases, tighter integrity bounds are demanded. A useful interpretation of the integrity requirement is the protection levels which are defined as probability bounds on the position estimation errors. They provide a spatial representation of the volume that contains the true position with a 1 - I_{REQ} probability. Figure 1.2 gives a graphical interpretation of the Horizontal Protection Level (HPL), Vertical Protection Level (VPL),

Horizontal Alert Limit (HAL), and Vertical Alert Limit (VAL); as long as the blue cylinder stays within the limits of the red one, the integrity requirement is met.

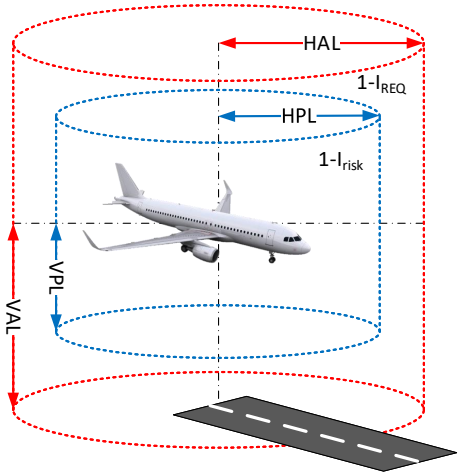

Figure 1.2: Protection level and alert limits graphical interpretation

As mentioned above, integrity is not the only requirement that the navigation systems must meet; continuity and accuracy must also be assured. The target LPV-200 operations for ARAIM are partially defined in the ICAO SARPS. The work in [10] provides an interpretation of the four vertical metrics for LPV-200 regarding VPL, accuracy, and Effective Monitor Threshold (EMT). ICAO SARPS requires that the 95 percentile vertical error remains below 4 meters, and that the fault-free system vertical error does not exceed 10 meters with a probability less than 10^{-7}. As detailed in [10], both tests are of identical form and can be translated to two maximum all-in-view vertical positioning accuracy values, $\sigma_{v,acc} = {}^{4}/_{1.96} = 2.04$ m and $\sigma_{v,acc} = {}^{10}/_{5.32} = 1.87$ m, with the later one being more stringent. Correspondingly, EMT can be interpreted as the maximum detection threshold of faults that have a prior probability of occurrence above 10^{-5}. The EMT must stay below 15 m.

Table 1.1 summarizes the navigation requirements based on different flight phases. Note that in the case of lateral navigation, the corresponding vertical requirements do not apply and the full integrity and continuity budget is allocated to the horizontal component.

Table 1.1: Navigation requirements established by ICAO [1]

Operation	Continental en-route	Terminal	NPA	APV-I LPV-250	LPV-200
HAL	3.7 km	1.85 km	556 m	40 m	40 m
VAL	N/A	N/A	N/A	50 m	35 m
TTA	5 min	15 s	10 s	10 s	6 s
Integrity requirement	10^{-7}/h	10^{-7}/h	10^{-7}/h	10^{-7} /150 s	10^{-7} /150 s
Continuity requirement	10^{-8}/h to 10^{-4}/h	10^{-8}/h to 10^{-4}/h	10^{-8}/h to 10^{-4}/h	8×10^{-6} /15 s	8×10^{-6} /15 s
σ_{acc} requirement	N/A	N/A	N/A	N/A	1.87 m
EMT	N/A	N/A	N/A	N/A	15 m

1.4 Prior Work and Motivation

RAIM has been a profuse topic within aviation for the past three decades experiencing special popularity after the introduction of the SoL concept. Traditional RAIM is the simplest and most cost efficient technique for integrity monitoring and was first introduced in the 980s by Lee [11], Parkinson [12], and Sturza [13] [14]. Respectively, they defined the *range-comparison method*, the *least-squared-residuals method*, and the *parity method* establishing the basis of autonomous integrity monitoring by leveraging measurement redundancy. Later, Brown unified the three techniques in [15] proving the equivalence among them and proposing a method to compute detection thresholds and test statistics. The original RAIM navigation system was foreseen to augment GPS L1 measurements only with no need for external input. This made the system widely accessible and low priced. However, this simplicity came at the cost of inherent limitations precluding the system from performing under more stringent requirements such as precision approaches.

The modernization of GPS and emergence of new GNSS constellations opened new opportunities to redesign traditional RAIM in order to target more demanding navigation requirements. In the frame of international collaboration, the US and the European Union (EU) signed in 2004 an agreement on GPS-Galileo cooperation activities in the field of satellite navigation. The agreement included "a working group to promote cooperation on the design and development of the next generation of civil satellite-based navigation and timing systems" fostering the creation of the US-EU Working Group C (WGC) and its ARAIM Technical Subgroup (ATS). This working group gathered experts from academia, research institutes, and civil aviation authorities from both Europe and the United States. Since then, several key players have contributed to the evolution of the original concept to today's Advanced RAIM. Pervan formalized the fundamentals of the MHSS concept in [16] establishing the basis of the current airborne algorithm based on the original approach initiated by Brown

in [17]. Later, Blanch expanded this work with the optimization of the PL equations leading to a more efficient allocation of the integrity budget [18]. In parallel, Joerger shaped the residual based ARAIM [19] and demonstrated its equivalence to solution separation [20]. Their work within WGC has contributed to the elaboration of three ARAIM milestone reports which are widely recognized as the guidance material for ARAIM development and implementation [21][22][3]. Further technical details on how traditional RAIM evolved into Advanced RAIM will be given in Sections 2.3 and 2.4 later in this dissertation.

The evolution to Multi-Frequency Multi-Constellation (MFMC) Advanced RAIM also entailed a redefinition of the ARAIM architecture and the introduction of the Integrity Support Message. The ISM includes parameters describing measurement errors and fault rates that the airborne algorithm utilizes to perform integrity, accuracy, and continuity checks. ISM design and dissemination is fully dependent on the ARAIM architecture: online or offline (more details in Section 2.4). Both architectures need the implementation of an ARAIM ground segment which is in charge of determining the ISM parameters by constellation monitoring throughout a global network of stations. The work presented in this thesis focuses on the design of an ISM covering GNSS performance monitoring, error correlation analysis, sample independence, and overbounding theory.

One of the key elements of the offline architecture is the GNSS performance monitoring with subsequent error characterization. Ultimately, the ISM broadcast to the users must provide the means to create a safe position error overbound whose protection levels stay below the alert limits. In the frame of GNSS Safety-of-Life applications, previous work done by Walter in [23], [2], and [24] has addressed the analysis of GPS satellites nominal performance and faults during the last decade. In parallel, studies based on GPS and Galileo nominal range error have been developed in [25] and [26]. One of the major challenges of characterizing constellation service history is the assessment of data files veracity and availability. Error analysis necessitates two sets of inputs: broadcast navigation data and precise reference orbits. As pointed out by Heng in [27], historical broadcast navigation data must be scrutinized and validated before they are used to characterize constellation performance. In addition, precise reference data might also present gaps or inconsistencies that need to be assessed to neither fabricate fictitious errors nor to overlook them [28]. Gunning [29] and Zhai [30] proposed two different methods to overcome this problem and compute reference products. The work in this dissertation leverages the deployed GNSS ground infrastructure from the MGEX to create a monitoring network for offline ARAIM.

A second aspect that this thesis addresses is the variability of the satellite ephemeris and clock errors. Both [26] and [23] illustrated the fluctuations on a monthly basis for GPS range error. The two studies deduced that sample correlation and data independence were behind that behavior. Understanding the nature of this correlation and the difference among satellites and constellations is also a goal within this document.

A key element of the GNSS SoL applications is the error overbound. In the GNSS integrity literature two extensively used bounding methods can be found: Gaussian

CDF bounding [31] and Gaussian Pair overbounding [32]. Both methodologies replace the unknown true error distribution by a Gaussian with standard deviation σ_{ob} which preserves its bounding properties after convolution in the position domain. In order to account for non-zero mean and shifted-median errors distributions, the pair overbounding introduced the so-called nominal bias b_{nom}. The pair overbounding theorem has been recently revisited in [33] where a relaxation of the bounding premises is proposed leading to a less conservative bound. The three previous overbounding methodologies have one common denominator; they do not account for error sample correlation and independence. Understanding how integrity monitoring shall inflate error bounds based on the amount of independent data falls within the scope of this thesis. Supported by a Bayesian inference analysis, this work proposes a simple modification of the Gaussian overbound for ARAIM which leads to better availability performance of the navigation system.

1.5 Dissertation Outline and Contributions

Chapter 1 - current section - provides the introduction of this dissertation. Chapter 2 covers the basic notions of MFMC GNSS positioning. It also provides the fundamentals of legacy RAIM and its evolution to today's state of the art ARAIM along with its different architectures. Chapter 3 proposes a technique to use existing GNSS ground infrastructure to validate orbit reference data and to generate precise clocks for both GPS and Galileo. In addition it details the methodology to compute orbit and clock errors along with the definition of satellite range error for integrity. Chapter 4 applies this monitoring methodology to characterize GPS and Galileo service history up to current dates. Chapter 5 analyzes satellite range error correlation and number of effectively independent samples. Chapter 6 carries out a Bayesian inference analysis of the data in order to determine the effect of correlation on Gaussian overbound. Chapter 7 collects inputs from the previous sections and proposes an overbounding methodology based on Multi Gaussian distributions implying a slight modification in the MHSS algorithm. Finally, Chapter 8 provides the main conclusions of this thesis and the future work to be developed.

The major contributions of this dissertation can be summarized in the following six subsections.

1.5.1 Design of a Validation Method for Using a non-Dedicated Network of GNSS Receivers for ISM Generation

We develop a technique to validate International GNSS Service (IGS) precise products applied in the characterization of the GPS and Galileo constellation performance and fault detection. First this methodology compares precise orbits coming from three different MGEX analysis centers and contrasts the level of agreement among them. The validated orbits are used along with the code and phase observations collected by a set of ground stations to simultaneously estimate receiver biases and satellite time

offsets. Once the network is synchronized, the retrieval of the missing orbit and clock products is attempted. Results will show that with a simple snapshot based model, orbit and clock products can be validated to decimeter level. The ultimate goal of this methodology is to serve as an integrity layer between the MGEX external products and the ISM generation.

1.5.2 Characterization of GPS and Galileo Service Nominal Performance

For each individual GPS and Galileo satellite, by comparing precise orbits to validated broadcast ephemeris data, we compute the SISRE which needs to be overbounded by the User Range Accuracy (URA) and Signal-in-Space Accuracy (SISA) value included in the ISM. Over ten years of service history data for GPS and four years for Galileo are computed in this analysis, showing that range error is mainly driven by satellite's clock performance. Results reveal that orbit and clock error distributions are non-zero mean on a monthly basis, although biases tend to reduce as sample set size increases. This observation provides the motivation to analyze the error correlation.

1.5.3 Determining the Time between Effective Independent Samples for GPS and Galileo Satellite Ranging Errors

We propose a technique to determine the time between effective independent samples based on estimation variance analysis. For GPS and Galileo satellite orbit and clock errors we determine the time between effectively independent samples finding significant discrepancies among them. Results will show how SISRE correlation exhibits substantial differences between GPS and Galileo satellites based on the onboard clock type. An amplitude spectral analysis of the range error shows how orbit errors transfer into user range creating 12-hour harmonic components (14 hours in the case of Galileo).

1.5.4 Quantifying the Impact of Sample Correlation on SISRE Overbound

We derive an analytical expression of the range error CDF based on the number of effectively independent samples. Using Bayes' theorem with a noninformative prior distribution of the standard deviation, we compute the factor by which the Gaussian distribution needs to be inflated to account for the sample independence. Analytical results will illustrate that the conditioned distribution matches the Gaussian CDF when the number of independent samples reach approximately 350. These results will show that the fact that Galileo SISRE presents a significantly shorter decorrelation time than GPS will speed up the SISRE characterization based on service history to support ARAIM.

1.5.5 Developing a Multi-Gaussian Overbound

We leverage the knowledge of the error distribution to generate an adaptive MG range overbound. We propose to use two weighted Gaussian distributions with different standard deviations σ: one with smaller $\sigma_c \sim$ 0.2-0.4 m to bound the core of the distribution and one with larger $\sigma_t \sim$ 1.2-2 m. For a given range error distribution, the separation between core and tail sections will be given by the weighting factor w_c which ranges between 0.90-0.99. The determination of the individual standard deviations are based on the results of the Bayesian inference analysis. Since the MG overbound is a linear combination of two Gaussian distributions in the range domain, the convolution in the position domain guarantees a safe overbound. The comparison between the traditional Gaussian and MG overbounds shows that tighter and equally safe protection levels can be achieved with a core/tail partition of the data having a positive impact on the system availability.

1.5.6 Prototyping an ISM Generation Method for Offline ARAIM

We combine the five prior contributions into an ISM generation method which accounts for sample correlation and core-tail error distribution. With a minor modification of the MHSS algorithm, we propose three different methods to perform the MG overbound. The first one is the inclusion of the three parameters σ^c_{ob}, σ^t_{ob}, and w_c. The second option, a compromise, is to broadcast just σ^c_{ob} and σ^t_{ob} having w_c hard-coded within the user algorithm. The third one, the simplest, does not require a modification of the user algorithm by assigning $\sigma_{\text{URA}} = \sigma^t_{\text{ob}}$ and $\sigma_{\text{URE}} = \sigma^c_{\text{ob}}$. The three methods are compared to the state of the art SG bounding showing how better availability figures can be achieved with a slight modification of the ISM.

2 Advanced Receiver Autonomous Integrity Monitoring Concept

This chapter provides the basic notion of GNSS positioning under a dual constellation scenario along with its ranging error sources. The least square estimator serves as an introduction for the measurement redundancy and consistency idea. Then, the original RAIM concept is introduced describing how it evolved from the initial SFSC to today's MFMC Advanced RAIM. In addition, this chapter includes a detailed description of the different ARAIM architectures and how they impact the ISM design and dissemination. Particularly, it focuses on the ground segment of the offline ARAIM architecture setting the basis for the work developed within the following chapter of this dissertation.

2.1 GPS-Galileo Multiconstellation Scenario

Navigation satellites are equipped with signal generators which broadcast electromagnetic waves traveling from space to users and GNSS ground segments; the so-called Signal-in-Space (SIS). Modernized GPS satellites disseminate four different signals for civilian use; L1 centered on 1575.42 MHz frequency, L2 and L2C centered on 1227.60 MHz, and L5 centered on 1176.45 MHz. Respectively, Galileo Open Service (OS) is provided through three signals for civilian use; E1 centered on 1575.42 MHz, E5a centered on on 1176.45 MHz, and E5b centered on 1207.14 MHz. These frequency bands are reserved and protected against interference within the Aeronautical Radio Navigation Service (ARNS). This multi-GNSS scenario is designed for interoperability and compatibility between GPS and Galileo constellations this being the reason why L1/E1 and L5/E5a are transmitted in exactly the same frequency within the L-band. These two pairs of signals form the Multi-Frequency Multi-Constellation scenarios for GNSS-based aviation that this dissertation works with.

Satellites are equipped with precise onboard atomic clocks which enable the system to identify the signal time of transmission. By estimating the time elapsed between transmission and reception, users retrieve the so-called *pseudorange* measurements. Satellites also provide to users navigation data which contain information regarding satellite ephemeris, clock bias, and health status. As depicted in Figure 2.1, combining ranging measurements from several satellites, users can determine their 3-D position along with their receiver clock bias. Technically, only four satellites (five if two constellations are used) would be necessary to calculate the position and time solution. It is here where the autonomous integrity monitoring capability resides; the

fact that GNSS provides more ranging measurements than strictly necessary grounds the RAIM concept.

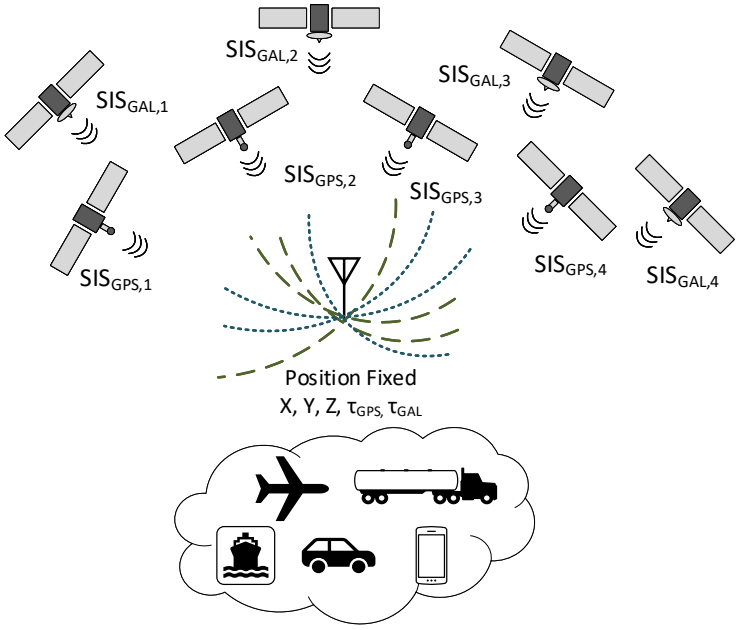

Figure 2.1: Concept of GNSS Positioning

2.1.1 Measurement Model

GNSS receivers provide two types of pseudorange measurements; code (ρ) and phase (φ). Receivers obtain code measurements by aligning the received GNSS signal with the code replica in their database and then computing the difference between reception and transmission time of the signal. Because receiver and satellite clocks are not synchronized, these measurements are biased. Let γ be the travel time for a given GNSS signal received at time t measured in system time. The time in which this signal was emitted by the satellite is $t_e(t-\gamma)$ and $t_r(t)$ is the reception time measured by the user's clock. Then the pseudorange can be defined as the apparent travel time as

$$\rho(t) = c\,[t_r(t) - t_e(t-\gamma)] \tag{2.1}$$

with c being the speed of light in vacuum. Since emission and reception times are referred to satellite and user clocks, respectively, they can be commonly expressed in GNSS system time. Accounting for the corresponding satellite (δ) and receiver (τ) bias

$$\rho(t) = c\,[\tau(t) - \delta(t-\gamma)] + \nu_\rho(t). \tag{2.2}$$

The first term of (2.2) can be modeled as the sum of the true range $R(t, t-\gamma)$, the tropospheric delay $T_d(t)$, and the ionospheric delay $I_d(t)$ that signals experience during their propagation through the atmosphere. True range is the geometric difference between satellite position at emission time $\boldsymbol{x}^s(t-\gamma)$ and user position at reception time $\boldsymbol{x}_r\ (t)$. In order to obtain reliable measurements, the GNSS operator must accurately predict satellite orbit and clock states and encapsulate them within the navigation message to be applied by users. Introducing these terms in (2.1) the code measurement model takes the following form

$$\rho = R + c\,[\tau - \delta] + T_d + I_d + \nu_\rho. \tag{2.3}$$

Note that for simplicity, we omitted the time reference t in the previous expression. The term ν_ρ accounts for the set of nominal range errors that can affect the code measurements and it is discussed in the Section 2.1.2.

GNSS receivers also provide carrier phase measurements which are inherently more precise than code measurements. Users are able to compute the phase difference between the GNSS carrier signal at the time of emission $\phi^s(t-\gamma)$ and the receiver generated carrier at the time of reception $\phi_r(t)$. Analogous to the code definition in (2.1), the phase difference can be written in terms of the emission and travel time as

$$\phi(t) = \phi_r(t) - \phi^s(t-\gamma) + N_\phi. \tag{2.4}$$

Phase differences are intrinsically ambiguous since there is no *a priori* information about the number of full cycles N_ϕ elapsed between emission and reception. This is the so-called *integer ambiguity*. For a given GNSS signal centered in the frequency f and with a corresponding wavelength λ, the equation above can be expressed in units of distance as

$$\lambda\phi(t) = \lambda\,[\phi_r(t) - \phi^s(t-\gamma) + N_\phi] = R(t, t-\gamma) + \lambda N_\phi. \tag{2.5}$$

We can now include satellite and receiver clock biases along with the tropospheric and ionospheric delay to obtain a closed form of the carrier phase measurement equivalent to (2.3). In order to express the phase measurements in meters, let us rename the terms including λ in (2.5) as φ and η

$$\varphi = R + c\,[\tau - \delta] + T_d - I_d + \eta + \nu_\varphi. \tag{2.6}$$

Terms T_d and I_d are identical to the ones affecting code measurements in (2.3). While the troposphere introduces the same delay in code and phase measurements, the ionosphere defers code but accelerates phase, this being the reason for the negative sign in expression (2.6). The full derivation of the measurement models which this subsection is based on can be found in Chapter 5 of [34]. Section 3.3 in the next chapter points out the challenges of using carrier phase measurements and how to apply an Ionosphere Free Geometry Free (IFGF) linear combination to implement them in our proposed ARAIM ground segment.

2.1.2 GNSS Error Sources

There are several potential sources of errors that can affect GNSS signals. They have been clustered in the corresponding terms ν_ρ and ν_φ for code and phase measurements in Equations (2.3) and (2.6). Ultimately, aviation users (and GNSS users in general) are more concerned about how these errors translate into their position solution accuracy and integrity. In ARAIM-based navigation, the knowledge and characterization of these inaccuracies play a paramount role with this being one of the goals of this dissertation. These GNSS error sources can be classified in four types. First, errors related to erroneous navigation message and/or malfunctions in the control segment including ephemeris and clock errors or unflagged maneuvers. Second, errors related to the satellite payload behavior including signal deformation and onboard clock anomalies. The third type of errors are those linked to signal propagation anomalies including tropospheric and ionospheric delays. The fourth type are errors affecting GNSS signals at the receiver proximity.

Orbit and clock errors are normally the ones that drive constellation performance. Their characterization has been a vast topic of research within the GNSS integrity literature ([35], [2], [36]). Chapters 3 and 4 provide a comprehensive analysis of how these errors are generated and their impact on the range overbound. Results will illustrate that modernized GPS and Galileo satellites show typical 1-σ values below 50 cm.

When GNSS signals travel through the atmosphere, the electrons and water particles contained in the ionosphere and troposphere create delays in the signal propagation that need to be modeled. Because of the large magnitude of the ionospheric delay (2-10 m in the zenith direction, highly depending on the atmospheric activity) and the impact that it has on the Single Frequency (SF) service, several models have been developed through the years. The most widely applied for SF GPS is the Klobuchar model, first introduced in [37]. The European Commission, recommends the use of the NeQuick electron density model developed by the Abdus Salam International Center of Theoretical Physics and the University of Graz [38]. The major advantage of dual frequency measurements is the ability of working around the ionospheric delay by creating the so-called Ionosphere Free (IF) linear combination. Since the ionosphere is dispersive (the delay depends on the signal frequency), ARAIM users can eliminate the first order effects at the expense of increasing the receiver noise level.

On the contrary, troposphere is a non-dispersive media so the associated delay is independent of the carrier frequency. Tropospheric delays are smaller and less variable than the ionospheric ones and their models are typically more accurate. There are unpredictable variations of atmospheric parameters that can alter the accuracy of the models like changes in the temperature, moisture, or barometric pressure. For aviation, a widely used tropospheric model is included in the Radio Technical Commission for Aeronautics (RTCA) GPS/WAAS Minimum Operational Performance Standards (MOPS) [39]. A full overview of the physics of the atmosphere can be found in Chapter 6 of [8].

Regarding the errors that affect the signals in the receiver proximity, multipath is the most relevant one. Multipath is the event in which a given GNSS signal reaches the receiver antenna via two or more directions due to reflections off of surrounding elements. The reflected signals travel a longer path than the original ones making them delayed and weaker (depending on the reflecting surface) copies. Although multipath impacts both code and phase pseudoranges, the effect on the former is significantly larger. Multipath is highly dependent on the actual environment in which the GNSS receiver operates. For aviation users, aircraft fuselage and wings are the primary source of multipath which is fundamentally different from the environment that surrounds a ground monitoring station. The use of modernized GNSS signals, beamforming techniques [40], and multipath limiting antennas [41] can reduce the effect of multipath range error to values below 30 cm. Chapter 15 in [8] provides a full description of the physicality behind the multipath effect.

Receiver noise term refers to all the random errors generated within the receiver hardware including antenna, amplifiers, and cables. The signal distortion can also occur within the receiver circuitry and it is responsible for the introduction of code and phase biases. These biases are inherently larger for code than for phase measurements and have the particularity of showing the same magnitude for receivers with the same configuration (i.e., same correlator spacing, bandwidth). The difference of the range biases between measurements in two different frequencies is called Inter-Frequency Bias (IFB). In the case of a non-nominal signal distortion, the so-called *signal deformation* event, detection by a monitoring network is not guaranteed unless hardware diversification is ensured through different receiver configurations. Code carrier incoherence and look-angle-dependent errors are also less frequent sources of error contemplated within WGC [21].

2.1.3 Range Error Models

A key aspect of SoL operations is the characterization and bounding of feared events for GNSS. Many of the errors listed in the previous sections have consolidated models with proved effectiveness over the years, like tropospheric and ionospheric delay. Although accurate, these mathematical representations always leave unmodeled parts that can be bounded in magnitude. Attending to its behavior, residual errors can be broken down in two components: random errors and biases. This distinction is quite useful in the frame of range overbounding since, as Rife established in [32], the error envelope is normally generated with two biased Gaussian distributions. More details regarding overbounding theory and how these nominal biases are bounded in magnitude are given in Chapter 6.

In the previous section, neither code (2.3) nor phase (2.6) measurement equations accounted for the offset related to signal generation. As supported by the Signal Quality Monitoring (SQM) analysis carried out in [42], satellite and receiver instrumental biases are not fully independent since they are linked through the transfer function of the emission, transmission, and reception of the signal. For the purpose of integrity monitoring, it is acceptable to follow IGS convention and break it into satellite

($B_{\rho f}^{\ i}$, $B_{\varphi f}^{\ i}$) and receiver contributions ($B_{\rho\, j,f}$, $B_{\varphi\, j,f}$) as indicated in [43]. For a given signal from a satellite i recorded by a receiver j in a frequency f, code and phase measurements can be expanded in the following forms

$$\rho_{j,f}^{i} = R_j^i + c\left[\tau_j - \delta^i\right] + T_{dj}^{\ i} + I_{dj}^{\ i} + B_{\rho\, j,f} - B_{\rho f}^{\ i} + \nu_{\rho\, j,f}^{\ i} \tag{2.7}$$

$$\varphi_{j,f}^{i} = R_j^i + c\left[\tau_j - \delta^i\right] + T_{dj}^{\ i} - I_{dj}^{\ i} + \eta_{j,f}^{i} + B_{\varphi\, j,f} - B_{\varphi f}^{\ i} + \nu_{\varphi\, j,f}^{\ i}. \tag{2.8}$$

The phase bias and integer ambiguity terms in (2.8) need to be estimated together; Section 3.3 discusses a method to work around this issue fitting the accuracy levels that we need for integrity monitoring. It is important to remark that the presence of those biases is more relevant when using receivers with different configurations. For example, when monitoring constellation performance through a network of receivers, an accurate estimation of satellite orbit and clock states shall account for these effects. When performing pseudorange-based single-point positioning, the term $B_{\rho\, j,f}$ will be commonly absorbed in the receiver clock estimation while the term $B_{\varphi f}^{\ i}$ will be partially modeled by the broadcast satellite clock model. The terms $\nu_{\rho\, j,f}^{\ i}$ and $\nu_{\varphi\, j,f}^{\ i}$ account for residual errors still present in code and phase measurements. Typically, they are modeled by zero-mean Gaussian distributions as $\nu_{\rho\, j,f}^{\ i} \sim \mathcal{N}\left(0, \left(\sigma_{\rho,j,f}^{i}\right)^2\right)$ and $\nu_{\varphi\, j,f}^{\ i} \sim \mathcal{N}\left(0, \left(\sigma_{\varphi,j,f}^{i}\right)^2\right)$ where the standard deviations collect the contribution from the listed error sources as

$$\left(\sigma_{\rho,j,f}^{i}\right)^2 = \left(\sigma_{\mathrm{orb,clk}}^{i}\right)^2 + \left(\sigma_{\mathrm{tropo},j}^{i}\right)^2 + \left(\sigma_{\rho,\mathrm{user},j,f}^{i}\right)^2 \tag{2.9}$$

$$\left(\sigma_{\varphi,j,f}^{i}\right)^2 = \left(\sigma_{\mathrm{orb,clk}}^{i}\right)^2 + \left(\sigma_{\mathrm{tropo},j}^{i}\right)^2 + \left(\sigma_{\varphi,\mathrm{user},j,f}^{i}\right)^2 \tag{2.10}$$

The term $\sigma_{\mathrm{orb,clk}}^{i}$ provides an overbound for satellite i orbit and clock errors in the range domain (further discussion in Annex A). Chapters 5, 6, and 7 cover the determination of this value based on GNSS service history and an associated overbounding methodology for offline ISM generation. In the current multi-GNSS scenario, $\sigma_{\mathrm{orb,clk}}^{i}$ is provided within the broadcast navigation message, $\sigma_{\mathrm{URA}}^{i}$ for GPS, and $\sigma_{\mathrm{SISA}}^{i}$ for Galileo. The rest of the terms in (2.9) and (2.10) are based on models provided in Annex A along with the atmospheric delays. The value $\sigma_{\varphi,\mathrm{user},j,f}^{i}$ accounts for the user User Range Error (URE) budget for multipath and noise error. Multipath and noise for phase measurements are inherently smaller than for code observations at the expense of being ambiguous. Typically, phase multipath and noise RMS stays between 0.5-1 cm while multipath and noise RMS for SF measurements ranges between 0.5 and 1 m (1.5-2.6 m for dual frequency observations).

Because the ionospheric delay is inversely proportional to the square of the carrier frequency f, ARAIM users leverage the multi-frequency GNSS scenario to create the IF linear combination. For a pair of generic GNSS signals in frequencies f_{A} and f_{B}, the IF code and phase linear combination can be computed as

$$\begin{aligned}\rho_{j,\mathrm{IF}}^{i} &= \frac{f_{\mathrm{A}}^2}{f_{\mathrm{A}}^2 - f_{\mathrm{B}}^2}\rho_{j,\mathrm{A}}^{i} - \frac{f_{\mathrm{B}}^2}{f_{\mathrm{A}}^2 - f_{\mathrm{B}}^2}\rho_{j,\mathrm{B}}^{i} \\ &= R_j^i + c\left[\tau_j - \delta^i\right] + T_{dj}^{\ i} + B_{\rho\, j,\mathrm{AB}} - B_{\rho\mathrm{AB}}^{\ i} + \nu_{\rho\, j,\mathrm{AB}}^{\ i}\end{aligned} \tag{2.11}$$

$$\begin{aligned}\varphi^i_{j,\mathrm{IF}} &= \frac{f_\mathrm{A}^2}{f_\mathrm{A}^2 - f_\mathrm{B}^2}\varphi^i_{j,\mathrm{A}} - \frac{f_\mathrm{B}^2}{f_\mathrm{A}^2 - f_\mathrm{B}^2}\varphi^i_{j,\mathrm{B}} \\ &= R^i_j + c\left[\tau_j - \delta^i\right] + T_d{}^i_j + \eta^i_{j,\mathrm{AB}} + B_{\varphi_{j,\mathrm{AB}}} - B_{\varphi}{}^i_{\mathrm{AB}} + \nu_{\varphi}{}^i_{j,\mathrm{AB}}.\end{aligned} \tag{2.12}$$

This IF linear combination has the disadvantage of enlarging the receiver noise and multipath by a factor of almost three. This can be mitigated by using carrier phase measurements to smooth the code noise and multipath. For SoL applications, it is important to acknowledge that the application of carrier phase smoothing introduces the code-carrier divergence fault in the threat space. Chapter 7 and Annex A provide further details on how ARAIM users bound the range error nominal bias with the introduction of the b_{nom} term.

2.1.4 Position Velocity and Time Solution and Least Square Estimator

The estimation of a Position Velocity and Time (PVT) solution is executed by user algorithms employing pseudorange measurements (code, phase, or both) and navigation data. When this estimation is carried out with no external augmentation, it is called *standalone* GNSS. PVT estimation is performed on a snapshot basis using knowledge from prior epochs to accelerate the convergence of the solution. For a given epoch, let a multi-GNSS user collect n_A and n_B pseudorange code measurements from constellation A and B, the linearization of the observation model can be written in a matrix form as (Chapter 5 of [34])

$$\boldsymbol{z} = \boldsymbol{G}\mathbf{x} + \boldsymbol{\nu}. \tag{2.13}$$

Measurement equations can be separated in two blocks corresponding to each constellation

$$\begin{bmatrix}\boldsymbol{z}_\mathrm{A} \\ \boldsymbol{z}_\mathrm{B}\end{bmatrix} = \begin{bmatrix}\boldsymbol{G}_\mathrm{A} \\ \boldsymbol{G}_\mathrm{B}\end{bmatrix}\mathbf{x} + \begin{bmatrix}\boldsymbol{\nu}_\mathrm{A} \\ \boldsymbol{\nu}_\mathrm{B}\end{bmatrix} \tag{2.14}$$

where $\boldsymbol{G}_\mathrm{A}$ and $\boldsymbol{G}_\mathrm{B}$ are the geometry matrices $n_\mathrm{A} \times m$ and $n_\mathrm{B} \times m$ and $\mathbf{x}$ is the $m \times 1$ state vector containing user position and receiver clock biases τ_A and τ_B given that each constellation runs on its own system time. The terms $\boldsymbol{\nu}_\mathrm{A}$ and $\boldsymbol{\nu}_\mathrm{B}$ are $n_\mathrm{A} \times 1$ and $n_\mathrm{B} \times 1$ measurement error vectors defined by expression (2.9).

A Weighted Least-Squares Estimator (WLSE) is used to compute the position solution and its corresponding estimation covariance. The state estimate vector $\hat{\mathbf{x}}$ and least-squares estimation matrix $\boldsymbol{S}$ are defined as

$$\hat{\mathbf{x}} = \boldsymbol{S}\boldsymbol{z} \tag{2.15}$$

$$\boldsymbol{S} = (\boldsymbol{G}^T\boldsymbol{W}\boldsymbol{G})^{-1}\boldsymbol{G}^T\boldsymbol{W} \tag{2.16}$$

where the weighting matrix $\boldsymbol{W}$ is the inverse of the covariance matrix $\boldsymbol{C}$. This is a diagonal matrix which contains the corresponding σ^i_ρ for each i measurement (2.9). The estimated error vector $\boldsymbol{\varepsilon}$ is defined as the difference between the estimation $\hat{\mathbf{x}}$ and the true state $\mathbf{x}$

$$\boldsymbol{\varepsilon} \equiv \hat{\mathbf{x}} - \mathbf{x}. \tag{2.17}$$

Position error is modeled as a normal distribution based on the covariance matrix $\boldsymbol{P}$

$$\boldsymbol{\varepsilon} \sim \mathcal{N}(0, \boldsymbol{P}) \text{ where } \boldsymbol{P} = (\boldsymbol{G}^T \boldsymbol{W} \boldsymbol{G})^{-1}. \tag{2.18}$$

Finally, the estimated error of the single state of interest can be obtained by extracting the corresponding row $\boldsymbol{s}^T$ of the least-squares estimation matrix $\boldsymbol{S}$. Let us particularize for the vertical coordinate (although it can be applied to the horizontal coordinates) as

$$\boldsymbol{s}_v^T = \boldsymbol{\alpha}_v^T \boldsymbol{S} \text{ and } \boldsymbol{\alpha}_v^T = [0\ 0\ 1\ 0\ 0]. \tag{2.19}$$

The vertical estimation error variance σ_v^2 is simply obtained by selecting the corresponding diagonal element of the error covariance matrix. The state of interest, vertical in this example, is obtained as follows

$$\varepsilon_v = \boldsymbol{\alpha}_v^T \boldsymbol{\varepsilon} \tag{2.20}$$

and modeled as a normal distribution

$$\varepsilon_v \sim \mathcal{N}\left(0, \sigma_v^2\right) \text{ where } \sigma_v^2 = \boldsymbol{\alpha}_v^T \boldsymbol{P} \boldsymbol{\alpha}_v. \tag{2.21}$$

The definitions in this section have only attended to the nominal range error in the presence of no fault events for stand alone GNSS solution. Note that the nominal receiver and satellite dependent biases $B_{\rho_{j,\mathrm{AB}}}$ and $B_{\rho^i_{\mathrm{AB}}}$ introduced in (2.11) are typically absorved by the receiver clock bias estimation. This leads to an unbiased position error as reflected in (2.18). Section 2.3 extends this approach under a generic fault hypothesis.

2.2 Principles of Integrity Monitoring

The concept of integrity self-monitoring is grounded on the fact that GNSS users have more measurements available than strictly necessary to obtain a position solution. This makes the system of equations in (2.13) overdetermined. Ultimately, users need to guarantee navigation safety evaluating the risks associated to their position solution. The integrity risk or Probability of Hazardous Misleading Information (PHMI) is defined as the joint probability of the estimated error ε_l being larger than a specified alert limit AL while the test statistic q remains lower than a detection threshold T,

$$P_{HMI} \equiv P\left(|\varepsilon_l| > AL, |q| < T\right). \tag{2.22}$$

Let N_f be the number of fault hypotheses. PHMI can be expressed considering a set of $N_f + 1$ complementary, mutually exclusive hypotheses H_k (including the fault-free hypothesis H_0). Using the law of total probability, [19] establishes the criterion for availability of integrity as

$$P_{HMI} = \sum_{k=0}^{N_f} P\left(\left|\varepsilon_l^{(k)}\right| > AL, \left|q^{(k)}\right| < T_k | H_k\right) p_{f,k} \leq I_{REQ} - P_{NM} \tag{2.23}$$

where $p_{f,k}$ is the prior probability of fault occurrence, H_k is set of hypothesis for $k = 0, .., .N_f$, P_{NM} is the prior probability of the unmonitored events ($P_{NM} \ll I_{REQ}$), and I_{REQ} is the navigation in integrity requirement from Table 1.1. Equation (2.23) accounts for the contribution of each fault hypothesis to the total integrity risk. The ARAIM user algorithm in [3] describes how to determine the subset of fault hypotheses for a given geometry and their associated probabilities.

The magnitude of the detection threshold is set by the false alarm probability which is evenly distributed among all fault hypotheses. The probability allocation must fulfill the continuity requirement from Table 1.1 as

$$\sum_{k=0}^{N_f} P\left(\left|q^{(k)}\right| \geq T_k \mid H_k\right) \leq C_{REQ}. \tag{2.24}$$

For a given position solution with an associated error and test statistic, Figure 2.2 illustrates the four situations that can be encountered. The top left area represents the situations in which users are not warned of excessive position error. The probability of being in that area is the integrity risk. The bottom right area contains the false alarm cases. They refer to situations in which a position solution is flagged even if it does not represent a threat. The top right area, detection, attends to the cases in which a legitimate alert is raised due to excessive position error. In the bottom left zone, nominal operations, both I_{REQ} and C_{REQ} are met and the approach can be executed.

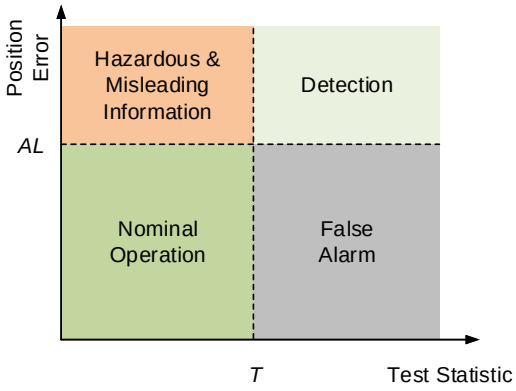

Figure 2.2: PHMI graphical interpretation

An essential aspect of PHMI computation is the selection of the test statistic. In the original concept, RAIM contemplated two approaches: measurement residuals [12] and Solution Separation (SS) [17]. The first one checks the consistency among measurements in the range domain. Based on expression (2.13), in the case of biased or faulted measurements, the residual vector is defined as

$$\boldsymbol{r} \equiv \boldsymbol{z} - \boldsymbol{G}\hat{\mathbf{x}} = (\boldsymbol{I} - \boldsymbol{GS})\boldsymbol{z} = (\boldsymbol{I} - \boldsymbol{GS})(\boldsymbol{\varepsilon} + \boldsymbol{f}) \tag{2.25}$$

where $\boldsymbol{I}$ is the $n \times n$ identity matrix and $\boldsymbol{f}$ is the range fault $n \times 1$ vector associated with a generic fault hypothesis. the residual based RAIM approach is based on the use of the residual vector ($\boldsymbol{r}$) magnitude as a test statistic. The residual-based test statistic q^2 is the weighted norm of $\boldsymbol{r}$

$$q^2 = \boldsymbol{r}^T \boldsymbol{W} \boldsymbol{r}. \tag{2.26}$$

Under a fault hypothesis, the test statistic follows a non-central χ^2 distribution with $(n-m)$ degrees of freedom and a non-centrality parameter λ:

$$q^2 \sim \chi^2 \left(n-m, \lambda^2\right) \text{ where } \lambda^2 = \boldsymbol{f}^T \boldsymbol{W} (\boldsymbol{I} - \boldsymbol{G}\boldsymbol{S}) \boldsymbol{f}. \tag{2.27}$$

Under nominal conditions ($\boldsymbol{f} = 0$), the test statistic follows a central χ^2 distribution ($\lambda = 0$) with $(n-m)$ degrees of freedom $q_{FF}^2 \sim \chi^2(n-m)$. Note that expressions (2.25)-(2.27) have been written in a general form without particularizing for any hypothesis k.

The approach based on solution separation checks the consistency among different position solutions associated with each fault hypothesis k. For a given h_k, with a set of presumptively faulted satellites s, let $\hat{\boldsymbol{x}}^{(k)}$ be the fault-tolerant position solution obtained by excluding those satellites (note that the position vector $\hat{\boldsymbol{x}}^{(k)}$ is part of the state vector solution $\hat{\mathbf{x}}^{(k)}$). This hypothesis h_k is compared against the fault-free h_0 in order to evaluate the test statistic for coordinate l as

$$q_l^{(k)} = \left| \hat{\mathrm{x}}_l^{(k)} - \hat{\mathrm{x}}_l^{(0)} \right| \text{ where } \hat{\mathrm{x}}_l^{(k)} = \boldsymbol{\alpha}_l \hat{\mathbf{x}}^{(k)}. \tag{2.28}$$

Looking at Equations (2.20) and (2.21) it can be deduced that the SS test statistic follows a normal distribution

$$q_l^{(k)} \sim \mathcal{N}\left(\left(\boldsymbol{s}_l^{(k)}\right)^T \boldsymbol{f}, \left(\sigma_{ss,l}^{(k)}\right)^2 \right) \tag{2.29}$$

where

$$\left(\boldsymbol{s}_l^{(k)}\right)^T = \boldsymbol{\alpha}_l^T (\boldsymbol{S}^{(k)} - \boldsymbol{S}^{(0)}) \text{ and } \left(\sigma_{ss,l}^{(k)}\right)^2 = \left(\sigma_l^{(k)}\right)^2 - \left(\sigma_l^{(0)}\right)^2 \tag{2.30}$$

A further discussion regarding the conditions for equivalence between both approaches was done by Joerger in [20]. The MHSS topic is resumed in Chapter 7 where a modification of the ARAIM user algorithm is proposed in order to provide tighter integrity bounds.

2.3 Legacy RAIM

Legacy Receiver Autonomous Integrity Monitoring (RAIM) has been used for lateral navigation since the approval of GPS for supporting oceanic navigation by the Federal Aviation Administration (FAA) in 1995 [44]. Classic RAIM only augments GPS L1 providing error bounds of one nautical mile with high availability for global non-precision lateral navigation service. GPS RAIM is the most extended augmentation

system in GNSS navigation due to its implementation simplicity and autonomy from external inputs, unlike SBAS or GBAS. Since only L1 is approved for use, no IF linear combinations are possible and thus the ionospheric delay must be computed based on the parameters broadcast within the GPS navigation message [45]. Generous error bounds due to ionospheric model uncertainty along with high Dilution Of Precision (DOP) lead to unacceptably large protection levels for vertical navigation.

A major characteristic of traditional RAIM is the omission of multiple faults hypothesis and constellation fault. Looking at Equation (2.23), this is equivalent to imposing $p_{f,k} = 0$ to the corresponding constellation fault hypothesis ($P_{const} = 0$). According to the WGC Milestone 3 Report [3], this assumption is acceptable for GNSS horizontal navigation but not for vertical guidance for precision approach. The next section details how the original RAIM concept has evolved into today's ARAIM.

2.4 Advanced RAIM Fundamentals

The modernization of GPS along with the deployment of emerging GNSS constellations brings the opportunity to expand legacy RAIM to Advanced RAIM. This will allow ARAIM to provide aircraft guidance for enroute, terminal, and approach operations for civil aviation. Based on the same idea of consistency check, ARAIM introduces three new aspects with respect to the legacy system. First, the inclusion of multi-frequency measurements facilitates the use of IF linear combinations to mitigate ionospheric uncertainty that at the same time allows single frequency users (L1/E1-only or L5/E5a-only) to reduce the effect of radio frequency interference. Second, it increases the strength of satellite geometries and consequently provides tighter protection levels. Third, the introduction of a second GNSS allows constellation fault monitoring which is a requirement for vertical guidance.

Figure 2.3 illustrates ARAIM system architecture that comprises space segment, ground segment, airborne segment, and Integrity Support Message [22]. The space segment includes GNSS core constellations operated by their corresponding Constellation Service Provider (CSP). It consists of all processes and infrastructures involved in the constellation operations such as monitoring stations, mission segment, Orbit Determination and Time Synchronization (ODTS), and performance commitments. The ground segment includes the stations employed (exclusively or not) in the monitoring of the constellation performance. It is in charge of collecting the data used as input for the ISM generation. The airborne segment comprises all the aviation users equipped with ARAIM avionics. Finally, the ISM provides the set of inputs which users need to evaluate the performance metrics.

ISM contains satellite and constellation *a priori* fault probabilities along with nominal error bounds for SIS errors. In legacy RAIM, GPS parameters are hard-coded in the receiver making the architecture quite inflexible to changes in the core constellation. Among others, ISM parameters reflect performance commitments guaranteed by the CSP. It is here where the ANSP plays an essential role in the definition of the ARAIM architecture. The differences between them wrap around three aspects:

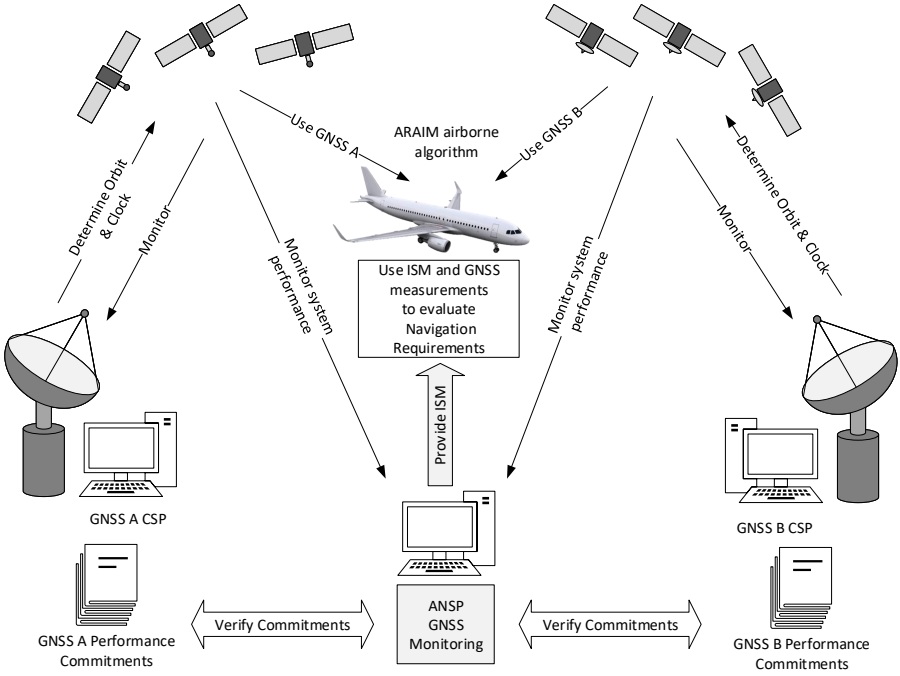

Figure 2.3: ARAIM system architecture

ARAIM ground monitoring segment, duties trade-off between CSP and ANSP, and ISM structure (discussed in Section 2.5).

Depending on the navigation requirements for different phases of flight, WGC identifies two services, Horizontal ARAIM (H-ARAIM) and Vertical ARAIM (V-ARAIM). H-ARAIM targets Required Navigation Performance (RNP) 0.1 and 0.3 for enroute, terminal and non-precision approach operations [1]. H-ARAIM ISM is intended to be updated only when significant changes in the constellations occur like the inclusion of new available GNSS. One of the most relevant features of the H-ARAIM architecture is the acceptance of $P_{const} = 0$ for GPS constellation [3]. V-ARAIM is a significant upgrade with respect to Horizontal ARAIM in targeted operational levels and commitments that users need from both CSP and ANSP. V-ARAIM aspires to provide world-wide LPV-200 precision approach operations through the implementation of one of the two proposed architectures: offline and online ARAIM.

In the offline architecture, ARAIM users fully relay on the performance commitments published by CSPs. In the case of GPS, current operational commitments regarding fault rate and nominal error bounds are set by the GPS Standard Positioning Service Performance Standard [46]. They are based on the level of assurance that the CSP has over its operations and system deployment for both ground and space

segments. Due to the long service history since the publication of these commitments in 2008, they can be substantiated by measurements as done in [24]. This enables GPS CSP to guarantee fault probabilities of $P_{sat} = 10^{-5}$ and $P_{sat} = 10^{-4}$ in accordance with Design Assurance Level (DAL) C as specified by RTCA-DO-178C [47].

In the offline scenario, the ANSP takes a supervisory role by verifying the performance commitments and elaborating the ISM. This dissertation proposes a methodology to monitor GNSSs performance that an ANSP can implement by using already existing ground infrastructures. Chapters 3 through 7 detail the full process from data collection and validation to error statistical analysis and overbounding theory, ultimately leading to the design of an offline ISM.

Online ARAIM is a significant upgrade with respect to the offline architecture. In this case, the ANSP takes a more active role in the performance commitments by carrying out an independent real-time ODTS process for the GNSS constellations. In this architecture the integrity assurance is now shared between CSP and ANSP. This process requires a dedicated ground network that ANSP uses for implementing an SBAS-like architecture with two chains, prediction and integrity. Conceptually, online ARAIM is a simplified version of the SBAS structure with a relaxation of the TTA of 6 seconds due to the onboard detection capability. Online ISM conveys orbit and clock differential corrections that users apply along with the CSP navigation message. Further reading regarding online architecture and operations can be consulted in [22].

2.5 Integrity Support Message for Offline ARAIM

ISM encapsulates integrity parameters describing measurement errors and faults that the ARAIM airborne algorithm uses for performing integrity, accuracy, and continuity checks. The determination of the ISM parameters is a duty of the ARAIM ground segment which is performed by constellation monitoring throughout a global network of stations. ISM design and content are fully dependent on the ARAIM architecture. At the time of writing of this thesis, both the modernized GPS and Galileo constellations plan to broadcast the ISM through CNAV and I/NAV messages, respectively. This implies a direct data connection between ANSP and CSP which would need to be almost real-time in the case of the online architecture (update rate around 10-12 min). One of the advantages of the offline architecture is that the ISM has a latency of one month. This allows human interaction in the generation loop facilitating the implementation of the bounding methodology proposed in Chapters 6 and 7.

ISM parameters can be divided into two sets of values: fault probabilities and nominal error parameters. The first set describes the probability of a satellite, P_{sat}, and a constellation, P_{const}, being faulted at a given time. The second set characterizes the Signal-in-Space nominal error. Three parameters are broadcast within the ISM for the users to overbound the nominal pseudorange error: User Range Accuracy (URA), also called Signal-in-Space Accuracy (SISA), User Range Error (URE), also called Signal-in-Space Error (SISE), and nominal bias for integrity bound b_{nom}.

$\sigma_{\mathrm{URA}}/\sigma_{\mathrm{SISA}}$ is a one-sigma estimate which indicates confidence in the integrity of satellite ephemeris and clock prediction [46]. Correspondingly, $\sigma_{\mathrm{URE}}/\sigma_{\mathrm{SISE}}$ is a one-sigma expected ranging accuracy bound for payload nominal ephemeris and clock errors. These three parameters are combined in the user MHSS onboard algorithm to perform an integrity bound. Chapter 7 proposed a new method based on multigaussian bounding to provide tighter integrity bounds.

3 GNSS Ground Infrastructure to Monitor Constellation Performance

Ground monitoring is the core of constellation performance characterization. The concept of being able to track a full constellation at any time is the key of the offline ISM generation. For that purpose, a worldwide network of GNSS monitoring stations is needed. We present a methodology to make use of the currently deployed Multi-GNSS EXperiment (MGEX) ground infrastructure to illustrate the performance of a future ANSP ground network.

This chapter is organized in three parts. The first one provides an introduction to the MGEX monitoring network. The second part describes a methodology for validating MGEX products before they are employed in the ISM computation. It compares precise orbits coming from three different MGEX analysis centers and contrasts the level of agreement among them. The validated orbits are used along with code and phase observations collected by a set of ground stations to simultaneously estimate receiver biases and satellite offsets. The ultimate goal of this technique is to serve as an integrity layer between the MGEX products and ISM generation. The final part defines the computation of orbit and clock errors for GPS and Galileo satellites and discusses different techniques to calculate the user equivalent range error.

3.1 The Multi-GNSS EXperiment

The deployment of new GNSS constellations fostered the expansion of worldwide ground monitoring infrastructures in the past decade. Space agencies, universities, and institutes from all over the globe comprise a volunteer organization which aims to provide freely available GNSS data and products for the advancement of science, the so-called International GNSS Service (IGS). In 2011, IGS initiated the Multi-GNSS EXperiment (MGEX) which promoted the creation of a GNSS data service for American GPS, Russian GLONASS, European Galileo, Chinese BeiDou, Japanese QZSS, and Indian NAVIC along with SBAS. MGEX is organized by Analysis Centers (ACs) which are managed by individual institutions which compute their own GNSS products and make them publicly accessible [48].

The work in this dissertation makes use of products developed primarily by three European ACs: Centre National d'Études Spatiales (CNES), Center for Orbit Determination in Europe (CODE), and GeoForschungsZentrum (GFZ). In addition, measurement data from Australian, Japanese and Canadian IGS stations are incorporated into this analysis. All the inputs utilized are publicly available through the

IGS/MGEX online repository. More details regarding the generation of these products and their use for SoL applications are discussed in the following sections.

3.2 Using MGEX Products as Input Files

As of September 2018, the current MGEX network has over 200 MFMC GNSS stations deployed globally and managed by over 20 different institutions [49]. As depicted in Figure 3.1, data collected from those stations are transferred to each MGEX analysis center to compute their GNSS products. As pointed out in [48], each AC implements its own algorithms and models (that might differ among institutions) and creates a diverse catalog of products. They include precise orbit and clock files, code and phase measurement data, broadcast navigation data, tropospheric delay, Total Electron Content (TEC) maps, and Differential Code Bias (DCB) files among others. The products of interest for our Dual Frequency (DF) ARAIM offline monitor are described in the following subsections.

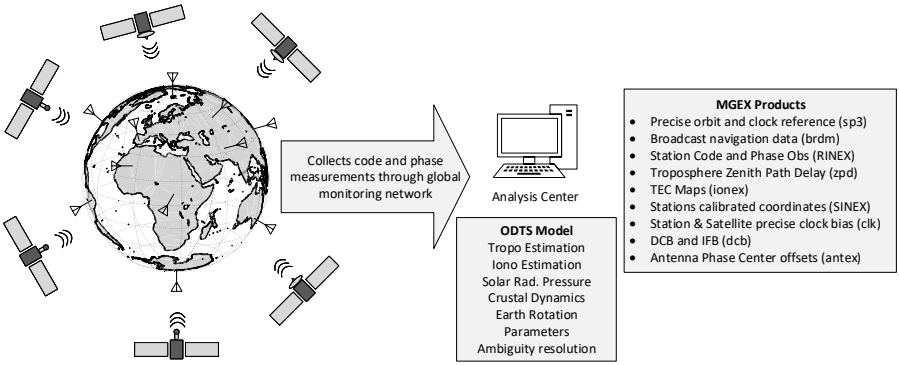

Figure 3.1: MGEX analysis center architecture and products

3.2.1 Precise Reference Orbit and Clocks

Precise Reference Orbit (PRO) datasets contain accurate satellite position and clock information considered as *true* reference data. Each individual MGEX analysis center applies dynamic models in the post-processing satellite orbit determination and they accurately account for astrophysical effects such as solar radiation pressure, variations in the gravitational field, and solar-lunar interaction, reaching a level of agreement on GPS and Galileo orbit products among different centers between 5-10 cm (with exception of outliers [50]). The presence of outliers (can reach meters) in this difference represents an integrity concern for the performance characterization since there is an ambiguous true satellite position. The ANSP must ensure that the reference products employed in the ISM computation are validated.

In order to legitimize the PRO, is proposed a comparison of satellite position from three different ACs products: GFZ (*gbm* files), CODE (*cod* files), and CNES (*grm* files). They elaborate daily sp3 files available in the MGEX online repository [51]. More details about files formatting, naming convention, and sampling rate are given in [48].

While orbit models are concordant among ACs, the same does not apply to satellite clock estimation. Each computation center needs to synchronize their stations by the implicit or explicit establishment of a time reference and posterior alignment to GPS time [52]. This can be done in many ways: having access to the true system time, zero averaging among a set of stations, taking one golden station as reference, etc. Some ACs determine the orbit solution in a first step, estimating the clock kinematically (no dynamic model) afterwards, whereas other ACs estimate orbit and clock in a batch. As a consequence, clock products cannot be directly compared among institutions without removing the common constellation bias. Based on the previous statements and due to the inherent variability of the onboard clock, we propose to validate MGEX clock products by estimating our own receiver and satellite clock bias.

3.2.2 Broadcast Navigation Data

BroadCast Ephemeris (BCE) datasets contain 24 hours of satellite navigation message in Receiver INdependent EXchange (RINEX) 3 Navigation format [53]. The multi-GNSS *brdm* files generated by the Technical University of Munich (TUM)/German Aerospace Center (DLR) contain broadcast navigation data for GPS, GLONASS, Galileo, Beidou, QZSS, SBAS, and NAVIC and are available at [54]. Despite the great effort invested in the generation of these files, inconsistencies in their compilation can lead to fabricated satellite faults that were never present. Along this line, previous work has exposed inconsistencies within *brdm* files which do not fully correspond to the actual message broadcast by the satellites [27]. Discrepancies mainly affected Time of Clock (ToC), Time of Transmission of the Message (TTOM), and Issue of Data Clock (IODC). Two institutions have developed cleaning and validation algorithms for GPS and Galileo BCE. Stanford University provides daily *sugl* files in RINEX 2.11 Navigation format in [55] for GPS satellites. Correspondingly, CNES supplies clean Galileo RINEX 3 Navigation files through its online *brdc* repository [56]. The performance analysis in this dissertation uses these two validated datasets.

3.2.3 Observation Files

The third dataset required to perform our analysis is the ranging measurements. This methodology makes use of the code and phase pseudorange observations collected by a set of 29 MGEX ground stations. Multi-GNSS observations are provided throughout station specific daily RINEX 3 files [53] with a sampling rate of 30 seconds [57]. Galileo data began to be recorded by MGEX stations in early 2013. Prior to that, IGS stations

collected GPS only (or GPS and GLONASS) observations which provided RINEX 2.11 files.

3.2.4 Tropospheric Files

For correcting the Tropospheric effects within the ranging measurements, we need to estimate the corresponding delay. Two possibilities arise: the use of precise post-processed tropo solutions or the use of an atmospheric model (i.e., RTCA-MOPS-229D [39]). The first solution has mm level accuracy whereas the atmospheric model might present centimeter level uncertainty. Precise tropo data is provided in daily Solution INdependent EXchange (SINEX) tropo files [58] computed by the US Naval Observatory (USNO) and available through its online repository [59]. Each file provides Total Troposphere Zenith Path Delay (T_{zpd}) for a large number of MGEX ground stations. By default, our software attempts to ingest SINEX products as inputs, and in case they are not available, the atmospheric model is applied with the corresponding inflation of the ranging error uncertainty (Annex A details the error model assumptions).

3.2.5 ANTEX and SINEX files

According to IGS convention, orbit products apply to satellite Center of Mass (CoM) whereas precise clock states are referred to satellite Antenna Phase Center (APC). Both orbit and clock parameters included in the navigation message are also referred to the satellite APC. As pointed out in [35], it is a very common error to believe that there is a unique satellite APC. Unlike CoM, APC is an adopted point by convention which does not necessarily coincide for precise products and navigation data. Obviating this fact might create inconsistencies in the radial and clock error components which translate into fictitious range error biases. The offsets between CoM and APC are provided through the ANTenna EXchage (ANTEX) files [60] for each individual GPS and Galileo satellite.

Because there are two defined APC, two sets of files will be needed for each constellation. In the case of GPS satellites, the US National Geospatial-Intelligence Agency (NGA) provides an estimation of the offsets used in the generation of the broadcast ephemeris [61]. For Galileo broadcast navigation APC offset, more accurate data are provided by the European GNSS Agency (GSA) in the Galileo Metadata files [62]. Galileo and GPS APC offsets used in the generation of precise orbits and clocks are included in the IGS ANTEX files. Note that through the last decade three conventions have been used: IGS05, IGS08, and IGS14 [63]. Depending on the monitoring period, the applicable file must be properly employed.

In order to execute a constellation monitoring function, precise reference locations of ground stations are needed. This information is provided in daily SINEX for IGS stations in [51]. Table 3.1 summarizes the set of inputs used in the monitoring of both GPS and Galileo constellations. All files utilized here are publicly available through the different IGS analysis center repositories.

Table 3.1: Summary of the input data used for the constellation monitoring for GPS and Galileo

Input Data	GPS	Galileo
Precise Orbit & Clock Data	CODE cod.sp3 files [64]	GFZ gmb.sp3 files [64]
Clean Broadcast Ephemeris Data	Stanford University sulg RINEX 2.11 files [55]	CNES brdc RINEX 3 files [56]
Navigation Data APC Offset Files	NGA Offset Data [61]	GSA Galileo Satellite Metadata [62]
Precise Products APC Offset Files	AIUB University of Bern IGS ANTEX Files [63]	
	Station-specific Files	
Code and Phase Measurement Data	TUM/DLR RINEX 3 observation files [57]	
Tropospheric* Zenith Path Delay	US Naval Observatory SINEX Tropo files [59]	
Reference Station Precise Position	IGS combination of AC global solutions (SINEX files[51])	

*In case missing files use RTCA-MOPS-229D Tropospheric Model [39]

3.2.6 Ground Stations

As mentioned in the previos sections, the Multi-GNSS Experiment provides daily observation data collected through more than 200 ground stations. In this work, the selected network of 29 stations guarantees a minimum Degree of Coverage (DOC) of 4 (an average DOC 6 is provided) which is the minimum number to perform reverse positioning. Figure 3.2 illustrates the location of the selected stations and their corresponding affiliation. Station WTZR located in Wettzell (Germany) and managed by the Bundesamt für Kartographie und Geodäsie (BKG) (German Federal Agency for Cartography and Geodesy) is equipped with external hydrogen maser providing an excellent clock stability for our synchronization purpose. Figure 3.3 indicates the maximum and minimum number of simultaneously tracked GPS and Galileo satellites per ground stations. Note that these figures of merit correspond to the constellations status in July 2017. More detailed information about MGEX stations can be found in [65].

Despite the efforts from different analysis centers, daily RINEX observation files are not always complete or available. Given the large number of stations, it does not represent an issue for our analysis since we can always replace unavailable stations with other facilities without impacting the DOC. However, from an operational ANSP point of view, the access to the data pipe from these stations must be guaranteed for effective monitoring. Actually, a total of 29 stations were selected in order to avoid degradation in the accuracy of the prediction in case of data outage within the online repository.

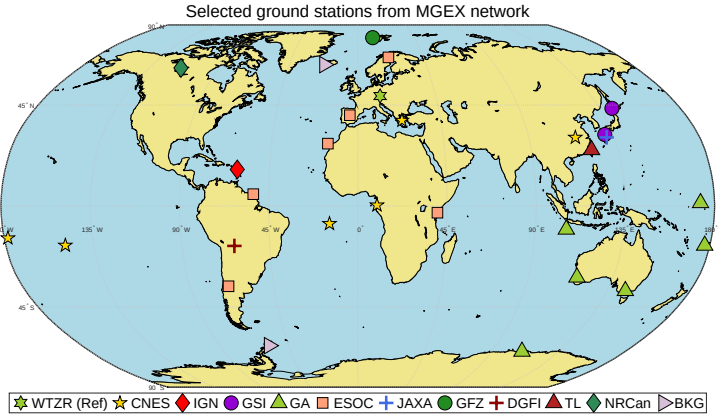

Figure 3.2: Selected MGEX Stations for ARAIM ground network

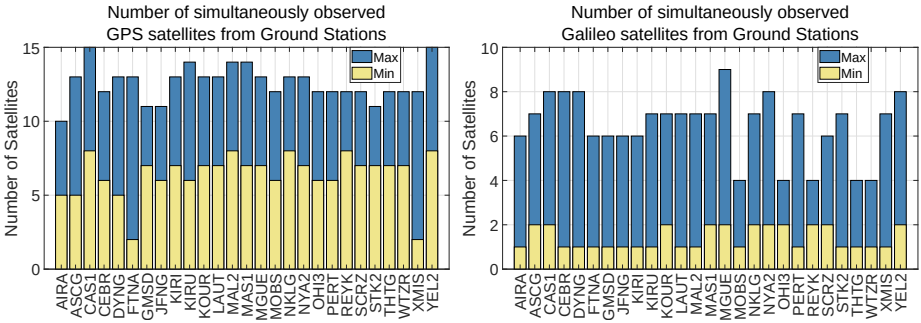

Figure 3.3: Number of simultaneously observed GPS and Galileo satellites from ground stations (as of July 2017)

3.3 Measurement Model

This section formalizes the observation model used in the computation of our own satellite clock reference. The scope of this estimation is not to redo what MGEX analysis centers already provide (years of experience endorse their quality) but to build an integrity layer between those products and the ISM generation. Let us depart from the IF code (2.11) and phase (2.12) observation equations derived in Chapter 2. As discussed, code and phase biases are defined by the transfer function between satellite and receiver and only if two receivers have the same configuration will they experience the same bias for the same satellite. This is not the case of our monitoring network in which at least four different types of multi-GNSS receivers are included. Technically, a reference receiver must be used as bias-free and the rest of the network shall be referred to that one. For the level of accuracy that we target in this work, we split these biases in receiver and satellite contributions and assume that for a given epoch k,

$B^{i}_{f,k}$ can be absorbed in satellite clock bias $\delta^{i,k}$ and $B^{k}_{j,f}$ can be absorbed in receiver clock bias τ^{k}_{j}. The non-common component remains unmodeled and consequently affects the accuracy of our clock estimation. In order to minimize the effect of the residual bias, the code and phase observations are carefully selected to match the GPS ionosphere-free linear combination of L1 and L2 P(Y)-code observations [43]. We will revise this assumption in Section 3.5 and observe how it affects the clock results.

Let us call J the total number of receivers within the network tracking a total number of n_{GPS} GPS and n_{GAL} Galileo satellites. For a given epoch k the goal is estimating a total of $2 \times J$ receiver clock biases and $n_{GPS} + n_{GAL}$ satellite clock biases. Since each GNSS runs on its own system time and given the linearity of the equations, GPS and Galileo clock biases can be solved independently. This option is computationally more efficient since both processes can be parallelized. Without loss of generality, let us write the code and phase IF combinations (frequencies A and B) based on (2.11) and (2.12) for a receiver j tracking a satellite i at epoch k

$$\rho^{i,k}_{j,\mathrm{IF}} = R^{i,k}_{j} + c\left[\tau^{k}_{j} - \delta^{i,k}\right] + T_{d}{}^{i,k}_{j} + \nu_{\rho}{}^{i,k}_{j,\mathrm{AB}} \tag{3.1}$$

$$\varphi^{i,k}_{j,\mathrm{IF}} = R^{i,k}_{j} + c\left[\tau^{k}_{j} - \delta^{i,k}\right] + T_{d}{}^{i,k}_{j} + \eta^{j}_{i,\mathrm{AB}} + \nu_{\varphi}{}^{i,k}_{j,\mathrm{AB}}. \tag{3.2}$$

where the geometric range $R^{i,k}_{j}$ is defined as the norm of the difference between satellite position $\boldsymbol{x}^{i,k}$ at the time of emission and user position at the time of reception $\boldsymbol{x}^{k}_{j}$. Because in this approach satellite and user positions are known and the tropospheric delay is either given by the SINEX Tropo files or modeled, there are only three unknowns in the above equations; the two clock biases and the integer ambiguity. Relativistic effects must also be accounted for when modeling the pseudorange equations. There are two components to be added to expressions (3.1) and (3.2); the relativistic clock $\delta^{i,k}_{\mathrm{rel}}$ and path $\Delta^{i,k}_{\mathrm{relpath},j}$ corrections. The first term accounts for sinusoidal variation in the apparent satellite clock and it is defined by GPS Specifications [45] as

$$\delta^{i,k}_{\mathrm{rel}} = -2\frac{\boldsymbol{x}^{i,k}\boldsymbol{v}^{i,k}}{c^2} \tag{3.3}$$

where $\boldsymbol{v}^{i,k}$ is satellite velocity. Not accounting for this effect can lead to errors up to 23 ns in the range observations. The second relativistic term is significantly smaller and accounts for variations in the gravitational field which deviates the signal path from a straight line. The relativistic path correction is defined as [66]

$$\Delta^{i,k}_{\mathrm{relpath},j} = \frac{2\mu_g}{c^2}\ln\left[\frac{|\boldsymbol{x}^{i,k}|+|\boldsymbol{x}^{k}_{j}|+R^{i,k}_{j}}{|\boldsymbol{x}^{i,k}|+|\boldsymbol{x}^{k}_{j}|-R^{i,k}_{j}}\right] \tag{3.4}$$

where μ_g is Earth's standard gravitational parameter. As pointed out in [66], the relativistic path correction is in the order or magnitude of 1-2 cm. Including these two terms in the above equations, IF code and phase observations can be rewritten as

$$\rho^{i,k}_{j,\mathrm{IF}} = R^{i,k}_{j} + c\left[\tau^{k}_{j} - \delta^{i,k} - \delta^{i,k}_{\mathrm{rel}}\right] + \Delta^{i,k}_{\mathrm{relpath},j} + T_{d}{}^{i,k}_{j} + \nu_{\rho}{}^{i,k}_{j,\mathrm{AB}} \tag{3.5}$$

$$\varphi_{j,\mathrm{IF}}^{i,k} = R_j^{i,k} + c\left[\tau_j^k - \delta^{i,k} - \delta_{\mathrm{rel}}^{i,k}\right] + \Delta_{\mathrm{relpath},j}^{i,k} + T_{d_j}^{i,k} + \eta_{j,\mathrm{AB}}^{i} + \nu_{\varphi_{j,\mathrm{AB}}}^{i,k}. \tag{3.6}$$

The ambiguity resolution is a broad topic within GNSS, in particular for Precise Point Positioning (PPP) applications using carrier phase measurements. Precise MGEX orbit products are generated by means of carrier phase positioning which requires ambiguity fixing methods. As we mentioned before, this methodology does not aim to redo what is already achieved by MGEX but to propose a validation method for integrity purposes. In this work we treat the ambiguity as a nuisance parameter that needs to be accounted for. The term $\eta_{j,\mathrm{AB}}^{i}$ is a linear combination of the two ambiguities in frequencies A and B. As long as no cycle slips occur in one of the frequencies, $\eta_{j,\mathrm{AB}}^{i}$ remains constant over the tracking period. Two options to deal with the ambiguity term arise. The first one is estimating it in a batch filter imposing its constant behavior over time. The second option, and the one followed in this chapter, is to substitute it throughout the Ionosphere Free Geometry Free (IFGF) linear combination

$$\mathrm{IFGF}_j^{i,k} = \rho_{j,\mathrm{IF}}^{i,k} - \varphi_{j,\mathrm{IF}}^{i,k} = \nu_{\rho_{j,\mathrm{AB}}}^{i,k} - \eta_{j,\mathrm{AB}}^{i} - \nu_{\varphi_{j,\mathrm{AB}}}^{i,k}. \tag{3.7}$$

As long as no cycle slip occurs, the IFGF combination provides the constant value of the integer ambiguity linear combination $\eta_{i,\mathrm{AB}}^{j}$ along with time-variant multipath and noise. The geometry-free cycle slip detector defined in [67] is implemented in this work. The 30 second measurement interval provides enough samples to average most of the white noise over a pass. Assuming that $E[\nu_{\rho_{j,\mathrm{AB}}}^{i,k}] \approx 0$ and $E[\nu_{\varphi_{j,\mathrm{AB}}}^{i,k}] \approx 0$, the mean value of the IFGF combination can be written as

$$E\left[\mathrm{IFGF}_j^{i,k}\right] =< \rho_{j,\mathrm{IF}}^{i,k} - \varphi_{j,\mathrm{IF}}^{i,k} >= -\eta_{j,\mathrm{AB}}^{i} - \epsilon_j^{i,k}. \tag{3.8}$$

Note that at the beginning of this section, the satellite-user specific bias contribution was included in $\nu_{\rho_{j,\mathrm{AB}}}^{i,k}$. The constant part of these terms (there are some variations with elevation) will be averaged out in (3.8). The term $\epsilon_j^{i,k}$ accounts for all the remaining errors which are satellite-position dependent and not averaged out over a pass and will be absorbed in $\nu_{\rho_{j,\mathrm{AB}}}^{i,k}$. Introducing (3.8) in (3.6) we arrive to the corrected pseudorange equation $z_j^{i,k}$ as a linear function of the two clock states to estimate, receiver bias τ_j^k and satellite bias $\delta^{i,k}$,

$$\begin{aligned} z_j^{i,k} &= \varphi_{j,\mathrm{IF}}^{i,k} + < \rho_{j,\mathrm{IF}}^{i,k} - \varphi_{j,\mathrm{IF}}^{i,k} > - R_j^{i,k} - T_j^{i,k} + c\cdot\delta_{\mathrm{rel}}^{i,k} - \Delta_{\mathrm{relpath},j}^{i,k} \\ &= c\cdot\tau_j^k - c\cdot\delta^{i,k} + \nu_{\rho_{j,\mathrm{AB}}}^{i,k}. \end{aligned} \tag{3.9}$$

3.3.1 Corrected Pseudorange Modeling

Four terms need to be computed in order to obtain corrected pseudorange $z_j^{i,k}$ in (3.9). The geometric range, tropospheric delay, and relativistic clock and path delay components are a function of satellite-user position and velocity. Since receiver stations are static, the only time variant component is due to satellite motion. As mentioned in Section 3.2.1, GPS and Galileo satellite precise orbits are taken from validated

CODE and GFZ sp3 files. Orbit states are given in discrete samples every 5 or 15 min which in general will not coincide with the time of emission in which we need the satellite position. Consequently, interpolation of sp3 files is required. There are several methods for orbit interpolation but according to [68], nine term Lagrange polynomials are the most suitable ones for 15 minute spaced knots. For a position vector in Earth-Centered Earth-Fixed (ECEF) $\boldsymbol{x}^i$, given a set of $n+1$ knots in t_s, the interpolating polynomial of order n can be expressed as

$$\boldsymbol{x}^i(t) = \sum_{m=0}^{n} \boldsymbol{x}_s^i l_s(t) \text{ where } l_s(t) = \prod_{s=0, s\neq m}^{n} \frac{t - t_s}{t_m - t_s}. \tag{3.10}$$

In addition, as indicated in (3.3), the satellite velocity vector is also needed to compute the relativistic clock component. Although the sp3 format supports satellite velocity data, most of the MGEX PRO only contains position information so the velocity data can be obtained by means of the first derivate of the Lagrange polynomial. The velocity vector in ECEF $\boldsymbol{v}^i$ can be computed as

$$\boldsymbol{v}^i(t) = \sum_{m=0}^{n} \boldsymbol{x}_s^i l_s'(t) \text{ where } l_s'(t) = \sum_{q=0, q\neq m}^{n} \frac{1}{t - t_q} \prod_{s=0, s\neq m}^{n} \frac{t - t_s}{t_m - t_s}. \tag{3.11}$$

A second aspect of the pseudorange modeling is the CoM to APC conversion. Precise reference positions are referred to satellite CoM whereas range observations are measured from satellite APC. The offset between these two points are provided by the antenna files (Table 3.1) in satellite Body-Fixed (BF) frame. Due to satellite motion, the conversion between BF and ECEF is time dependent since the rotation matrix $\boldsymbol{R}_{\mathrm{BF,ECEF}}^{i,k}$ changes for each epoch k due to satellite-earth Line-Of-Sight (LOS). The APC position for a given satellite i in an epoch k $\boldsymbol{x}_{\mathrm{APC}}^{i,k}$ is obtained by the transformation

$$\boldsymbol{x}_{\mathrm{APC}}^{i,k} = \boldsymbol{x}_{\mathrm{CoM}}^{i,k} + \boldsymbol{R}_{\mathrm{BF,ECEF}}^{i,k} \boldsymbol{\Delta}\mathrm{APC}_{\mathrm{BF}}^{i} \tag{3.12}$$

where $\boldsymbol{\Delta}\mathrm{APC}_{\mathrm{BF}}^{i}$ is the satellite APC offset vector provided within the ANTEX files. The computation of the BF to ECEF frame transformation matrix is based on the satellite attitude model detailed in Annex B. Satellite APC also needs to account for the rotation of the ECEF frame during the signal travel time, the so-called Sagnac effect. $\boldsymbol{x}_{APC}^{i,k}$ has to be rotated around the z-axis by an angle of $\omega_E \gamma$ where ω_E is the earth's rotation rate and γ is the travel time defined in (2.1).

Regarding the tropospheric delay, SINEX Tropo files also include discrete values of the Zenith Path Delay (ZPD) for each corresponding monitor station. A simple spline interpolation can be applied to obtain the value at the desired instant t. As mentioned, if the daily SINEX file is not available, the RTCA-MOPS-229D tropospheric model provides a continuous function to compute $T_j^{i,k}$ [39]. Either way, the ZPD needs to be mapped through the slant factor $M\left(\theta_j^{i,k}\right)$

$$T_{d_j}^{i,k} = M\left(\theta_j^{i,k}\right) T_{d_j}^{zpd,k} \tag{3.13}$$

where $\theta_j^{i,k}$ is the satellite i elevation viewed from station j at epoch k. More details regarding models for $T_{d_j}^{zpd,k}$ and $M\left(\theta_j^{i,k}\right)$ are given in Annex A.

Expressions (3.10)-(3.13) provide continuous functions of the four terms $R_j^{i,k}$, $T_{d_j}^{i,k}$, $\delta_{\text{rel}}^{i,k}$, and $\Delta_{j,\text{rel,path}}^{i,k}$ needed to compute the corrected pseudoranges for the observation model in (3.9).

3.3.2 Measurement Error Model

The final term $\nu_{\rho_{j,AB}}^{i,k}$ in (3.9) accounts for four residual error contributions: orbit, troposphere, multipath, and noise for both code and phase measurements. Given that noise and multipath effects for code are typically two orders of magnitude larger than for phase observations, it is legitimate to disregard the phase contribution. In that case, based on the error model from (2.9), the IF code error term can be modeled as a zero mean Gaussian distribution with standard deviation $\sigma_{\rho,j,AB}^{i}$

$$\nu_{\rho_{j,\text{AB}}}^{i,k} \sim \mathcal{N}\left(0, \left(\sigma_{\rho,j,\text{AB}}^{i,k}\right)^2\right) \tag{3.14}$$

where the four contributions are modeled as

$$\left(\sigma_{\rho,j,\text{AB}}^{i}\right)^2 = \left(\sigma_{\text{orb}}^{i}\right)^2 + \left(\sigma_{\text{trop},j}^{i}\right)^2 + K_{\text{user,AB}}\left[\left(\sigma_{\rho_{\text{noise},j,\text{AB}}}^{i}\right)^2 + \left(\sigma_{\rho_{\text{mp},j,\text{AB}}}^{i}\right)^2\right]. \tag{3.15}$$

Note that code error variance is satellite-user specific and changes over time due to satellite elevation. The orbit contribution is associated with the accuracy of the sp3 files and it is provided per satellite within the header of each AC's daily file. The residual troposphere term depends on how the delay has been computed. In the case of SINEX tropo file, it represents the accuracy of the estimation which is also contained in the precise SINEX products. In the case where it has been computed through a tropospheric model, $\sigma_{\text{trop},j}^{i}$ refers to the inaccuracy of that model (see Annex A). The accuracy of the precise tropo reference is typically on the order of 2-5 mm whereas the uncertainty of the model is on the order of 15 cm in the zenith direction. Noise and multipath contributions are highly dependent on the receiver environment. Models for ground and airborne receivers are given in Annex A.

3.3.3 Synchronization Methodology

Let us construct the system of equations gathering each of the measurements in (3.9) in a given epoch k. For a number of J receivers monitoring a constellation of I satellites,

the system of equations is

$$\begin{bmatrix} z_1^1 \\ \vdots \\ z_1^I \\ \vdots \\ z_J^1 \\ \vdots \\ z_J^I \end{bmatrix} = \begin{bmatrix} 1 & 0 & \dots & 0 & -1 & 0 & \dots & 0 \\ \vdots & \vdots & & \vdots & \vdots & \vdots & & \vdots \\ 1 & 0 & \dots & 0 & 0 & 0 & \dots & -1 \\ \vdots & \vdots & & \vdots & \vdots & \vdots & & \vdots \\ 0 & 0 & \dots & 1 & -1 & 0 & \dots & 0 \\ \vdots & \vdots & & \vdots & \vdots & \vdots & & \vdots \\ 0 & 0 & \dots & 1 & 0 & 0 & \dots & -1 \end{bmatrix}^k \cdot c \cdot \begin{bmatrix} \tau_1 \\ \vdots \\ \tau_J \\ \vdots \\ \delta^1 \\ \vdots \\ \delta^J \end{bmatrix}^k + \begin{bmatrix} \nu_{\rho_2^1} \\ \vdots \\ \nu_{\rho_1^I} \\ \vdots \\ \nu_{\rho_J^1} \\ \vdots \\ \nu_{\rho_J^I} \end{bmatrix}^k \tag{3.16}$$

which can be written in a compact way as

$$\boldsymbol{z}^k = \boldsymbol{H}^k \mathbf{x}^k + \boldsymbol{\nu}^k. \tag{3.17}$$

The state vector $\mathbf{x}^k$ contains the set of receiver and satellite clock biases (expressed in meters). The determination of these biases can only be made in a differential way so a time reference must be implicitly established, the so-called *synchronization condition*. In fact, not including this condition will result in a rank deficient observation matrix $\boldsymbol{H}^k$ and the impossibility of solving the system. As indicated in Section 3.2.6, station WTZR equipped with an external hydrogen maser is taken as a reference (Figure 3.2). The synchronization condition is $\tau_{WTZR} = 0$. Note that other possibilities exist, for example the establishment of the zero-mean condition within the constellation where the synchronization equations would be $\sum_{i=1}^{I} \delta^i = 0$.

In order to improve the accuracy of the estimation, the observation system of equations is intentionally overdetermined. For a GPS scenario, there are typically 58-60 total unknowns depending on the number of healthy GPS satellites and whether or not the full 29 stations are operational during that period. Applying an elevation mask of 5 degrees, depending on the site location, each receiver tracks an average of 6-8 simultaneous satellites (Figure 3.3). Typically a total of 180-200 measurements are available to solve 58-60 unknowns making the system overdetermined. Thus, equations (3.17) can be solved using a WLSE approach. An estimation of the clock bias states $\hat{\mathbf{x}}^k$ can be computed as

$$\hat{\mathbf{x}}^k = \left({\boldsymbol{H}^k}^T \boldsymbol{W}^k \boldsymbol{H}^k \right)^{-1} {\boldsymbol{H}^k}^T \boldsymbol{W}^k \boldsymbol{z}^k \tag{3.18}$$

where $\boldsymbol{W}^k$ is the weighting matrix. This is a diagonal matrix whose elements contain the squared inverse of the corresponding $\sigma^i_{\rho,j,AB}$ for each measurement in (3.16). The covariance matrix of the estimation $\boldsymbol{P}^k$ is defined as

$$\boldsymbol{P}^k = \left({\boldsymbol{H}^k}^T \boldsymbol{W}^k \boldsymbol{H}^k \right)^{-1}. \tag{3.19}$$

Each diagonal element of $\boldsymbol{P}^k$ contains the estimation variance of each clock state. This will be used in the next section to contrast our covariance model with the actual accuracy of this methodology.

3.4 Products Validation Algorithm Description

The proposed ANSP products validation scheme is foreseen in three steps: precise orbits consistency check, network synchronization, and satellite data retrieval. Figure 3.4 depicts the data flow between the three repositories and the different modules. This process can be independently applied to GPS and Galileo constellations allowing the parallelization of the process for time optimization.

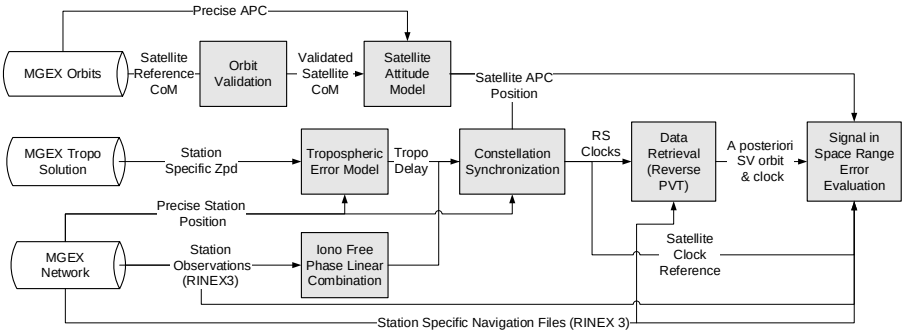

Figure 3.4: ARAIM ground segment architecture

Step 1: Precise Orbit Validation

The algorithm performs a consistency check of the satellite orbits position among the three cited ACs: CODE, GFZ, and CNES. Orbits are validated when the norm of the difference between the analysis centers does not exceed a certain threshold,

$$\Delta^i_{\text{orb}} = \left\| \boldsymbol{x}^{i,\text{AC}_\text{s}}_{\text{CoM}} - \boldsymbol{x}^{i,\text{AC}_\text{p}}_{\text{CoM}} \right\| \leq T_{\text{orb}}. \tag{3.20}$$

In case of discrepancy a majority voting criteria is applied. Based on prior studies which compared orbit products from different ACs ([48] and [52]), 40 cm seems a reasonable value for the validation threshold, T_{orb}. Validation can fail under two circumstances: lack of precise reference orbit or discrepancy between ACs. For both cases the software acts similarly - it excludes the corresponding satellite from the synchronization process and retrieves its position and clock states once the stations are synchronized.

Step 2: Synchronization Process

Once the precise orbits are validated, they are taken as input to build the system of equations (3.17). As pointed out in the previous section, discrete values from sp3 files need to be interpolated and then transformed from satellite CoM to APC using expressions (3.10) to (3.12). As in a typical PVT process, corrected pseudoranges $\boldsymbol{z}^k$ need to be recomputed at the end of each iteration of $\hat{\mathbf{x}}^k$. Once the pseudoranges are properly corrected, the new system of equations in (3.16) is built and the new solution

$\hat{\mathbf{x}}^k$ is computed. Given the large measurement redundancy, it is possible to filter some observations by a simple residual check after the computation of each solution $\hat{\mathbf{x}}^k$ by

$$\boldsymbol{r}_k = \boldsymbol{z}^k - \boldsymbol{H}^k \hat{\mathbf{x}}^k. \tag{3.21}$$

In case certain measurements exhibit large residuals, they are excluded from the synchronization process and a new solution is recomputed. There must be a compromise between exclusion and observability - the system needs to guarantee that reverse positioning (one satellite seen by four stations) is possible. Out of the 180-200 original, 10-15 measurements are excluded which typically correspond to satellites with low elevation. For a given epoch k, the loop would stop once the difference between two consecutive iterations reaches the required level of numerical accuracy which is set to 10^{-7} m. It is also important to mention that for integrity purposes only satellites with healthy signal status are included in this computation (note that MGEX AC disregards satellite health status). Section 3.5 provides more details regarding GPS and Galileo clock estimation results.

Step 3: Data Retrieval

Once the full synchronization is finished, the retrieval of missing data is carried out. Let us remember that orbits were not validated when the difference between two ACs was larger than T_{orb}. Given that our network guarantees a minimum DOC of four, reverse positioning is possible. Equation (3.9) can be written as a function of the satellite position $\boldsymbol{x}^{j,k}$ and clock bias $\delta^{j,k}$

$$\begin{aligned} \tilde{z}_j^{i,k} &= \varphi_{j,\mathrm{IF}}^{i,k} + < \rho_{j,\mathrm{IF}}^{i,k} - \varphi_{j,\mathrm{IF}}^{i,k} > - c\tau_j^k - {T_d}_j^{i,k} + c\delta_{\mathrm{rel}}^{i,k} - \Delta_{\mathrm{relpath},j}^{i,k} \\ &= \left|\left| \boldsymbol{x}_j^k - \boldsymbol{x}^{i,k} \right|\right| - c\delta^{i,k} + \tilde{\nu}_{\rho_{j,\mathrm{AB}}}^{i,k} \end{aligned} \tag{3.22}$$

where $\tilde{\nu}_{\rho_{j,\mathrm{AB}}}^{i,k}$ is a modification the ranging errors model in (3.15) to include the uncertainty of the receiver clock estimation. It is modeled as a zero-mean Gaussian distribution with standard deviation

$$\tilde{\sigma}_{\rho,j,\mathrm{AB}}^{i,k} = \left(\sigma_{\mathrm{syn},j}^k\right)^2 + \left(\sigma_{\mathrm{trop},j}^{i,k}\right)^2 + K_{\mathrm{user,AB}} \left[\left(\sigma_{\rho_{\mathrm{noise},j,\mathrm{AB}}}^{i,k}\right)^2 + \left(\sigma_{\rho_{\mathrm{mp},j,\mathrm{AB}}}^{i,k}\right)^2 \right] \tag{3.23}$$

where $\left(\sigma_{\mathrm{syn},j}^k\right)^2$ is the estimation variance of the reviver clock τ_j^k provided by the diagonal elements of the synchronization covariance matrix $\boldsymbol{P}^k$ in (3.19). As done for user PVT, expression (3.23) can be linearized and a system of equations can be built. For those satellites excluded in Step 1, the reference orbit and clock data retrieval can be archived by applying WLSE to the system of equations

$$\tilde{\boldsymbol{z}}^k = \tilde{\boldsymbol{H}}^k \tilde{\mathbf{x}}^k + \tilde{\boldsymbol{\nu}}^k. \tag{3.24}$$

In this case vector, $\tilde{\mathbf{x}}_k$ contains satellite position and clock states for epoch k and $\tilde{\boldsymbol{H}}_k$ is the observation matrix obtained by the linearization of the observation equation. Note that satellite PVT follows the same principle as that of traditional user PVT. The derivation of the linearized equations will not be included here and can be consulted in Chapter 6 of [34].

3.5 Methodology Performance

This validation methodology for reference products is meant to be applied to modernized GPS L1/L5 and Galileo E1/E5a measurements. At the time of writing of this thesis, only 12 out of 31 operational GPS satellites broadcast L5 signals. In order to use the full currently operational GPS space segment, this methodology is applied to the legacy dual frequency L1/L2 combination. In the case of Galileo, as of September 2018, 17 operational satellites comprise the current space segment. Note that the future ARAIM space segment (Section 2.4) requires fully deployed GPS and Galileo constellations providing L1/L5 and E1/E5a DF measurements.

This section presents the results of this methodology for GPS and Galileo satellites in two subsections. It first illustrates the performance of the orbit validation algorithm from 28-29 February 2016. This period has been selected to exemplify the response of the system when orbits cannot be validated in the case of discrepancy among ACs. The second subsection shows the accuracy of the clock state estimation. For both GPS and Galileo satellites, data from 1-7 July 2017 are used.

3.5.1 Precise Orbit Validation and Data Unavailability Assessment

Figure 3.5 shows the output of the orbit validation process for GPS satellites during 28-29 February 2016. As can be seen, the difference between CODE and GFZ lies well below the 40 cm threshold for all GPS satellites except for SVN43/PRN13. Note that the comparison between CODE and CNES have not been included since they reported similar results. The system reported invalid reference orbits for SVN43 starting at 15:00:00 GPS time on February 28 2016. As seen in Figure 3.5, the disagreement escalates during the next 24 hours reaching a maximum difference of 4.69 m. The fact that ACs do not coincide in their estimation indicates a possible integrity issue.

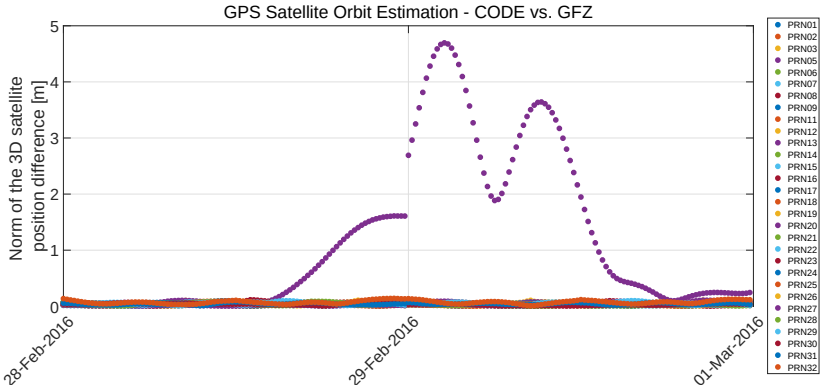

Figure 3.5: Comparison of GPS satellite precise position estimation CODE vs. GFZ showing large discrepancy for SVN43/PRN13

The algorithm would reject any non-validated orbit position and try to retrieve it in Step 3. Let us analyze the availability of the RINEX observation. Figure 3.6 displays the timeline of PRN13 measurements recorded by ground stations during the two day period. As can be observed, SVN43 experienced an outage at 14:30:00 GPS time on 28 February. As mentioned in previous error studies like [2] and [26], orbit position must be accompanied with clock references. In other words, in order to obtain a valid SISRE, both orbit and clock reference data must be available. Looking at the clock information contained in the sp3 files, clock products were available until 14:36:30 GPS time on 28 February. In theory, satellite orbit and clock error for SVN43 could be computed until 14:36:30 GPS time and included in the SISRE distribution. Here is where the true potential of this methodology resides; the employment of observations allows for monitoring the validity of the products that are used to characterize the constellation performance. If we computed orbit and clock errors based on products availability, we would include over six minutes of fabricated data that users never got to see.

As mentioned earlier in this chapter, ACs apply different orbital models for determining satellite position. These estimations can be extended even when no input data are available with its consequent degradation as seen in Figure 3.5. If these six minutes of fictitious error are included in the SVN43 range error analysis they would enlarge the tails of the distribution having a detrimental impact in the range overbounding. This aspect is further addressed in Chapter 7.

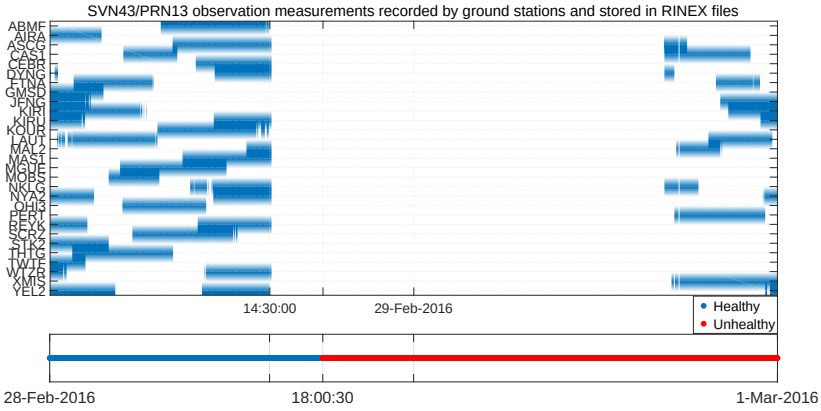

Figure 3.6: SVN43/PRN13 Signal-in-Space outage on February 2016

3.5.2 Network synchronization and accuracy of the estimation

Prior subsection addressed the algorithm's response in case of discrepant orbit products among ACs. Although extremely relevant from an integrity perspective, it does not entail a dense computational load. This subsection addresses the outputs of the synchronization methodology and how the assumptions made in the observation model

in Section 3.3 affect the accuracy of our products generation. In order to have good Galileo coverage, the selected monitoring period is 1-7 July 2017 where 13 Galileo satellites were operational. During this period, only 27 out of the selected 29 stations recorded RINEX observation data thus still providing still good DOC to implement this technique. A total of 20,160 epochs were analyzed for the 31 and 12 operational GPS and Galileo satellites reporting a total of 1,169,280 clock states in GPS sytem time and 806,400 in Galileo system time with a 30 s sampling interval. In order to assess the accuracy of our estimation, clock biases for both GPS and Galileo satellites are compared to the reference products provided by CNES and GFZ sp3 files. As mentioned before, note that the comparison cannot be made without the removal of the constellation mean for each epoch.

Figure 3.7a plots the time difference of our internally estimated GPS satellite clock references and the ones produced by CNES. The maximum error observed for this period is 86 cm for SVN69/PRN03 which is associated with an RMS difference of 38 cm. The upper plot in Figure 3.9a displays the RMS of the difference between our own clock generation and CNES products. Except for four satellites, the rest show RMS on the order of 20 cm or below. In fact the mean RMS of the difference across constellation is 17 cm. These results are in line with the plots provided in [29] where a batch filter approach is implemented to estimate satellite and receiver clock biases.

An analogous comparison is done with GFZ clock products in Figure 3.7c reporting very similar results. In order to address the level of agreement between the two ACs, Figure 3.7c presents the time series of the difference between CNES and GFZ products. As can be seen in the lower plot of Figure 3.9a, our model is less accurate than the ones implemented by MGEX ACs. As foreseen in the prior section, the simplification of the observation model leads to larger inaccuracy in our solution but for our validation goal it is sufficient. For an integrity purpose we can be certain that the GPS products used by the ANSP for ISM computation are validated on the order of 20 cm. The half side-real day sinusoidal behavior is also noticeable in the time series of the estimation difference between CNES, GFZ, and our own clock states. As seen in Figures 3.7a, 3.7b, and 3.7c there is a harmonic component that repeats every 12 hours which coincides with the orbital period of GPS satellites.

Let us now analyze the performance of the Galileo satellite clock estimation. Figures 3.8a and 3.8b plot the time series of the difference between our estimation and CNES and GFZ clock products correspondingly. Although the largest difference is 83 cm for E26 (same order as for GPS), the RMS is almost half for Galileo satellites than for GPS. As inferred from the top chart of Figure 3.9b, the mean of the RMS difference across constellations is 10 cm. Note that exactly the same algorithm is applied for the estimation of GPS and Galileo clock biases so a plausible reason for the better accuracy of Galileo results can be the enhanced signal quality. The E1/E5a linear combination has significantly better noise behavior than that L1/L2 combination leading to a more accurate estimation based on Galileo measurements. At the same time, since we are not accounting for the receiver-dependent residual code bias, the fact that Galileo signals present smaller DCB values than GPS also justifies the better results [69].

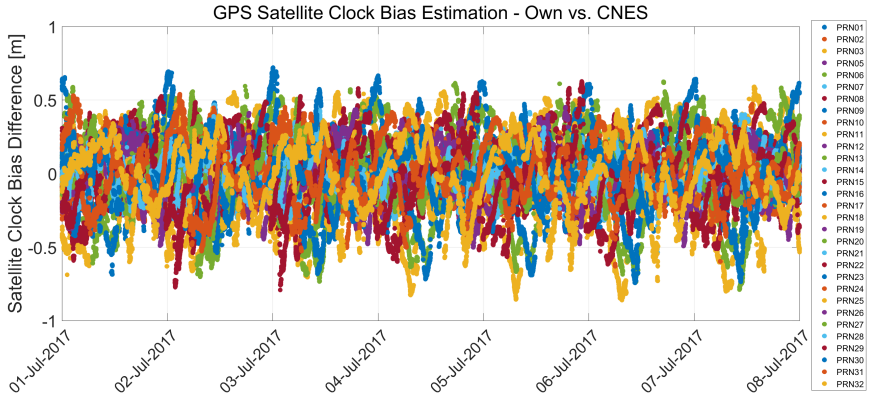

(a) Own vs. CNES

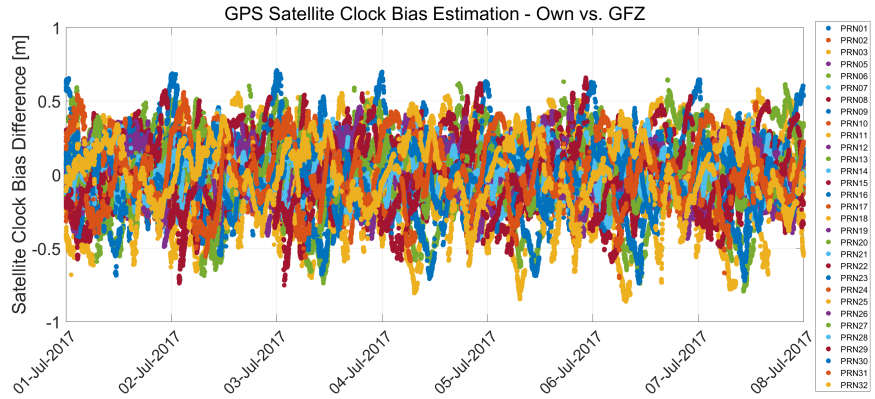

(b) Own vs. GFZ

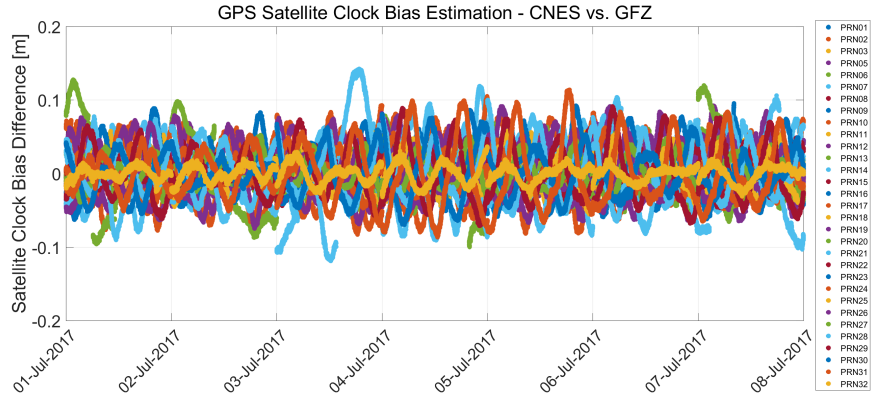

(c) CNES vs. GFZ

Figure 3.7: Comparison between GPS satellite precise clock bias estimation: CNES, GFZ and own products

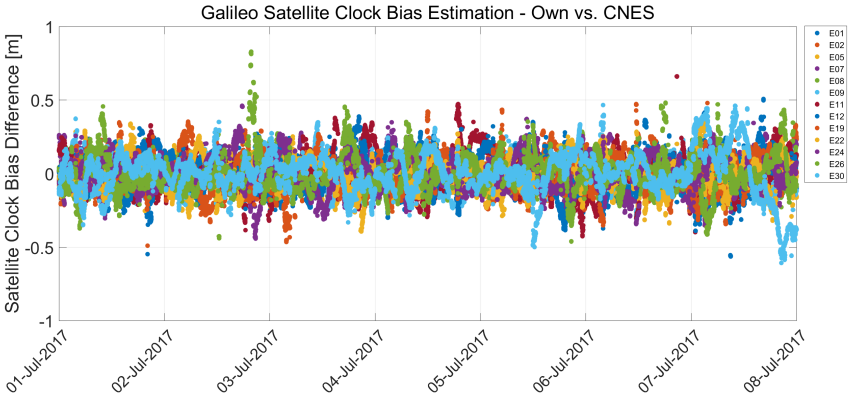

(a) Own vs. CNES

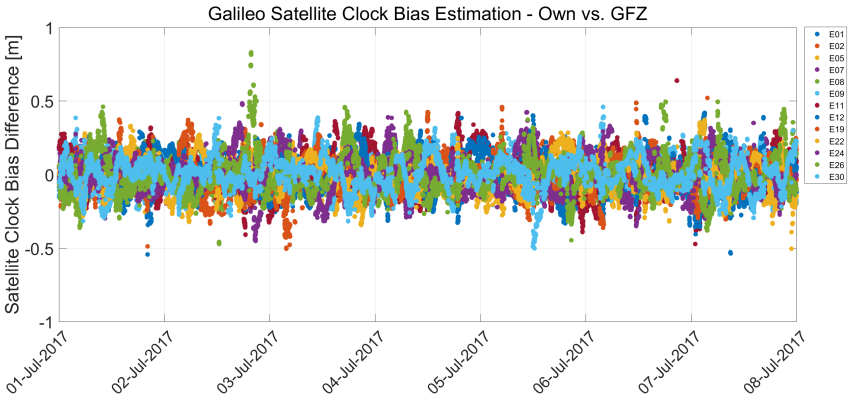

(b) Own vs. GFZ

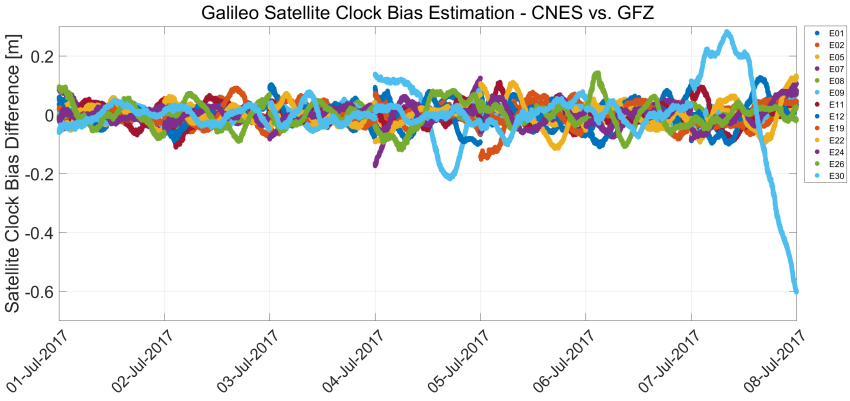

(c) CNES vs. GFZ

Figure 3.8: Comparison between Galileo satellite precise clock bias estimation: CNES, GFZ and own products

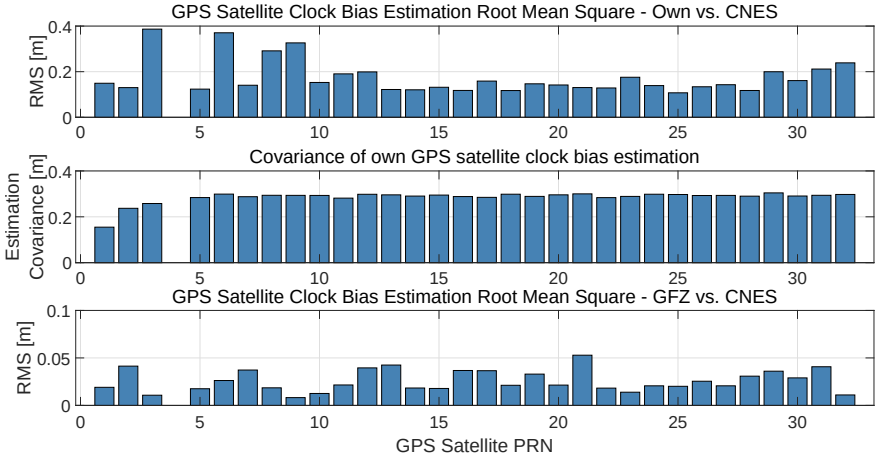

(a) Estimation accuracy: Own, CNES and GFZ

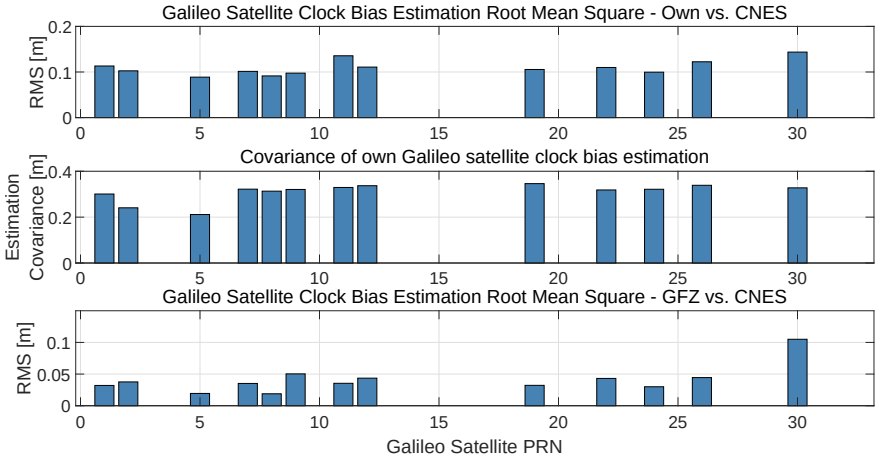

(b) Estimation accuracy: Own, CNES and GFZ

Figure 3.9: Comparison between GPS and Galileo satellite precise clock bias estimation: CNES, GFZ and own products

It is also interesting to mention the particular case of GSAT0206/E30 during 7 July 2017. As depicted by the cyan dots in Figure 3.8c, there is a relatively large disagreement between the clock estimations from CNES and GFZ reaching a mismatch up to 61 cm. As described in the prior Section 3.4, Step 1 validates precise orbits by majority voting. Figure 3.10 presents the time series of the orbit validation process for GSAT0206/E30 during 7 July 2017 comparing the products from the three selected ACs. As can be observed, CODE and GFZ results agree down to 10 cm with thise not being this the case for CNES orbits. Starting at 8:30:00 the norm of

the three-dimensional difference between CNES and the other two ACs crosses the 40 cm threshold established in (3.20). By majority voting, CNES orbits are rejected and CODE and GFZ are validated. Since the selected Galileo references are GFZ products (Table 3.1) the algorithm did not raise a flag for our selected repository and legitimately computed a clock solution. Unlike the case of PRN13 in the prior subsection, there was no satellite outage or unhealthy flag so a clock solution must be computed. Note that using CNES products for E30 during this day represents and integrity issue since the true satellite position cannot be validated. This explains the discrepancy for E30 between our estimation and CNES reference products on 7 July 2017 in Figure 3.8a. Contrarily this difference is not present in the comparison between GFZ and our estimated clocks in Figure 3.8b. This particular example exposes the relevance of the validation of the input products before they are used in the orbit and clock error analysis. Ultimately, fabricated errors can lead to fictitious integrity events that were never present in the real data.

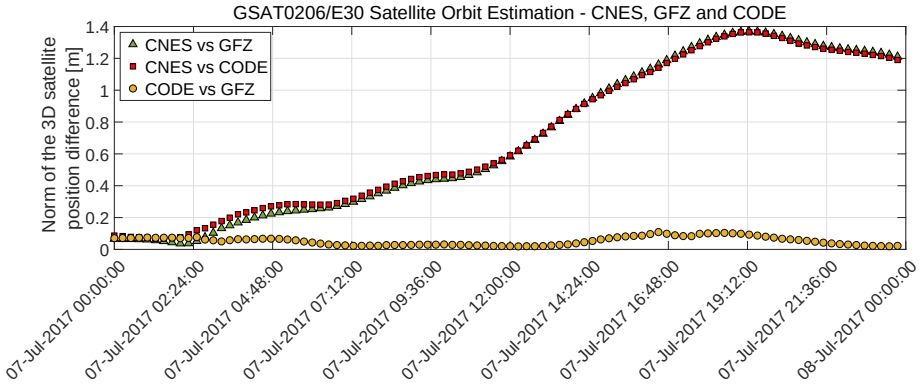

Figure 3.10: Time series of the norm of 3D satellite position difference for GSAT0206 / E30 during 07/07/2017 between CNES, GFZ and CODE products

Let us mention one last aspect regarding the covariance of our clock estimation included in the second plot of Figures 3.9a and 3.9b for GPS and Galileo satellites, respectively. The code measurement error models assumed in (3.15) are in fact pessimistic. It can be observed that the RMS of the difference is actually better than the covariance of our estimation. For both Galileo and GPS the estimation standard deviation is around 30 cm while the actual estimation error is below that value. In other words, our methodology is more accurate than expected. Note that these values are below the target tail overbounding σ which is on the order of 1.5-1.8 m as detailed in Chapter 7. With this method we can guarantee the integrity of the precise reference data utilized in the generation of the ISM to a 20-25 cm level.

To corroborate this last statement, Figure 3.11 plots the navigation clock error computed by using our internally generated clock products versus GFZ products. It can be seen that the assessment of the navigation clock error stands on the order of

the 20 cm 1-σ difference for both GPS and Galileo constellations.

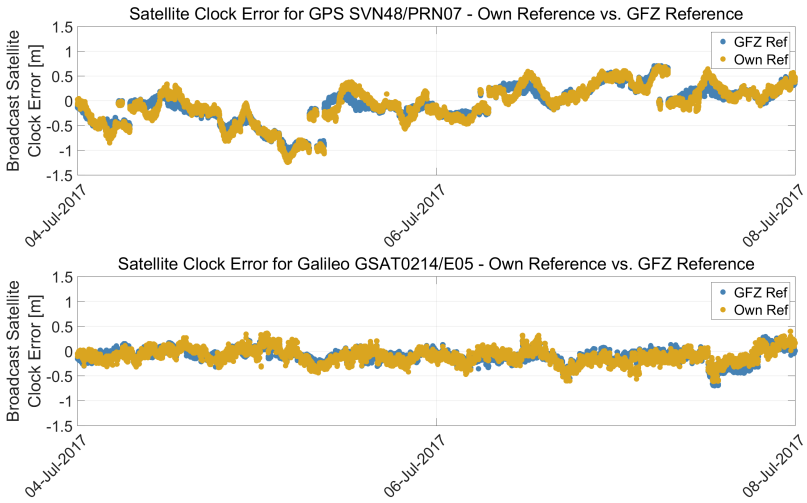

Figure 3.11: Broadcast satellite clock error for GPS and Galileo using own reference products vs. GFZ

3.6 Error Computation

Once the products have been validated, the algorithm can carry out satellite Signal-in-Space Range Error (SISRE) computation based on orbit and clock errors as depicted in Figure 3.4.

3.6.1 Satellite Orbit and Clock Error

Throughout this work, satellite orbit and clock errors are defined as the deviations of the instantaneous satellite APC and clock provided in the BCE from the precise position and satellite clock bias. BCE datasets are utilized to emulate user's calculation of satellite position and clock bias based on orbital parameters contained in the navigation message. In a post-process analysis, estimated satellite positions are compared to the precise reference orbits. The resulting discordance between these two inputs is the so-called satellite orbit and clock error vector.

As discussed through this chapter, although satellite positions provided in BCE and PRO are expressed in the same coordinate system ECEF, they refer to two different points: precise orbit products provide the ECEF coordinates of satellite CoM while broadcast ephemerides datasets are meant to supply satellite's APC ECEF coordinates along with the satellite bias estimation. Clock solutions provided in PRO datasets are also referred to satellite APC. However, as discussed in [35], there is no

reason to assume that both APCs (the one applied by the GNSS ground segment and the one used by the MGEX network) are in fact the same point. In order to compare broadcast and reference data, satellite position and clock bias need to be converted to a common reference. For that purpose, two sets of satellite APC offsets need to be used as reflected in Table 3.1, $\boldsymbol{\Delta}\mathrm{APC}_{\mathrm{BCE}}$ and $\boldsymbol{\Delta}\mathrm{APC}_{\mathrm{PRO}}$. For a given satellite i at epoch k , BCE position $\boldsymbol{x}^{i,k,\mathrm{BCE}}_{\mathrm{APC,ECEF}}$ needs to be converted to CoM by

$$\boldsymbol{x}^{i,k,\mathrm{BCE}}_{\mathrm{CoM,ECEF}} = \boldsymbol{x}^{i,k,\mathrm{BCE}}_{\mathrm{APC,ECEF}} - \boldsymbol{R}^{i,k}_{\mathrm{BF,ECEF}}\boldsymbol{\Delta}\mathrm{APC}^{i}_{\mathrm{BCE}} \tag{3.25}$$

where the rotation matrix $\boldsymbol{R}^{i,k}_{\mathrm{BF,ECEF}}$ is defined based on the satellite attitude model described in Annex B and depicted in Figure 3.12.

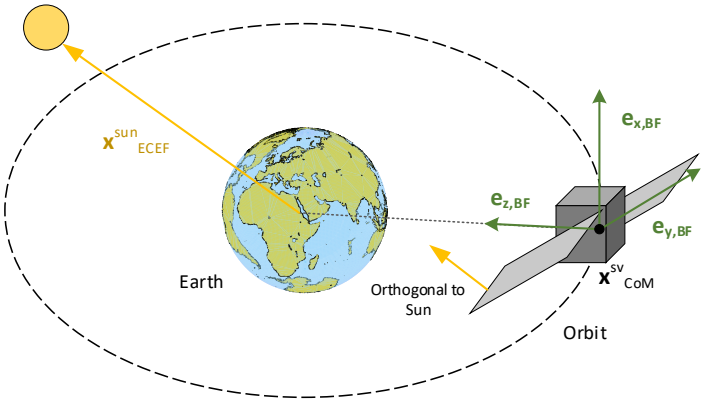

Figure 3.12: Satellite Body Fixed frame determination as a function of Earth and Sun position

Then, satellite orbit error vector $\boldsymbol{\varepsilon}^{i,k}_{\mathrm{orb,ECEF}}$ can be defined as

$$\boldsymbol{\varepsilon}^{i,k}_{\mathrm{orb,ECEF}} = \boldsymbol{x}^{i,k,\mathrm{BCE}}_{\mathrm{CoM,ECEF}} - \boldsymbol{x}^{i,k,\mathrm{PRO}}_{\mathrm{CoM,ECEF}}. \tag{3.26}$$

For illustrative purposes, it is typical to transform the ECEF error vector into Radial, Along-Track, Cross-Track (RAC) frame. This transformation is depicted in Figure 3.13 and the corresponding rotation matrix $\boldsymbol{R}^{i,k}_{\mathrm{ECEF,RAC}}$ is also defined in Annex B. The orbit error can be converted to RAC frame by

$$\boldsymbol{\varepsilon}^{i,k}_{\mathrm{orb,RAC}} = \boldsymbol{R}^{i,k}_{\mathrm{ECEF,RAC}}\boldsymbol{\varepsilon}^{i,k}_{\mathrm{orb,ECEF}}. \tag{3.27}$$

Analogously, satellite clock error needs to be referred to the common CoM point. In this case, it is sufficient to take the nadir component of $\boldsymbol{\Delta}\mathrm{APC}_{\mathrm{BCE}}$ and $\boldsymbol{\Delta}\mathrm{APC}_{\mathrm{PRO}}$ so the clock error can be defined as

$$\tilde{\varepsilon}^{i,k}_{\mathrm{clk}} = \left[c\,\delta^{i,k}_{\mathrm{BCE}} + \Delta\mathrm{APC}_{\mathrm{BCE},z}\right] - \left[c\,\delta^{i,k}_{\mathrm{PRO}} + \Delta\mathrm{APC}_{\mathrm{PRO},z}\right]. \tag{3.28}$$

Because of the different realization of the reference time (different synchronization), apparent clock error $\tilde{\varepsilon}^{i,k}_{\text{clk}}$ needs to be corrected by removing the constellation mean for each epoch k so that

$$\varepsilon^{i,k}_{\text{clk}} = \tilde{\varepsilon}^{i,k}_{\text{clk}} - \frac{1}{I}\sum_{i=1}^{I} \tilde{\varepsilon}^{i,k}_{\text{clk}} \tag{3.29}$$

with being I the total number of satellites belonging to the corresponding constellation.

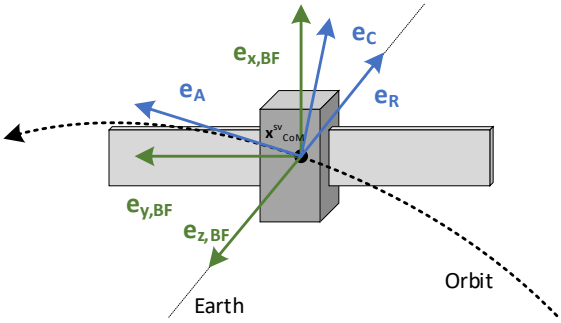

Figure 3.13: Satellite Radial, Along-Track and Cross-Track frame definition

3.6.2 SISRE Definition

ISM must include parameters to safely and tightly overbound satellite ranging errors. Ultimately, users are interested in how orbit and clock errors project into their LOS. Every user located at a point within the satellite's coverage footprint possesses a different LOS vector $\boldsymbol{e}_s$ and will consequently experience a different Instantaneous User Range Error (IURE). There are three definitions of the range error: Global Average $SISRE_{GA}$, Worst User Location $SISRE_{WUL}$, and Instantenoeus User Projection $SISRE_{IUP}$. The first option is defined by the GPS Standard Positioning Service Performance Standard (GPS-SPS-PS) as the average contribution over all the IURE values of users located within a satellite's visibility cone [46]. This does not serve our integrity purpose since the averaged value would not cover the worst case.

The second option proposes a different interpretation of SISRE. For any given satellite orbit error vector, instead of averaging, we define SISRE as the worst user projection of the error within satellite's footprint. In other words, it accounts for the maximum absolute value of IURE. The determination of the WUL is originally three-dimensional although due to the axial symmetry, it can be reduced to a 2D problem in the *worst case plane* ($\mathcal{W}$). For the following derivation, a spherical Earth is assumed.

Plane $\mathcal{W}$ is defined by the satellite orbit error vector $\boldsymbol{\varepsilon}^{i}_{\text{orb,ECEF}}$ and radial unit vector $\boldsymbol{e}_R$ (pointing from the Earth's center to satellite CoM). Note that any plane which is not the *worst case plane* will contain a projection of the original orbit error

$\boldsymbol{\varepsilon}^{i,k}_{\text{orb,ECEF}}$ with a consequent reduction of its norm. Let $\boldsymbol{e}_V$ be a unit vector, contained in $\mathcal{W}$ and orthogonal to $\boldsymbol{e}_R$ so that $\{\boldsymbol{e}_R, \boldsymbol{e}_V\}$ is an orthonormal basis of $\mathcal{W}$. As shown in Figure 3.14, $\mathcal{W}$-cone section defines an arc of a circle on Earth's surface where the WUL should be contained.

The projection of the orbit error vector into the candidate worst user location's LOS can be parametrized with β. Each angle β_i defines a LOS vector $\boldsymbol{e}^i_s$ into which $\boldsymbol{\varepsilon}^i_{ECEF,\text{orb}}$ is projected

$$IURE^i_{s,\text{orb}} = {\boldsymbol{e}^i_s}^T \boldsymbol{\varepsilon}^i_{\text{orb,ECEF}} \tag{3.30}$$

where

$$\boldsymbol{e}^i_s = -\cos\beta_s \boldsymbol{e}_R - \sin\beta_s \boldsymbol{e}_V \quad \text{and} \quad \beta_s \in [-\xi, \xi]\,. \tag{3.31}$$

As represented in Figure 3.14 the semi-angle of the visibility cone ξ is unique for each constellation and depends on the semi-major axis of the satellite orbit: $\xi_{\text{GPS}} = 13.9°$ and $\xi_{\text{GAL}} = 12.4°$. Satellite clock error $\varepsilon^i_{\text{clk}}$ equally influences all user range measurements and its effect shall be subtracted in the final IURE computation as follows

$$IURE^i_s = IURE^i_{s,\text{orb}} - \varepsilon^i_{\text{clk}}. \tag{3.32}$$

Finally, SISRE evaluation selects the worst case from the $IURE^i_s$ set,

$${SISRE_{WUL}}^i = \max(|IURE^i_s|)\text{sgn}(IURE^i_s). \tag{3.33}$$

Note that for simplicity of notation, the epoch index k has been dropped and the above expressions apply to a generic time t.

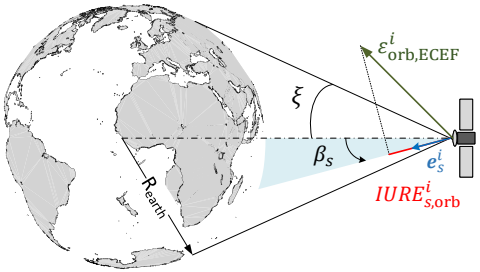

Figure 3.14: Illustration of the worst user location projection

The main difference between this last expression and the one obtained by averaging is the preservation of the actual sign of IURE in SISRE (second term of the right-hand part of (3.33)). An important aspect of this definition shall be pointed out. SISRE distribution cannot present zero values given that the maximum IURE is taken for each given orbit error. Unless satellite orbit and clock errors are numerically zero, there will always be a non-zero IURE. As a consequence, SISRE will present a bimodal distribution. In addition, the inherent definition of SISRE as the worst case IURE makes it intrinsically conservative, but integrity bounds must apply for all the cases.

In order to avoid the bimodality of $SISRE_{WUL}$, the third option projects satellite orbit vector $\boldsymbol{\varepsilon}^i_{\text{orb,ECEF}}$ over a grid of users located under the satellite's footprint as depicted in Figure 3.15. The user locations are based on a 642-vertexes icosahedron in order to guarantee that the area between grid points remains constant. For each user point s which sees the satellite i above a 5° elevation mask, the orbit component of the range error $SISRE_{IUP}{}^i_{s,\text{orb}}$ is defined as

$$SISRE_{IUP}{}^i_{s,\text{orb}} = \boldsymbol{e}_s^{\,i\,T}\,\boldsymbol{\varepsilon}^i_{\text{orb,ECEF}}. \tag{3.34}$$

Unlike expression (3.30), the advantage of the above definition is that it preserves the unimodality of the orbit error distribution. This is particularly convenient for range overbounding (as Chapter 6 will point out) since one of the major assumptions is that distributions are 'Gaussian overboundable.' Subtracting satellite clock error, the range error can be written as

$$SISRE_{IUP}{}^i_s = SISRE_{IUP}{}^i_{s,\text{orb}} - \varepsilon^i_{\text{clk}}. \tag{3.35}$$

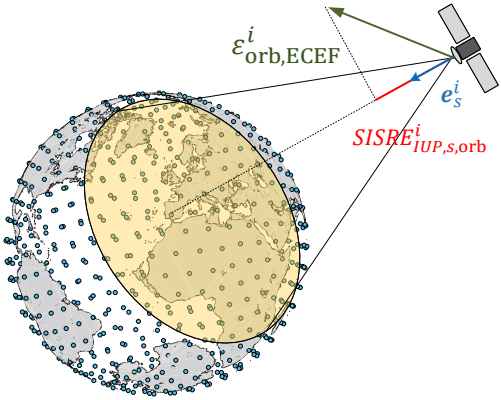

Figure 3.15: Illustration of SISRE projection over a grid of users

It is relevant to acknowledge that expression (3.33) reports one value per satellite per epoch where as definition (3.35) reports several replicas of the same error providing a better representation of the error over users. With an elevation mask of 5 degrees, typically one satellite has 205-210 users under its visibility cone. This implies higher granularity adding more samples to the error distribution but it does not affect the number of effectively independent samples as Chapter 5 will discuss.

4 GPS and Galileo Service History

This chapter presents a quantitative characterization of nominal orbit and clock errors across GPS and Galileo satellites. For each individual spacecraft, by comparing precise orbits to validated broadcast ephemeris data introduced in Chapter 3, we compute the corresponding satellite range error. These distributions are analyzed attending to spacecraft diversity with the onboard clock being the driver of satellite's performance. The work here presented targets the characterization of the unfaulted error bounds for GPS and Galileo meaning that the identified faulty events are listed but excluded from this study. The first part of this chapter justifies the selection of the monitoring period for GPS and Galileo constellations and the pertinent satellites to be included. It also compares the different methods to compute SISRE introduced in Chapter 3 and their suitability for analyzing the distribution's core and tail.

The second and third parts provide a thorough description of GPS and Galileo constellation performance. The novelty introduced in this work is the analysis of orbit and clock errors over time. Breaking service history down into monthly, biannual and annual datasets let us address the changes in biases and standard deviations. Results will reveal major differences between the stationary analysis (as in [70] and [2]) and the time-dependent approach, revisiting the assumption of zero mean distributions over a short time frame.

4.1 Time Frame and Monitored Satellites

The selection of the service period under analysis and the choice of satellites that will be included in this study have been done with special care. Three factors are taken into account when selecting the proper data sample from all the available service history: major updates in the Operational Control Segment (OCS) ground infrastructure, publication of written performance commitments, and decommission of old satellites.

GPS was declared operational in 1995 and since then a series of enhancements in both control and space segments have improved the constellation performance. In particular, the addition of eleven NGA monitor stations by the end of 2006 provided triple visibility to the ODTS process enhancing ranging accuracy [71]. The current GPS commitments were published in 2008 within the GPS-SPS-PS [46]. For integrity purposes, data prior to this declaration might not be representative of the current and/or future constellation performance.

Unlike GPS, the European constellation has not reached its full Full Operational Capability (FOC) yet. Since the large system upgrade implemented during February-

March 2015 with a full-scale hardware and software reconfiguration, Galileo ranging and positioning accuracy has dramatically increased. As shown in [25], the 1-σ SISRE reduced over 50% between March 2015 and June 2016. The European Commission declared Galileo Initial Services (GIS) on 15 December 2016. Although no commitments are published at the time of writing this thesis, it seems more adequate to base the performance characterization on service history after the GIS declaration.

With respect to decommissioned satellites, this work does not analyze orbit and clock errors corresponding to satellites that were retired from duty before December 2017. Results will expose substantial differences among GPS blocks which will reinforce the idea of only analyzing currently operational satellites to assess future performance. On those grounds, only block IIR and IIF GPS satellites are included in this study, discarding already decommissioned block IIA. For Galileo satellites, as of June 2018, fourteen operational satellites are transmitting healthy SIS. Data from satellites GSAT0201 and GSAT0202 inserted in a highly elliptical orbit are not included in this study since they were never incorporated into the constellation. According to Galileo status in [72], in December 2017 GSAT0204 was retired from active duty for constellation management purposes, however this particular satellite has been kept in our analysis.

This work has been careful to keep track of SVN/PRN changes during the course of this analysis. PRN/SVN information can be found in the Notice Advisory to Navstar Users (NANU) files provided by the US Coast Guard Navigation Center [73]. In the case of Galileo, although also taken into account, no PRN changes have been applied in the current constellation history.

4.2 Nominal Performance Characterization

As described in Chapter 2, the ISM contains two sets of parameters; the ones that model the nominal error bounds, σ_{URA}, σ_{URE}, and b_{nom} and the ones that model the *a priori* fault probabilities, P_{sat} and P_{const}. According to GPS-SPS-PS [46], a satellite is considered to present a major fault if its average projected error over its visibility cone is greater than 4.42 σ_{URA}. The goal of this thesis is the analysis of the nominal error for providing efficient and safe overbounds which lead to better ARAIM service availability. Although satellite fault detection and characterization is an essential task to asses GNSS integrity, the identification of faulty events falls outside the scope of this study. Exhaustive and documented work has been presented by Walter in [2] where five major GPS faults were identified since 2008. The error computation in this dissertation has consequently suppressed the samples coming from those five corresponding periods listed in Table 4.1.

A methodology for the determination of fault probabilities for ARAIM was presented by Walter in [24]. The analyzed data indicated that the GPS commitments have been met through the past decade and that in fact they were quite conservative relative to the actual GPS operation. The lack of performance commitments (as of September 2018) for the Galileo constellation makes the frontier between nominal and

Table 4.1: Identified GPS fault events occurred between 2008 and 2017 (Taken from [2])

PRN	SVN	Date	Cause
25	25	26 June 2009	Clock error
08	38	5 November 2009	Clock error
30	30	22 February 2010	Clock error
09	39	25 April 2010	Ephemeris error
19	59	17 June 2012	Ephemeris error

faulty operation diffuse. A recent publication by the European Space Agency (ESA) has included a list of three faulty events for Galileo satellites since the declaration of initial services [36]. This list has recently been updated for H-ARAIM by the European Commission (EC) in [74]. These faulty events have been included in Table 4.2 with their corresponding justification. Attending to the nominality of the error distribution and tail behavior, two additional events were observed in GSAT0204 (decommissioned) and GSAT0203. In both cases, an excessive clock error (ramp or step) created an anomaly in the error distribution. Note that there is no official confirmation via Notice Advisory to Galileo Users (NAGU) files or written statement of these two errors. Since the scope in this dissertation is the study of the unfaulted error bounds, we can safely exclude them until the institutional corroboration or invalidation.

Table 4.2: Identified Galileo fault events occurred between December 2016 and June 2018

PRN	GSAT	Date	Cause
30*	0206	7 March 2017	SIS health flag
02*, 08, 12	0211, 0208, 0102	9-10 May 2017	Unspecified
All*	All	14-15 May 2017	Navigation Message not refreshed
26*	0203	6 June 2017	Incorrect SIS Health during clock maintenance
22**	0204	2 August 2017	Clock Error (not confirmed)
24*	0205	28 November 2017	Clock Error
11*	0101	25 December 2017	Clock Error
26	0203	17 April 2018	Clock Error (not confirmed)
All*	All	7 May 2018	Unspecified

*Events confirmed by European Commission in [74]
** Satellite removed from active service on 8 December 2017

4.3 Ephemeris and Clock Results Representation

The scope of error characterization is to model a continuous random process x based on a series of realizations measured in instants x_k conforming a dataset X. In order words, we are interested in modeling the error population through a series of error samples collected in time. As defined in Chapter 3 of [75], the probability distribution of a random variable x is a description of the probabilities associated with the possible values of x. The statistical characterization of random error processes are presented in this work in three different formats: Relative Frequency Histogram (RFH), Cumulative Distribution Function (CDF), and tables of statistics. An RFH is a normalized frequency histogram by the number of total samples. It provides a good estimation of the population Probability Density Function (PDF). The CDF is a discrete integration (sum) of the RFH by

$$F(\mathrm{x}) = \Pr\left(\mathrm{X} \leq \mathrm{x}\right) = \sum_{\mathrm{x}_i \leq \mathrm{x}} f(\mathrm{x}_i) \text{ where } f(\mathrm{x}_i) = \frac{\text{Number of Samples in bin } i}{\text{Total Number of Samples}}. \quad (4.1)$$

Further reading on random sampling and bin selection techniques can be found in Chapter 6 of [75]. A peculiar type of CDF is applied in this dissertation; the so-called Folded Cumulative Distribution Function (FCDF) or mountain plot [76]. This technique folds the second half of the CDF plot by representing $1 - y$ for values of $\mathrm{X} \in [m_\mathrm{x}, \infty)$, with m_x being the median of the distribution. Contrary to traditional CDF curves, mountain plots ease the visualization of the tails of both sides of the distribution as well as the evaluation of the distribution symmetry.

The estimated population mean $\hat{\mu}_\mathrm{x}$, standard deviation $\hat{\sigma}_\mathrm{x}$, and Root Mean Square (RMS) based on a given sample set are defined as

$$\hat{\mu}_\mathrm{x} = \bar{\mathrm{x}} = \frac{1}{N}\sum_{k=1}^{N} \mathrm{x}(k) \quad (4.2)$$

$$\hat{\sigma}_\mathrm{x} = \sqrt{\frac{1}{N}\sum_{k=1}^{N} \left(\mathrm{x}(k) - \bar{\mathrm{x}}\right)^2}. \quad (4.3)$$

$$RMS = \sqrt{\frac{1}{N}\sum_{k=1}^{N} \mathrm{x}(k)^2}. \quad (4.4)$$

Note that through this chapter $\hat{\mu}_\mathrm{x}$, $\hat{\sigma}_\mathrm{x}$, and RMS will be estimated for different error data partitions based on monthly, biannually and annually datasets.

4.3.1 Mapping Ephemeris and Clock Errors into User Range

Section 3.6 introduced the different frames in which orbit error could be expressed. ISM parameters are meant to provide bounds in the range domain for each satellite measurement. These bounds must be safe for any user within the satellite's footprint;

that it is why the worst user location was defined in Figure 3.14. $SISRE_{WUL}$ will always conservatively account for the distribution tails at the expense of introducing bimodality in the error distribution. A second range error projection technique was described in Figure 3.15 where a given orbit error was projected into a grid of users equally distributed over the satellite's visibility cone. Here a third option to describe satellite range error is introduced, the so-called Radial-Minus-Clock (RMC) distribution. As defined in Equation (3.27), satellite orbit error can be expressed in the RAC frame where the radial direction is defined by the vector between Earth's center and satellite's CoM (Figure 3.13). Depending on the location, the scaling factor of the radial error into user's LOS would range between 1 and $\cos\xi$. Since $\cos\xi \simeq 0.98$ for both Galileo and GPS orbits, it seems clear that RMC error would be a good estimate of the range error distribution.

In order to compare the three SISRE estimators, Figure 4.1 presents the time series of the satellite range error for GSAT0208/E08 during January 2018. Note that both RMC and $SISRE_{WUL}$ include one value per epoch k whereas $SISRE_{IUP}$ presents a total of $\sim$ 210 values (one per user within a satellite's footprint). In terms of error representation, one could say that the more granularity, the better the true distribution can be characterized. This statement is true as long as we acknowledge the fact that samples are highly correlated and we account for it. Chapter 5 is fully dedicated to understanding how correlation for orbit and clock error works. As expected, for each epoch k, $SISRE_{WUL}$ (black triangles) always takes the largest possible value of the projection whereas RMC takes an intermediate value. Even more interesting is the RFH and CDF plots included in Figure 4.2 for data collected between January and June 2018. As introduced before, RFH clearly shows the bimodality and high asymmetry of the $SISRE_{WUL}$ distribution.

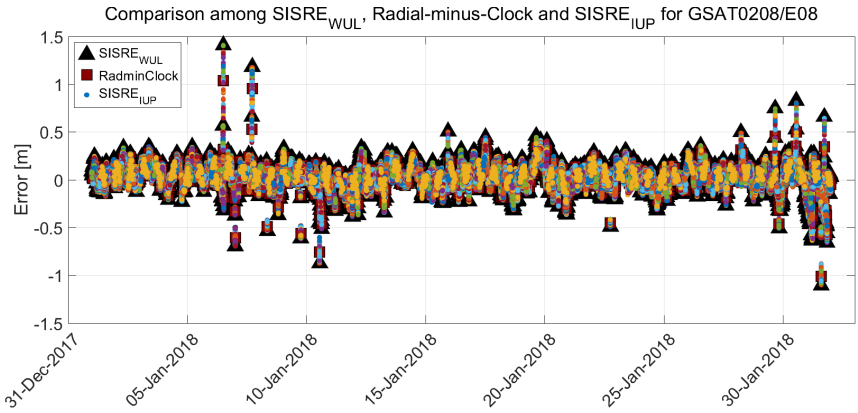

Figure 4.1: Time series for comparison of SISRE methods for January 2018 for GSAT0208 / E08

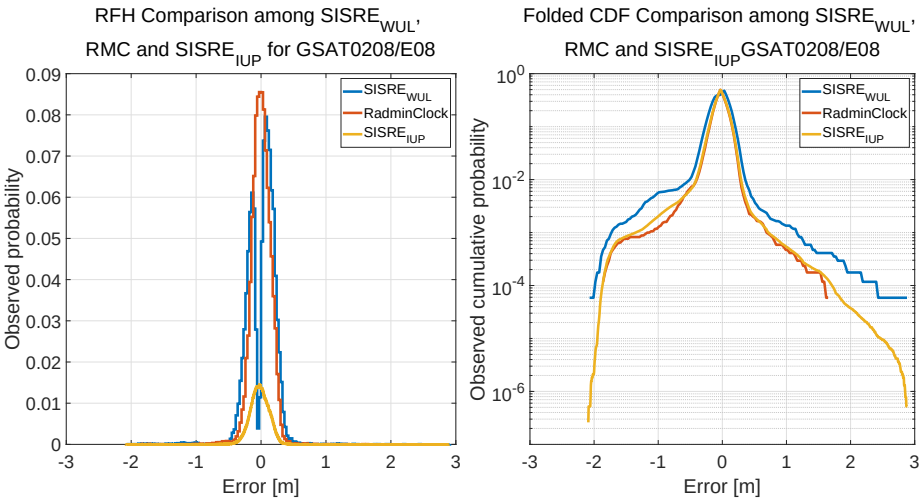

Figure 4.2: Relative Frequency Histogram and Folded CDF for comparison of SISRE methods for January-June 2018 for GSAT0208 / E08

As can be seen in the FCDF plot, RMC distribution perfectly fits the core of the $SISRE_{IUP}$. In fact, Table 4.3 indicates that $\hat{\mu}_x$, $\hat{\sigma}_x$, and RMS almost match for both distributions. As expected, $\hat{\sigma}_x$ is more conservative for $SISRE_{WUL}$ where given the bimodality, $\hat{\mu}_x$ is not a representative value. According to expression (3.30), this bimodality is a consequence of the orbit projection since the clock error adds linearly to all users. Let us name $SISRE_{WUL,\text{orb}}$ to the orbit contribution so that ${SISRE_{WUL}}^i = {SISRE_{WUL,\text{orb}}}^i - \varepsilon^i_{\text{clk}}$. Both $SISRE_{WUL,\text{orb}}$ and clock error statistics are included in Table 4.3 for comparison.

Table 4.3: Statistics for comparison of SISRE methods for January-June 2018 for GSAT0208/E08 (in cm)

Distribution	$\hat{\mu}_x$	$\hat{\sigma}_x$	RMS
$SISRE_{IUP}$	-2.9	12.0	12.4
RMC	-2.8	11.5	11.8
$SISRE_{WUL}$	6.3*	15.3	16.6
$SISRE_{WUL,\text{orb}}$	1.7*	13.6	13.7
Clock Error	-3.4	11.4	12.0

*Mean values of bimodal distributions are not representative

In this Chapter we admit that $SISRE_{IUP}$ is the best representation available of the true distribution but due to the large amount of data that is handled in this analysis, it becomes impractical to deal with $SISRE_{IUP}$. For 10 years of GPS data, we have a

total of over 8 million data points for a $SISRE_{WUL}$ distribution. Using $SISRE_{IUP}$ for characterizing service history would imply over 1.6 billion data points. Consequently, the RMS of the $SISRE_{WUL}$ distribution will be used to characterize constellation nominal performance in this chapter. The other distribution, $SISRE_{IUP}$, will be taken for the overbounding methodology in Chapter 6.

4.4 GPS Service History

This section presents the results of the GPS performance analysis carried out between 1/1/2008 and 12/31/2017 for LNAV ephemeris and clock data applied to the DF L1/L2 combination. As discussed in Chapter 3, Table 3.1 summarizes the input data utilized and Section 3.6 details how orbit and clock errors are computed. Apart from the traditional methodology where all data are condensed in a unique set for the full monitoring period, this section introduces a new way of partitioning the data: we analyze the time-variant component of the error. This paves the ground for the correlation analysis done in Chapter 5.

4.4.1 GPS Full Constellation Performance

A total of 31 GPS satellites have been analyzed during ten years reporting a total of 8,184,071 orbit and clock nominal error samples. Figure 4.3 includes the RFH and FCDF plots merging all GPS samples in a single error distribution. $SISRE_{WUL}$ bi-modality again becomes clear in the RFH plot in Figure 4.3. It can also be observed that the satellite along-track direction presents the largest error magnitude and dispersion. This trend repeats over all the analyzed satellites and it can be attributed to poor observability of the ODTS equations in that direction. Cross-track ranks second in error magnitude and dispersion. This error presents a peculiar half-sidereal day periodicity (relevant for the error correlation analysis) which can be explained by the harmonic component of the satellite's equations of motion [77]. The radial direction typically exhibits the smallest error magnitude and dispersion although as seen in the previous section, its contribution plots almost directly into the range error. In order to compare the performance among GPS blocks, Figure 4.4 includes the FCDF for each error contribution. These data are further detailed in Table 4.4 where mean and standard deviation are given for each individual RAC and clock component along with RMS for $SISRE_{WUL,\text{orb}}$ and $SISRE_{WUL,\text{orb}}$.

In order to compare the differences among blocks, it is important to remember that precise orbit and clock accuracy stands between 3-4 cm for GPS. Over a long term period of several years, orbit and clock error distributions are nearly zero mean. That is reflected in both Figures 4.3 and 4.4 and Table 4.4 where the mean values of the distributions are on the order of the reference truth orbit accuracy. Along-track error is an exception to the previous statement which can be explained by the observability issue mentioned above. Note that for the block categorization, SVN65 and SVN72 have been included in a separate group. These two block IIF satellites operate an

onboard Cesium (Cs) clock whereas the the rest of the block IIF and IIR satellites function with Rubidium (Rb) clocks.

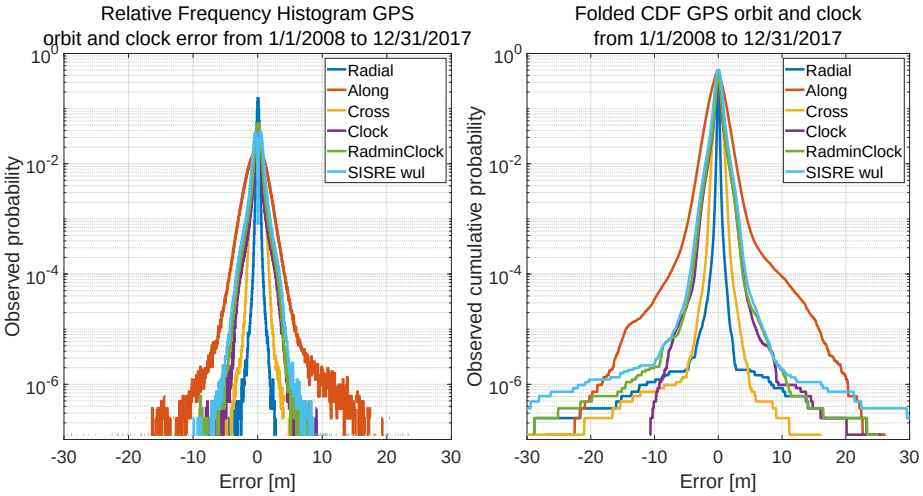

Figure 4.3: GPS orbit and clock error RFH and FCDF from 1/1/2008 to 12/31/2017

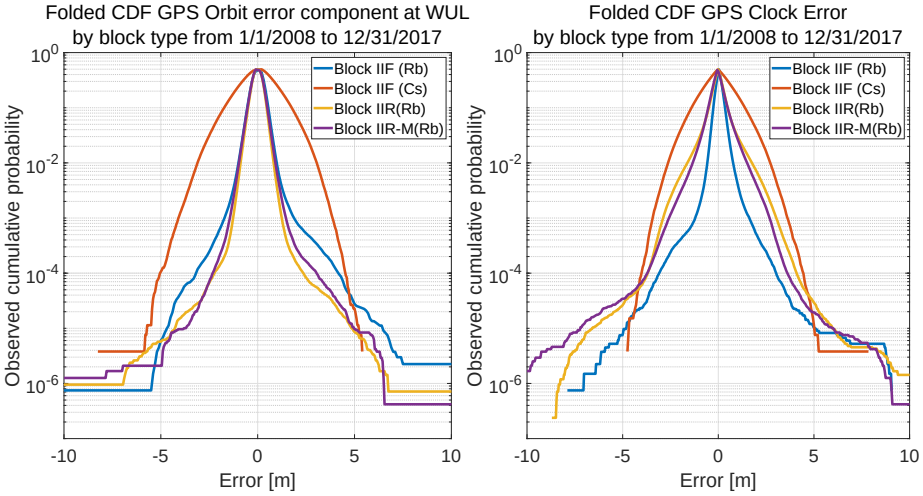

Figure 4.4: GPS orbit error component at WUL and clock error FCDF from 1/1/2008 to 12/31/2017 by block type

Orbit errors are not significantly different among blocks. Radial, along-track, and cross-track errors (and consequently $SISRE_{WUL,\mathrm{orb}}$) show a similar performance for blocks IIR-M and block IIF(Rb) with a marginal improvement for block IIR. However

$\hat{\sigma}_{\text{clk}}$ exhibits an enormous contrast among blocks which directly impacts the SISRE RMS. Table 4.4 shows that $\hat{\sigma}_{\text{clk}}^{\text{IIR}} \simeq \hat{\sigma}_{\text{clk}}^{\text{IIR-M}} \gg \hat{\sigma}_{\text{clk}}^{\text{IIF(Rb)}}$ and $\hat{\sigma}_{\text{clk}}^{\text{IIF(Cs)}} \gg \hat{\sigma}_{\text{clk}}^{\text{IIR}}$ which indicates that SISRE performance is driven by satellite clock error. The domineering trend of the clock is also visible in the RMC error distribution where $\hat{\sigma}_{\text{rmc}}^{\text{IIR}} \simeq \hat{\sigma}_{\text{rmc}}^{\text{IIR-M}} \gg \hat{\sigma}_{\text{rmc}}^{\text{IIF(Rb)}}$. As can be extracted from Table 4.4, for blocks IIR, IIR-M, and IIF(Cs) satellites, clock preeminence over radial is so pronounced that $\hat{\sigma}_{\text{rmc}} \backsimeq \hat{\sigma}_{\text{clk}}$. In the case of block IIF(Rb), as the clock performance improves, leverage is shared between radial and clock error. This trend of the clock has also been pointed out in [26] and [35].

Table 4.4: Statistics for orbit and clock errors by GPS satellite block (in cm)

Satellite	**Radial**		**Along-Track**		**Cross-Track**		**SISRE Orb**
Block	$\hat{\mu}$	$\hat{\sigma}$	$\hat{\mu}$	$\hat{\sigma}$	$\hat{\mu}$	$\hat{\sigma}$	RMS
IIR(Rb)	0.4	12.3	-15.5	118.9	-0	48.6	40
IIR-M(Rb)	0.7	13.3	-9.8	129	-0	47.7	43
IIF(Rb)	-0.6	19.9	-9.5	124.9	-0.1	40.2	46.6
IIF(Cs)	-0.2	24.9	-11.6	138.4	-0.3	39.5	54
All	0.3	14.6	-12.7	123.6	-0.1	46.8	42.5

Satellite	**Clock**		**Rad-Clock**		**SISRE WUL**	**Number of**
Block	$\hat{\mu}$	$\hat{\sigma}$	$\hat{\mu}$	$\hat{\sigma}$	RMS	**Samples**
IIR(Rb)	-0.3	53.7	0.7	56.4	75.9	4199065
IIR-M(Rb)	-4.6	49.9	5.3	53.4	75.1	2385535
IIF(Rb)	8.3	28.3	-8.9	34.7	59.7	1335968
IIF(Cs)	-1.3	110.2	1.1	113.3	137.6	263503
All	-0.2	52.4	0.5	55.6	76.1	8184071

It is of particular interest analyzing the clock error performance of block IIF satellites. Figure 4.5 presents the clock error FCDF for the 12 block IIF operational satellites as of December 2017. Cesium-equipped SVN72 and SVN65 show distinctive distributions (solid and dashed red lines) with respect to the Rb-equipped ones. As pointed out in [78], Cesium clock satellites have a better long term stability but higher noise level implying a less accurate prediction through the navigation message. As discussed in [26], block IIF(Cs) satellites present $\hat{\sigma}_{\text{clk}}^{\text{IIF(Cs)}} \sim 110$ cm which is comparable to the 1996-launched block IIA SVN40 that is also equipped with a Cesium clock. However, due to its stability, error distributions show a reliable Gaussian behavior. For block IIF(Rb) satellites SVN62 and SVN63, distribution cores are significantly narrower but large tails appear. Section 4.4.3 indicates that many of these large values occur during the first weeks of operation. Chapter 5 will show that the onboard clock type is crucial in the error correlation study and will be used in the time between effective independent samples.

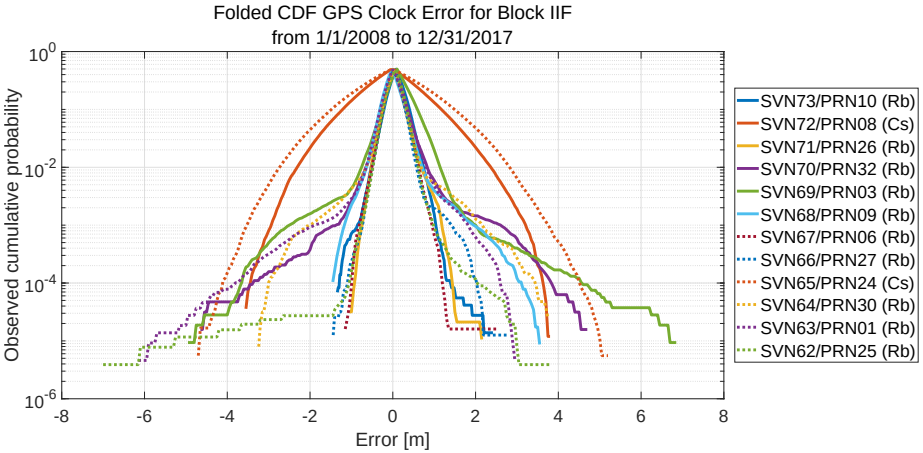

Figure 4.5: GPS clock error FCDF from 1/1/2008 to 12/31/2017 for Block IIF satellites

4.4.2 GPS Stationarity Analysis

The characterization of satellite orbit and clock errors by merging all the service history data (as done in the previous section) does not provide sufficient information about the behavior of the error in a short-term frame. This work revisits the stationarity assumption and addresses the evolution of orbit and clock error biases and standard deviations over time. Satellite's service history is divided in monthly, biannual and yearly datasets. For each GPS satellite, Tables 4.6, 4.7 and 4.8 compare the two approaches: stationarity versus time-dependence. The columns of each table respectively show maximum values of mean and standard deviation reached in a monthly, biannually and yearly error analysis. Table 4.6 includes the mean values $\hat{\mu}_{\mathrm{m}}$, $\hat{\mu}_{\mathrm{b}}$, and $\hat{\mu}_{\mathrm{y}}$ for RAC, clock and RMC distributions for each timely dataset and compares it to values obtained by merging all available service history data $\hat{\mu}_{\mathrm{all}}$. Analogously Table 4.7 includes the corresponding $\hat{\sigma}$. Finally Table 4.8 includes the maximum RMS values in a monthly, biannual and yearly basis for both $SISRE_{WUL,\mathrm{orb}}$ and $SISRE_{WUL}$.

In order to analyze the time-variant component of the error, let us introduce the waterfall diagrams. They are three-dimensional plots which concatenate each FCDF for every individual dataset. For illustrative purposes, SVN67/PRN06 has been taken as example. In order to separately study the behavior of orbit and clock components over time, Figures 4.6 through 4.8 include the waterfall diagrams for $SISRE_{WUL,\mathrm{orb}}$ and clock error for monthly, biannual and yearly datasets.

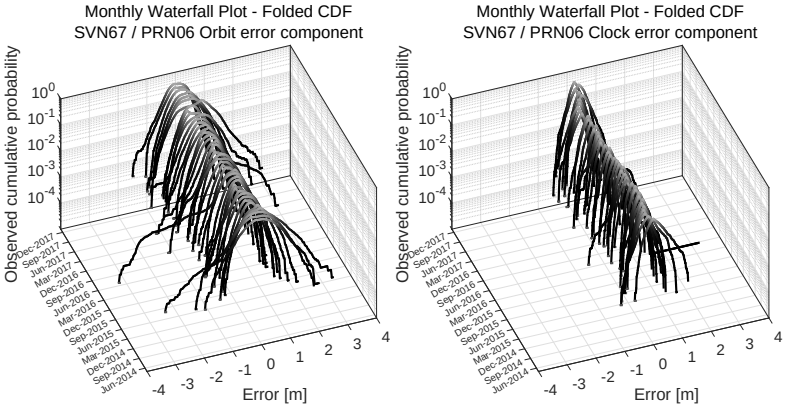

Figure 4.6: Monthly waterfall Folded CDF for SVN67/PRN06 orbit and clock errors (Rb)

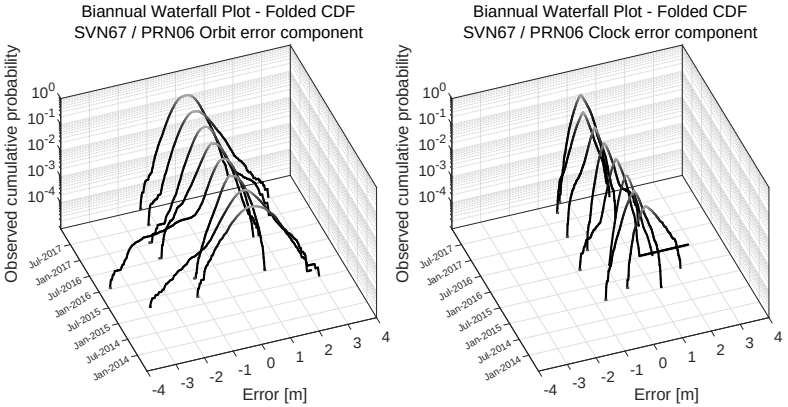

Figure 4.7: Biannual waterfall Folded CDF for SVN67/PRN06 orbit and clock errors (Rb)

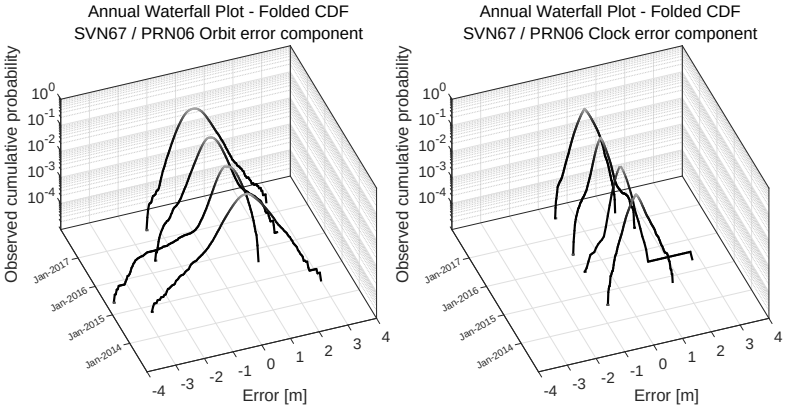

Figure 4.8: Annual waterfall Folded CDF for SVN67/PRN06 orbit and clock errors (Rb)

As can be inferred from the monthly waterfall diagrams in Figure 4.6, clock error mean tends to be more erratic than the orbit. This is a characteristic typically observed in all GPS satellites; orbits predictions tend to be more accurate than clock predictions themselves given the inherent lack of robustness of atomic clock models. As a consequence, clock errors are more inclined to show larger means over time. In general it can be stated that range errors are not zero mean in a short-term frame. As the observation period increases up to six months, error distributions tend to homogenize. In the case of clock error, mean values oscillate between 4-5 times the reference truth accuracy (as seen in Table 4.6, $\hat{\mu}_{\mathrm{clk,b}}^{\mathrm{SVN67}}$=20 cm), still too large to be considered negligible. However, by the time datasets increase to a year period (Figure 4.8), statistics are close to the stationary case when all the available data is merged together. By looking at Tables 4.6 and 4.7, one can realize that in general $\hat{\mu}_{\mathrm{m}} > \hat{\mu}_{\mathrm{q}} \gg \hat{\mu}_{\mathrm{y}} \simeq \hat{\mu}_{\mathrm{all}}$ and $\hat{\sigma}_{\mathrm{m}} > \hat{\sigma}_{\mathrm{b}} \gg \hat{\sigma}_{\mathrm{y}} \simeq \hat{\sigma}_{\mathrm{all}}$ where $\hat{\mu}_{\mathrm{all}}$ is on the order of magnitude of the precise orbit accuracy.

In order to analyze the temporal evolution of the range error mean, Figure 4.9 includes the monthly range error mean value for each GPS satellite from January 2008 to December 2017. The upper plot represents the bias of the range error distribution for each individual monthly dataset whereas the lower plot represents the cumulative mean value using a sliding window. As can be observed, on a monthly basis, range error distributions are not zero-mean and some satellites even show half meter biases (corroborated by Walter in [23]). Particularly eye-catching are the cases of SVN63 and SVN65 where biases over 80 cm are observed. The common denominator of these large values is that they occurred right at the beginning of satellite operation. This abnormal behavior has been named the *initialization period* which is further analyzed in Section 4.4.3.

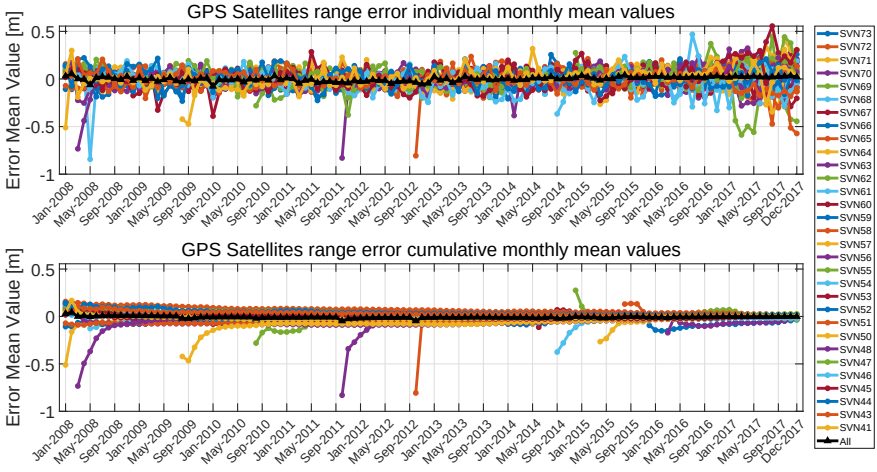

Figure 4.9: Monthly mean values of GPS satellite range errors

Analogously, Figure 4.9 presents the monthly RMS value for each GPS satellite

from January 2008 to December 2017. As observed for distribution means, RMS and standard deviation values undergo large variations on a monthly basis and a stationary behavior cannot be assumed. Again, large values are displayed by some satellites during their first months of operation.

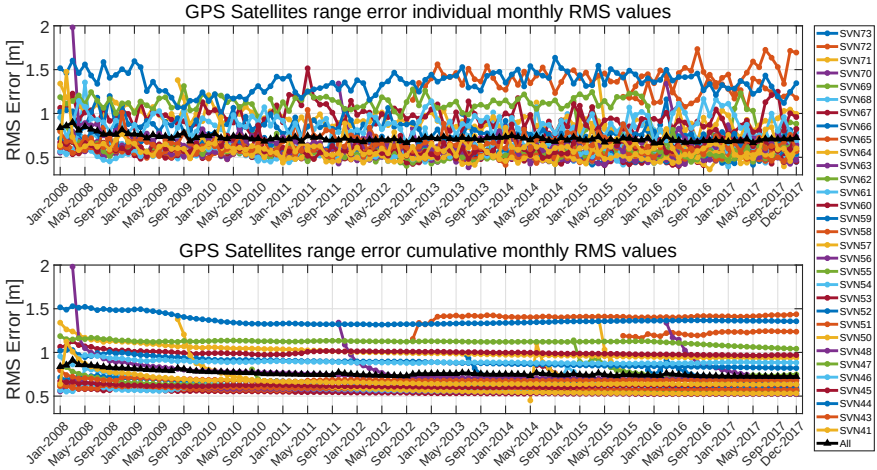

Figure 4.10: Monthly RMS values of GPS satellite range errors

4.4.3 Initialization Period

We define the satellite initialization as the period during the first weeks of operation in which an abnormal behavior is exhibited (as introduced by Figures 4.9 and 4.10). Note that during this period GPS SIS status is set to healthy within the navigation message. Let us analyze the time series of SVN63/PRN01 satellite clock error between October and December 2011, right after the SIS was first declared healthy. Figure 4.11 shows how clock error presents unusual ramps during its first two weeks of operation. Note that these ramps reset with the application of a new navigation dataset. Judging from the shape of the error, the ground segment was having issues in estimating the linear drift of the true clock behavior. This ended on 2 November 2011 when the clock error reduced over 60%. The time series of the clock error normalized by broadcast URA is also included. As can be seen, the transmitted URA was not increased to account for this effect.

Similar to PRN63 case, Figure 4.12 plots the clock error time series for SVN64 / PRN30. Again, anomalously large errors are showed in the first two months of operations. This initialization period also creates big errors in the first weeks of operations for SVN48, SVN50, SVN57, SVN62, SVN68, SVN69, SVN70, SVN71, and SVN72. Given this typical behavior, it does not seem irrational to wait a couple months until new satellites are incorporated within the ISM for ARAIM users.

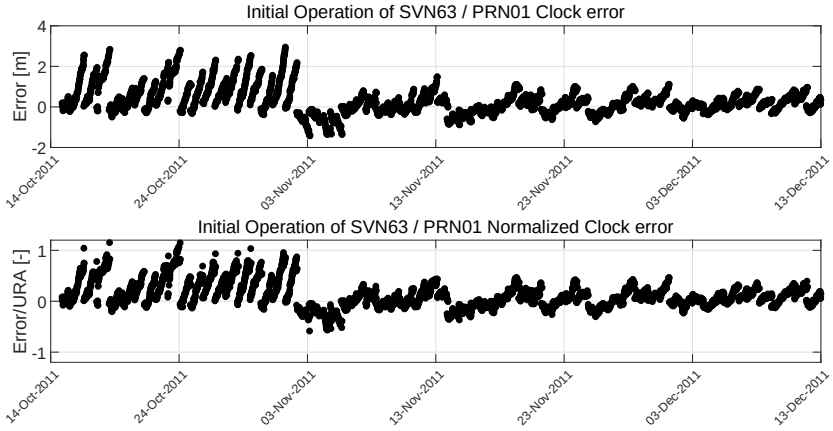

Figure 4.11: GPS SVN63 / PRN01 absolute and normalized clock error time series from 10/14/2011 to 12/13/2011

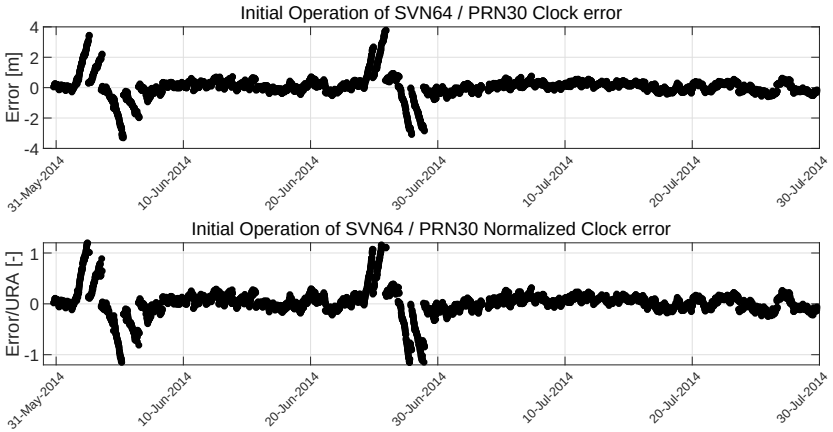

Figure 4.12: GPS SVN64 / PRN30 absolute and normalized clock error time series from 05/31/2014 to 07/30/2014

4.4.4 Rubidium vs Cesium Onboard Clocks

Results presented through this chapter have shown that error performance is driven by the onboard clock type. Satellites equipped with Cs clocks show significantly larger error magnitude than the ones operating Rb clocks. As seen in Table 4.4, block IIF(Cs) satellites show an error RMS of 138 cm whereas IIF(Rb) satellites have an error RMS half that value. However, the differences between Cs and Rb do not only attend to error magnitude but also to time variability. Figures 4.13-4.15 present the monthly, biannual and yearly waterfall diagrams for SNV65 / PRN24. One can see that already on a monthly basis both clock and orbit contributions stay almost immutable. In fact, a quasi Gaussian distribution is shown for each individual dataset.

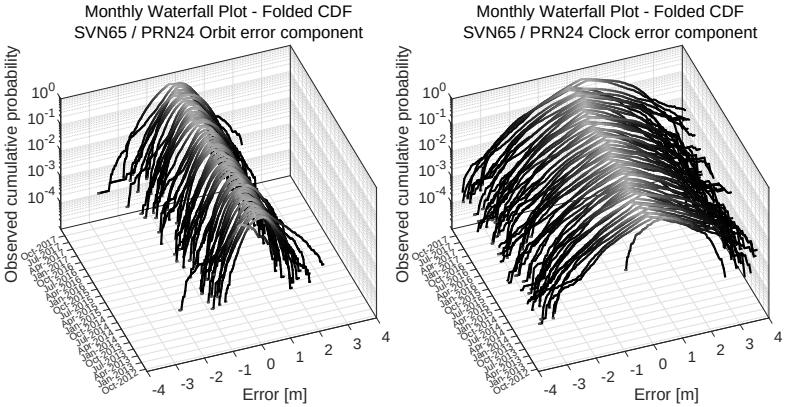

Figure 4.13: Monthly waterfall Folded CDF for SVN65/PRN24 orbit and clock errors (Cs)

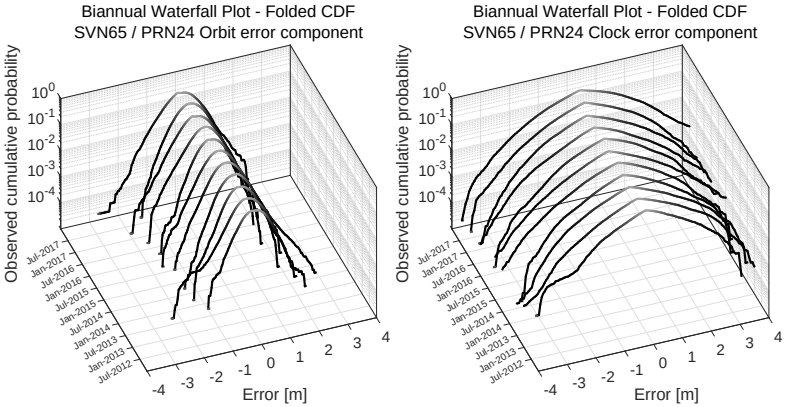

Figure 4.14: Monthly waterfall Folded CDF for SVN65/PRN24 orbit and clock errors (Cs)

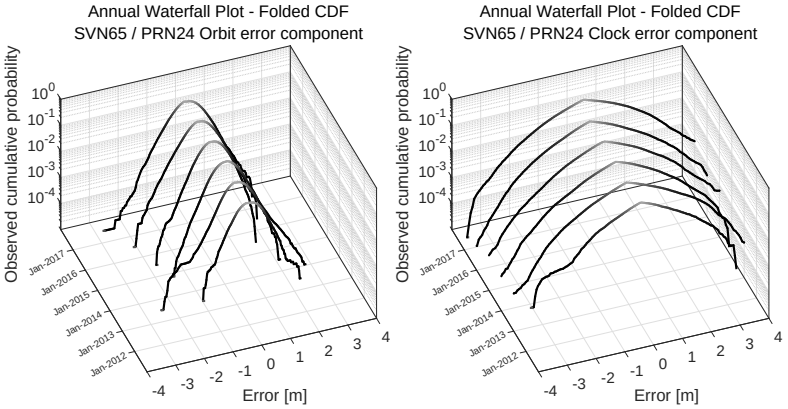

Figure 4.15: Monthly waterfall Folded CDF for SVN65/PRN24 orbit and clock errors (Cs)

The fact that over short periods an error distribution shows variability which tends to dissipate as more data are incorporated suggests data correlation. We can already anticipate that the fact that Cs-equipped satellites show less time variation than Rb-equipped spacecraft indicates that correlation is more dominant in the second ones. Chapter 5 formalizes these observations and derives a methodology to calculate the number of effectively independent samples.

4.5 Galileo Service History

From the five Open Services that the Galileo system offers [79], this work focuses on the Dual Frequency E1/E5a since it is the one used by civil aviation and consequently by ARAIM users. This section evaluates the performance of Galileo FNAV ephemeris and clock error since the declaration of initial services on 15 December 2016 until June 2018. One major difference between Galileo and GPS performance monitoring is the sampling rate. In the case of GPS, taking samples every 15 minutes is sufficient since the navigation message is typically refreshed every 2 hours. However, Galileo satellites send new data packages every 8-12 minutes. Having a 15 minute sampling interval might imply overlooking certain FNAV datasets thus jeopardizing the integrity of the study. As a consequence, a five minute sampling interval is selected for orbit and clock monitoring. As discussed at the beginning of this chapter, having more samples does not mean a deeper probability coverage. Table 3.1 summarizes the input data utilized and Section 3.6 details how orbit and clock error is computed. A similar approach to the one used in the GPS analysis is followed here: full constellation performance and stationarity analysis.

4.5.1 Galileo Full Constellation Performance

A total of 15 Galileo satellites have been analyzed during 19 months reporting a total of 2,092,785 orbit and clock nominal error samples (GSAT0204 was decommissioned in December 2017). Note that the anomalous events listed in Table 4.2 have been excluded from the nominal characterization. Figure 4.16 includes RFH and FCDF plots when merging all Galileo samples in a single error distribution. Instead of classifying Galileo satellites based on In Orbit Validation (IOV) and FOC blocks, we opt for clustering them by clock type in Table 4.5: Passive Hydrogen Maser (PHM) and Rubidium Atomic Frequency Standard (RAFS) clocks.

The qualitative distribution of RAC errors follows a similar trend to GPS with $\hat{\sigma}_{\text{aln}} > \hat{\sigma}_{\text{crs}} > \hat{\sigma}_{\text{rad}}$. It is also observed that clock error dominates the RMC distribution $\hat{\sigma}_{\text{rmc}} \simeq \hat{\sigma}_{\text{clk}}$. Unlike GPS, no distinctive behavior can be detected base on clock type. However it can be seen that orbits are significantly more accurate for Galileo. In particular, $SISRE_{WUL,\text{orb}}$ for Galileo shows an RMS of 22 cm whereas it was 42 cm in the GPS case. Even for the newest block IIF(Rb) satellites, Galileo presents a 50% reduction with respect to GPS orbit errors. In addition, comparing Tables 4.4 and 4.5 it can be inferred that nominal Galileo clock errors present a 40% smaller $\hat{\sigma}_{\text{clk}}$ than

GPS' newest IIF(Rb) satellites. Based on data after the initial service declaration, it can be stated that Galileo nominal ranging accuracy almost doubles GPS.

Table 4.5: Statistics for orbit and clock errors by Galileo satellite block (in cm)

Satellite Block	**Radial**		**Along-Track**		**Cross-Track**		**SISRE Orb**
	$\hat{\mu}$	$\hat{\sigma}$	$\hat{\mu}$	$\hat{\sigma}$	$\hat{\mu}$	$\hat{\sigma}$	RMS
PHM	2.1	16.9	-5.6	34.5	-1.7	19.2	23.5
RAFS	0.5	15.7	-6.5	34.7	0.9	19.1	22.1
All	0.7	15.8	-6.4	34.7	0.6	19.2	22.3

Satellite Block	**Clock**		**Rad-Clock**		**SISRE WUL**	**Number of Samples**
	$\hat{\mu}$	$\hat{\sigma}$	$\hat{\mu}$	$\hat{\sigma}$	RMS	
PHM	2.4	19.1	-0.3	19	37.2	258301
RAFS	0.1	17.1	0.4	17.4	34.1	1834490
All	0.3	17.4	0.3	17.6	34.5	2092791

In order to individually compare the performance of the 15 operational Galileo satellites, Figure 4.17 includes the FCDF plots for orbit and clock errors. The left chart shows that no significant differences in the orbit error can be spotted among Galileo satellites. In the case of clock errors, although $\hat{\sigma}_{\text{clk}}$ are very similar over the full constellation, tails are not. It can be seen that clock error distribution tails present more diversity among satellites than in case of orbit errors. Tables included in Section 4.6 provide orbit and clock statistics for each individual satellite.

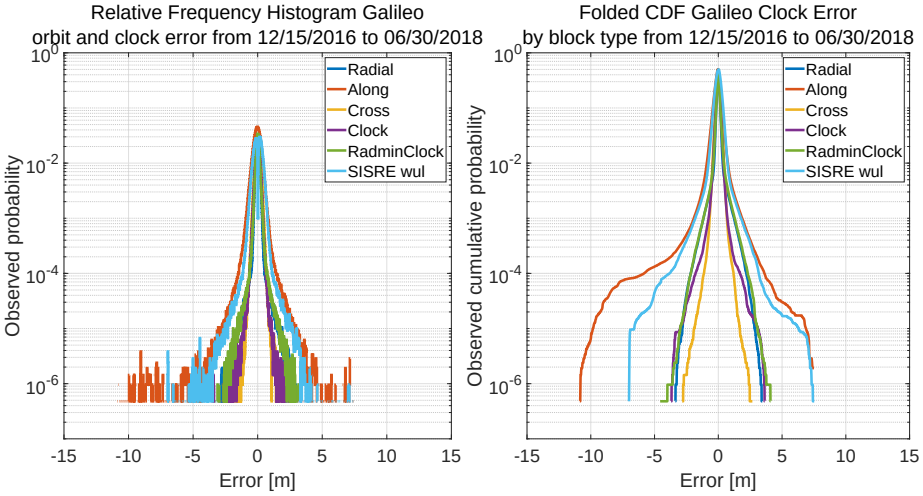

Figure 4.16: Galileo orbit and clock error RFH and FCDF from 12/15/2016 to 06/30/2018

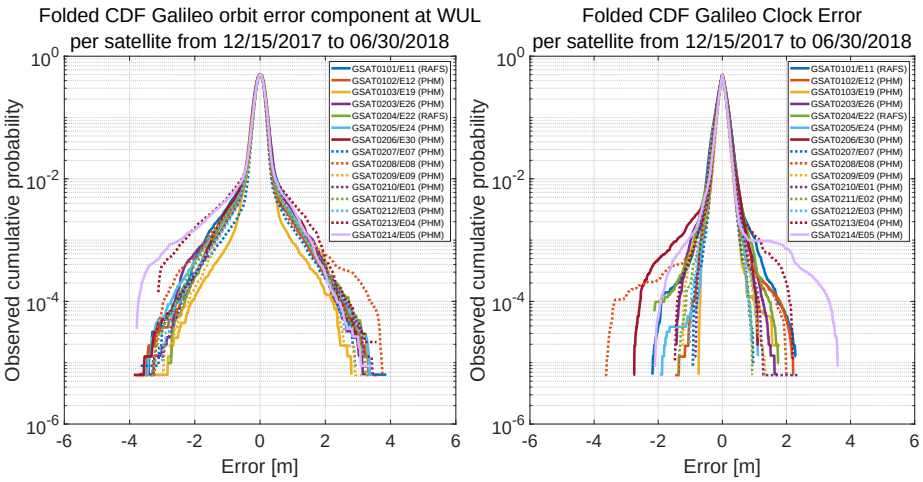

Figure 4.17: Galileo orbit error component at WUL and clock error FCDF from 1/1/2008 to 12/15/2016 to 06/30/2018

4.5.2 Galileo Stationarity Analysis

As was done in the GPS case, each satellite's service history is divided into monthly, biannual and yearly datasets. For each Galileo satellite, Tables 4.9, 4.10, and 4.11 compare the two approaches: stationarity versus time-dependence. The columns of each table respectively show maximum values of mean and standard deviation reached in a monthly, biannual and yearly error analysis. Table 4.6 presents the means value $\hat{\mu}_{\mathrm{m}}$, $\hat{\mu}_{\mathrm{b}}$, and $\hat{\mu}_{\mathrm{y}}$ for RAC, clock and RMC distributions for each timed dataset and compares it to values obtained by merging all available service history data $\hat{\mu}_{\mathrm{all}}$. Analogously Table 4.7 includes the corresponding $\hat{\sigma}$. Finally, Table 4.11 shows the maximum RMS values on a monthly, biannual and yearly basis for both $SISRE_{WUL,\mathrm{orb}}$ and $SISRE_{WUL}$.

To illustrate the temporal variation of orbit and clock components, GSAT0205 / E24 is taken as an example. Figures 4.18 to 4.20 include the waterfall diagrams for $SISRE_{WUL,\mathrm{orb}}$ and clock error for monthly, biannual and yearly datasets. FCDF distributions do not vary as much as they do for GPS on a monthly basis. In fact, besides the flat tail occurring in April 2017, the error distribution does not vary significantly among monthly datasets. This can be corroborated by inspecting column $\hat{\sigma}_{\mathrm{clk,m}}$ in Table 4.7 where (for most of the Galileo satellites) the variations are smaller than in the GPS case. Similar results can be extracted by comparing $RMS_{\mathrm{wul,m}}$ for GPS and Galileo in the corresponding Tables 4.8 and 4.11. It can be seen that monthly variations are smaller for Galileo than for GPS satellites.

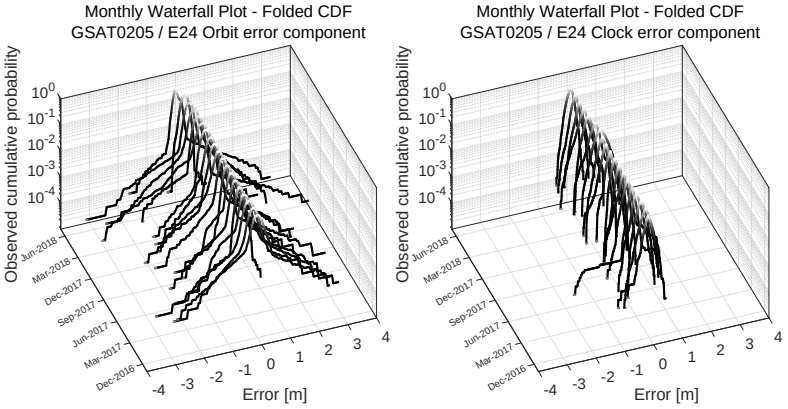

Figure 4.18: Monthly waterfall Folded CDF for GSAT0205/E24 orbit and clock errors

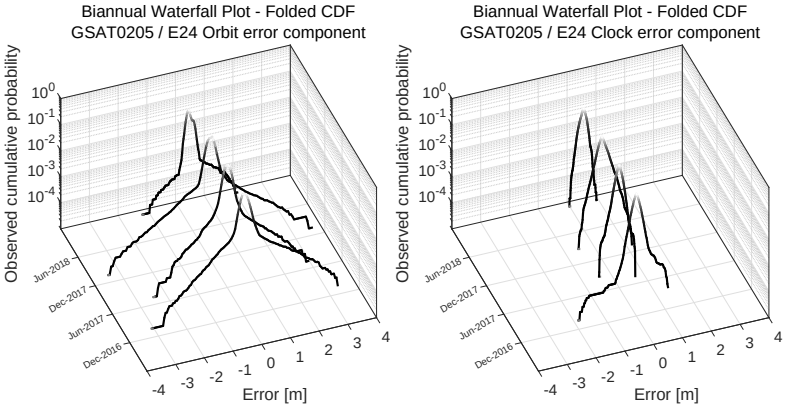

Figure 4.19: Biannual waterfall Folded CDF for GSAT0205/E24 orbit and clock errors

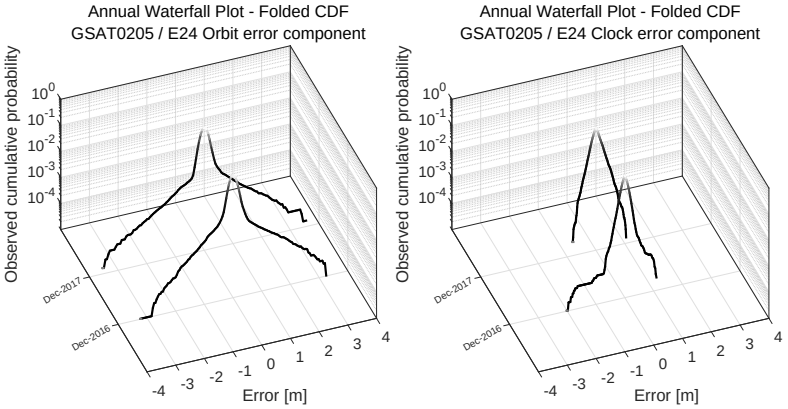

Figure 4.20: Annual waterfall Folded CDF for GSAT0205/E24 orbit and clock errors

In order to analyze the temporal evolution of the range error mean, as was done for GPS data, Figure 4.21 includes the monthly average value for each GPS satellite from December 2016 to June 2018. The upper plot represents the bias of the range error distribution for each individual monthly dataset whereas the lower plot represents the cumulative mean value using a sliding window. During the first months of 2018 a certain bias is observed in the range error for GSAT0203. A similar effect was reported by Galluzzo in [36] where a 20 cm bias in the radial component is exposed. Let us remember that according to Section 3.6.1 a permanent bias in the range error can be attributed to a misalignment in the APCs (BCE and/or PRO). Due to the ongoing deployment of the Galileo ground segment, the bias observed can be a consequence of the misuse of the APC offset linear combination between BCE and PRO. Further confirmation from the Galileo operator regarding the APC linear combination to which FNAV ephemeris and clock data are referred is expected. In any case, the biases are small compared to the ones observed on a monthly basis for GPS and they stay well below 12 cm.

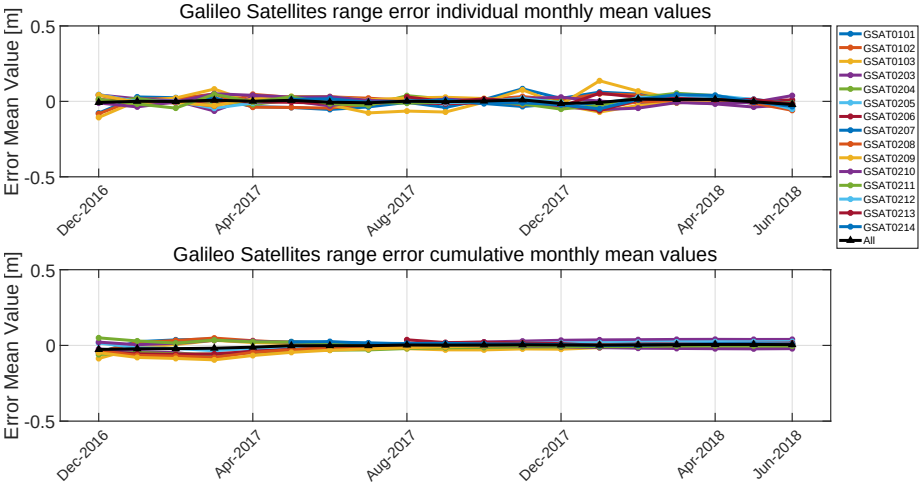

Figure 4.21: Monthly mean values of Galileo satellite range errors

Regarding monthly range errors RMS, the variations over time are less remarkable than in the GPS case. With the exception of January and March 2018 (confirmed in the Galileo quarterly performance reports [80]), the variations in RMS do not exceed 8-10 cm. Comparing Figures 4.10 and 4.22 it becomes clear that variations in GPS monthly datasets are more pronounced than in the case of Galileo. Since we presumed that correlation was behind the monthly variations, the fact that Galileo nominal error is more steady than GPS implies that the range error is less correlated. As mentioned, Chapter 5 mathematically demonstrates this last statement. Unlike in the case of GPS, no particularly abnormal behavior has been observed after the inclusion of new Galileo satellites. It is fair to admit that because Galileo ground and space segment have not

yet reached their FOC, it would not be surprising to encounter abnormal error events due to the tunning of the constellation.

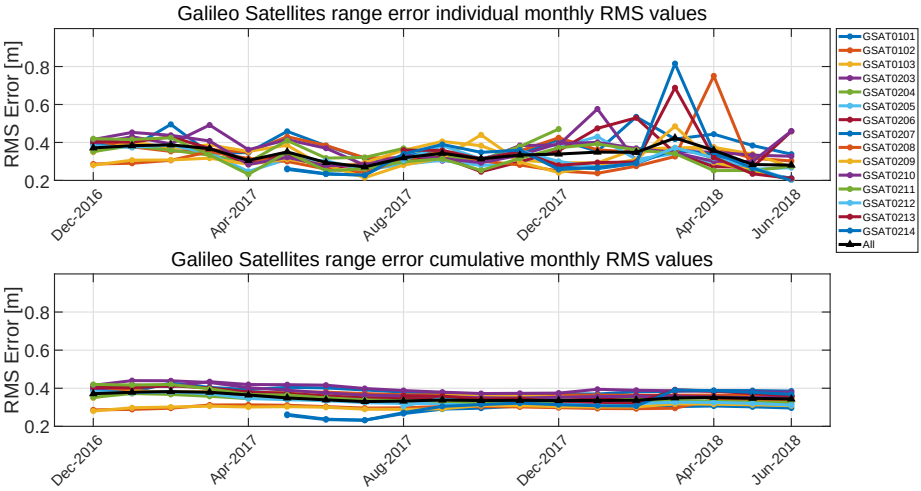

Figure 4.22: Monthly RMS values of Galileo satellite range errors

4.6 Individual Satellite Analysis

This section is dedicated to a detailed description of orbit and clock errors for each individual GPS and Galileo satellite. Each of the following tables combines mean, standard deviation, and RMS values for monthly, biannual, yearly and full datasets for each of the radial (rad), along-track (aln), cross-track (crs), clock (clk), RMC, $SISRE_{WUL,\mathrm{orb}}$, and $SISRE_{WUL}$ distributions. Let us take the following example as an illustration on how to read the tables. For a given satellite, $\hat{\mu}_{\mathrm{rad,m}}$ reports the maximum observed mean value for radial error (either positive or negative) on a monthly basis. Similarly, $\hat{\sigma}_{\mathrm{rad,m}}$ denotes the largest standard deviation for radial error on a monthly basis. Subindexes b and y correspond to the maximum observed values on a biannual and annual basis. Finally, subindex 'all' corresponds to values obtained when the full monitoring period is combined in a single dataset. All values included in the following tables are expressed in cm.

Table 4.6: GPS satellite orbit and clock error means (in cm): monthly, biannual and yearly datasets analysis

Satellite	Block	Radial				Along-Track				Cross-Track				Clock				Rad-Clock			
SVN	(Clock)	$\hat{\mu}_{\mathrm{rad,m}}$	$\hat{\mu}_{\mathrm{rad,b}}$	$\hat{\mu}_{\mathrm{rad,y}}$	$\hat{\mu}_{\mathrm{rad,all}}$	$\hat{\mu}_{\mathrm{aln,m}}$	$\hat{\mu}_{\mathrm{aln,b}}$	$\hat{\mu}_{\mathrm{aln,y}}$	$\hat{\mu}_{\mathrm{aln,all}}$	$\hat{\mu}_{\mathrm{crs,m}}$	$\hat{\mu}_{\mathrm{crs,b}}$	$\hat{\mu}_{\mathrm{crs,y}}$	$\hat{\mu}_{\mathrm{crs,all}}$	$\hat{\mu}_{\mathrm{clk,m}}$	$\hat{\mu}_{\mathrm{clk,b}}$	$\hat{\mu}_{\mathrm{clk,y}}$	$\hat{\mu}_{\mathrm{clk,all}}$	$\hat{\mu}_{\mathrm{rmc,m}}$	$\hat{\mu}_{\mathrm{rmc,b}}$	$\hat{\mu}_{\mathrm{rmc,y}}$	$\hat{\mu}_{\mathrm{rmc,all}}$
SVN41	IIR(Rb)	-5.3	3.6	3.6	-1.7	-136.1	-73.8	-73.8	-12.6	10.3	10.3	10.3	0.9	-21.6	12.9	12.9	1.7	22.5	-11.4	-9.3	-3.4
SVN43	IIR(Rb)	6.5	1.3	1.1	0.8	-121.5	-55	-51.4	-36.5	6.3	3.3	3.3	0.5	26.2	9.6	-4	-0.3	-25.8	-8.9	5.1	1.1
SVN44	IIR(Rb)	13.3	4.7	-1.5	-0.3	-193.3	-66.9	20.6	3	2.9	2.6	1.2	0.4	39.8	18.9	5.2	0.4	-26.5	-14.2	-4.5	-0.6
SVN45	IIR(Rb)	6.4	-2.5	-1.4	-1.3	-95.7	-35	-7.2	-5.8	17.5	4.7	0.8	0.5	-22.5	-9.8	6.6	0.8	27.5	9.2	-7.7	-2.1
SVN46	IIR(Rb)	19.9	19.9	19.9	-0.6	-237.4	-237.4	-237.4	-4.9	12.7	12.7	12.7	0.6	60.2	32	22	2.6	-58.8	-34.3	27.5	-3.2
SVN47	IIR(Rb)	-6.7	-1.2	-1.2	-0.5	60.7	14.1	12.5	-0.3	-12.6	-5.1	-5.1	-0.6	30.1	10.3	10.3	-0.2	-36.7	-11.5	-11.5	-0.4
SVN48	IIR-M(Rb)	12.5	2.4	2.1	0.5	-178.4	-51.4	-50.3	-19.6	-31.1	-31.1	-3.4	-0.7	25.9	14.9	4.8	0.5	-28.9	-13.6	-5.4	0
SVN50	IIR-M(Rb)	9	9	0.8	0.4	-149.2	-149.2	-21.6	-11.3	3.8	-1.6	1.2	0.2	22.1	-9.7	-7.6	0.7	-25.6	-10.2	8	-0.3
SVN51	IIR(Rb)	-35.7	-3.1	-1.5	-0.6	128.7	53.2	-31.9	0	-16	-4.1	-4.1	-0.6	51.3	21.3	15	-0	-80.6	-24.4	-16.5	-0.6
SVN52	IIR-M(Rb)	-4.3	-1.6	-1	-0.5	95.7	39.1	26.7	22.2	-12.3	-1.2	-0.7	-0.3	30.2	7	3.2	0.7	-34.4	-8.5	-4.2	-1.2
SVN53	IIR-M(Rb)	-6.2	-4.1	-1.8	-0.8	-127.7	-81.8	-68.7	-32.4	-8.3	2.6	2.6	-0.1	80.7	25.4	25.4	0.3	-83	-27.1	-27.1	-1.1
SVN54	IIR(Rb)	-9.5	-2.7	-2.7	-1.2	138.3	-37.6	-33.4	-10	7.1	3.1	3.1	-0.3	30	13.8	13.8	1.2	-29	-16.5	-16.5	-2.4
SVN55	IIR-M(Rb)	7	3.7	2	0.3	-75.3	-41.1	-17.5	-4.1	14.2	4.8	0.7	0.2	79.2	-11.4	-7.4	-0.3	-84.3	15.1	9.4	0.6
SVN56	IIR(Rb)	7.3	5.2	2.9	1.6	-96.6	-54.6	-33.3	-16.6	13.1	3.2	0.7	0.3	19.8	13.3	8.6	0.4	-18.9	-12.2	6.1	1.2
SVN57	IIR-M(Rb)	7.6	3	2.3	0.5	-91.4	-70.4	-62.9	-24	-14.1	4.4	-0.9	-0.3	-25.9	-16.4	-14.5	0.9	28.6	17.9	16.7	-0.5
SVN58	IIR-M(Rb)	6.8	3.1	2.7	0.9	-134	-54.4	-40.4	-8.5	-8	-3.8	-0.6	-0.3	28.9	18.1	-11.8	-0.5	-30.3	-15.6	12	1.4
SVN59	IIR(Rb)	9.5	7.1	4.8	1.1	190.7	-67.8	-42.8	-0.1	-11.9	-4.9	-0.6	-0.2	48.4	-17.5	-11.7	-1.6	-51.1	24.6	16.5	2.7
SVN60	IIR(Rb)	6.2	2.8	2.5	0.3	-96	-43.1	-25.3	-14.3	6.9	3.7	0.7	0.4	-30.2	-18.9	-15.5	0.1	32.3	21.5	18	0.2
SVN61	IIR(Rb)	12.3	4.1	2.9	0.4	-158.9	-69.6	-57.7	-21.6	12.9	-4.4	-1	-0.4	-31.8	-15	-9.9	-1.3	44.1	19.1	12.5	1.7
SVN62	IIF(Rb)	7	3.5	1.8	0.1	-114.7	-49.7	-42	-4.3	-12.2	3.8	0.6	0.1	27.6	8.9	6.1	0.4	-29.2	-9.7	-5.5	-0.3
SVN63	IIF(Rb)	18.9	5.6	3.7	0.5	-193	-76.4	-50	-7.2	13.5	4.9	0.9	0.2	-46.1	-20	-12.7	-0.3	55.6	25.6	16.4	0.8
SVN64	IIF(Rb)	-8.1	3.9	3.3	0.7	136.6	-48	-30.9	-4.7	7.6	-4.1	0.6	0.2	24.5	5.3	4.1	0.5	-23.2	-6.2	-4.6	0.3
SVN65	IIF(Cs)	6.3	3.1	2.3	0.6	-124.9	-65.9	-51.6	-34	15.6	-4.2	-1.1	-0.3	-22.3	-17.9	-15.3	0.2	24.4	19.9	17.6	0.4
SVN66	IIF(Rb)	-18.2	-7.4	-7.4	0.2	146.4	-36.5	32	-12	-15.8	-4.3	2	-0.3	30.6	-15.3	-15.1	-0.4	-47.3	18.9	17.6	0.7
SVN67	IIF(Rb)	-9.1	3.7	3.1	1	-136.7	-57.3	-43.6	-15.1	8.2	4.5	-0.9	0.5	79.6	20.7	7.1	0.6	-73.3	-23	7.3	0.5
SVN68	IIF(Rb)	6.8	3	2.5	0.7	106.5	-44.9	-39.2	-13.3	-16.8	-4.7	-0.7	-0.3	40.1	-12.9	-10.2	-1.9	-37.8	15.9	12.7	2.6
SVN69	IIF(Rb)	-11.4	-3.8	-2.5	-1.6	151.7	42.5	26.6	-8.4	-17.9	-5.8	-0.7	-0.3	-39.1	10.3	-6.9	0.4	46.9	-10.9	-8.2	-2.1
SVN70	IIF(Rb)	11.8	3.4	2	0.4	-132.9	-58.2	-25.4	-13.8	-14.4	5.3	-0.7	-0.1	-29.1	-24	-19.2	-0.5	30.5	25.5	20	0.8
SVN71	IIF(Rb)	9.4	5	2.7	1.2	-104.2	-61.8	-47.4	-27.7	-10.8	-5	-0.7	-0.1	-22.4	-9.6	-8.5	-0.5	22.2	10.2	9.2	1.6
SVN72	IIF(Cs)	7.8	3.1	2.2	0.4	-90.2	-55.3	-39.3	-19.3	-14.4	-5.1	0.6	0.1	-23.2	14.2	11.8	0.5	21	-14	-12	-0.1
SVN73	IIF(Rb)	-10.5	-2.8	2.1	0.3	176.1	92.2	74.9	-6.7	13.7	-4.9	-0.4	-0.2	-31.1	9.6	4.9	-0.2	29.9	-10.3	-5.8	0.5

Table 4.7: GPS satellite orbit and clock error standard deviations (in cm): monthly, biannual and yearly datasets analysis

Satellite	Block	Radial				Along-Track				Cross-Track				Clock				Rad-Clock			
SVN	(Clock)	$\hat{\sigma}_{\mathrm{rad,m}}$	$\hat{\sigma}_{\mathrm{rad,b}}$	$\hat{\sigma}_{\mathrm{rad,y}}$	$\hat{\sigma}_{\mathrm{rad,all}}$	$\hat{\sigma}_{\mathrm{aln,m}}$	$\hat{\sigma}_{\mathrm{aln,b}}$	$\hat{\sigma}_{\mathrm{aln,y}}$	$\hat{\sigma}_{\mathrm{aln,all}}$	$\hat{\sigma}_{\mathrm{crs,m}}$	$\hat{\sigma}_{\mathrm{crs,b}}$	$\hat{\sigma}_{\mathrm{crs,y}}$	$\hat{\sigma}_{\mathrm{crs,all}}$	$\hat{\sigma}_{\mathrm{clk,m}}$	$\hat{\sigma}_{\mathrm{clk,b}}$	$\hat{\sigma}_{\mathrm{clk,y}}$	$\hat{\sigma}_{\mathrm{clk,all}}$	$\hat{\sigma}_{\mathrm{rmc,m}}$	$\hat{\sigma}_{\mathrm{rmc,b}}$	$\hat{\sigma}_{\mathrm{rmc,y}}$	$\hat{\sigma}_{\mathrm{rmc,all}}$
SVN41	IIR(Rb)	19.4	14.1	13.4	11.8	189.3	144.4	137.9	124.5	68.7	56.7	53.9	43.8	112.5	57.6	50.3	38.1	119.4	61.9	53.8	41.2
SVN43	IIR(Rb)	27.1	15.3	13.7	11.6	161.9	136.5	127	112.9	79.2	61.2	54.6	45.4	84	51	48.2	43.8	87.1	55	50.5	46.2
SVN44	IIR(Rb)	21	15.8	14.2	13	236.3	143.4	137.3	121.4	69	51	48.1	41.9	137.1	123.9	122.6	113	139.3	126	124.8	114.8
SVN45	IIR(Rb)	33.5	18.3	16.6	13.5	206.7	155.2	148.5	127.1	85.8	67.5	59.6	54	86.6	53	44.1	35.1	89.9	56.7	47.7	39.1
SVN46	IIR(Rb)	24.6	17.1	16	14.8	172.6	155.6	147.4	129.3	79.5	58.6	54.8	43.2	89	74.1	70.3	64.7	95.1	79.1	75.2	69
SVN47	IIR(Rb)	23.4	15.5	14.3	12.3	207.5	150.5	142.1	123.8	112.8	95.2	87.2	57.7	103.3	92.8	91.9	78.9	106.5	95.8	94.6	81.4
SVN48	IIR-M(Rb)	49.8	20.9	17.4	13.5	312.3	179.7	156.6	116	84.9	72.7	63	55.3	77.5	57.7	53.2	43.7	89.4	62.4	57.4	46.9
SVN50	IIR-M(Rb)	69.3	25.9	25.9	13.1	235.9	183.4	183.4	111.1	61.3	46.1	43.6	36.4	77.2	45.6	45.6	29.8	105	56.6	56.6	34.9
SVN51	IIR(Rb)	26.8	14.7	13.5	11.1	173.5	136.2	129.2	118	98.1	60.4	54.9	47.9	65.8	44.1	38	30.5	68.6	46.7	41.3	33.6
SVN52	IIR-M(Rb)	17.1	13.8	13.5	12.6	149.3	140.8	133.5	123.4	83.7	61.2	52.6	44.6	102.9	79.2	74.8	58.2	108.5	82.6	78.3	61.1
SVN53	IIR-M(Rb)	21.3	15.6	15.6	13.1	240.2	166.7	160.9	140.3	111.4	82.1	75.7	55.8	97.2	84.1	80	70.4	100.4	86.3	82.3	73.6
SVN54	IIR(Rb)	31.1	17.5	16.2	12.8	162.3	140.7	135.8	119	83.8	64.5	60.9	49	87.5	58.1	47	39.5	90	63.2	50.8	43.3
SVN55	IIR-M(Rb)	18.5	13.4	12.4	11.8	172.3	149	135	122.7	85.7	66.3	56.9	45.7	39.1	32.2	30.1	26	44	36.9	34.2	30.3
SVN56	IIR(Rb)	45.3	22.1	17.7	13.2	159.7	129.8	129.7	112.5	82.6	65.4	62.5	46.7	38.2	35.9	32.6	27.8	52.7	40	36.2	33.1
SVN57	IIR-M(Rb)	32.1	20.4	17.9	14.9	247.6	175.2	169.9	151.2	99.9	70.6	62.6	49	96.5	83.4	82	63.6	107	89.2	86.8	67.5
SVN58	IIR-M(Rb)	24.1	16.5	16.3	13.9	212.5	152.1	139.4	129.4	73.6	55.9	51.2	42.4	64.9	37.1	33.5	29.9	69.2	41.8	38.8	35.6
SVN59	IIR(Rb)	17.5	12.2	12	10.7	171.3	143.9	133.7	112.9	103.8	81.9	73.4	56.8	42.1	38.6	37.1	31.9	45.3	41.3	39.7	34.8
SVN60	IIR(Rb)	15.3	13	11.8	10.8	141.8	122	120.2	108.8	76	60.7	54.4	45.4	39.4	30.9	30.3	26.7	41.9	33	32.9	29.2
SVN61	IIR(Rb)	22.2	14.3	12.6	11	148.3	133.4	130.8	109.9	80.4	60.2	54.8	48.6	86.6	56	47.3	35.3	86.7	59.2	50.2	38
SVN62	IIF(Rb)	34.9	26.9	23	19.1	191	144.8	144.8	119.5	59.4	45.5	45.3	38.2	36.8	28.7	26.3	23.4	46.2	34.8	34.8	29.6
SVN63	IIF(Rb)	29.7	21.4	20.1	16.8	172.5	158.2	158.2	126.5	64.5	54	48.9	41.9	72	59.8	59.8	30.2	75.4	63.6	63.6	34.4
SVN64	IIF(Rb)	44.3	25.2	23.3	19.7	238.6	143.8	137	115	80.4	48.2	43.9	38.1	93.5	91.7	44.9	28.9	98.1	96.3	50.5	36
SVN65	IIF(Cs)	38.8	28.3	27.4	25	187.4	155.8	148.4	137.9	61.7	43.8	40.2	39	137	128.7	123.5	116.6	143.3	131.7	126.9	119.6
SVN66	IIF(Rb)	39.2	39.2	23.7	18.2	240.5	157.2	147.9	125.5	66.1	43.8	36.9	33.6	40.6	30.3	27.5	22.6	49.2	42	33.4	28.4
SVN67	IIF(Rb)	43.7	39.4	28.7	20.4	179.3	140	129	121	68	68	46.7	42.1	33.6	33.6	26.3	22.9	53.8	51.3	39	30.8
SVN68	IIF(Rb)	44.7	34.4	34.4	20.4	215.5	159.2	159.2	114.5	58.1	44.7	42.8	38.3	59.4	35.5	35.5	27.8	63.9	51.6	51.6	35
SVN69	IIF(Rb)	51	30	25.6	20.8	222	214.6	214.6	132.5	59.9	59.9	59.9	40.4	57.7	48.8	46	39.4	71.6	52	50	45.2
SVN70	IIF(Rb)	64.9	48.7	33.1	26	248.9	191.6	156.9	146.8	52.7	46.5	41.2	40.8	57.4	42.6	37.6	30.8	83.4	65.3	50.5	40.8
SVN71	IIF(Rb)	44.4	33.6	27	23.5	211.2	151	136.5	122.7	62.1	39.2	35.6	34.3	41.2	38.4	29.5	23.9	57.8	49.3	39.3	33.2
SVN72	IIF(Cs)	45.7	33.1	33.1	24.7	223.5	150.1	150.1	136.2	56	43	41.7	40.5	118.3	100.8	97	95	120.9	102.5	99.8	98.3
SVN73	IIF(Rb)	56.2	31.8	25	20.4	258.1	151.3	134.6	131	85.9	75.1	67	60.1	41.8	35	35	25.3	75.5	44.1	36.8	32.8

Table 4.8: GPS satellite $SISRE_{WUL,\text{orb}}$ and $SISRE_{WUL}$ RMS (in cm): monthly, biannual and yearly datasets analysis

Satellite Name	Block (Clock)	$SISRE_{WUL,\text{orb}}$				$SISRE_{WUL}$			
		$RMS_{\text{orb,m}}$	$RMS_{\text{orb,b}}$	$RMS_{\text{orb,y}}$	$RMS_{\text{orb,all}}$	$RMS_{\text{wul,m}}$	$RMS_{\text{wul,b}}$	$RMS_{\text{wul,y}}$	$RMS_{\text{wul,all}}$
SVN41	IIR(Rb)	71.4	50.4	45	40.5	147.6	83.9	75.9	63.4
SVN43	IIR(Rb)	52.2	43.2	41	37.9	104	74.3	73.6	67.3
SVN44	IIR(Rb)	73.3	48.2	46.5	41	163.6	150.8	148.3	135.6
SVN45	IIR(Rb)	79	52.5	49.5	43.1	108.8	83.9	74.3	63.1
SVN46	IIR(Rb)	65.6	52	49.5	44.1	116.4	102.4	96.4	88.3
SVN47	IIR(Rb)	72.3	51.7	49.7	42.1	131.3	118.5	117.3	104.2
SVN48	IIR-M(Rb)	119	62.1	54.9	41	198.1	99.6	88.1	69.3
SVN50	IIR-M(Rb)	106.8	66.3	66.3	37.9	138	84.3	84.3	53.1
SVN51	IIR(Rb)	56.9	44.2	42.5	39.6	84.1	69.2	64.8	56.8
SVN52	IIR-M(Rb)	51.2	45.5	43.9	40.8	119.9	101.6	98.7	82.1
SVN53	IIR-M(Rb)	100.9	60.9	56.6	46.3	151.5	119.8	111.6	97
SVN54	IIR(Rb)	54.5	47.4	45.9	40.1	107.1	84.5	73.8	63.2
SVN55	IIR-M(Rb)	61	47.8	44.3	40.6	85.3	71.9	65.3	56.2
SVN56	IIR(Rb)	59.7	44.4	43	38.8	79.4	64.9	61.9	52.3
SVN57	IIR-M(Rb)	82.1	56.9	54.6	49.2	134	114.7	112.1	93.8
SVN58	IIR-M(Rb)	72.2	50.3	46.1	43	90.6	65.3	61.3	57
SVN59	IIR(Rb)	57.9	48.8	44.4	38.7	79	72.9	70.1	58.9
SVN60	IIR(Rb)	50.1	41.8	40.7	36.5	67.8	58.1	58	52.2
SVN61	IIR(Rb)	49.9	42.3	42.2	36.7	135.4	80.3	73	58.5
SVN62	IIF(Rb)	73.7	55.3	52.9	44.9	80.6	66.8	66.8	56.4
SVN63	IIF(Rb)	80.2	56.1	56.1	45.7	134.1	97.4	97.4	60.7
SVN64	IIF(Rb)	90.7	54.7	52.3	44.7	112.5	110.7	68	56.9
SVN65	IIF(Cs)	76.1	61.2	57.9	53.9	173.4	161.2	153.1	143.7
SVN66	IIF(Rb)	85.8	85.6	54.4	45.3	99.5	99.5	67.8	55.5
SVN67	IIF(Rb)	74.9	71.9	57.4	46.3	85.2	85.2	65.8	55.6
SVN68	IIF(Rb)	88.6	66.7	66.7	43.8	99.4	77.9	77.9	55.8
SVN69	IIF(Rb)	100.3	100.3	100.3	48.7	123	113.8	113.8	74.8
SVN70	IIF(Rb)	107.8	87.5	64.7	56	133.9	102.2	80.2	68.1
SVN71	IIF(Rb)	105.1	67.2	55.1	49.5	141.2	90.2	67.8	58.6
SVN72	IIF(Cs)	90.1	64.7	64.7	54.2	144.2	128.4	124.3	123.7
SVN73	IIF(Rb)	107.4	63.6	54	49.8	116.1	79.9	79.9	63.5

Table 4.9: Galileo satellite orbit and clock error means (in cm): monthly, biannual and yearly datasets analysis

Satellite Number	Clock Type	Radial				Along-Track				Cross-Track				Clock				Rad-Clock			
		$\hat{\mu}_{\mathrm{rad,m}}$	$\hat{\mu}_{\mathrm{rad,b}}$	$\hat{\mu}_{\mathrm{rad,y}}$	$\hat{\mu}_{\mathrm{rad,all}}$	$\hat{\mu}_{\mathrm{aln,m}}$	$\hat{\mu}_{\mathrm{aln,b}}$	$\hat{\mu}_{\mathrm{aln,y}}$	$\hat{\mu}_{\mathrm{aln,all}}$	$\hat{\mu}_{\mathrm{crs,m}}$	$\hat{\mu}_{\mathrm{crs,b}}$	$\hat{\mu}_{\mathrm{crs,y}}$	$\hat{\mu}_{\mathrm{crs,all}}$	$\hat{\mu}_{\mathrm{clk,m}}$	$\hat{\mu}_{\mathrm{clk,b}}$	$\hat{\mu}_{\mathrm{clk,y}}$	$\hat{\mu}_{\mathrm{clk,all}}$	$\hat{\mu}_{\mathrm{rmc,m}}$	$\hat{\mu}_{\mathrm{rmc,b}}$	$\hat{\mu}_{\mathrm{rmc,y}}$	$\hat{\mu}_{\mathrm{rmc,all}}$
GSAT0214	PHM	7.8	4.3	3.8	3.6	-15.9	-6.4	-4.6	-4.5	-15.4	-7.7	-6.5	-2.2	8.5	5	3.5	2.7	8.3	-3.6	1.7	0.8
GSAT0213	PHM	5.6	4.2	3.4	3.1	-20.2	-16	-11.4	-11.1	20.1	10.6	-7.2	-1.9	7.5	3.7	2.3	1.6	-8.2	2.6	2	1.5
GSAT0212	PHM	4.5	3.4	2.8	1.8	-32.7	-10.6	-8	-6	-19	6.6	4.5	2.1	13.3	6.4	3.6	3.4	13.6	-6.2	-2.3	-1.5
GSAT0211	PHM	-5.7	-3.1	-1.2	-0.6	-19.1	-14.9	-11.4	-8.5	-13.2	-7.2	-5.7	-2.4	-9.5	-6.8	-5.6	-4.6	-6.4	7.5	5.7	4
GSAT0210	PHM	-6.6	4.9	4.9	-0.1	-28.3	-28.3	-28.3	-7.3	-14.6	-9.9	7.5	-1.1	4.1	4.1	4.1	0.9	3.8	-3.6	-1.1	-1.1
GSAT0209	PHM	2.7	1.3	0.9	0.3	-15.2	-5.2	-4.9	-3.7	-13.5	7.4	6.4	2.5	5.6	-5.5	-2.9	-2.2	-4.5	4.4	3.9	2.5
GSAT0208	PHM	-7	-3.2	1.5	-0.1	-15.4	-9.9	-8.5	-7.1	12.9	7.9	5.2	1.4	-7.9	-5.1	-2.8	-1.7	5.4	4.3	4.3	1.5
GSAT0207	PHM	3	1.6	1.2	0.4	-17.1	-15.7	-11.2	-9.4	-12.9	-8.4	-2	-0.4	-4.1	-1.9	1.3	0.6	-3.4	2.4	-0.2	-0.2
GSAT0206	PHM	-7.7	-3.9	-1.8	-0.8	-16	-10.7	-9.1	-9	10.4	3.1	1.5	0.1	-7.5	-3.8	-2.5	-1.6	-5.9	3.8	0.9	0.8
GSAT0205	PHM	-9.3	-4.9	-2.6	-1.6	-13.3	-4.2	-4.1	-1.8	18.2	5.1	2.6	0.8	-7.5	-4.2	-2.3	-1.3	-7.1	-4.6	-0.3	-0.3
GSAT0204	RAFS	2.9	1.7	1.3	1.2	-17.1	-11.2	-10.7	-8.7	14.5	6	5.9	2.7	10	7.8	6.5	3.3	-5.5	-6.1	-5.2	-2.1
GSAT0203	PHM	2.2	-1.4	0.8	0.8	-8.6	-4	-2.9	-2.3	14	7.7	6	2	-7.8	3.1	1.7	1.2	5.4	-2.5	-0.9	-0.4
GSAT0103	PHM	2.4	-1.6	0.5	0.5	-10.4	-6.1	-6.1	-4.9	12.7	0.9	0.9	0.9	5.2	2.7	-0.9	-0.4	-5.6	-4.2	1.4	0.9
GSAT0102	PHM	2.3	-1.7	1	0.8	-13.4	-9.7	-8.4	-6.3	17.1	3.7	2.9	2.4	5.9	-0.8	-0.7	0.1	-6.2	1.7	1.7	0.7
GSAT0101	RAFS	2.8	-2	0.6	0.2	-19.4	-10.5	-8.4	-5.8	16.9	2.7	2.4	1.9	5.3	-1.4	-1	-0.5	-4.9	-2.6	0.8	0.7

Table 4.10: Galileo satellite orbit and clock error standard deviations (in cm): monthly, biannual and yearly datasets analysis

Satellite SVN	Clock Type	Radial				Along-Track				Cross-Track				Clock				Rad-Clock			
		$\hat{\sigma}_{\mathrm{rad,m}}$	$\hat{\sigma}_{\mathrm{rad,b}}$	$\hat{\sigma}_{\mathrm{rad,y}}$	$\hat{\sigma}_{\mathrm{rad,all}}$	$\hat{\sigma}_{\mathrm{aln,m}}$	$\hat{\sigma}_{\mathrm{aln,b}}$	$\hat{\sigma}_{\mathrm{aln,y}}$	$\hat{\sigma}_{\mathrm{aln,all}}$	$\hat{\sigma}_{\mathrm{crs,m}}$	$\hat{\sigma}_{\mathrm{crs,b}}$	$\hat{\sigma}_{\mathrm{crs,y}}$	$\hat{\sigma}_{\mathrm{crs,all}}$	$\hat{\sigma}_{\mathrm{clk,m}}$	$\hat{\sigma}_{\mathrm{clk,b}}$	$\hat{\sigma}_{\mathrm{clk,y}}$	$\hat{\sigma}_{\mathrm{clk,all}}$	$\hat{\sigma}_{\mathrm{rmc,m}}$	$\hat{\sigma}_{\mathrm{rmc,b}}$	$\hat{\sigma}_{\mathrm{rmc,y}}$	$\hat{\sigma}_{\mathrm{rmc,all}}$
GSAT0214	PHM	30.6	17.7	17.3	17	110.8	52	49	42.4	25.4	20.3	19.5	18.9	39.7	21	19.8	17.4	35.6	20.1	19	18.4
GSAT0213	PHM	29.9	19.1	19.1	17.5	103.2	49.4	46.7	43	24	19.4	19.4	18.8	29.6	17.9	17.1	16.2	29.5	18.7	18.7	18
GSAT0212	PHM	19.9	17.8	17.8	15	42.6	36.6	36.6	31.8	19.3	18.6	18.6	18	20.3	16	15.3	15.3	24.1	18.6	18.6	16.8
GSAT0211	PHM	21.8	17.9	15.9	15.7	45.1	35	32.1	31.3	18.7	18	17	16.9	20.1	17.3	16.2	15.8	24.3	19.4	17.3	17
GSAT0210	PHM	21.8	18.3	16.1	15.7	41.2	34.8	33	32.3	22.3	19.4	18.7	18	19.9	18.1	17.2	16.8	20.3	17.5	16	16.1
GSAT0209	PHM	20.9	15.9	15.3	14.6	74.5	40.6	38.4	34.4	21	20.1	19.5	18.8	20.1	14.5	14.1	14.1	19.7	17.4	15.8	15
GSAT0208	PHM	33.2	17.4	16.4	15	63.5	35.7	34.2	32.6	21.4	19.6	19.3	18.4	31.9	17.9	17	15.7	21.2	17.6	15.7	14.8
GSAT0207	PHM	18.9	14.6	14.6	13.4	35.5	29.3	29.3	27.9	20.9	19.8	19.8	18.4	18.5	15.1	14.6	14.6	20.1	15	14.9	14.4
GSAT0206	PHM	22.9	20	16.5	16.4	46.5	46.5	35.2	33.7	21.8	20.7	19.4	18.6	34.8	21.8	21.5	18	36.8	20	19.1	17.4
GSAT0205	PHM	23.6	17.6	16.2	16	38.1	33.4	31.5	31.4	21.3	19	18.5	18	18.5	15.9	15.5	14.6	21.8	18	16.5	16.2
GSAT0204	RAFS	23.2	23.2	23.2	16	36.9	34	32.5	32.6	18.2	17.7	18.8	18.7	23.5	23.1	23.1	18.5	26.3	26.3	26.3	19
GSAT0203	PHM	26.1	18.1	15.9	16	57	36.9	36.9	34.9	24.2	21.6	19.9	19.3	25.3	20	19	18.6	21.1	18.3	16.4	16.2
GSAT0103	PHM	19.6	17.7	16.1	14.5	54.4	45.3	41.7	39.1	25.4	24.5	24.6	22.7	22.4	17	16.4	16.1	19.1	17.9	17	16.1
GSAT0102	PHM	24.4	18.2	16.8	16.3	42.4	40.5	37.4	35.6	24.3	21.6	22.7	21.3	24	17.9	16.6	16.4	24.4	20.3	17.1	16.3
GSAT0101	RAFS	25.2	19.4	18	17.4	52.7	41.7	36.6	35.6	23	19.4	20.4	19.5	26.3	19.6	18.9	17.8	22.9	19.9	17.3	17.3

Table 4.11: Galileo satellite $SISRE_{WUL,\text{orb}}$ and $SISRE_{WUL}$ RMS (in cm): monthly, biannual and yearly datasets analysis

Satellite Name	**Clock Type**	$SISRE_{WUL,\text{orb}}$				$SISRE_{WUL}$			
		$RMS_{\text{orb,m}}$	$RMS_{\text{orb,b}}$	$RMS_{\text{orb,y}}$	$RMS_{\text{orb,all}}$	$RMS_{\text{wul,m}}$	$RMS_{\text{wul,b}}$	$RMS_{\text{wul,y}}$	$RMS_{\text{wul,all}}$
GSAT0214	PHM	50	26.9	25.4	24.4	81.6	42.9	40.4	36.8
GSAT0213	PHM	46.4	25.8	25.4	24.8	68.8	38.9	36.8	36
GSAT0212	PHM	27.6	24.4	24.4	20.9	38.3	34.1	34.1	31.2
GSAT0211	PHM	28.4	24.1	21.7	21.3	42.4	36.4	32.5	32.5
GSAT0210	PHM	29.7	24.9	22.5	21.8	46	46	37.1	35.7
GSAT0209	PHM	33.8	23.2	21.7	21.2	48.5	32.2	30.9	30.8
GSAT0208	PHM	45.7	24.4	23.1	21.4	75.1	39.4	37.3	33
GSAT0207	PHM	24.7	20.4	20.3	19	36.3	30.7	30.6	29.6
GSAT0206	PHM	31.9	27.9	23.1	22.7	53	45.8	39.5	35.7
GSAT0205	PHM	30.7	23.9	22	21.9	43.1	34	33	32
GSAT0204	RAFS	30.8	30.8	30.8	22.1	47.1	47.1	47.1	35
GSAT0203	PHM	36.9	25.8	22.9	22.7	57.6	41.9	38.7	37.9
GSAT0103	PHM	28.3	26.1	24	22.1	40.5	37.7	35.9	34.8
GSAT0102	PHM	32.8	26.4	24.4	23.5	43	37.9	35.9	35.9
GSAT0101	RAFS	35	27.1	24.6	24.3	53.5	42.8	41.6	38.5

5 Error Correlation and Sample Independence

Chapter 4 exposed evidence of time correlation in range error data for both GPS and Galileo satellites. This chapter takes a step further and investigates the origin of this correlation and the consequences that it directly has for satellite range error overbounding. The first part of this chapter focuses on the dynamic process behind the error correlation in order to understand where the fundamental differences between GPS and Galileo errors lie. By performing an error autocovariance study along with a spectral density analysis, this chapter reveals the influence of onboard clock on error correlation it being the major driver for data independence. The second part presents a methodology to determine the time between effectively independent samples. Based on an estimation variance analysis, this work computes the fraction of independent samples for a given orbit and clock error dataset. Results show that the time between effective independent samples is highly dependent on the constellation and onboard clock type. This ultimately justifies the different levels of variation when clustering satellite error data in monthly, biannual and yearly datasets along with the implications that it has on the range overbound for ARAIM.

5.1 Mapping Ephemeris and Clock errors for Correlation Analysis

When it comes to analyzing the correlation characteristic to satellite range error, some discussion is needed regarding how to map the three orbit error components and the clock into the range domain. Unlike the study carried out in Chapter 4, this chapter does not focus on the projection of the error over different users within the footprint but instead it analyzes the error from a satellite payload perspective. As discussed in Section 4.3.1, three options for representing the range error are available: $SISRE_{WUL}$, $SISRE_{IUP}$, and Radial-Minus-Clock (RMC). The first option does not provide a continuous function in the sense that for each epoch k the worst user projection corresponds to different locations; a correlation analysis of this dataset has no physical meaning. The second option, $SISRE_{IUP}$, is not a continuous function either. Each individual user (a total of 642) can only unceasingly track a given satellite during 5-6 hours, limiting the correlation study. The best alternative to create a continuous function of the satellite payload range error is the RMC distribution. As shown in Figures 4.1 and 4.2 and Table 4.3, RMC error provides an excellent representation of the core of real error distribution. Although distribution tails are extremely relevant for the integrity analysis (as discussed in Section 4.2), they do not have a large impact on the correlation study outcome since they represent just a few values of the full distribution. Finally, it is important to remark that RMC is a continuous function

across ephemeris changeovers or uploads being this a key aspect for time-dependent analysis.

5.2 Data Autocorrelation and Autocovariance

The determination of the number of independent samples is paramount for error overbounding. Inferring properties of the underlying distribution from a given dataset is always challenging. As pointed out in Sections 4.4 and 4.5, satellite range error is eminently correlated over time creating high variability of the distribution core parameters ($\hat{\mu}_{\mathrm{x}}$ and $\hat{\sigma}_{\mathrm{x}}$) on a monthly basis. In order to perform safe and efficient (preventing availability risk) SISRE overbounds, the error autocorrelation needs to be addressed within ISM generation [81].

For a given random process $\mathrm{x}(t)$, let us define the autocorrelation R_{xx} and autocovariance C_{xx} functions as

$$R_{\mathrm{xx}}(\tau) = E\left[\mathrm{x}(t)\ \mathrm{x}(t+\tau)\right] \tag{5.1}$$

$$C_{\mathrm{xx}}(\tau) = R_{\mathrm{xx}} - \mu_{\mathrm{x}}^2 \tag{5.2}$$

where $\mu_{\mathrm{x}} = E\left[\mathrm{x}(t)\right]$ is the mean value of the random variable $\mathrm{x}(t)$.

Let us assume that over the interval of data collection $0 < t < T$, our error data $\mathrm{x}(t)$ comes from a stationary, ergodic random process with mean μ_{x}, variance σ_{x}^2, autocorrelation function R_{xx}, and autocovariance C_{xx}. Because the process is ergodic, those parameters can be estimated using the following expressions (following Chapter 5 in [82]):

$$\hat{\mu}_{\mathrm{x}} = \frac{1}{T}\int_0^T \mathrm{x}(t)dt \tag{5.3}$$

$$\hat{\sigma}_{\mathrm{x}}^2 = \frac{1}{T}\int_0^T \mathrm{x}^2(t)dt - \hat{\mu}_{\mathrm{x}}^2 \tag{5.4}$$

$$\hat{R}_{\mathrm{xx}}(\tau) = \frac{1}{T-\tau}\int_0^{T-\tau} \mathrm{x}(t)\mathrm{x}(t+\tau)dt \tag{5.5}$$

$$\hat{C}_{\mathrm{xx}}(\tau) = \hat{R}_{\mathrm{xx}}(\tau) - \hat{\mu}_{\mathrm{x}}^2. \tag{5.6}$$

Since the error data is collected in discrete time $\mathrm{x}(k)$, let us write the expressions above in discrete form as

$$\hat{\mu}_{\mathrm{x}} = \frac{1}{N}\sum_{k=0}^{N-1} \mathrm{x}(k) \tag{5.7}$$

$$\hat{\sigma}_{\mathrm{x}}^2 = \frac{1}{N}\sum_{k=0}^{N-1} \mathrm{x}^2(k) - \hat{\mu}_{\mathrm{x}}^2 \tag{5.8}$$

$$\hat{R}_{\mathrm{xx}}(k) = \frac{1}{N-k} \sum_{i=-N+k+1}^{N-k-1} \mathrm{x}(i)\mathrm{x}(i+k) \tag{5.9}$$

$$\hat{C}_{\mathrm{xx}}(k) = \hat{R}_{\mathrm{xx}}(k) - \hat{\mu}_{\mathrm{x}}^2. \tag{5.10}$$

The autocovariance provides a temporal representation of the correlation between the error and a delayed copy of itself. Typically, the autocovariance function is normalized by the sample variance so that lag zero is equal to one. Doing this is useful because the correlation is a scale-free measure of the statistical independence of the error. Let us define the normalized estimated autocovariance matrix as $\bar{C}_{\mathrm{xx}}(k) = \hat{C}_{\mathrm{xx}}(k)/\hat{\sigma}_{\mathrm{x}}^2$.

As exposed in Chapter 4, SISRE distribution is mainly driven by the onboard clock type. Consequently, in this chapter, error data are clustered in four different groups: GPS-Rb, GPS-Cs, Galileo-RAFS, and Galileo-PHM. For each of the four groups, a representative satellite is taken to generate the autocovariance and spectral density plots in Figures 5.1-5.5: SVN67 / PRN06 (Rb), SVN65 / PRN24 (Cs), GSAT0101 / E11 (RAFS), and GSAT0205 / E24 (PHM).

Figure 5.1 illustrates the large differences in the clock autocovariance for Rubidium clock-equipped GPS satellites versus Cesium. Orbit error components (radial, along, and cross-track error) show no significant disparity between satellite types having a 12-hour harmonic component which remains over several days. This sinusoidal behavior is attributed to the inherent dynamics of the satellite throughout its orbital motion. In particular, it is due to the limitation of the 15 quasi-Kleperian parameters used to model the satellite motion [77]. Apart form this half-sidereal day harmonic component, the along-track error also shows a 2-hour sinusoidal behavior which coincides with the nominal update rate of the GPS navigation message.

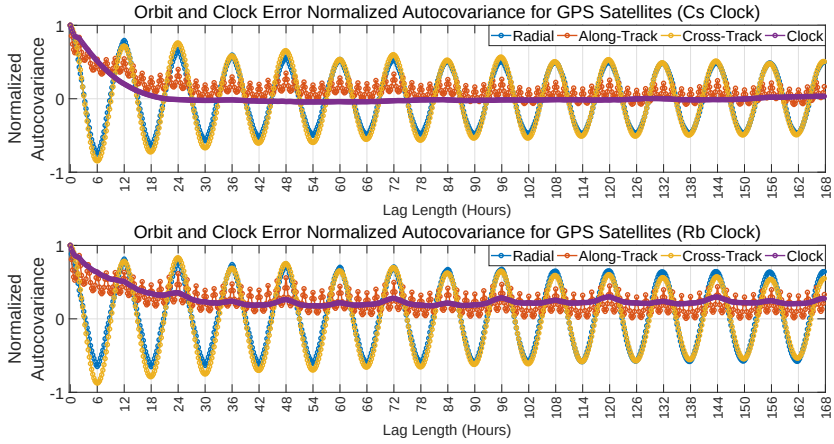

Figure 5.1: Sample autocovariance for GPS orbit and clock (Cs and Rb) errors

Unlike orbit components, clock error (purple lines in Figure 5.1) shows considerable

contrast between satellite types not only in the harmonic element but also in the convergence time. This suggests that within the ODTS process the estimation of the satellite clock prediction gets 'contaminated' by the residuals of orbital model fitting. Since orbit and clock states are jointly estimated using code and phase observations (ODTS models in [77]), their computation are highly coupled and hence the correlation of the orbit prediction error maps into the clock prediction error. In order to better understand these effects, let us analyze the error correlation in the frequency domain. For a given signal x(t), the Wiener-Khinchin relation defines the link between its autocorrelation function $R_{\mathrm{xx}}(\tau)$, in the time domain, and its power spectral density $S_{\mathrm{xx}}(f)$, in the frequency domain, as follows

$$S_{\mathrm{xx}}(f) = \int_{-\infty}^{\infty} R_{\mathrm{xx}}(\tau)\, e^{-j2\pi f \tau} d\tau. \tag{5.11}$$

Figure 5.2 includes the Singled-Sided Amplitude Spectrum (SSAS) for orbit and clock errors for both GPS satellite types. The dominant harmonic component for orbit error corresponds to the 12-hour frequency ($2.31 \times 10^{-5} Hz$) showing also several $n \times 12$-hour components. As pointed out above, there is no significant contrast in the orbit error between the two satellite types. However, the difference lies in the relative power density between the orbit elements and clock noise level. One can be misled by results shown in Figure 5.1 thinking that Rb clocks induce larger range errors than Cs clocks - this is actually not true. The normalized autocovariance does not indicate anything about the distribution variance but about its correlation. In fact, as shown in Table 4.8, Cs-equipped SISRE RMS is typically twice as big as Rb-equipped satellite values (80-100 cm vs. 40-50 cm) due to better short term stability [78]. In Figure 5.2, it can be observed that the error noise level in Cs clocks is significantly higher than in Rb clocks. On the left side, it is illustrated that the power level of clock error noise (yellow line) is above the power level of the harmonic components of the orbit error. As a consequence the orbit correlation has a larger impact on range error for Rb-equipped satellites than for Cs-equipped.

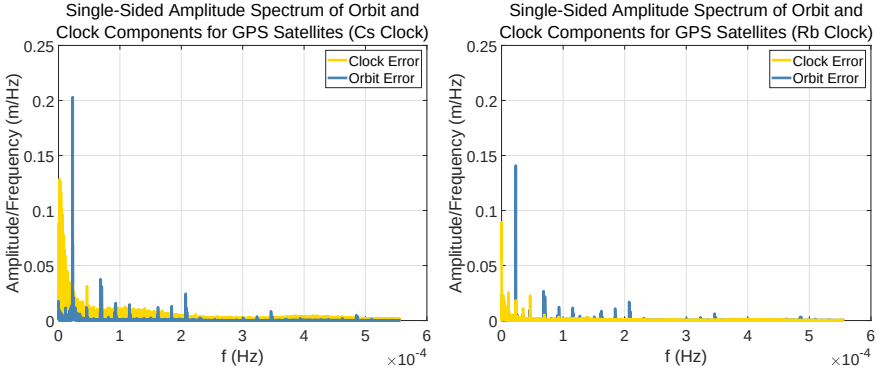

Figure 5.2: Single-Sided Amplitude Spectrum of orbit and clock error contribution to range error for GPS satellites

A similar analysis is carried out for Galileo satellites in Figure 5.3. Unlike in the GPS case, the onboard clock does not create substantial differences in the normalized autocovariance between clock types. Figure 5.4 includes the orbit and clock component SSAS for RAFS and PHM Galileo satellites. A 14-hour harmonic component is observed for orbit error in both cases which is compliant with the Galileo orbital period ($1.98 \times 10^{-5}\, Hz$). However no significant contrast can be detected among clock types. In particular, both yellow lines in Figure 5.4 indicate similar noise level for PHM and RAFS clocks. The next section will prove that in fact there is a slight difference between the two satellite types impacting the time between effectively independent samples.

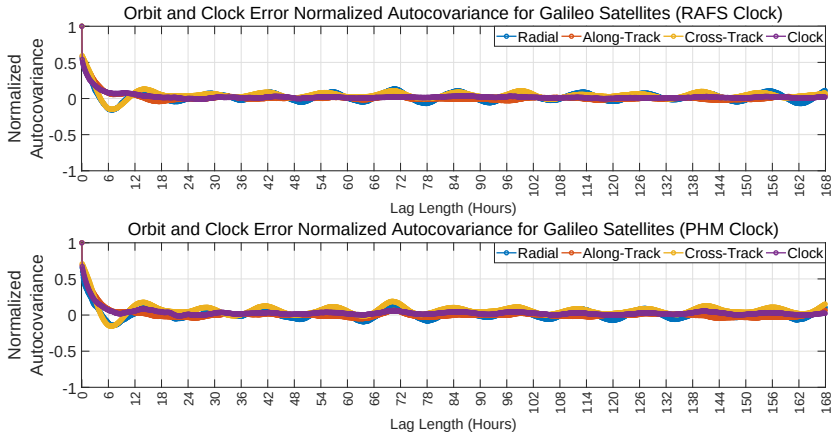

Figure 5.3: Sample autocovariance for Galileo orbit and clock (RAFS and PHM) errors

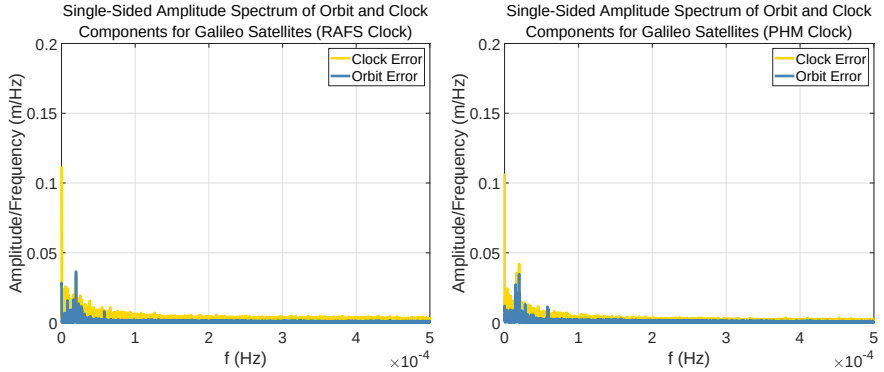

Figure 5.4: Single-Sided Amplitude Spectrum of orbit and clock error contribution to range error for Galileo satellites

A comparison between Figures 5.1 and 5.3 exposes the differences in error correlation between GPS and Galileo satellites. The Galileo orbit error sinusoidal component decays significantly faster than GPS. This is corroborated by the range error spectral density depicted in Figure 5.5. Unlike GPS, Galileo only shows one harmonic component corresponding to the 14 hour orbital period. However the power associated with this component is lower relative to lag zero ultimately leading to a less dominant orbit correlation for Galileo range error than for GPS.

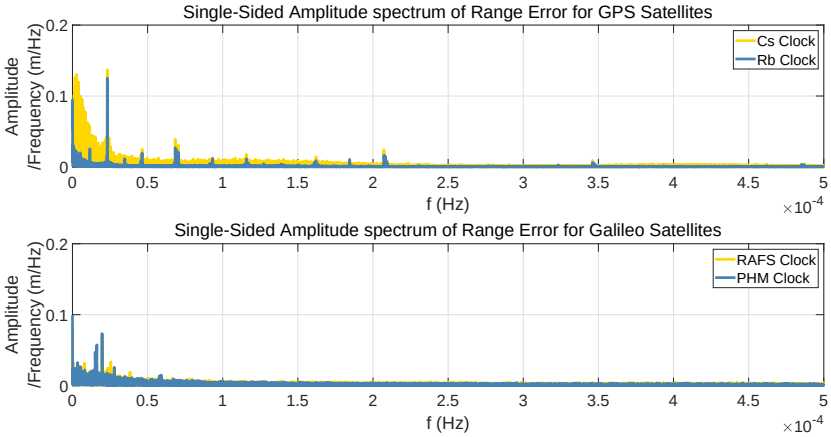

Figure 5.5: Single-Sided Amplitude Spectrum of range error for GPS (Cs and Rb clocks) and Galileo (RAFS and PHM clocks)

5.3 Covariance Analysis for Effectively Independent Samples Determination

The error temporal correlation shown in the prior section only provides a qualitative notion of sample independence. Figures 5.1, 5.3, and 5.5 exposed the differences between constellations and satellite type showing that range errors for GPS Rb clock satellites are significantly more correlated than GPS Cs clock and Galileo errors. However, it does not bring a specific procedure to determine the number of effectively independent samples given a certain dataset. This section takes a step further and proposes a method based on estimation variances for sample mean and standard deviation.

Let us assume again that error data $\mathrm{x}(t)$ comes from a stationary, ergodic random process with mean μ_{x}, variance σ^2_{x}, autocorrelation function R_{xx}, and autocovariance C_{xx} (defined in expressions (5.3)-(5.6)). Given a monitoring period for which we intend to characterize the satellite range error, confidence in the estimation of $\hat{\mu}_{\mathrm{x}}$ and $\hat{\sigma}^2_{\mathrm{x}}$ will be given by their variances $\mathrm{Var}[\hat{\mu}_{\mathrm{x}}]$ and $\mathrm{Var}[\hat{\sigma}^2_{\mathrm{x}}]$. While the first variance term is easy to obtain, the variance of the estimated sample variance does not have a simple form.

In this regard, we define the mean square value of $\mathrm{x}(t)$ as $\psi_{\mathrm{x}}^2 = E[\mathrm{x}^2(t)]$ which can be estimated by

$$\hat{\psi}_{\mathrm{x}}^2 = \frac{1}{T}\int_0^T \mathrm{x}^2(t)dt. \tag{5.12}$$

Using expression (5.12) in (5.4), the estimated sample variance can be written as

$$\hat{\sigma}_{\mathrm{x}}^2 = \hat{\psi}_{\mathrm{x}}^2 - \hat{\mu}_{\mathrm{x}}^2. \tag{5.13}$$

Chapter 8 in [82] provides a closed-form expressions for both $\mathrm{Var}[\hat{\mu}_{\mathrm{x}}]$ and $\mathrm{Var}[\hat{\psi}_{\mathrm{x}}^2]$,

$$\mathrm{Var}[\hat{\mu}_{\mathrm{x}}] = \frac{1}{T}\int_{-T}^{T}\left(1 - \frac{|\tau|}{T}\right) C_{\mathrm{xx}}(\tau)d\tau \tag{5.14}$$

$$\mathrm{Var}[\hat{\psi}_{\mathrm{x}}^2] = \frac{2}{T}\int_{-T}^{T}\left(1 - \frac{|\tau|}{T}\right)\left(C_{\mathrm{xx}}^2(\tau) + 2\mu_{\mathrm{x}}^2 C_{\mathrm{xx}}(\tau)\right)d\tau. \tag{5.15}$$

Again, since our error data is collected in discrete time $\mathrm{x}(k)$, expressions (5.12), (5.14), and (5.15) can be written as

$$\hat{\psi}_{\mathrm{x}} = \frac{1}{N}\sum_{k=0}^{N-1} \mathrm{x}^2(k) \tag{5.16}$$

$$\mathrm{Var}[\hat{\mu}_{\mathrm{x}}] = \frac{1}{N}\sum_{-N}^{N}\left(1 - \frac{|k|}{N}\right)\hat{C}_{\mathrm{xx}}(k) \tag{5.17}$$

$$\mathrm{Var}[\hat{\psi}_{\mathrm{x}}^2] = \frac{2}{N}\sum_{-N}^{N}\left(1 - \frac{|k|}{N}\right)\left(\hat{C}_{\mathrm{xx}}^2(k) + 2\hat{\mu}_{\mathrm{x}}^2\hat{C}_{\mathrm{xx}}(k)\right). \tag{5.18}$$

Note that Equations (5.14) and (5.15) require the true values of the error autocovariance $C_{\mathrm{xx}}(k)$, which is unknown. They have been substituted by its estimated value obtained using expression (5.10). This is an important step that needs further motivation. Technically, the true values shall be substituted with a range of values around the sampled ones given by confidence interval. According to the Central Limit Theorem (CLT), the observed $\hat{C}_{\mathrm{xx}}$ will be close to the true one if the number of independent samples is big enough (typically larger than 30). Since the estimation of the autocovariance function is carried out based on several years of SISRE data, the use of (5.10) is legitimized. The scope of this derivation is to determine how many of those N samples are effectively independent N^*. It is important to clarify that we will use as many samples as available in our dataset X to compute $\hat{\mu}_{\mathrm{x}}$ and $\hat{\sigma}_{\mathrm{x}}^2$, but their variances will be driven by the number of independent samples.

Consider the special case where $\mathrm{x}(k)$ is a white noise process with mean μ_{x} and variance σ_{x}^2. By definition, the autocovariance is $C_{\mathrm{xx}} = \sigma_{\mathrm{x}}^2\delta(k)$ (where $\delta(k)$ is the Kronecker delta function) implying that all samples contained in the dataset are independent, $N = N^*$. Then, variances in (5.17) and (5.18) reduce to

$$\mathrm{Var}[\hat{\mu}_{\mathrm{x}}] = \frac{\hat{\sigma}_{\mathrm{x}}^2}{N^*} \tag{5.19}$$

$$\mathrm{Var}[\hat{\psi}_{\mathrm{x}}^2] = \frac{2(\hat{\sigma}_{\mathrm{x}}^4 + 2\hat{\mu}_{\mathrm{x}}^2\hat{\sigma}_{\mathrm{x}}^2)}{N^*}. \tag{5.20}$$

The underlying idea is to compare the white noise results with the general case (colored noise) and determine the number of samples N that will result in parameter estimate error variances equal to those in (5.19) and (5.20). The ratio N^*/N will then be the fraction of the N^* samples that are effectively independent for the estimation of μ_{x} and σ_{x}^2 out of the total N (colored). Setting expression (5.17) equal to (5.19) and expression (5.18) equal to (5.20) the ratio N^*/N can be obtained from the variance in the estimation of μ_{x} and ψ_{x}^2 as

$$\frac{N^*}{N}\Big|_{\hat{\mu}_{\mathrm{x}}} = \frac{\hat{\sigma}_{\mathrm{x}}^2}{\sum_{-N}^{N}\left(1 - \frac{|k|}{N}\right)\hat{C}_{\mathrm{xx}}(k)} \tag{5.21}$$

$$\frac{N^*}{N}\Big|_{\hat{\psi}_{\mathrm{x}}^2} = \frac{\hat{\sigma}_{\mathrm{x}}^4 + 2\hat{\mu}_{\mathrm{x}}^2\hat{\sigma}_{\mathrm{x}}^2}{\sum_{-N}^{N}\left(1 - \frac{|k|}{N}\right)\left(\hat{C}_{\mathrm{xx}}^2(k) + 2\hat{\mu}_{\mathrm{x}}^2\hat{C}_{\mathrm{xx}}(k)\right)}. \tag{5.22}$$

Note that the fractions identified in the previous expressions will not be identical since they are conditioned to the variance of the estimation of two different parameters. In general, for a given dataset, $\mathrm{Var}[\hat{\mu}_{\mathrm{x}}]$ and $\mathrm{Var}[\hat{\psi}_{\mathrm{x}}^2]$ will not be equal and hence (5.21) and (5.22) will report different values depending on how much confidence we can place on the estimation of each parameter. Since in order to obtain $\hat{\sigma}_{\mathrm{x}}^2$ we need both $\hat{\mu}_{\mathrm{x}}$ and $\hat{\psi}_{\mathrm{x}}^2$, the limiting factor will be the smallest ratio between $N^*/N_{\hat{\mu}_{\mathrm{x}}}$ and $N^*/N_{\hat{\psi}_{\mathrm{x}}^2}$.

Let us assume that over the period of data collection $0 < t < T$, we have a sampling interval ΔT (time which elapses between two samples) so that the total number of collected samples is $N = T/\Delta T$. The selection of the sampling interval only affects the number of colored samples but not the number of effectively independent samples contained in the dataset X. One might be tempted to assume that the ratio N^*/N shall be independent of the sampling interval; however let us look at the following example. Let us assume that two processing facilities monitor the same satellite range error during 10 days. Monitor A has a sampling interval of 5 minutes while monitor B has a sampling interval of 15 minutes. After the full period, monitor A has collected a total $N_{\mathrm{A}} = 2880$ correlated samples while monitor B gathered $N_{\mathrm{B}} = 960$ correlated samples. Since A and B have different sampling intervals, N_{A} and N_{B} are different, however they must contain the same number of effectively independent samples (same monitoring period) so $N_{\mathrm{A}}^* = N_{\mathrm{B}}^*$. That yields to

$$\frac{N_{\mathrm{A}}^*}{N_{\mathrm{A}}} = \frac{\Delta T_{\mathrm{A}}}{\Delta T_{\mathrm{B}}} \cdot \frac{N_{\mathrm{B}}^*}{N_{\mathrm{B}}}. \tag{5.23}$$

For performance characterization and error overbound, our goal is to determine the time between effective independent samples ΔT_{ind}. It is formally defined as the time elapsed between two consecutive effectively independent samples. The determination of ΔT_{ind} is relevant since it allows us to discern how many independent samples we can collect in a given monitoring time. Let us assume that in our example the true ΔT_{ind} is 15 min. In that case, $N_{\mathrm{B}}^* = N_{\mathrm{B}}$ and according to (5.23) the ratio of effectively

independent samples for the dataset collect by monitor A is $N^*_{\mathrm{A}}/N_{\mathrm{A}} = 1/3$. In the general case, we do not know the actual ΔT_{ind} and the only way to estimate it is through the computed values of N^*/N. Let us call N_{J} the total samples of the data set $\mathrm{X_J}$ collected by a generic monitor J with a sampling interval ΔT_{J}. We want to compare our monitor J with the monitor whose sampling interval is the actual ΔT_{ind} so that $N^*/N = 1$. Using expression (5.23), the time between effectively independent samples can be estimated as:

$$\Delta T_{\mathrm{ind}} = \frac{\Delta T_{\mathrm{J}}}{\left.\frac{N^*}{N}\right|_{\mathrm{J}}}. \tag{5.24}$$

Figure 5.6 presents the values of $N^*/N_{\hat{\mu}_{\mathrm{x}}}$ and $N^*/N_{\hat{\psi}^2_{\mathrm{x}}}$ for GPS satellite range error for both Cs and Rb clock types as a function of the sampling interval. As pointed out before, both (5.21) and (5.22) are built under the assumption that C_{xx} can be substituted by its estimated value $\hat{C}_{\mathrm{xx}}$ if a large number of independent samples are included in the dataset. In particular, SISRE data from January 2015 to December 2017 is taken for the GPS and Galileo correlation analysis. Although we have not defined yet the technique to determine the number of effective independent samples in a given set, results from GPS and Galileo stationary analysis in Sections 4.4.2 and 4.5.2 indicate that several years of SISRE data contain enough independent points to support the CLT. This assumption will be revisited after the determination of the time between independent samples.

As presented in Figure 5.6, both $N^*/N_{\hat{\mu}_{\mathrm{x}}}$ and $N^*/N_{\hat{\psi}^2_{\mathrm{x}}}$ are monotonous functions (ideally linear) of the sampling interval. According to expression (5.24), the ΔT_{ind} can be estimated as the inverse of the slope of these functions. Note that choosing a different sampling interval does not imply a modification of the total monitoring period (three years with sufficiently large number of independent samples) but different time elapsed between the collected measurements. As mentioned above, the confidence in the estimation of $\hat{\sigma}^2_{\mathrm{x}}$ will be limited by the smallest N^*/N ratio. In other words, the time between effective independent samples ΔT_{ind} will be determined by longest $\Delta T_{\mathrm{ind},\hat{\mu}_{\mathrm{x}}}$ or $\Delta T_{\mathrm{ind},\hat{\psi}^2_{\mathrm{x}}}$.

As expected, for a given sampling interval, the number of effectively independent samples for Rb clock satellites are approximately ten times smaller than for Cs clock satellites. For example, if we choose a sampling interval of 2 hours, the ratio of effectively independent samples for Cs clock satellites is 0.5 while it is just 0.05 for Rb clock satellites. Table 5.1 provides an average range of values for $\Delta T_{\mathrm{ind},\hat{\mu}_{\mathrm{x}}}$ and $\Delta T_{\mathrm{ind},\hat{\psi}^2_{\mathrm{x}}}$ applying expression (5.24) for each point of Figure 5.6. Note that the shaded cells indicate the limiting parameters. The time between effectively independent samples for Rb clock GPS satellites ranges between 50-60 hours whereas it is ten times shorter, 5-6 hours, for Cs clock satellites.

Figure 5.7 includes the results of a similar analysis for Galileo satellites (RAFS and PHM onboard clocks). Although not as pronounced as in the GPS case, there is a difference in the number of independent samples between PHM and RAFS-equipped

spacecraft. For example, for a sampling interval of one hour, the ratio of effectively independent samples for PHM clock satellites is 0.5 while it is 0.4 for RAFS clock satellites. Table 5.1 indicates that the time between effectively independent samples for PHM clock satellites ranges between 2.5-3.5 hours while it is a a few hours longer for RAFS clock satellites, around 4-5 hours. Note that as of June 2018, there is only one Galileo satellite in active service which operates with a RAFS onboard clock (GSAT0101).

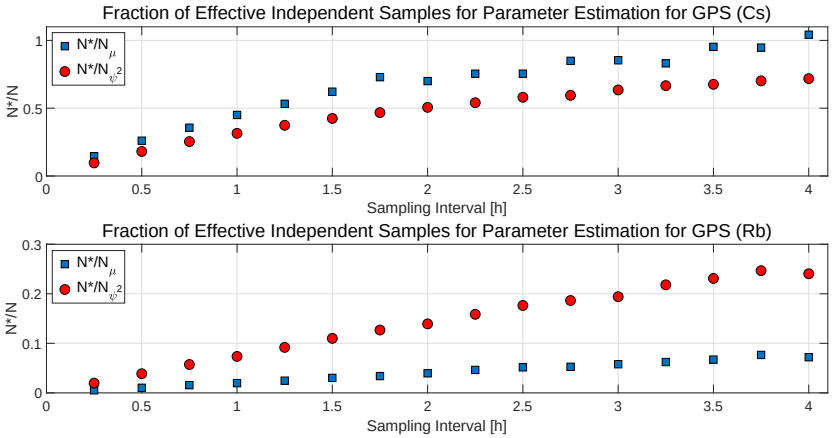

Figure 5.6: Ratio of correlated versus independent samples for GPS range error (Cs clock and Rb clock) as a function of the sampling interval. Note the different scale.

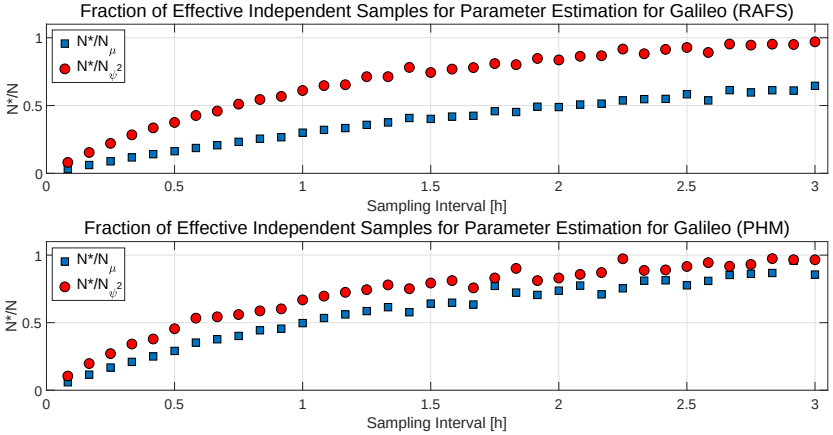

Figure 5.7: Ratio of correlated versus independent samples for Galileo range error (RAFS and PHM clock) as a function of the sampling interval.

Table 5.1: Time between effectively independent samples for GPS and Galileo Satellites based on clock type

Constellation	Clock Type	$\Delta T_{\text{ind}\,\hat{\mu}_x}$ $[h]$	$\Delta T_{\text{ind}\,\hat{\psi}_x}$ $[h]$
GPS	Cesium	4-5	5-6
GPS	Rubidium	50-60	24-32
Galileo	RAFS	4-5	3-4
Galileo	PHM	2.5-3.5	2-3

Shaded cells correspond to limiting parameter, $\hat{\mu}_x$ or $\hat{\psi}_x^2$

It is worth pointing out again the inherent differences determined by the onboard clock type. Cs clock-equipped GPS satellites are the only cases in which the estimation of $\hat{\psi}_x^2$ is the limiting factor to determine the time between effective independent samples. In the rest of the satellites under study (both Rubidium and passive Hydrogen masers), $\hat{\mu}_x$ is the limiting factor instead. Although not significantly relevant for the integrity analysis carried out here, a plausible explanation to this behavior is the short term versus long term clock stability. As illustrated in the Allan deviation plots in [78], Cs atomic clocks present a better long term stability whereas Rb and passive Hydrogen maser clocks show an extremely stable short term behavior.

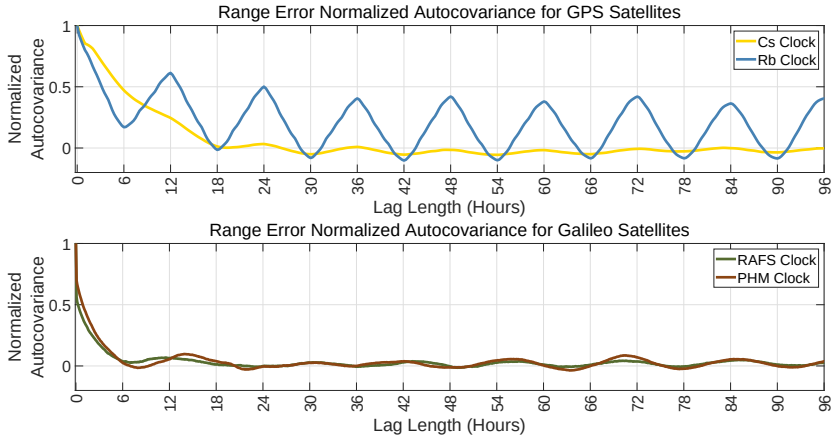

Figure 5.8: Range error normalized autocovariance for GPS and Galileo satellites for each clock type

The initial correlation analysis that was performed in [26] was based on autocovariance plots. Those figures provided a notion of the error temporal behavior but it is actually quite complex to extract anything more than qualitative conclusions. Looking at the range error autocovariance in Figure 5.8, one could, for example, fix a 0.5 threshold value from which we can expect the data to be uncorrelated. However this criteria is not sufficiently motivated. Looking at the Rb GPS satellites autocovariance

plot (blue line in Figure 5.8), it is quite hard to extract any conclusion about ΔT_{ind} from that sinusoidal behavior. Even more challenging is to infer the time between effectively independent samples in the Galileo case. The green and brown lines in Figure 5.8 show very similar trends but in fact, as shown in Table 5.1, they do not have the same ΔT_{ind}. The methodology here presented overcomes this problem by defining the N^*/N ratio.

5.4 Assertions about Range Error Time Dependence

After having determined the time between effectively independent samples, the conclusions empirically stated in Sections 4.4.2 and 4.5.2 regarding error variability over months for GPS and Galileo can be mathematically seconded. In the previous chapter, the waterfall diagram in Figure 4.6 exposed the broad variability in error CDF over months for Rb-equipped GPS satellites whereas in the case of Cs clocks, the errors were quite stable over time. With the results obtained in this chapter, we can now state that in the case of Rb clocks only 14-16 samples collected in a month are independent. Trying to characterize a population with only 16 independent data points is certainly adventurous leading to discordant results on a monthly basis. As the monitoring time increases to biannual and yearly datasets (Figures 4.7 and 4.8, respectively) the number of independent samples grows providing more confident estimations of the true distributions. In the case of Cs-equipped satellites, one month of data contains around 120 independent samples, making the monthly estimations less changeable as displayed in the waterfall diagrams in Figure 4.13. Similar grounds can be given to explain the smaller variability observed for Galileo waterfall diagrams (after initial service declaration) shown in Figures 4.18 and 4.19.

A discussion regarding whether or not satellite range error distributions are biased is herein addressed. The final section the in WGC Milestone 3 Report (published by Walter in [24]) collects a series of assertions related to the ARAIM system architecture. Among others, they state that the ANSP will implement a ground-based offline monitoring of satellite measurements to compute a safe overbound using the distributions $\mathcal{N}(-b_{nom}, \sigma_{\text{ob}})$ and $\mathcal{N}(b_{nom}, \sigma_{\text{ob}})$. Both parameters b_{nom} and σ_{ob} account for: a) Repeatable or persistent biases in receiver observed SIS errors, for example signal deformation or interfrequency biases; b) Statistical uncertainty due to limited sample sizes available to the offline monitor function. This work asserts that orbit and clock errors do not create permanent bias in SISRE so they should not be accounted in b_{nom}. This statement has also been supported by Walter in [83]. In case permanent biases are observed in the range error due to clock and ephemeris error, it can be attributed to a misalignment in the reference APCs (BCE and/or PRO as specified in Section 3.6.1). Our allegations are based on the findings in Chapters 4 and 5 of this thesis:

- GPS: SISRE distributions for Rb-equipped satellites do not exhibit a significant bias after 6-8 months of data collection (see Figure 4.9). Since only 14-16 independent samples can be collected in a month it would take at least 10-12 months to have a reliable estimation of the mean. Once enough significant data

have been collected the distribution mean is on the order of reference products accuracy (2-3 cm) as shown in Table 4.6.

- Galileo: Due to the short time between independent samples, Galileo SISRE has around 180 independent samples a month. This explains why no significant bias (on the order of the products accuracy 4-5 cm) was observed in the monthly error CDFs for Galileo. In the case of the European constellation, one must acknowledge that ground segment ODTS is subject to updates. As displayed in the time line of the SISRE RMS in Figure 4.22, certain ground segment modifications can violate the stationarity of the error (March 2018). Since they do not belong to the nominality of the distribution, these events do not invalidate the results from this chapter which apply to unfaulted error distributions.

Finally we can validate the assumptions made when C_{xx} was substituted by its estimated value $\hat{C}_{\mathrm{xx}}$ in expressions (5.21) and (5.22). As indicated, three years of SISRE data have been included in this analysis which implies that over 500 independent samples for GPS-Rb satellites have been utilized and the CLT is legitimately applied.

6 Bayesian Inference for Multi Gaussian Overbound

The previous chapter has provided a statistical method to determine the number of independent samples for a given dataset. Ultimately, the statistical independence of the data needs to be accounted for in the satellite ranging error overbound within ISM generation. Using a Bayesian inference approach, this chapter obtains an analytical expression of the range error CDF as a function of sample standard deviation and the number of independent samples. Then, it analyzes the inflation factor that needs to be applied to a Gaussian bound in order to safely account for the error variability.

The second part of this chapter proposes the replacement of the traditional Single Gaussian (SG) overbound by a Multi Gaussian (MG) distribution. Leveraging the fact that error distributions have two distinct partitions, core and tail, Section 6.4 formalizes this new approach. The underlying idea is to compute two separate distributions, one for the core and one for the tail, which are weighted to create a tighter and equally safe range overbound.

6.1 Existing overbounding methods

Range error overbounding plays a pivotal role in GNSS Safety-of-Life (SoL) applications. The high integrity requirement demanded by GBAS, SBAS, and ARAIM necessitates a thorough analysis of the GNSS range errors that lead to a safe overbound. In the GNSS integrity literature two extensively used bounding methods can be found: DeCleene's Gaussian CDF bounding [31] and Rife's Gaussian pair overbounding [32] (see Annex C). Both methodologies replace the unknown true error distribution by a Gaussian with standard deviation σ_{ob} which preserve its bounding properties after convolution in the position domain. In order to account for arbitrary (non-symmetric, non-zero mean) error distributions, the pair overbounding introduced the so-called nominal bias b_{nom}. This term is also meant to overbound other errors that are not always observable in the sample data (i.e. nominal signal deformation biases) and whose distributions might be unknown. Among others, σ_{ob} and b_{nom} are encapsulated within the ISM and transmitted to the ARAIM users. Based on these inputs users evaluate whether or not the integrity requirement is fulfilled [3]. The pair overbounding theorem has been recently revisited in [33] (Blanch's two step Gaussian bounding) where a relaxation of the bounding premises is proposed leading to a less conservative bound.

The three previous overbounding methodologies have one common denominator; they assume that the observed distribution is the actual and they do not need to be

concerned with correlation and independence. As demonstrated in Chapters 4 and 5, given the high correlation of the data, the characterization of the SISRE based on service history gets more cumbersome for new constellations where less data is available. Pervan introduced in [84] the use of Bayesian inference as a mean to account for the statistical uncertainties in the knowledge of error standard deviation and the correlation across the multiple reference receivers to be used in the GBAS ground segment. The work presented in this chapter takes a step forward and analyzes the effect of error correlation in the SISRE bounding for GPS and Galileo.

6.2 Effect of Sample Correlation on Range Overbound

Gaussian distributions are typically used in estimation theory to model error bounds. Their simplicity along with their desirable mathematical properties make them convenient for creating error envelopes in the range domain. The major hypothesis of this section is accepting that the sampled error derives from a zero mean Gaussian population. The empirical evidences and the assertions to support this hypothesis were discussed in Section 5.4. Correspondingly, Section 6.3 proves that this assumption is not far from reality and that a Gaussian function is a good approximation for the major part of the true error distribution. This section interprets the correlation results obtained in Chapter 5 and applies them to the estimation process of Gaussian distributions.

6.2.1 Ranging Error CDF based on Sample Independence

Given a range error dataset, our scope is to obtain a CDF of the ranging error F_ε as a function of the sample standard deviation s and the number of independent samples n. Let us define the following probability functions

- f_ε: Marginal Probability Density Function of the ranging error
- f_σ: *A priori* Marginal Probability Density Function of the distribution standard deviation
- $f_{\varepsilon|\sigma}$: Conditional Probability Density Function of the ranging error to σ
- F_ε: Marginal CDF of the ranging error.

The marginal probability of the ranging error is written as

$$f_\varepsilon = \int_0^\infty f_{\varepsilon,\sigma}(\varepsilon,\sigma)d\sigma. \tag{6.1}$$

Marginalizing out σ variable, Equation (6.1) can be expressed as

$$f_\varepsilon = \int_0^\infty f_{\varepsilon|\sigma}(\varepsilon|\sigma)f_\sigma(\sigma)d\sigma. \tag{6.2}$$

Integrating the range error pdf to obtain the cdf and rearranging terms, we can write

$$F_\varepsilon(\mathrm{x}) = \int_{-\infty}^{\mathrm{x}} f_\varepsilon(\varepsilon)d\varepsilon = \int_0^\infty \int_{-\infty}^{\mathrm{x}} f_{\varepsilon|\sigma}(\varepsilon|\sigma)d\varepsilon f_\sigma(\sigma)d\sigma. \tag{6.3}$$

Note that the integral over $d\varepsilon$ can be expressed in terms of the error function (erf) as follows:

$$\int_{-\infty}^{\mathrm{x}} f_{\varepsilon|\sigma}(\varepsilon|\sigma)d\varepsilon = P(\varepsilon \leq \mathrm{x}) = \frac{1}{2} + \frac{1}{2}\mathrm{erf}\left(\frac{-\mathrm{x}}{\sqrt{2}\sigma}\right). \tag{6.4}$$

A suitable posterior distribution f_σ derived from a non informative prior coming from a Gaussian population is given in Section 2.3 of [85]

$$f_\sigma = p(\sigma|s,n) = \left[\frac{1}{2}\Gamma\left(\frac{n}{2}\right)\right]^{-1}\left(\frac{ns^2}{2}\right)^{\frac{n}{2}}\sigma^{-(n+1)}\exp\left(-\frac{ns^2}{2\sigma^2}\right) \tag{6.5}$$

where s is the sample standard distribution and n the number of effective independent samples. The expression above represents the PDF of the error standard deviation conditioned to n and s based on the assumption that the actual error derives from a zero-mean Gaussian distribution (discussed in Section 5.4). For simplicity, let us rename the constants

$$c = \left[\frac{1}{2}\Gamma\left(\frac{n}{2}\right)\right]^{-1}\left(\frac{ns^2}{2}\right)^{\frac{n}{2}} \text{ and } b = \sqrt{\frac{ns^2}{2}}.$$

Introducing (6.4) and (6.5) in (6.3), we can write the range error CDF as

$$F_\varepsilon = \frac{1}{2}c\int_0^\infty \sigma^{-(n+1)}\exp\left(-\frac{b^2}{\sigma^2}\right)d\sigma + \frac{1}{2}c\int_0^\infty \sigma^{-(n+1)}\exp\left(-\frac{b^2}{\sigma^2}\right)\mathrm{erf}\left(\frac{\mathrm{x}}{\sqrt{2}\sigma}\right)d\sigma. \tag{6.6}$$

For the sake of clarity, let us rewrite expression (6.6) as $F_\varepsilon = \frac{1}{2}c(I_1 + I_2)$. Applying the variable change $u = 1/\sigma$, substituting $d\sigma = -\sigma^2 du$ and correspondingly changing the integration limits, the two terms of expression (6.6) can be expressed as

$$I_1 = \int_0^\infty u^{n-1}\exp(-b^2u^2) \tag{6.7}$$

$$I_2 = \int_0^\infty u^{n-1}\exp\left(-b^2u^2\right)\mathrm{erf}\left(au\right)du. \tag{6.8}$$

Using the table of integrals provided in [86], both terms I_1 and I_2 have analytical solutions

$$I_1 = \frac{1}{2}b^{-n}\Gamma\left(\frac{n}{2}\right) \tag{6.9}$$

$$I_2 = \frac{\mathrm{x}}{\sqrt{2\pi}}b^{(-n-1)}\Gamma\left(\frac{n+1}{2}\right){}_2F_1\left(\frac{1}{2}, \frac{n+1}{2}; \frac{3}{2}; -\frac{\mathrm{x}^2}{2b^2}\right) \tag{6.10}$$

where $\Gamma(n)$ is the Gamma function and ${}_2F_1\left(a_1, a_2, a_3; a_4\right)$ is the Gaussian hypergeometric function. Introducing (6.9) and (6.10) in (6.6) the range error CDF can be expressed as an explicit function of the number of effective independent samples n, the sample standard deviation s, and the error magnitude x as

$$F_\varepsilon(\mathrm{x}|s,n) = \frac{1}{2} + \frac{\mathrm{x}}{s\sqrt{n}}\frac{1}{\sqrt{\pi}}\frac{\Gamma\left(\frac{n+1}{2}\right)}{\Gamma\left(\frac{n}{2}\right)}{}_2F_1\left(\frac{1}{2}, \frac{n+1}{2}; \frac{3}{2}; -\frac{\mathrm{x}^2}{ns^2}\right). \tag{6.11}$$

6.2.2 Overbound Inflation Factor to Account for Sample Independence

According to the CDF overbound theorem [31] (detailed in Annex C), a given random variable $A(\mathrm{x})$ with CDF $F_A(\mathrm{x})$, is bounded by a second distribution $O(\mathrm{x})$ with CDF $F_O(\mathrm{x})$ if

$$\begin{cases} F_O(\mathrm{x}) \geq F_A(\mathrm{x}) \; \forall \, \mathrm{x} \leq 0 \\ F_O(\mathrm{x}) < F_A(\mathrm{x}) \; \forall \, \mathrm{x} > 0. \end{cases} \tag{6.12}$$

Given the measurement-dependent F_ε in (6.11), our goal is to find an F_O that fulfills the bounding conditions in (6.12). Figure 6.1 depicts the normalized Folded CDF and Quantile-Quantile (QQ) plot of F_ε for different values of n and compares them to the normal Gaussian distribution (no sample correlation). As can be seen, for a given error dataset with n independent samples and sample standard deviation s, the distribution derived from $\mathcal{N}(0, s)$ will not bound the ranging error. In order to find a safe overbounding σ_{ob} that accounts for the uncertainty due to the finite number of independent samples, the estimated sample standard deviation shall be inflated by factor $K_{\text{uncer}} \geq 1$ so that $\sigma_{\text{ob}} = K_{\text{uncer}}\, s$.

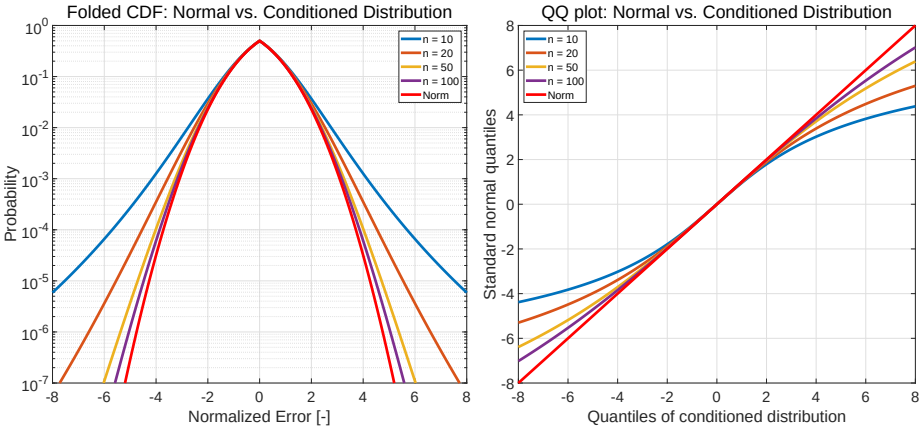

Figure 6.1: Range error Folded CDF and quantile-quantile plot for Gaussian distribution against measurement conditioned distribution as a function on the independent samples n

For the sake of generality, the error term x in (6.11) can be normalized by the sample standard deviation as $\mathrm{x}^* = {}^{\mathrm{x}}/_{s}$ leading to a measurement-dependent F_ε as a function of number of samples

$$F_\varepsilon(\mathrm{x}^*|n) = \frac{1}{2} + \frac{\mathrm{x}^*}{\sqrt{n}} \frac{1}{\sqrt{\pi}} \frac{\Gamma\left(\frac{n+1}{2}\right)}{\Gamma\left(\frac{n}{2}\right)} {}_2F_1\left(\frac{1}{2}, \frac{n+1}{2}; \frac{3}{2}; -\frac{\mathrm{x}^{*2}}{n}\right). \tag{6.13}$$

Figure 6.1 plots the above CDF expression for different numbers of independent samples. As can be inferred, K_{uncer} must be an inversely proportional function of the

number of independent samples contained in the error dataset which, in the limit case, will reach $K_{\text{uncer}} \approx 1$. Of course we do not want to unnecessarily inflate σ_{ob} so that it leads to availability risk. However we need to confidently overbound at least down to the P_{sat} committed by the CSP [3]. For a given error dataset X with n independent samples and estimated standard deviation s, K_{uncer} is the factor that fulfills:

$$\begin{cases} F_{\varepsilon}(\mathrm{x}^*_{P_{sat}}|n) = P_{sat} \\ \mathrm{x}^*_{P_{sat}} = \phi^{-1}\left(\frac{P_{sat}}{2}, 0, \sigma^*_{ob}\right) \\ \sigma^*_{\text{ob}} = \sigma_{\text{ob}}/s = K_{\text{uncer}}. \end{cases} \tag{6.14}$$

where $\phi^{-1}(P, \mu, \sigma)$ is the inverse CDF of a Gaussian distribution $\mathcal{N}(\mu, \sigma)$. Expression (6.14) provides an implicit function $K_{\text{uncer}} = f(n, P_{sat})$ that needs to be solved iteratively. The computed CDF F_O derived from $\mathcal{N}(0, \sigma^*_{\text{ob}})$ will guarantee a CDF bounding as

$$\begin{cases} F_O(\mathrm{x}^*) \geq F_{\varepsilon}(\mathrm{x}^*|n) \ \forall\, \mathrm{x}^* \in [-\mathrm{x}^*_{P_{sat}}, 0] \\ F_O(\mathrm{x}^*) < F_{\varepsilon}(\mathrm{x}^*|n) \ \forall\, \mathrm{x}^* \in (0, \mathrm{x}^*_{P_{sat}}]. \end{cases} \tag{6.15}$$

Figure 6.2 shows the folded CDF and QQ plots of the inflated Gaussian distribution that fulfills bounding conditions in (6.15) for a given $P_{sat} = 10^{-5}$. Figure 6.3 summarizes the values of the inflation factors K_{uncer} for different values of P_{sat} and n. The represented K_{uncer} is the inflation factor that provides the tightest safe overbound and, as can be seen in Figure 6.2, decreases as the number of independent samples grows. As shown in Figure 6.3, the inflation factor is close to 1 (data uncertainty does not play a role) once the dataset contains around 150-200 independent samples. According to the results from the correlation study in Chapter 5, this means around 1-1.5 months of Galileo SISRE data and 10-12 months of GPS (Rb) data.

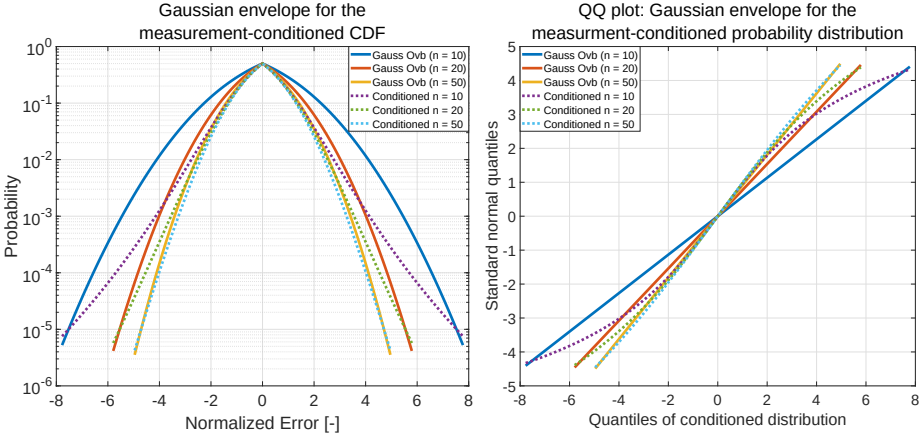

Figure 6.2: Range error Folded CDF and quantile-quantile plot for inflated Gaussian overbounding distribution against measurement conditioned distribution as a function on the independent samples n for $P_{sat} = 10^{-5}$

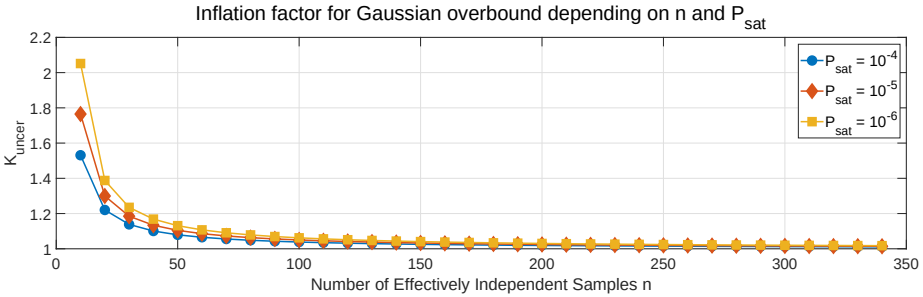

Figure 6.3: Inflation factor to account for the number of effectively independent samples used in the estimation of the overbound as a function of P_{sat} for a normalized standard deviation s=1

6.3 Motivation for Data Partitioning: Empirical Evidences

Through the past chapters it has been mentioned that the core of the distribution controls the nominal performance of the error. In particular, Section 5.2 argued that the correlation properties (time between effectively independent samples) are dominated by the core, leaving almost no influence to the tails. The stationarity analysis for both GPS and Galileo in Chapter 4 showed that once enough independent samples are collected, the core of the distribution settles and only differences in the tails are observed. Given these facts, it might be of interest to analyze whether or not the error distribution can be partitioned in two components: a quasi-Gaussian core containing most of the data and a flat tail distribution with just a few data points.

Figures 6.4 and 6.5 include the $SISRE_{IUP}$ (orbit and clock error projected over a grid of 642 global users, defined in (3.35)) FCDF and QQ plots for SVN67 and GSAT0207 correspondingly. They are both compared to the Gaussian fit generated by the sample standard deviation s. As shown on the right plot of both figures, the core of both distributions (blue lines) match the Gaussian reference (red line) following a straight line in the QQ plots. It has been observed in the analyzed data (both GPS and Galileo) that this Gaussianity is typically lost for quantiles larger than two, corresponding to *two sigmas* or the 95-percentile bound. Further discussion regarding the partition percentile is addressed in the next sections.

This 95-percentile bound is a typical measure of the range error accuracy. As illustrated in Figures 6.4 and 6.5, the sample estimated $\hat{\sigma}_{\mathrm{GAL}}$ is approximately half of the value of $\hat{\sigma}_{\mathrm{GPS}}$, more precisely, the 2-sigma bound for Galileo is 30 cm whereas it is 68 cm for the GPS sample. However, in this specific example, we can already see that Galileo errors have similar magnitudes to GPS for low probabilities. Ultimately, the integrity bound must safely account for the tails since large range errors can conspire to create large position errors with no integrity warning. This is a limitation of the Single Gaussian (SG) bounding; if only one distribution must be used to overbound the range error, despite the accuracy of the core, tails will always drive the overbounding value.

In this particular example, although Galileo is approximately 50% more accurate than GPS, similar bounding sigmas could be applied.

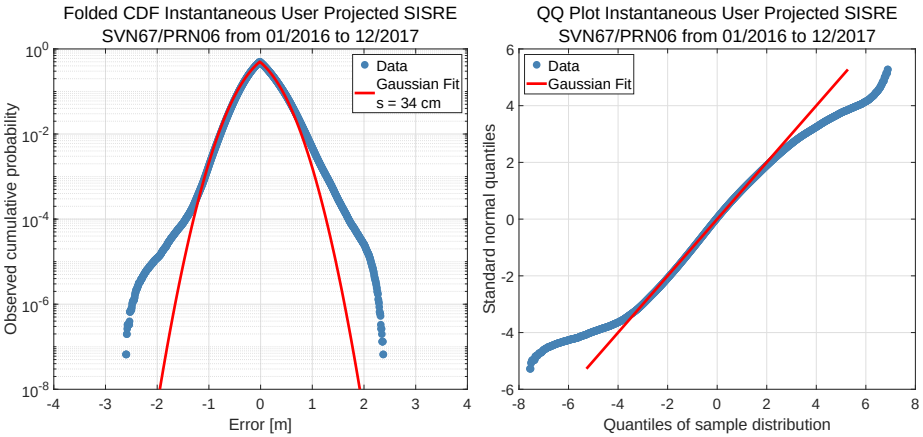

Figure 6.4: Empirical CDF and QQ plot of instantaneous user projection SISRE for SVN67 / PRN06 during 2016-2017

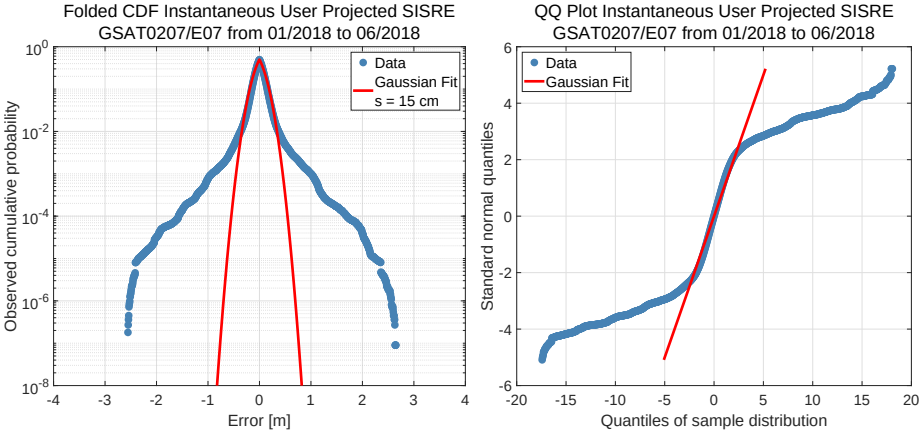

Figure 6.5: Empirical CDF and QQ plot of instantaneous user projection SISRE for GSAT0207 / E07 during 2018

The Bayesian analysis carried out in Section 6.2 assumed that range error distribution derived from a Gaussian population. As shown here, this is only valid for the core of the distribution and certainly not for the tails. These findings lead to the following concept: core and tail overbounds can be computed individually and later combined in a weighted function. This chapter proposes a Multi Gaussian bounding

distribution which leverages this idea ultimately leading to tighter protection levels and higher availability.

6.4 Multi Gaussian Overbound

6.4.1 Bounding Distribution Definition

Traditional integrity bounds used in SoL applications (Section 6.1) are based on SG distributions defined by a standard deviation σ_{ob}. As detailed in Annex C, pair overbound is an extension of the CDF theorem using two symmetric Gaussian distributions shifted by b_{nom}. The common characteristic of both theories is that a single distribution $O(\text{x})$ is used to overbound the full error dataset $A(\text{x})$

$$\begin{aligned} F_{O_{SG}}(\text{x}) &\geq F_A(\text{x}) \; \forall \; F_A < 1/2 \\ F_{O_{SG}}(\text{x}) &\leq F_A(\text{x}) \; \forall \; F_A \geq 1/2 \end{aligned} \tag{6.16}$$

with $F_{O_{SG}}$ and F_A being the corresponding CDFs. The limitation of the SG bounding is the constraint to use only one function disregarding the fact that true distributions have two distinctive parts. As empirically supported by Figures 6.4 and 6.5, let us define a couple of complementary weighting factors w_c and $w_t = 1 - w_c$ that split the empirical dataset into core $C(\text{x})$ and tail $T(\text{x})$ distributions. The quantiles x_L and x_R that define the border between core and tail distributions are determined by the weighting factor w_t as

$$\Pr\left(\text{X} \leq \text{x}_\text{L}\right) = \frac{w_t}{2} \text{ and } \Pr\left(\text{X} \leq \text{x}_\text{R}\right) = 1 - \frac{w_t}{2}. \tag{6.17}$$

Each individual distribution is formally defined as

$$C(\text{x}) = \text{x} : \{\in [\text{x}_\text{L}, \text{x}_\text{R}]\} \tag{6.18}$$

$$T(\text{x}) = \text{x} : \{\in (-\infty, \text{x}_L) \cup (\text{x}_R, \infty)\} \tag{6.19}$$

where $C \cap T = \varnothing$ (disjoint) and $C \cup T = A$. The MG CDF overbounding distribution is computed as the weighted sum of the individual SG overbound for core and tail

$$F_{O_{MG}}(\text{x}) = w_c \; F_{O^c_{SG}}(\text{x}) + w_t \; F_{O^t_{SG}}(\text{x}) \tag{6.20}$$

where $F_{O^c_{SG}}$ and $F_{O^t_{SG}}$ are individual CDF bounds of $C(\text{x})$ and $T(\text{x})$. Let $F_C(\text{x})$ and $F_T(\text{x})$ be the corresponding CDF of random variables $C(\text{x})$ and $T(\text{x})$, then the determination of the CDF bounds for core and tail distributions must simultaneously guarantee

$$\begin{aligned} F_{O^c_{SG}}(\text{x}) &\geq F_C(\text{x}) \; \forall \; \text{x} \in [\text{x}_\text{L}, m_\text{x}) \\ F_{O^c_{SG}}(\text{x}) &\leq F_C(\text{x}) \; \forall \; \text{x} \in [m, \text{x}_\text{R}] \end{aligned} \quad \text{and} \quad \begin{aligned} F_{O^t_{SG}}(\text{x}) &\geq F_T(\text{x}) \; \forall \; \text{x} < \text{x}_L \\ F_{O^t_{SG}}(\text{x}) &\leq F_T(\text{x}) \; \forall \; \text{x} > \text{x}_R. \end{aligned} \tag{6.21}$$

Note that the formal bounding conditions (6.21) introduced the distribution median m_x which, as discussed in Chapters 4 and 5, is empirically zero.

6.4.2 Determination of Individual Single Gaussian Bounds

As stated in expression (6.20), there is one key parameter in the Multi Gaussian formulation that drives the determination of the individual overbounds; the core-tail weighting factor w_c. The determination of σ^c_{ob} and σ^t_{ob} not only must ensure the individual overbound of core and tail distributions but the combination of them (6.20) must also bound the full error distribution $A(\text{x})$. Empirical distributions (like the ones in Figures 6.4 and 6.5) show that the core contains 95-99% of the data. Section 6.4.5 will explore how the selection of w_c influences the final $F_{O_{MG}}$ bound.

Once the distributions $C(\text{x})$ and $T(\text{x})$ are determined, the individual SG bounding distributions must be found. Note that in this case the pair bounding can be taken to its limit where both left and right distributions overlap (single CDF bound) without violation of the bounding conditions. For sake of generality, the following notation will keep the median term m_{x} in the derivation although it can be assumed to be empirically zero. This point will be further elaborated in Section 6.4.6 when the integrity proof is discussed.

The corresponding core and tail overbounds are defined as

$$O^c_{SG}(\text{x}) \sim \mathcal{N}\left(m_{\text{x}}, \sigma^c_{\text{ob}}\right) \text{ and } O^t_{SG}(\text{x}) \sim \mathcal{N}\left(m_{\text{x}}, \sigma^t_{\text{ob}}\right). \tag{6.22}$$

This methodology leverages the fact that core and tail have distinctive behavior. Note that the fact that both distributions are overbounded by Gaussians does not mean that we presume Gaussian behavior of the true tail distribution. What we actually assume is that it is possible to overbound that distribution with a Gaussian down to P_{sat} probability.

Core Single Gaussian Bound: For a finite dataset $C(\text{x})$ defined in $[\text{x}_L, \text{x}_R]$, its sample CDF $F_C(\text{x})$ can be computed as indicated in (4.1) by clustering the data in n_b total bins. Let us define an intermediate normal distribution $\tilde{O}^c(\text{x}) \sim \mathcal{N}\left(m, \tilde{\sigma}^c\right)$ which fulfills

$$\begin{aligned} F_{\tilde{O}^c}(\text{x}) &\geq F_C(\text{x}) \; \forall \; \text{x} \in [\text{x}_L, m_{\text{x}}) \\ F_{\tilde{O}^c}(\text{x}) &< F_C(\text{x}) \; \forall \; \text{x} \in [m_{\text{x}}, \text{x}_R]. \end{aligned} \tag{6.23}$$

Finding a $\tilde{\sigma}^c$ that meets the above condition can be done by interval search over the n_b bins. Once the intermediate distribution $F_{\tilde{O}^c}$ is defined, the number of independent samples contained in the dataset needs to be considered. The Gaussianity assumptions on which the Bayesian analysis in Section 6.2 are based are valid for the core distribution. This implies that in order to account for the data dependence due to correlation, $\tilde{\sigma}^c$ needs to be inflated by K^c_{uncer} factor defined in (6.14).

To illustrate this process let us take $SISRE_{IUP}$ data from SVN67 during 2016. Figure 6.6 presents the Folded CDF and QQ plots of the core distribution C along with the intermediate distribution $\tilde{O}^c$ and core bound O^c_{SG}. As indicated by the blue dots, the core (95% data) follows a quasi-Gaussian distribution being corroborated by the fact that intermediate bounding $\tilde{O}^c$ and core samples have approximately the

same standard deviation ($s^c = 34$ cm, $\tilde{\sigma}^c = 36$ cm). Since on a monthly basis only 16 independent samples can be collected (Section 5.4), the intermediate bound needs to be inflated by $K^c_{\text{uncer}} = 1.41$ to account for data correlation.

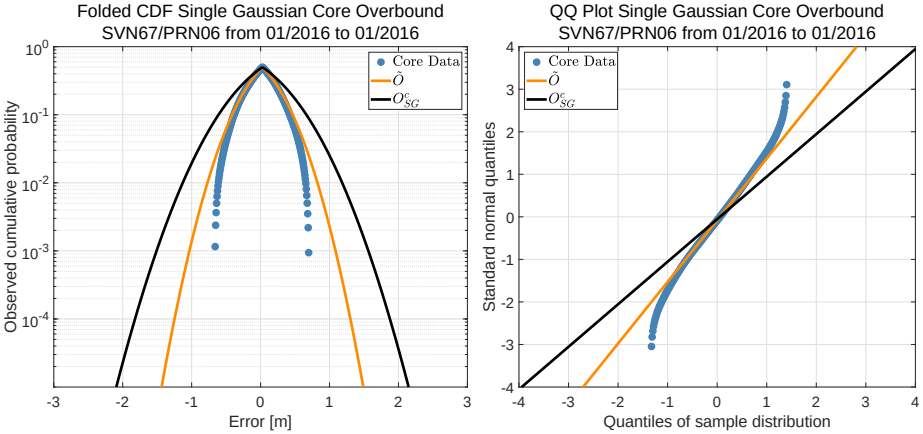

Figure 6.6: Empirical CDF and QQ plot for Single Gaussian overbound of instantaneous user projection SISRE for SVN67 during January 2016 ($s^c = 34$ cm, $\tilde{\sigma}^c = 36$ cm, $\sigma^c_{\text{ob}} = 50$ cm, $K^c_{\text{uncer}} = 1.41$)

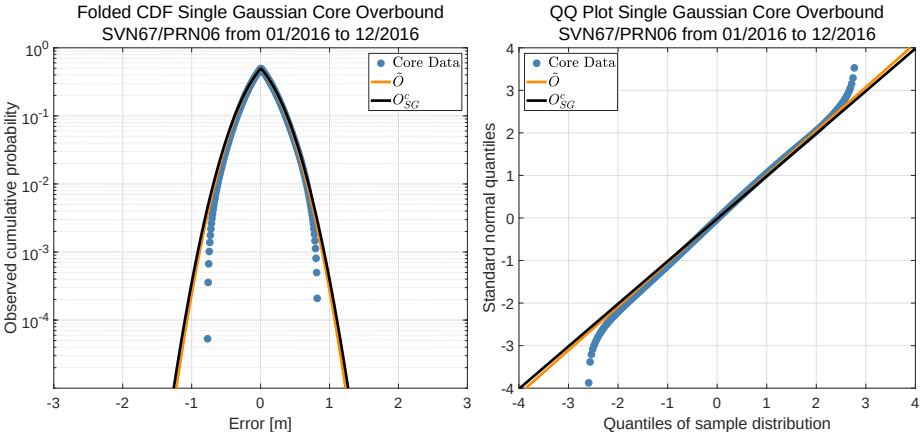

Figure 6.7: Empirical CDF and QQ plot for Single Gaussian overbound of instantaneous user projection SISRE for SVN67 during January-December 2016 ($s^c = 28$ cm, $\tilde{\sigma}^c = 29$ cm, $\sigma^c_{\text{ob}} = 30$ cm, $K^c_{\text{uncer}} = 1.03$)

Similar plots are included in Figure 6.7 where the monitoring time is increased to twelve months. Since a total of $\sim$ 190 samples can be considered in a year for

Rb-clock GPS satellites, the inflation factor drastically reduced to $K^c_{\text{uncer}} = 1.03$ and hence $s^c \simeq \tilde{\sigma}^c \simeq \sigma^c_{\text{ob}} \simeq 30$ cm. This is confirmed by the QQ where the normalized slopes for the three distributions are almost 1. Note that the core bound σ^c_{ob} has been reduced as the monitoring period has increased and more confidence in the estimation has been acquired.

Tail Single Gaussian Bound: The good Gaussian properties of the core allowed us to apply the Bayesian inference analysis results for inflating the intermediate distribution; in the case of tails it is not so simple. From an operational point of view, tails are created by abnormal events which were corrected before they crossed the error threshold (4.42 σ_{URA} in the case of GPS). Their random behavior makes them inherently unpredictable and hard to infer based on historical data. Ultimately, the GNSS operator adjusts the broadcast $\sigma_{\text{URA}}/\sigma_{\text{SISA}}$ values so unexpected tails are bounded according to their operational commitments. In this line the determination of the broadcast sigma values are driven by two aspects: design requirements and confidence in the operation.

As done in [32] and [33], it is not complicated to create a tight bound for a given sample distribution, the so-called intermediate $\tilde{O}$. The complexity resides in the computation of the inflation factor K^t_{uncer} to account for uncertainty. The potential of the MG is that it is able to create a tighter bound by weighting tail distribution bounds without sacrificing the accuracy of the core.

We first need to find an intermediate distribution $\tilde{O}^t(\mathrm{x}) \sim \mathcal{N}\left(m, \tilde{\sigma}^t\right)$ which bounds the tails as

$$\begin{aligned} F_{\tilde{O}^t}(\mathrm{x}) &\geq F_T(\mathrm{x}) \;\forall\; \mathrm{x} < \mathrm{x_L} \\ F_{\tilde{O}^t}(\mathrm{x}) &\leq F_T(\mathrm{x}) \;\forall\; \mathrm{x} > \mathrm{x_R}. \end{aligned} \tag{6.24}$$

An inflation K^t_{uncer} factor needs to be defined for the tails so that $\sigma^t_{\text{ob}} = K^t_{\text{uncer}}\,\tilde{\sigma}^t$ creating the SG tail bound as defined in (6.22). One possibility is to use the same factor defined in (6.14) by inputing the fraction of independent samples contained by the tails. From an operational perspective, if necessary, the ISM provider can increase the inflation of the tail bounding without affecting the core. This will have particular benefits in the MHSS algorithm (covered in Chapter 7) since the EMT and accuracy navigation requirements (defined in Table 1.1) depend on σ^c_{ob}.

6.4.3 Multi Gaussian Overbound Results for GPS

After detailing the individual computation of $C(\mathrm{x})$ and $T(\mathrm{x})$, let us take SVN67 and GSAT0207 range error distributions to illustrate the performance of the Multi Gaussian overbound.

GPS Range Error SVN67 is a GPS Block IIF satellite which operates a Rubidium clock. In order to exemplify the effect of the number of effective independent samples n, three different monitoring periods have been selected: January 2016 ($n = 16$), full year 2016 ($n = 192$), and full period 2016 and 2017 ($n = 384$) depicted in Figures 6.8, 6.9,

and 6.10 respectively. A fixed weighting factor of $w_c = 0.95$ has been selected based on the error empirical CDF. The corresponding values of sample standard deviation s, core overbound σ^c_{ob}, tail overbound σ^c_{ob}, core distribution inflation K^c_{uncer}, and tail distribution inflation factor K^t_{uncer} are collected in Table 6.1 for each monitoring period. Two different effects can be appreciated; the first and most obvious one is the reduction in the inflation factor as the monitoring period increases. As depicted in Figure 6.8 due to the small number of samples, the bounds are intentionally inflated to account for data uncertainty. It is interesting to point out that after a year of data collection, core bounding does not suffer a large variation (28 cm and 33 cm for one and two years of data monitoring). However the uncertainty in the tail estimation still makes a difference between the tail bounding in Figures 6.9 and 6.10.

The second effect is the dispersion of the tails. Figure 6.10 shows slightly larger right tail than Figure 6.9 but since the number of independent samples is double, the final tail overbound is smaller for two years of monitoring data. As mentioned above, the tail behavior does not respond to any predictable statistical behavior but to an operational aspect. Ultimately it will be the ISM provider's duty to select the inflation factor in their internal message generation process.

Table 6.1: Individual parameters for core and tail bounds for MG distributions for SVN67

Monitoring Period	s [cm]	σ^c_{ob} [cm]	σ^t_{ob} [cm]	K^c_{uncer}	K^t_{uncer}
Jan 2016	35	50	163	1.45	3.70
Jan-Dec 2016	29	28	98	1.03	1.79
Jan 2016-Dec 2017	34	33	74	1	1.33

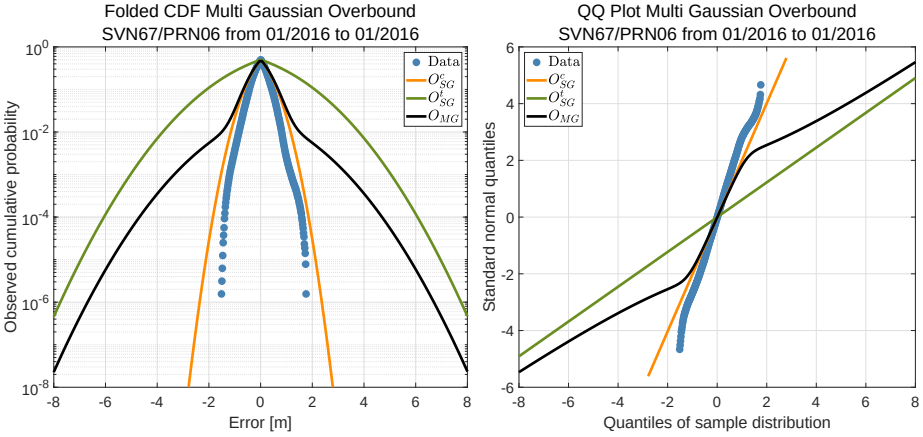

Figure 6.8: Empirical CDF and QQ plot for Single Gaussian overbound of instantaneous user projection SISRE for SVN67 during January 2016. Core-Tail weighting factor 0.95

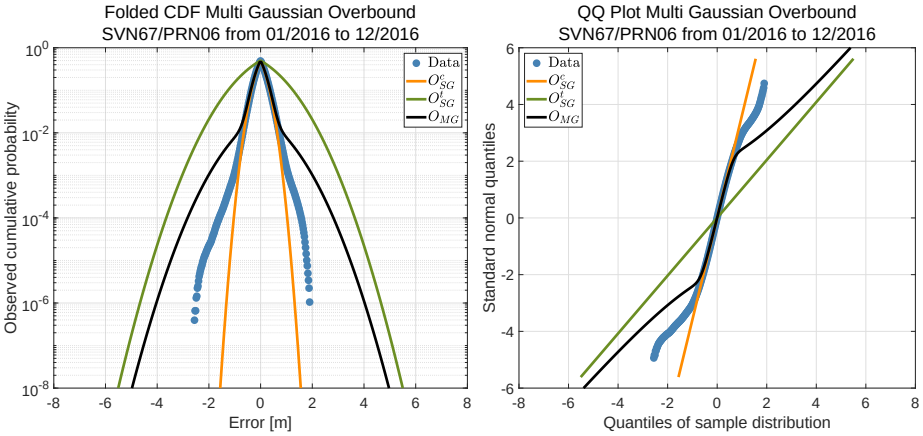

Figure 6.9: Empirical CDF and QQ plot for Single Gaussian Overbound of instantaneous user projection SISRE for SVN67 during January-December 2016. Core-Tail weighting factor 0.95

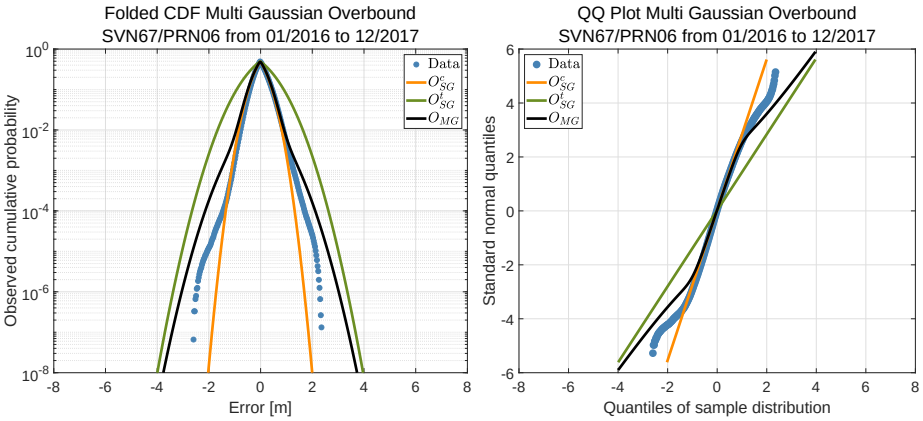

Figure 6.10: Empirical CDF and QQ plot for Single Gaussian Overbound of instantaneous user projection SISRE for SVN67 during 2016-2017. Core-Tail weighting factor 0.95

Galileo Range Error GSAT0207 is a Galileo FOC satellite which operates a PHM clock. Similar to the previous section, three different monitoring periods have been selected: January 2018 ($n = 180$), January to March 2018 ($n = 540$), and January to June 2018 ($n = 1080$) depicted in Figures 6.11, 6.12, and 6.13 respectively. A fixed weighting factor of $w_c = 0.95$ has also been selected based on the error empirical CDF. The corresponding values of the individual distributions are collected in Table 6.2 for each monitoring period.

Let us examine the main differences between GPS and Galileo overbounds. The first one is the variability of the error CDF itself. This is not a surprise and has been predicted in Chapter 5; Galileo nominal error is significantly less correlated than GPS and consequently less variable on a monthly basis. As shown in Table 6.2, the sample standard deviation takes the same value for the three monitoring periods. In this sense, this ratifies the statement made in the previous chapter; a month of Galileo range error data is a good representation of the underlying nominal distribution. This is reflected by the values of the core overbound which are already fixed by a month of data. As the monitoring period increases, tail distribution collects more independent samples and its inflation factor decreases.

A final consideration regarding Galileo tail overbounding might be added. Unlike GPS, the Galileo constellation has not reached its full operational capability yet and no performance commitments have been made public. Although the data shown here suggest that tight overbounds can be selected for Galileo range error, from an operational perspective, it will ultimately be up to the CSP and ANSP to fix the inflation values for integrity.

Table 6.2: Individual parameters for core and tail bounds for MG distributions for GSAT0207

Monitoring Period	s [cm]	σ^c_{ob} [cm]	σ^t_{ob} [cm]	K^c_{uncer}	K^t_{uncer}
Jan 2018	13	11	97	1.03	1.92
Jan-Mar 2018	15	12	87	1	1.22
Jan-Jun 2018	15	12	75	1	1.1

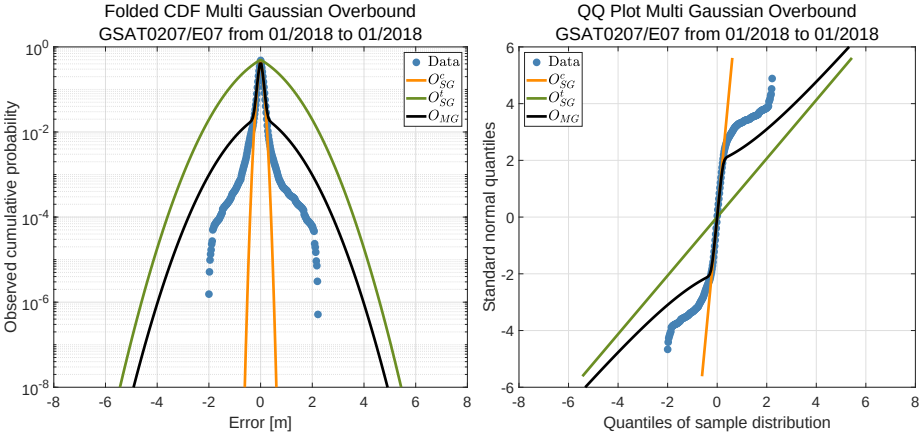

Figure 6.11: Empirical CDF and QQ plot for Single Gaussian Overbound of instantaneous user projection SISRE for SVN67 during January 2018. Core-Tail weighting factor 0.95

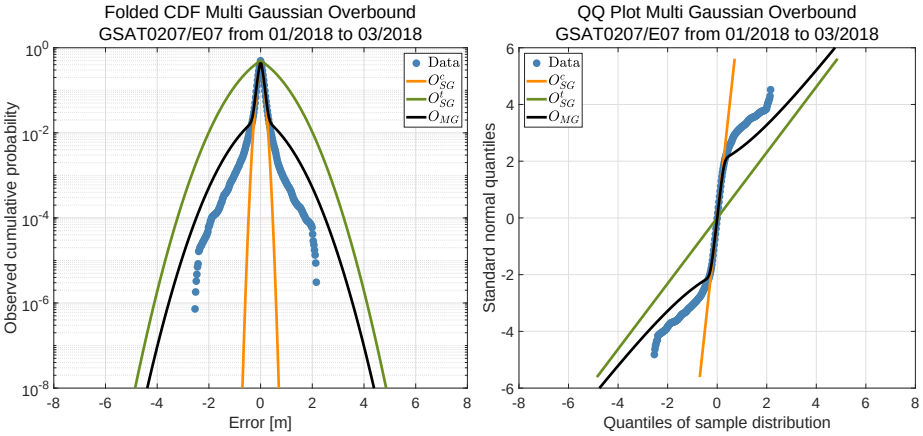

Figure 6.12: Empirical CDF and QQ plot for Single Gaussian Overbound of instantaneous user projection SISRE for GSAT0207 during January-March 2018. Core-Tail weighting factor 0.95

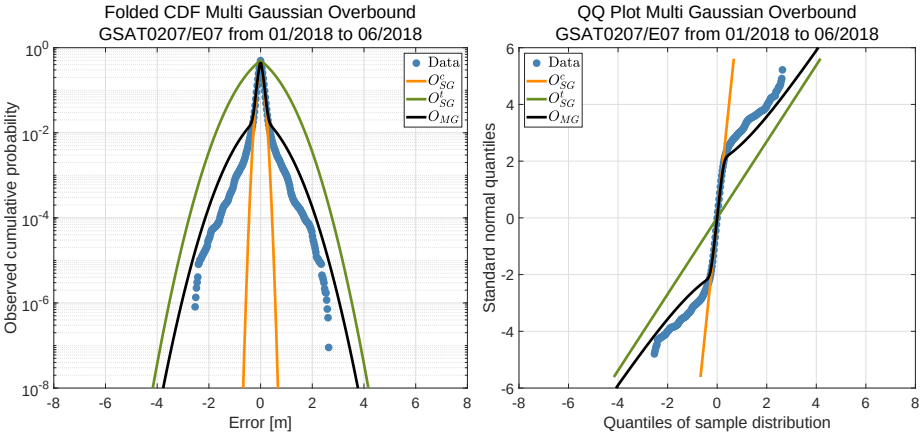

Figure 6.13: Empirical CDF and QQ plot for Single Gaussian Overbound of instantaneous user projection SISRE for GSAT0207 during January-June 2018. Core-Tail weighting factor 0.95

6.4.4 Particular Case: Cesium-equipped GPS Satellites

The Multi Gaussian overbound is motivated by the distinctive behavior exhibited between core and tail of error distributions. Empirical evidence supported this partition for GPS Rb-equipped and Galileo satellites. However, there is a particular case in which this division becomes vague; Cs-equipped GPS satellites. As observed in the

monthly waterfall diagrams for SVN65 in Figure 4.13, the full CDF presents a quasi-Gaussian behavior, not having particularly pronounced tails. In MG terms, 'the entire distribution is core.' Figure 6.14 implements the core bounding to the full dataset. Because a month of GPS Cs range error contains 120 independent samples, for two years of data $K_{\text{uncer}} = 1$ making $\tilde{\sigma} = \sigma^c_{\text{ob}} = 127$ cm. As seen in the figure below, the Gaussianity of the distribution does not recommend core and tail partition.

From an operational perspective in which a hypothetical Multi Gaussian ISM contains the three parameters w_c, σ^c_{ob}, and σ^t_{ob}, this design provides the flexibility to perform a Single Gaussian (legacy) overbound. By simply setting $w_c = 1$, the MG range overbound in (6.20) turns to $F_{O_{MG}}(\text{x}) = F_{O^c_{SG}}(\text{x})$. Chapter 7 will discuss the different ISM architecture options to accommodate the MG bounding and the corresponding dissemination strategies.

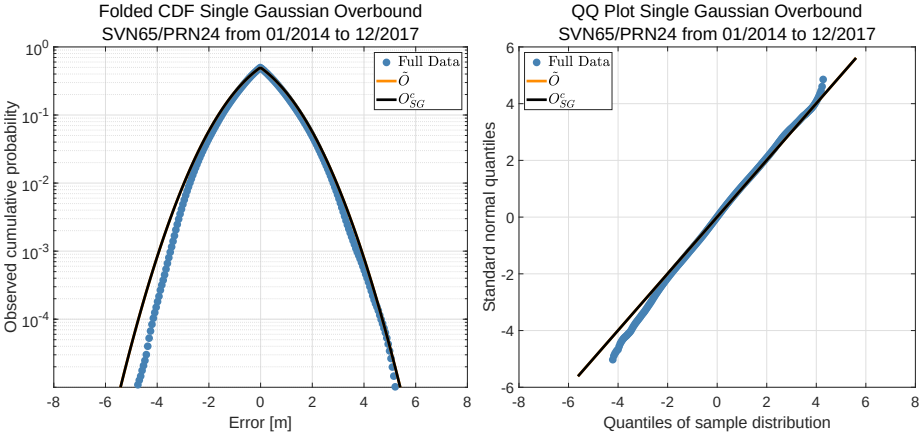

Figure 6.14: Empirical CDF and QQ plot for Single Gaussian Overbound of instantaneous user projection SISRE for SVN65 (Cs Clock) during 2016-2017 ($s = 117$ cm, $\tilde{\sigma} = 127$ cm, $\sigma^c_{\text{ob}} = 127$ cm, $K_{\text{uncer}} = 1$)

6.4.5 Influence of the Weighting Factor

The partition of error distributions in two datasets is highly influenced by the weighting factor w_c. As detailed in Section 6.3, range error empirical CDFs suggest the use of weighting factors between 0.90 and 0.99. Due to the variability of the tail error distribution, the optimal w_c might vary among satellites. Tables 6.3 and 6.4 include the individual SG parameters for GPS and Galileo satellites as a function of the weighting factor. For a monitoring period of two years (over 300 independent samples), Table 6.3 shows the variability of the σ^t_{ob} depending on the weighting factor for different GPS satellites. Finding the optimal combination is not always obvious; a larger w_c deweights the influence of the tail bound (as reflected in (6.20)) but it normally entails larger σ^t_{ob}. Due to the unpredictability of the tails, certain satellites might be optimally

partitioned at the 90% whereas others might be at the 95%. Note that in the case of Cs-clock equipped GPS satellites in Table 6.3, the partition is not applied and the full distribution is assumed to be core.

Analyzing Tables 6.3 and 6.4, it can be observed that core values do not undergo significant variations when selecting values between 0.9-0.95 (third and fifth column of both tables). However, when a limit value of 0.99 is chosen, the seventh column reveals larger changes in the σ^c_{ob}. By increasing w_c we are including portions of the tail into the core distribution, 'corrupting' its Gaussianity. At the same time, fewer independent samples are left for the tail distribution making the uncertainty factor K^t_{uncer} larger and ultimately increasing σ^t_{ob}. The optimal combinations are as diverse as the range error itself. Note that any selection (optimal or not) of the w_c, σ^c_{ob}, and σ^t_{ob} must always provide a safe bound that satisfies Equation (6.25). Chapter 7 elaborates further on the trade-off between w_c and tail probability along with the operational aspects of the ISM generation.

Table 6.3: Core and tail bounds for MG distributions under different weighting factors for GPS satellites (in cm)

Satellite SVN	**Block (Clock)**	$w_c = 0.90$		$w_c = 0.95$		$w_c = 0.99$	
		σ^c_{ob}	σ^t_{ob}	σ^c_{ob}	σ^t_{ob}	σ^c_{ob}	σ^t_{ob}
41	IIR(Rb)	32	88	34	100	38	158
43	IIR(Rb)	37	115	40	128	47	202
44	IIR(Rb)	116	203	124	191	126	261
45	IIR(Rb)	34	123	36	133	40	213
46	IIR(Rb)	62	211	72	243	86	375
47	IIR(Rb)	28	140	29	159	31	254
48	IIR-M(Rb)	47	91	51	94	54	140
50	IIR-M(Rb)	28	98	30	110	32	176
51	IIR(Rb)	30	54	31	61	34	97
52	IIR-M(Rb)	50	99	53	117	59	168
53	IIR-M(Rb)	63	173	74	197	88	227
54	IIR(Rb)	41	124	47	150	59	205
55	IIR-M(Rb)	26	77	27	89	30	143
56	IIR(Rb)	26	126	27	145	29	231
57	IIR-M(Rb)	57	187	71	209	89	231
58	IIR-M(Rb)	30	140	33	161	39	257
59	IIR(Rb)	29	68	31	79	33	124
60	IIR(Rb)	29	44	30	50	31	75
61	IIR(Rb)	31	154	34	174	38	277
62	IIF(Rb)	34	63	35	73	35	116
63	IIF(Rb)	33	165	36	186	43	353
64	IIF(Rb)	30	67	30	76	32	123
65	IIF(Cs)	131	N/A	131	N/A	131	N/A
66	IIF(Rb)	30	54	31	62	32	98
67	IIF(Rb)	34	64	36	74	38	114
68	IIF(Rb)	29	103	31	114	37	221
69	IIF(Rb)	45	132	47	147	51	233
70	IIF(Rb)	32	130	35	152	48	274
71	IIF(Rb)	33	61	35	71	35	113
72	IIF(Cs)	107	N/A	107	N/A	107	N/A
73	IIF(Rb)	31	138	34	159	40	255

For Cs clock satellites no core-tail partition is applied as detailed in Section 6.4.4

Table 6.4: Core and tail bounds for MG distributions under different weighting factors for Galileo satellites (in cm)

Satellite Name	Clock Type	$w_c = 0.90$		$w_c = 0.95$		$w_c = 0.99$	
		σ^c_{ob}	σ^t_{ob}	σ^c_{ob}	σ^t_{ob}	σ^c_{ob}	σ^t_{ob}
GSAT0214	PHM	15	121	16	132	30	243
GSAT0213	PHM	14	106	14	114	25	167
GSAT0212	PHM	16	63	16	64	23	116
GSAT0211	PHM	14	76	14	88	23	115
GSAT0210	PHM	20	73	21	77	22	183
GSAT0209	PHM	13	79	13	87	19	139
GSAT0208	PHM	13	71	13	78	18	142
GSAT0207	PHM	12	64	12	74	18	121
GSAT0206	PHM	11	115	12	121	36	343
GSAT0205	PHM	12	82	13	82	21	123
GSAT0203	PHM	15	80	16	91	20	123
GSAT0103	PHM	31	48	31	50	32	70
GSAT0102	PHM	25	77	26	80	26	110
GSAT0101	RAFS	34	77	36	81	36	127

In order to graphically illustrate the effect of the weighting factor in the MG bounding, Figures 6.15 and 6.16 include individual core and tail bounds for SVN47 range error during 2016-2017 for $w_c = 0.95$ and $w_c = 0.99$, respectively. As already mentioned, smaller weights do normally imply larger tail standard deviations since less independent data can be accounted for the tails. As shown in the fifth row of Table 6.3, the core bound does not get affected by the selection of w_c (around 30 cm) unlike the tail bound which does change significantly from 159 cm to 254 cm.

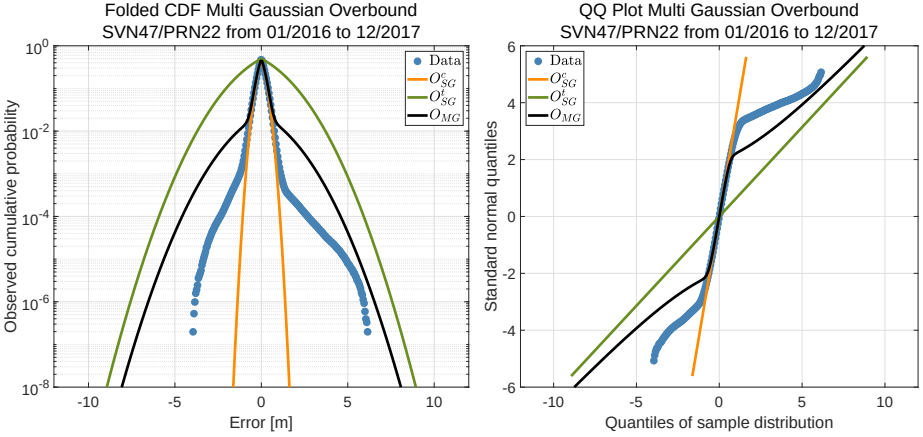

Figure 6.15: Empirical CDF and QQ plot for Single Gaussian Overbound of instantaneous user projection SISRE for SVN47 during 2016-2017. Core-Tail weighting factor 0.95

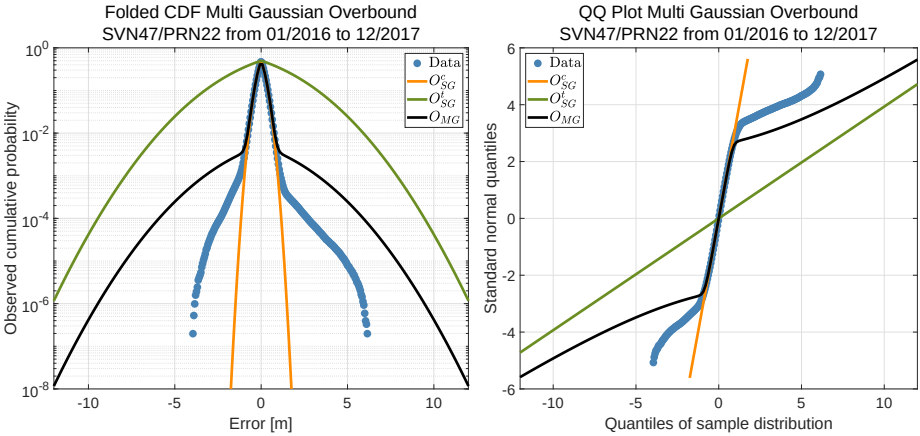

Figure 6.16: Empirical CDF and QQ plot for Single Gaussian Overbound of instantaneous user projection SISRE for SVN47 during 2016-2017. Core-Tail weighting factor 0.99

The potential of the MG bounding resides in the difference in the tail probabilities between the green and black lines in the QQ plots. As will be shown in the MG VPL equation (7.13), this new technique makes the bounds more efficient in the sense that their tail probabilities consume less integrity budget.

6.4.6 Integrity Proof

The Multi Gaussian approach provides a safe bound of individual satellite range errors. Safety-of-Life applications ultimately need to compute protection levels in the position domain obtained through the convolution of individual ranging error bounds. The scope of this section is to prove that the convolution of two MGs that individually bound two error distributions in the range domain, also bound the convolution of the error in the position domain. As indicated in expression (6.22) the individual overbounds were defined as Gaussian distributions both shifted by the sample median m_{x}. As service history data have empirically proved, satellite range error data do not show significant medians or mean values once enough independent samples have been collected. Therefore it is acceptable to assume $m = 0$. Consequently, the MG CDF bound can be expressed as

$$\begin{aligned} F_{O_{MG}}(\mathrm{x}) &\geq F_A(\mathrm{x}) \; \forall \; \mathrm{x} < 0 \\ F_{O_{MG}}(\mathrm{x}) &< F_A(\mathrm{x}) \; \forall \; \mathrm{x} \geq 0. \end{aligned} \tag{6.25}$$

As detailed in Annex C, for two given error distributions $A(\mathrm{x})$ and $B(\mathrm{x})$, the

convolution of $O_{MG,A}$ and $O_{MG,B}$ is also safe if

$$\begin{aligned} F_{O_{MG,A}+O_{MG,B}}(\mathrm{z}) &\geq F_{A+B}(\mathrm{z}) \; \forall \, \mathrm{z} \leq 0 \\ F_{O_{MG,A}+O_{MG,B}}(\mathrm{z}) &< F_{A+B}(\mathrm{z}) \; \forall \, \mathrm{z} > 0. \end{aligned} \tag{6.26}$$

DeCleene proved that in order for the expression above to hold, two sets of conditions need to be fulfilled. First, $O_{MG,A}$ and $O_{MG,B}$ must be symmetric and unimodal; these conditions are met by MG definition (6.20) as the weighted sum of two zero mean Gaussian Distributions (6.22). Second, the actual error distributions must be unimodal and symmetric. GPS and Galileo service history data included in Chapter 4 empirically proved that satellite orbit and clock errors are unimodal with a quasi-Gaussian core with zero mean and median.

It is import to remark that these assumptions only apply to range errors due to orbit and clock. As introduced in Section 2.1.2, there are a complete catalog of feared events for which the assumption of zero mean and median does not apply. In particular, errors like nominal signal deformation and APC variations severely violate these assumptions. Rife's pair overbounding introduced the b_{nom} to account for those types of errors (non-orbit and clock related). The introduction of the nominal bias in the MG bounding is discussed in the following chapter.

7 Integrity Support Message Design

Chapter 6 introduced the Multi Gaussian overbound concept and detailed the methodology to compute the individual values for core and tail bounds. Ultimately, these parameters need to be encapsulated within the ISM and broadcast to the ARAIM users in order to evaluate integrity, continuity, and accuracy requirements. This chapter unifies the analysis carried out through this dissertation and proposes an ISM design compatible with the MG overbound. The first part adjusts the baseline MHSS in order to accommodate the MG bounding methodology. Using availability simulations based on covariance analysis, it reveals the significant enhancement in service availability brought by the modified MG MHSS. The second part exposes the limitations of the current ISM structure. By a small modification, this chapter proposes three candidate ISM designs to include the MG bounding. Results show that a slight modification of the ISM and user algorithm boosts ARAIM service availability particularly in the case of weak geometries.

7.1 Inclusion of Nominal Bias with Multi Gaussian Bounding

The Multi Gaussian overbound theory developed in the previous chapter is based on two empirically proven facts regarding satellite ephemeris and clock errors: distributions have two noticeable core and tail parts and they do not show a significant bias once enough independent samples are collected. This last statement was mathematically proved in Chapter 5 through the determination of the time between effective independent samples for both GPS and Galileo satellites. Since it was designed for orbit and clock error overbounds, the MG bounding described in expression (6.25) does not account for error sources that introduce biases in the distributions.

Although ephemeris and clock errors are the main source of integrity events, the overbound transmitted through the ISM must also account for nominal signal deformation errors. These events nominally shift the SISRE distribution from the origin introducing a non-zero median value which violates the CDF overbound. For integrity purposes, Rife's pair bounding introduced the b_{nom} term to create a symmetric error envelope formed by two equally shifted Gaussian distributions (see Annex C). The Multi Gaussian bound can easily incorporate the same principle by redefining the MG CDF bounding function as

$$F_{O_{MG}} = \begin{cases} F_{O_{MG,L}}(\mathrm{x}) = w_c\, F_{O^c_{SG,L}}(\mathrm{x}) + w_t\, F_{O^t_{SG,L}}(\mathrm{x}) \;\forall\; F_{O_{MG,L}} \;< 1/2 \\ 1/2 \\ F_{O_{MG,R}}(\mathrm{x}) = w_c\, F_{O^c_{SG,R}}(\mathrm{x}) + w_t\, F_{O^t_{SG,R}}(\mathrm{x}) \;\forall\; F_{O_{MG,R}} \;> 1/2. \end{cases} \tag{7.1}$$

The individual core and tail bounding distributions are defined following pair-bounding's approach by introducing b_{nom}

$$\begin{array}{c} O^{c}_{SG,L}(\mathrm{x}) \sim \mathcal{N}\left(-b_{nom}, \sigma^{c}_{\mathrm{ob}}\right) \\ O^{c}_{SG,R}(\mathrm{x}) \sim \mathcal{N}\left(b_{nom}, \sigma^{c}_{\mathrm{ob}}\right) \end{array} \text{ and } \begin{array}{c} O^{t}_{SG,L}(\mathrm{x}) \sim \mathcal{N}\left(-b_{nom}, \sigma^{t}_{\mathrm{ob}}\right) \\ O^{t}_{SG,R}(\mathrm{x}) \sim \mathcal{N}\left(b_{nom}, \sigma^{t}_{\mathrm{ob}}\right). \end{array} \tag{7.2}$$

It is important to remark that the introduction of b_{nom} does not violate the integrity proof presented in Section 6.4.6. The modification of the bounding functions by a constant bias simply creates larger margins for the error distributions to present a non-zero mean due to signal deformation event. The proof of safety for the MG pair bound is included in Annex C.

Blanch's two-step Gaussian overbound modifies the pair bounding approach by introducing a symmetric and unimodal intermediate distribution. As discussed in [33], the trade-off between σ_{ob} and b_{nom} can be optimized by creating a pair-bound which minimizes the values of the bias term b_{nom}. It is left for future work to explore the synergies between two-steps Gaussian overbound and Multi Gaussian overbound.

7.2 MHSS algorithm for Multi Gaussian Bounding

The ARAIM user algorithm evaluates whether or not navigation requirements are met and an airport approach can be executed. The baseline algorithm recommended by WGC follows the Multiple Hypothesis Solution Separation (MHSS) method which checks the consistency among different position solutions associated with each fault hypothesis. The latest version of this ARAIM user algorithm was published by WGC in [4]. Annex D provides a succinct description of the algorithm where only the steps necessary to follow the Multi Gaussian derivation are taken.

The current MHSS algorithm uses two single Gaussian distributions to perform the range error integrity and accuracy overbounds defined in expressions (A.11) and (A.13) (see Annex A). The MG approach suggests two modifications of these bounds. The first one is related to the accuracy bound. As detailed in Figures 6.6 and 6.7, the accuracy of the distribution is dominated by the core, with $\sigma^{c,i}_{\mathrm{ob}}$ being a suitable representation of the so-called $\sigma^{i}_{\mathrm{URE}}$. Note that this statement is tailored to the selection of a weighting factor between 0.9 and 0.99. The second change suggests the implementation of two weighted Gaussian distributions for the integrity bound based on the theory presented in Chapter 6. The ranging accuracy and integrity bounds can be redefined per satellite i and user j as

$$\text{Accuracy: } \begin{cases} \mathcal{N}\left(0, \left(\bar{\sigma}^{i}_{\mathrm{acc},j}\right)^2\right) \\ \left(\bar{\sigma}^{i}_{\mathrm{acc},j}\right)^2 = \left(\sigma^{c,i}_{\mathrm{ob}}\right)^2 + \left(\sigma^{i}_{\mathrm{tropo},j}\right)^2 + \left(\sigma^{i}_{\rho,\mathrm{user},j,\mathrm{IF}}\right)^2 \end{cases} \tag{7.3}$$

$$\text{Integrity: } \begin{cases} w^{i}_{c}\ \mathcal{N}\left(b^{i}_{nom}, \left(\sigma^{c,i}_{\mathrm{int},j}\right)^2\right) + \left(1 - w^{i}_{c}\right)\ \mathcal{N}\left(b^{i}_{nom}, \left(\sigma^{t,i}_{\mathrm{int},j}\right)^2\right) \\ \left(\sigma^{c,i}_{\mathrm{int},j}\right)^2 = \left(\sigma^{c,i}_{\mathrm{ob}}\right)^2 + \left(\sigma^{i}_{\mathrm{tropo},j}\right)^2 + \left(\sigma^{i}_{\rho,\mathrm{user},j,\mathrm{IF}}\right)^2 \\ \left(\sigma^{t,i}_{\mathrm{int},j}\right)^2 = \left(\sigma^{t,i}_{\mathrm{ob}}\right)^2 + \left(\sigma^{i}_{\mathrm{tropo},j}\right)^2 + \left(\sigma^{i}_{\rho,\mathrm{user},j,\mathrm{IF}}\right)^2. \end{cases} \tag{7.4}$$

Since two weighted Gaussian distributions are used for overbounding the ranging error, the position estimate shall reflect this modification. Let us go back to the basic definition of the least-squares estimation matrix $\boldsymbol{S}$ in Equation (2.16). In the MG case, the weighting matrix $\boldsymbol{W}$ shall account for core $\boldsymbol{W}_C$ and tail distribution errors $\boldsymbol{W}_T$ so that the $\boldsymbol{S}$ is redefined as

$$\boldsymbol{S} = w_c\boldsymbol{S}_C + w_t\boldsymbol{S}_T \text{ where } \begin{cases} \boldsymbol{S}_C = (\boldsymbol{G}^T\boldsymbol{W}_C\boldsymbol{G})^{-1}\boldsymbol{G}^T\boldsymbol{W}_C \\ \boldsymbol{S}_T = (\boldsymbol{G}^T\boldsymbol{W}_T\boldsymbol{G})^{-1}\boldsymbol{G}^T\boldsymbol{W}_C. \end{cases} \tag{7.5}$$

Accordingly, the state estimate vector $\hat{\mathbf{x}}$ for MG bounding is rewritten as

$$\hat{\mathbf{x}} = \boldsymbol{S}\boldsymbol{z} = (w_c\boldsymbol{S}_C + w_t\boldsymbol{S}_T)\,\boldsymbol{z} = w_c\hat{\mathbf{x}}_c + w_t\hat{\mathbf{x}}_t, \tag{7.6}$$

and the error vector estimate is redefined from (2.17) as

$$\boldsymbol{\varepsilon} \equiv \hat{\mathbf{x}} - \mathbf{x} = w_c\hat{\mathbf{x}}_c + w_t\hat{\mathbf{x}}_t - w_c\mathbf{x}_c - w_t\mathbf{x}_t = w_c\boldsymbol{\varepsilon}_c + w_t\boldsymbol{\varepsilon}_t. \tag{7.7}$$

As introduced in Section 2.2, the solution separation test statistic is built as the difference between the position solution for hypothesis h_k and the all-in-view h_0 in expression (2.28). The SS test statistic f is then redefined for Multi Gaussian MHSS for coordinate l as

$$q_l^{(k)} = \left|\hat{\mathrm{x}}_l^{(k)} - \hat{\mathrm{x}}_l^{(0)}\right| = w_c^{(k)}\left|\hat{\mathrm{x}}_{l,c}^{(k)} - \hat{\mathrm{x}}_{l,c}^{(0)}\right| + w_t^{(k)}\left|\hat{\mathrm{x}}_{l,t}^{(k)} - \hat{\mathrm{x}}_{l,t}^{(0)}\right|. \tag{7.8}$$

Following the MHSS algorithm steps (Annex D), for a user j with a given geometry $\boldsymbol{G}$ let H_k be the set of $N_f + 1$ mutually exclusive fault hypotheses determined by expression (D.3). MG bounding introduces a major difference with respect to the baseline MHSS; each core-tail combination must be accounted for in the convolution to the position domain. For each fault hypothesis (k) where position solution is obtained through N_k ranging measurements, a total of $S = 2^{N_k}$ different core-tail combinations need to be taken into account. The associated PHMI for each fault hypothesis can be expressed as the weighted sum of each individual convolution $P_{HMI,s}^{(k)}$ as

$$P_{HMI}^{(k)} = \sum_{s=1}^{S} w_s^{(k)} P_{HMI,s}^{(k)}. \tag{7.9}$$

Each combination s convolves the cores from measurements d with the tails of measurements r out of the total N_k measurements included in the fault tolerant solution (k). As indicated in (7.4), note that each range measurement i can have different core and tail weights so that the weighting factor of the combination s is defined as

$$w_s^{(k)} = \prod_{\substack{d=1 \\ d\neq r}}^{N_k} w_c^d \prod_{\substack{r=1 \\ r\neq d}}^{N_k} w_t^r. \tag{7.10}$$

Using the total law of probabilities in (D.13), the total PHMI can be computed as the sum of each individual hypothesis

$$P_{HMI} = \sum_{k=0}^{N_f} P_{HMI}^{(k)}. \tag{7.11}$$

Introducing (7.9) in (7.11), the criterion for availability of integrity for MG bounding can be written as

$$\sum_{s=1}^{S} w_s^{(0)} P_{HMI,s}^{(0)} + \sum_{k=1}^{N_f} \left\{ \sum_{s=1}^{S} w_s^{(k)} P_{HMI,s}^{(k)} \right\} \leq I_{REQ} - P_{NM}. \tag{7.12}$$

Given the linearity, the derivation of the protection level equations departing from the above expression is similar to the one followed in [87] to obtain the baseline VPL and HPL equations in (D.14) and (D.15). Accommodating the MG method within the protection level equations is uncomplicated and yields

$$\begin{aligned} &\sum_{s=1}^{S} 2w_s^{(0)} \bar{Q}\left(\frac{VPL - b_{3,s}^{(0)}}{\sigma_{3,s}^{(0)}}\right) + \sum_{k=1}^{N_f} \left\{ \sum_{s=1}^{S} w_s^{(k)} p_{f,k} \bar{Q}\left(\frac{VPL - T_{k,3,s} - b_{3,s}^{(k)}}{\sigma_{3,s}^{(k)}}\right) \right\} \\ &= I_{REQ,V}\left(1 - \frac{P_{NM}}{I_{REQ,V} + I_{REQ,H}}\right). \end{aligned} \tag{7.13}$$

For a typical GPS-Galileo scenario, one user can see up to 18 simultaneous satellites which implies a total of over 200,000 different core-tail combinations for each fault hypothesis. Computing each one of the terms in the expression above can be prohibitive for the onboard algorithm. Let us find an upper bound that reduces the number of core-tail combinations to be monitored at the expense of obtaining more generous protection levels. As described in (2.23), each term in (7.13) represents the tail probabilities in the position domain of each fault tolerant hypothesis for each core-tail combination s. Let $s = 1$ be the combination of all cores C, $s = S = 2^{N_k}$ the combination of all tails T, and $2 \leq s \leq S-1$ all the intermediate combinations. The fault-free hypothesis (0) term can then be expressed as

$$\begin{aligned} &\sum_{s=1}^{S} 2w_s^{(0)} \bar{Q}\left(\frac{VPL - b_{3,s}^{(0)}}{\sigma_{3,s}^{(0)}}\right) = 2w_C^{(0)} \bar{Q}\left(\frac{VPL - b_{3,C}^{(0)}}{\sigma_{3,C}^{(0)}}\right) \\ &+ \sum_{s=2}^{S-1} 2w_s^{(0)} \bar{Q}\left(\frac{VPL - b_{3,s}^{(0)}}{\sigma_{3,s}^{(0)}}\right) + 2w_T^{(0)} \bar{Q}\left(\frac{VPL - b_{3,T}^{(0)}}{\sigma_{3,T}^{(0)}}\right) \end{aligned} \tag{7.14}$$

where the weighting factors for combinations C and T can be computed according to the definition in (7.10) as

$$w_C^{(k)} = \prod_{i=1}^{N_k} w_c^i \;\text{ and }\; w_T^{(k)} = \prod_{i=1}^{N_k} w_t^i. \tag{7.15}$$

According to expression (D.4) it is true that $\sigma_{3,T}^{(k)} \geq \sigma_{3,s}^{(k)}$ for all s given that $\sigma_{\text{int}}^{t,i} \geq \sigma_{\text{int}}^{c,i}$ for all measurements i. In other words, the standard deviation of the position solution error for the combination of all tails is larger than for the rest of s combinations. Consequently the following bound can be established

$$\bar{Q}\left(\frac{VPL - b_{3,T}^{(0)}}{\sigma_{3,T}^{(0)}}\right) \geq \bar{Q}\left(\frac{VPL - b_{3,s}^{(0)}}{\sigma_{3,s}^{(0)}}\right) \;\forall\, s. \tag{7.16}$$

Introducing the expression above in (7.14), the following inequality can be found

$$\begin{aligned}\sum_{s=1}^{S} 2w_s^{(0)}\bar{Q}\left(\frac{VPL-b_{3,s}^{(0)}}{\sigma_{3,s}^{(0)}}\right) \leq & 2w_C^{(0)}\bar{Q}\left(\frac{VPL-b_{3,C}^{(0)}}{\sigma_{3,C}^{(0)}}\right) \\ & + 2\sum_{s=2}^{S} w_s^{(0)}\bar{Q}\left(\frac{VPL-b_{3,T}^{(0)}}{\sigma_{3,T}^{(0)}}\right).\end{aligned} \tag{7.17}$$

A similar expression can be found for the fault-tolerant cases (k) leading to an analogous upper bound

$$\begin{aligned}\sum_{s=1}^{S} w_s^{(k)}\bar{Q}\left(\frac{VPL-T_{k,3,s}-b_{3,s}^{(k)}}{\sigma_{3,s}^{(k)}}\right) \leq & w_C^{(k)}\bar{Q}\left(\frac{VPL-T_{k,3,C}-b_{3,C}^{(k)}}{\sigma_{3,C}^{(k)}}\right) \\ & + \sum_{s=2}^{S} w_s^{(k)}\bar{Q}\left(\frac{VPL-T_{k,3,T}-b_{3,T}^{(k)}}{\sigma_{3,T}^{(k)}}\right).\end{aligned} \tag{7.18}$$

Since for a given ranging measurement core and weighting factors are complementary ($w_c^i + w_t^i = 1 \; \forall \; i$), it is not necessary to compute the corresponding $w_s^{(k)}$ term for each combination s. Given that $\sum_{s=1}^{S} w_s^{(k)} = 1$, the summation term in expressions (7.17) and (7.18) can be written as

$$w_{CT}^{(k)} = \sum_{s=2}^{S} w_s^{(k)} = 1 - w_C^{(k)} = 1 - \prod_{i=1}^{N_k} w_c^i. \tag{7.19}$$

Finally, introducing the upper bounds from (7.17) and (7.18) into (7.13), VPL equations for MG overbounding can be expressed as

$$\begin{aligned}& 2w_C^{(0)}\bar{Q}\left(\frac{VPL-b_{3,C}^{(0)}}{\sigma_{3,C}^{(0)}}\right) + 2w_{CT}^{(0)}\bar{Q}\left(\frac{VPL-b_{3,T}^{(0)}}{\sigma_{3,T}^{(0)}}\right) \\ & + \sum_{k=1}^{N_f} p_{f,k}\left\{w_C^{(k)}\bar{Q}\left(\frac{VPL-T_{k,3,C}-b_{3,C}^{(k)}}{\sigma_{3,C}^{(k)}}\right) + w_{CT}^{(k)}\bar{Q}\left(\frac{VPL-T_{k,3,T}-b_{3,T}^{(k)}}{\sigma_{3,T}^{(k)}}\right)\right\} \\ & = I_{REQ,V}\left(1 - \frac{P_{NM}}{I_{REQ,V}+I_{REQ,H}}\right).\end{aligned} \tag{7.20}$$

Analogously, the HPL equation for MG overbound can be written as

$$2w_C^{(0)}\bar{Q}\left(\frac{HPL_l - b_{l,C}^{(0)}}{\sigma_{l,C}^{(0)}}\right) + 2w_{CT}^{(0)}\bar{Q}\left(\frac{HPL_l - b_{l,T}^{(0)}}{\sigma_{l,T}^{(0)}}\right) + \sum_{k=1}^{N_f} p_{f,k}\left\{w_C^{(k)}\bar{Q}\left(\frac{HPL_l - T_{k,l,C} - b_{l,C}^{(k)}}{\sigma_{l,C}^{(k)}}\right) + w_{CT}^{(k)}\bar{Q}\left(\frac{HPL_l - T_{k,l,T} - b_{l,T}^{(k)}}{\sigma_{l,T}^{(k)}}\right)\right\} = \frac{1}{2}I_{REQ,H}\left(1 - \frac{P_{NM}}{I_{REQ,V} + I_{REQ,H}}\right). \tag{7.21}$$

Comparing the modified protection level equations above to the SG baseline MHSS in (D.14) and (D.15), one can see that the new ones consist of a set of fault hypotheses with associated complementary prior probability of occurrence of $w_C^{(k)}p_{f,k}$ and $w_{CT}^{(k)}p_{f,k}$ where $w_C^{(k)} + w_{CT}^{(k)} = 1$. Regarding the computational effort, the number of evaluations gets increased by a factor of two, not presenting a prohibitive burden to the user algorithm.

As was done in the SG MHSS case, the protection level equations can be solved iteratively as indicated in Appendix B of [10]. The corresponding core and tail LSE matrices for all-in-view ($\boldsymbol{S}_C^{(0)}$, $\boldsymbol{S}_T^{(0)}$) and fault-tolerant solutions ($\boldsymbol{S}_C^{(k)}$, $\boldsymbol{S}_T^{(k)}$) can be determined as indicated by expressions (D.4) and (D.5). Note that the corresponding weighting matrices $\boldsymbol{W}_C$ and $\boldsymbol{W}_T$ are based on each individual integrity bound $\sigma_{\text{int},j}^{c,i}$ and $\sigma_{\text{int},j}^{t,i}$ defined by (7.4)

$$\boldsymbol{W}_C^{(k)}(i,i) = \begin{cases} 0 \text{ if } i \in h_k \\ \left(1/\sigma_{\text{int},j}^{c,i}\right)^2 \text{ otherwise} \end{cases} \qquad \boldsymbol{W}_T^{(k)}(i,i) = \begin{cases} 0 \text{ if } i \in h_k \\ \left(1/\sigma_{\text{int},j}^{t,i}\right)^2 \text{ otherwise.} \end{cases} \tag{7.22}$$

Respectively, the covariance associated with the all-in-view ($\sigma_{l,C}^{(0)}$, $\sigma_{l,T}^{(0)}$) and fault-tolerant solutions ($\sigma_{l,C}^{(k)}$, $\sigma_{l,T}^{(k)}$) are given by Equation (D.7) inserting the corresponding $\boldsymbol{W}_C^{(k)}$ and $\boldsymbol{W}_T^{(k)}$ matrices. The test statistics standard deviations $\sigma_{ss,l,C}^{(k)}$ and $\sigma_{ss,l,T}^{(k)}$ are computed as indicated by Equation (D.9). Note that the covariance matrix for accuracy $\boldsymbol{C}_{acc}$ is defined by $\bar{\sigma}_{\text{acc},j}^{i}$ in (7.4).

The solution separation detection threshold is calculated for each fault hypothesis as done in (D.8)

$$T_{k,l,C} = K_{fa,l}\sigma_{ss,l,C}^{(k)} \quad \text{and} \quad T_{k,l,T} = K_{fa,l}\sigma_{ss,l,T}^{(k)}. \tag{7.23}$$

Each core and tail contribution of the nominal bias can be computed similarly to (D.10). For each coordinate l they are projected into the position domain as

$$b_{l,C}^{(k)} = \sum_{i=1}^{N_{sat}} \left|\boldsymbol{S}_{C,l,i}^{(k)}\right| b_{nom}^{i} \quad \text{and} \quad b_{l,T}^{(k)} = \sum_{i=1}^{N_{sat}} \left|\boldsymbol{S}_{T,l,i}^{(k)}\right| b_{nom}^{i}. \tag{7.24}$$

There are still two metrics that need to be modified with respect the baseline algorithm; fault-free accuracy and EMT. The first one is based on the accuracy overbound $\bar{\sigma}^i_{\text{acc},j}$ defined in (7.4) and is computed as

$$\sigma_{v,acc} = \sqrt{\boldsymbol{\alpha}_3^T \boldsymbol{S}_C^{(0)} \boldsymbol{C}_{acc} \boldsymbol{S}_C^{(0)^T} \boldsymbol{\alpha}_3}. \tag{7.25}$$

Out of all the vertical detection thresholds for core and tail, the EMT is computed as

$$EMT = max_{k|p_{k,f} \geq P_{EMT}} \left\{ T_{k,3,C}, T_{k,3,T} \right\}. \tag{7.26}$$

Note that as long as the core bounding sigma values are significantly smaller than the tail ones, $T_{k,3,T}$ will be larger than $T_{k,3,C}$. Finally, the evaluation of the navigation requirements for the modified Multi Gaussian MHSS algorithm can be done through expressions (7.20), (7.21), (7.25), and (7.26). To complement this derivation, Annex E provides a definition of the design parameters along with the integrity and continuity allocation for horizontal and vertical coordinates.

7.3 ARAIM Availability Simulations

Once the MHSS algorithm has been modified to accommodate the Multi Gaussian bounding, service volume simulations are carried out to evaluate the effect of the new bounding methodology on ARAIM service availability. The implementation of the algorithm has followed the baseline description and recommendations indicated by the WGC in the ARAIM Milestone 3 Report [3] (including its latest update [4]). Annex A provides further information regarding error models for covariance analysis needed in this section. In addition, Annex E details the simulation configuration parameters such as user grid, time step, and constellation almanacs. These have been intentionally aligned to the MHSS reference algorithm parameters in order to make a fair comparison between single and Multi Gaussian approaches. The probability allocations for horizontal and vertical components are detailed in Table E.1.

Table 7.1: Single and Multi Gaussian Simulation Parameters Reciprocity

Parameter	Single Gaussian	Multi Gaussian
Integrity Bound	$\sigma_{\text{URA}} = \sigma^t_{\text{ob}}$	$\sigma^c_{\text{ob}},\ \sigma^t_{\text{ob}},\ w_c$
Accuracy Bound	$\sigma_{\text{URE}} = 2/3\ \sigma^t_{\text{ob}}$	σ^c_{ob}
b_{nom}	75 cm	75cm
P_{sat}	10^{-5}	10^{-5}
P_{const}	10^{-4}	10^{-4}

The ultimate scope is to illustrate how a small modification in the offline ISM entails a large improvement in the ARAIM service availability. In the case of MG MHSS, three parameters are modified in each simulation scenario, σ^c_{ob}, σ^t_{ob}, and w_c.

As illustrated in Section 6.4, the fact that only one single parameter is used for the integrity bound in the current MHSS obliges us to broadcast the most conservative one; that implies $\sigma_{\mathrm{URA}} = \sigma^t_{\mathrm{ob}}$. Table 7.1 expresses the reciprocity between SG and MG parameters to be compared in the simulations. Note that the accuracy bound for SG follows WGC's recommended $\sigma_{\mathrm{URE}} = {}^2\!/_3\, \sigma^t_{\mathrm{ob}}$.

Before analyzing the results, it is worth defining the following metrics:

- Availability: Percentage of time that a given user location meets the navigation requirements (or one requirement in particular) during the full simulation period.
- 99.5% Coverage: Percentage of users in latitudes between 70° N and 70° S that have an availability larger or equal to 99.5%. It is understood as a global representation of the service availability.
- 99.5% VPL: For a given location, 99.5-percentile of the VPL distribution during the full simulation period. This definition also applies to 99.5% HPL.

Seven sets of values for σ^c_{ob}, σ^t_{ob}, and w_c have been selected in order to reflect empirical data values from Tables 6.3 and 6.4. Each set has been simulated under two scenarios: nominal 24/24 and depleted 23/23 satellites per constellation (further details in Annex E). Tables 7.2 and 7.3 collect the 99.5% coverage values for each scenario. Additional columns have been added to illustrate the coverage associated with each of the four LPV-200 navigation requirements from Table 1.1. There are two different ways of looking at these tables; horizontally and vertically.

In the first case we are comparing availability results provided by the SG versus MG approaches. Note that in the SG side of the tables some values are repeated; this is intentionally done so that each row allows a direct comparison between the two methods for a given simulation scenario. When comparing MG scenarios vertically, we are examining the influence of each of the three bounding parameters (σ^c_{ob}, σ^t_{ob}, and w_c) on the service availability. Scenarios 1 to 4 have been selected to compare the influence of the weighting factors of 0.9 and 0.95. Scenarios 5 and 6 have been chosen to show how two different sets of bounding parameters can report similar availability figures. Scenario 7 has been selected to analyze the benefit of the MG versus SG when large values of σ_{URA} are demanded.

Figures 7.1 and 7.2 compare the availability results between SG and MG for simulation scenario 3 for nominal 24/24 constellations. As reflected in Table 7.2, MG bounding provides a 99.26% coverage whereas the SG method constrains it to 95.16%. As seen in the maps, it is the VPL requirement that limits the performance. This difference is more accentuated for simulation scenario 5 where the σ_{URA} is increased to 1.5 m plotted in Figures 7.3 and 7.4. Traditional SG bounding cannot meet the target coverage value of 90% whereas it is loosely fulfilled by the new approach. The weighted MG bounds consume significantly less integrity budget leading to smaller protection levels. As the σ_{URA} grows to 1.8 m, coverage drops down to 35.82% whereas it is maintained at 94.58% using MG bounds. In this particular case, one can see that the new methodology not only enhances the VPL values but also provides a more accurate fault-free solution and EMT. As discussed in Chapter 6, the fact that the core is

significantly narrower than the tails can be leveraged in the creation of accuracy and continuity bounds generating smaller $\sigma_{v,acc}$ and EMTs. Even more accentuated is the difference between SG and MG approaches under depleted scenarios as depicted in Table 7.3.

Let us resume the discussion regarding the influence of the weighting factor on service availability. As reflected in Tables 6.3 and 6.4, the w_c value that optimizes σ^c_{ob} and σ^t_{ob} might vary among satellites. Typically, lower values of tail weighting factor translate into larger tail bounds at the same time that they have less influence in the protection level computation (7.20). Figures 7.5 and 7.6 compare the availability and VPL maps for scenarios 5 and 6 under nominal constellations. These values intend to represent a typical w_c, σ^c_{ob}, and σ^t_{ob} combination extracted from data in Tables 6.3 and 6.4. It can be seen that the individual coverage values in Table 7.2 are quite similar for both scenarios despite having different core and tail overbounds. This supports the fact that in order to optimize the MG bounding potential, the ISM generator shall have the freedom to modify these three parameters. One of the advantages of the offline architecture is the one month ISM latency. This allows human interaction in the generation loop facilitating the implementation of the bounding methodology here proposed.

Table 7.2: 99.5% Coverage values for Single and Multi Gaussian bounding under nominal 24/24 satellites scenario

Sim ID	Single Gaussian						Multi Gaussian							
	σ_{URA}	Cov LPV-200	Cov VPL	Cov HPL	Cov EMT	Cov Acc	σ^c_{ob}	σ^t_{ob}	w_c	Cov LPV-200	Cov VPL	Cov HPL	Cov EMT	Cov Acc
1	100	98.71	98.71	100	99.86	100	40	100	0.9	99.5	99.5	100	100	100
2	100	98.71	98.71	100	99.86	100	40	100	0.95	99.57	99.57	100	100	100
3	120	95.16	95.16	100	98.66	100	40	120	0.95	99.26	99.26	100	100	100
4	120	95.16	95.16	100	98.66	100	40	120	0.9	98.78	98.78	100	100	100
5	150	86.12	86.3	100	91.73	98.97	30	150	0.95	98.71	98.71	100	100	100
6	180	35.82	58.89	100	68.54	41.92	50	180	0.99	97.49	97.49	100	100	100
7	180	35.82	58.89	100	68.54	41.92	50	180	0.95	94.57	94.57	100	100	100

Table 7.3: 99.5% Coverage values for Single and Multi Gaussian bounding under depleted 23/23 satellites scenario

Sim ID	Single Gaussian						Multi Gaussian							
	σ_{URA}	Cov LPV-200	Cov VPL	Cov HPL	Cov EMT	Cov Acc	σ^c_{ob}	σ^t_{ob}	w_c	Cov LPV-200	Cov VPL	Cov HPL	Cov EMT	Cov Acc
1	100	79.66	79.78	98.16	84.8	100	40	100	0.9	84.29	84.34	98.31	88.22	100
2	100	79.66	79.78	98.16	84.8	100	40	100	0.95	84.59	84.64	98.36	88.22	100
3	120	69.67	70.11	98	79.64	100	40	120	0.95	82.9	83.69	97.38	88.14	100
4	120	69.67	70.11	98	79.64	100	40	120	0.9	81.61	82.61	97.18	88.14	100
5	150	27.12	39.63	92.93	54.47	72.47	30	150	0.95	75.72	78.7	94.98	90.03	100
6	180	0.08	2.02	88.92	5.67	2.59	50	180	0.99	71.86	76.28	92.3	86.93	100
7	180	0.08	2.02	88.92	5.67	2.59	50	180	0.95	56.33	61.03	90.95	86.73	100

σ values are given in cm, 99.5% coverage values are given in % and w_c are non-dimensional.
The 99.5% coverage values are provided individually for each requirement and for the combination of them.

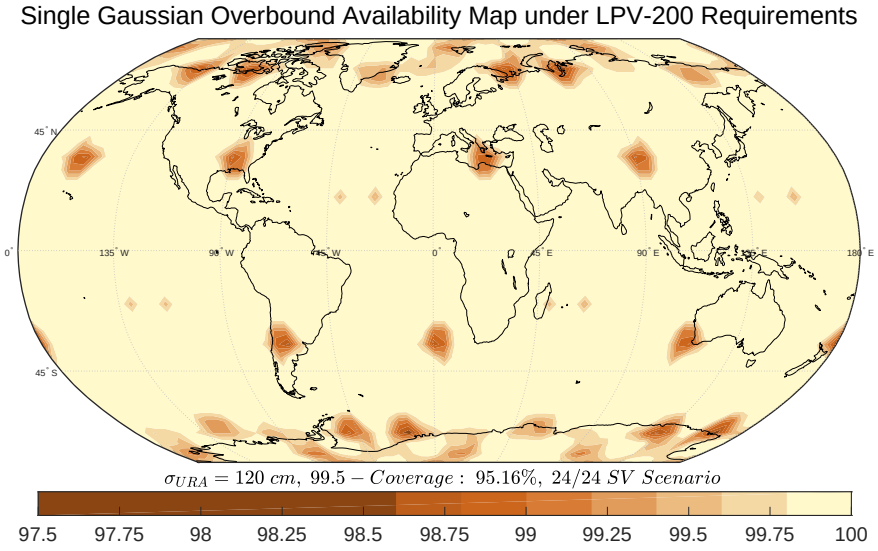

(a) Availability map for SG overbounding

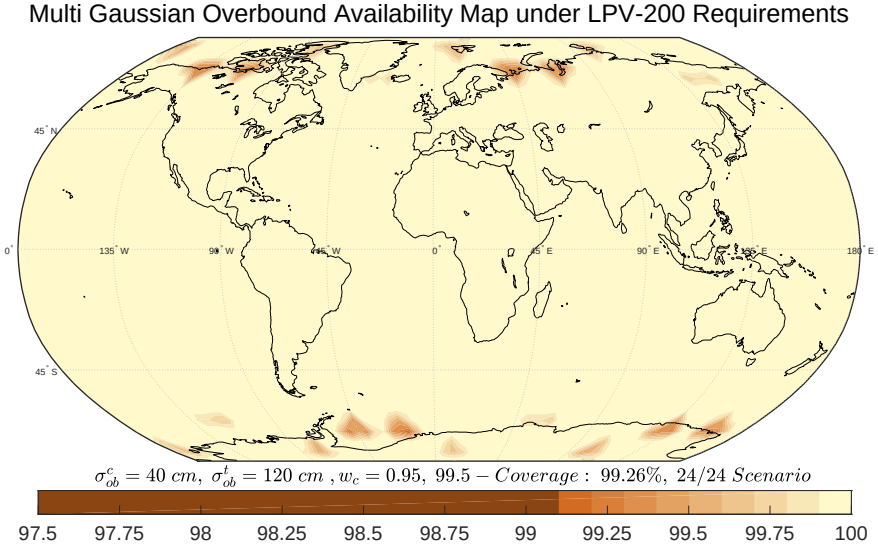

(b) Availability map for MG overbounding

Figure 7.1: Comparison between Single and Multi Gaussian VPL for simulation scenario 3 under 24/24 nominal constellations. Availability maps

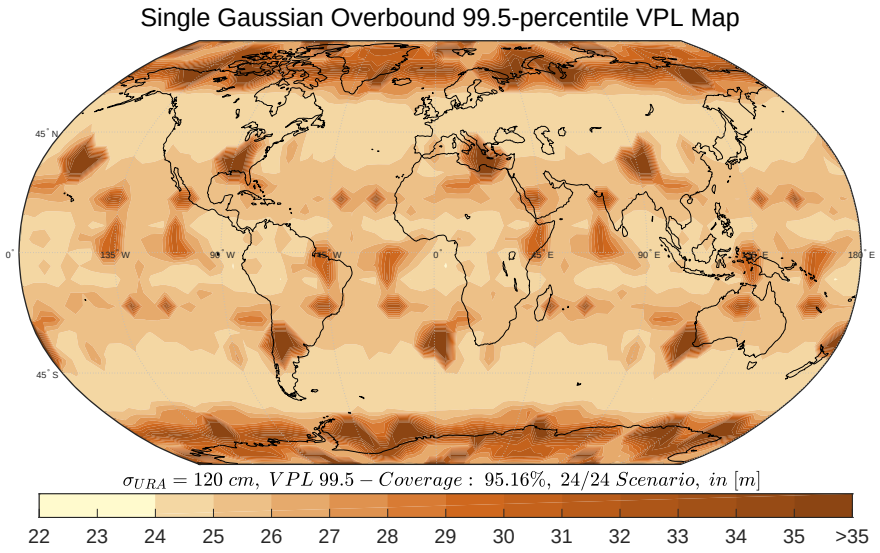

(a) 99.5-Percentile VPL map for SG overbounding

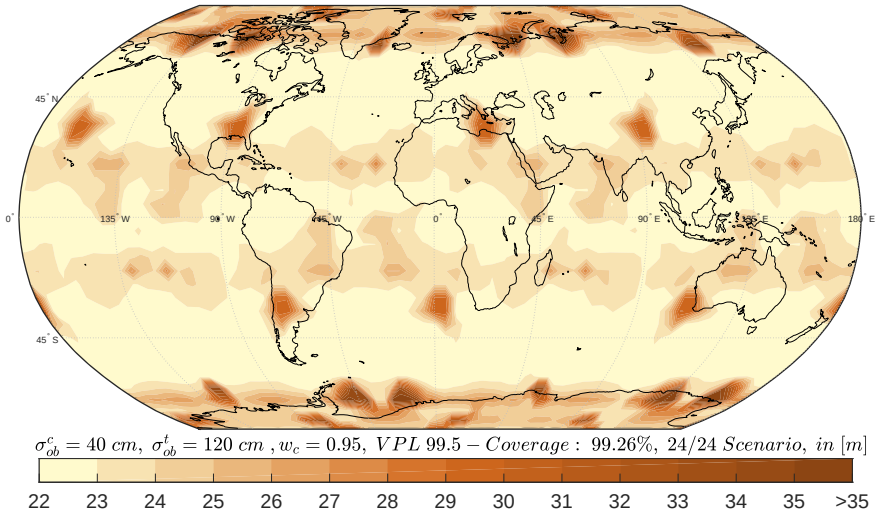

(b) 99.5-Percentile VPL map for MG overbounding

Figure 7.2: Comparison between Single and Multi Gaussian VPL for simulation scenario 3 under 24/24 nominal constellations. 99.5%-Percentile VPL maps

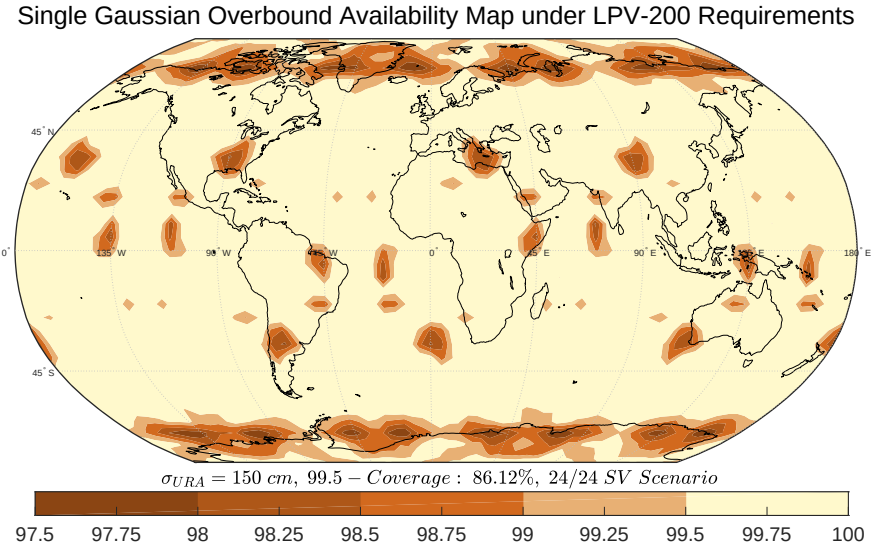

(a) Availability map for SG overbounding

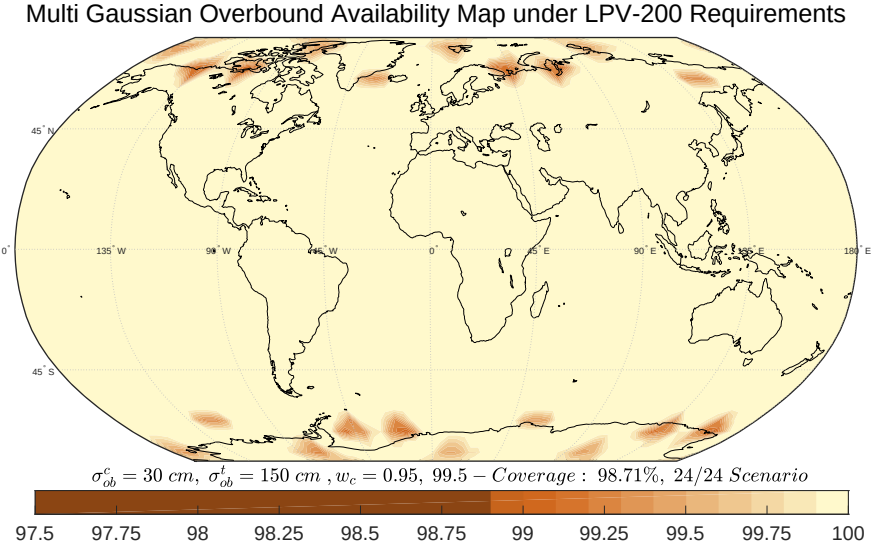

(b) Availability map for MG overbounding

Figure 7.3: Comparison between Single and Multi Gaussian bounding for simulation scenario 5 under 24/24 nominal constellations. Availability maps

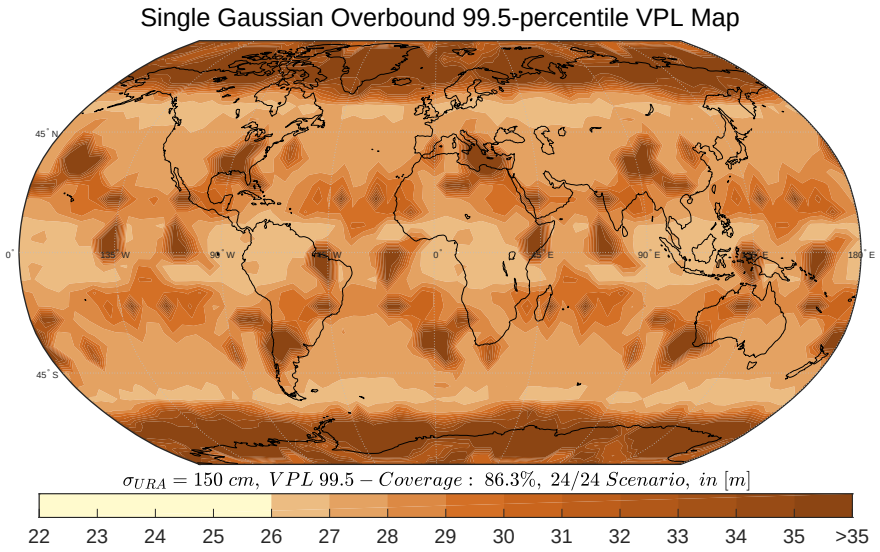

(a) 99.5-Percentile VPL map for SG overbounding

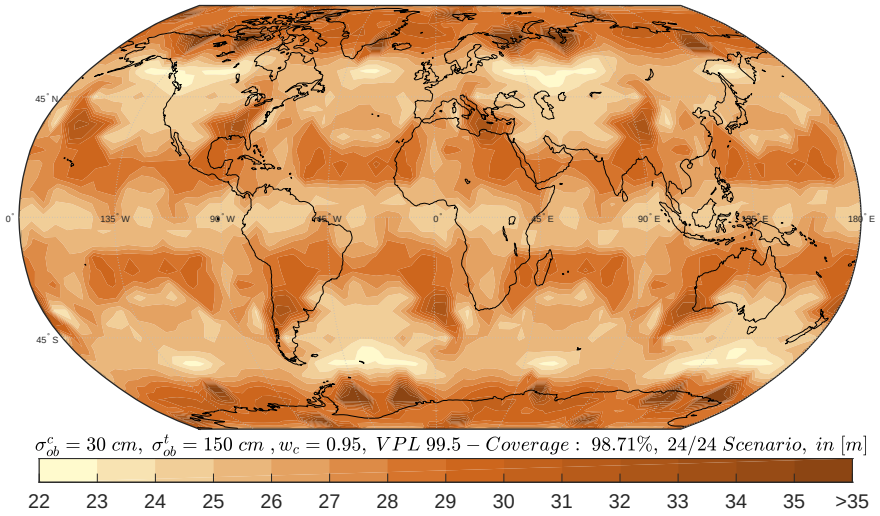

(b) 99.5-Percentile VPL map for MG overbounding

Figure 7.4: Comparison between Single and Multi Gaussian bounding for simulation scenario 5 under 24/24 nominal constellations. 99.5%-Percentile VPL maps

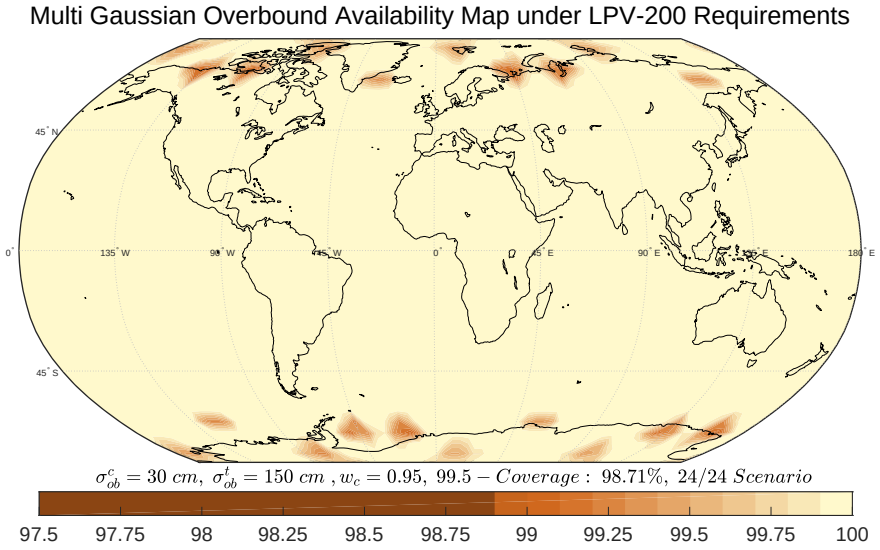

(a) Availability map for MG overbounding

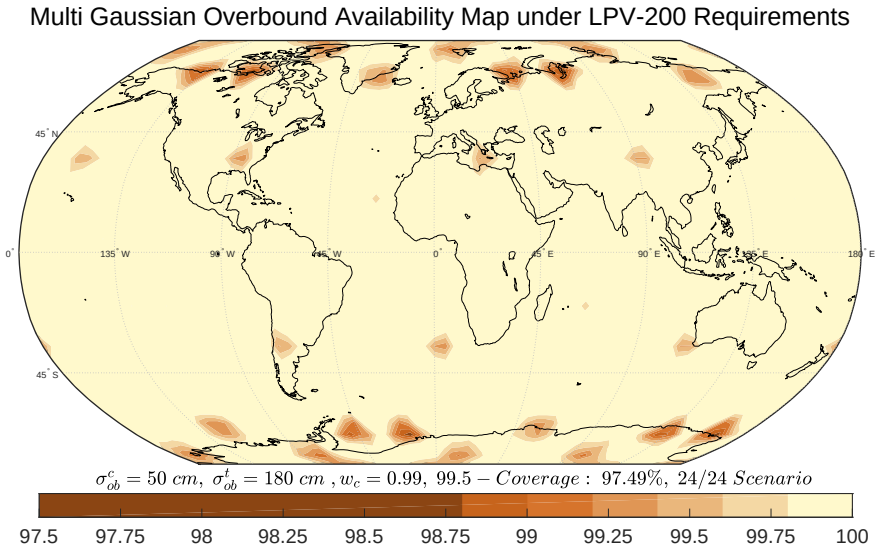

(b) Availability map for MG overbounding

Figure 7.5: Effect of the weighting factor in MG bounding: Comparison between simulation scenarios 5 and 6 under 24/24 nominal constellations. 99.5%-Percentile VPL maps

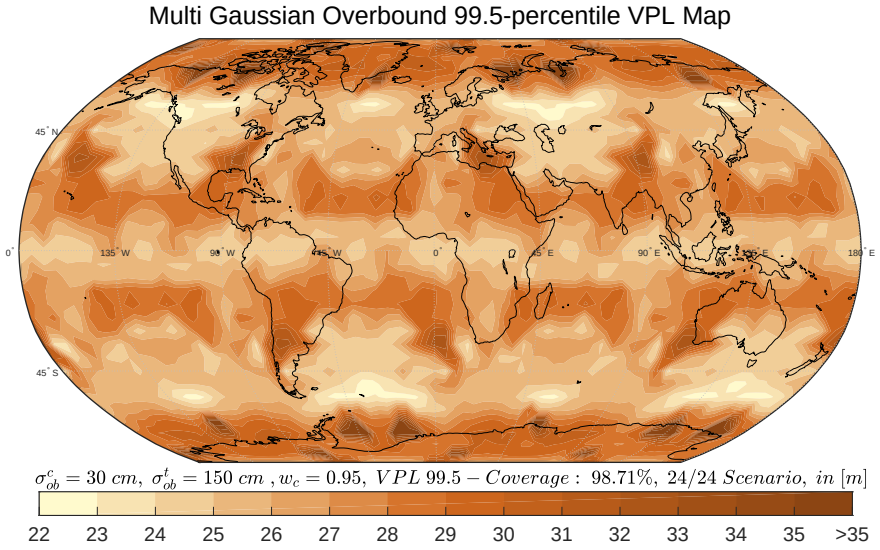

(a) 99.5-Percentile VPL map for MG overbounding

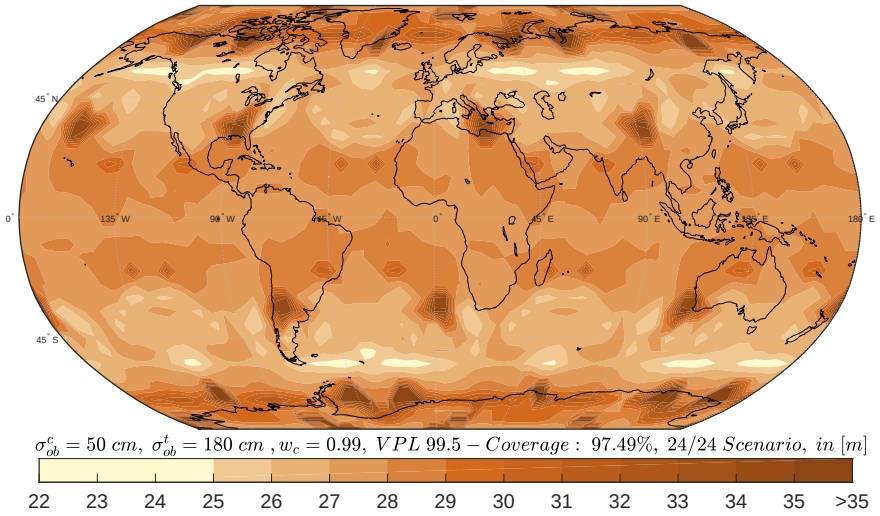

(b) 99.5-Percentile VPL map for MG overbounding

Figure 7.6: Effect of the weighting factor in MG bounding: Comparison between simulation scenarios 5 and 6 under 24/24 nominal constellations. 99.5%-Percentile VPL maps

7.4 Offline ISM for MultiGaussian Bounding

As shown in previous sections, the modified MHSS algorithm needs extra inputs with respect to those of baseline. This section suggests different dissemination options for adapting the current offline ISM format in order to fill the needs of the MG MHSS algorithm.

7.4.1 Current Offline ISM Design

The offline ISM structure defined by WGC is based on Single Gaussian pair-bounding. Fore each satellite within a GNSS constellation, Table 7.4 details the five main bounding parameters that ARAIM users combine to create integrity and accuracy bounds (see Annex A).

Table 7.4: List of parameters derived from current offline ISM [3]

Parameter	Definition
$\sigma^i_{\mathrm{URA}}\|\sigma^i_{\mathrm{SISA}}$	standard deviation of the clock and ephemeris error of satellite i used for integrity
$\sigma^i_{\mathrm{URE}}\|\sigma^i_{\mathrm{SISE}}$	standard deviation of the clock and ephemeris error of satellite i used for accuracy and continuity
b^i_{nom}	maximum nominal bias for satellite i used for integrity
P^i_{sat}	prior probability of fault in satellite i per approach
P^g_{const}	prior probability of fault in satellite g per approach

This ISM design is tailored to the current MHSS algorithm where one value of σ^i_{ob} is used to create the integrity bound. In order for ARAIM users to apply the Multi Gaussian overbound, $\sigma^{c,i}_{\mathrm{ob}}$, $\sigma^{t,i}_{\mathrm{ob}}$, and w^i_c need to be included in the new ISM format.

7.4.2 ISM Dissemination Options and Backwards Compatibility

The implementation of the Multi Gaussian overbound for ARAIM users comes at the price of a slight modification in the ISM design. The derivation carried out in Section 7.2 indicated that three parameters are needed for each satellite: $\sigma^{c,i}_{\mathrm{ob}}$, $\sigma^{t,i}_{\mathrm{ob}}$, and w^i_c. Note that, as proposed in Equation (7.3), the σ^i_{URE} will be substituted by $\sigma^{c,i}_{\mathrm{ob}}$ for creating the accuracy bound and σ^i_{URA} will be substituted by $\sigma^{t,i}_{\mathrm{ob}}$, so technically only one extra parameter would be demanded.

As shown in the coverage results in the previous section, the ideal option would be to broadcast an individual weighting factor for each satellite. By doing this, the ISM generator would have the flexibility to compute the three parameters that better fit each individual error distribution.

According to a recent FAA-EC join publication [88], for offline ARAIM, it is foreseen that each GNSS constellation will broadcast its own ISM through their corresponding navigation message. The proposed message type 38 for GPS ISM would in principle allow the inclusion of the extra two parameters that the MG bounding requires. However, since some restrictions in terms of data capacity can be faced by the ANSP, this chapter proposes three different dissemination options.

Option A - Modified ISM structure with Modified Algorithm: This is the optimal dissemination solution giving the flexibility to create individual weights for each core-tail distribution. The current ISM would only have to incorporate an extra parameter, w_c^i. One of the advantages of this option is that the backwards compatibility is fully guaranteed. As indicated in Section 6.4.4, Cs-equipped GPS empirical data does not suggest a core-tail partition. In these cases, the corresponding weighting parameters can be set to 1 making MG protection level equations (7.20) and (7.21) mathematically equivalent to the Single Gaussian (D.14) and (D.15). A second operational option to guarantee backwards compatibility is the complementary use of w_c^i as a flag. In case $w_c^i = 1$ users must utilize the legacy MHSS mode taking core values for accuracy and tail for integrity.

Option B - Unmodified ISM structure with Modified Algorithm: This one is a compromise solution. It does not require the modification of the ISM structure at the expense of hard-coding the weighting factor. Of course this option reduces the flexibility of the MG bounds since a given value of w_c^i is in general not optimal for all satellites (as seen in Section 6.4.5). In fact, as shown in the previous coverage Table 7.2, there are multiple combinations of the overbounding set ($\sigma_{\text{ob}}^{c,i}$, $\sigma_{\text{ob}}^{t,i}$, and w_c^i) that yield similar availability results. A compromise value for w_c could be 0.95. In this case, the backwards compatibility is also guaranteed for the Cs-equipped GPS satellites. By simply establishing $\sigma_{\text{ob}}^{c,i} = \sigma_{\text{ob}}^{t,i} = \sigma_{\text{URA}}^i$, the MG integrity bound described in (7.4) is mathematically equivalent to the SG integrity bound in (A.13).

Option C - Unmodified ISM structure with Unmodified Algorithm: Although the simplest to implement, it does not exploit all the potential of the MG bound. In this case, no modifications in the ISM structure or onboard MHSS algorithm are required. It is a simple setting of $\sigma_{\text{URE}} = \sigma_{\text{ob}}^c$ instead of fixing it to $\sigma_{\text{URE}} = {}^2\!/_3\, \sigma_{\text{URA}}$ as recommended in Milestone 3 Report. The guarantee of the backwards compatibility is straightforward given that no modification in the onboard algorithm is implemented.

7.4.3 ISM Dissemination Options Comparison

In order to compare the performance of each dissemination option with respect to the baseline MHSS let us analyze the VPL and HPL time series for a given location. We select $\sigma_{\text{URA}} = 180$ cm for the baseline ISM, which according to WGC recommendations, entails a $\sigma_{\text{URE}} = {}^2\!/_3\, \sigma_{\text{URA}} = 120$ cm. As shown in Chapter 6, a fixed value of ${}^2\!/_3$ is actually quite conservative for the accuracy bounding. Based on results from Table 6.3, option C relaxes the σ_{URE} to a more realistic value of 50 cm. For a fair

comparison, MG options A and B use the same σ_{URA} and σ_{URE} values as option C for tail ($\sigma^c_{\mathrm{ob}} = 180$ cm) and core ($\sigma^c_{\mathrm{ob}} = 50$ cm) bounding. Then, different core-tail weighting factors are used: $w_c^{\mathrm{A}} = 0.99$ and $w_c^{\mathrm{B}} = 0.95$. For the simulations, the same values of $P_{sat} = 10^{-5}$, $P_{const} = 10^{-4}$, and $b_{nom} = 75$ cm have been selected from both GPS and Galileo constellations.

Figures 7.7 and 7.8 represent VPL and HPL time series during 24 hours for a user located at Seville airport in south Spain (37.42°N, 5.89°W). The benefits of MG bounding against baseline ISM are indisputable. The average VPL reduction of option A and B relative to baseline ISM are $\sim 25\%$ and $\sim 20\%$ correspondingly. It can be seen that slight change in the MHSS algorithm can significantly impact the protection levels at no extra computational effort. Comparing VPL equations for MG (7.20) and SG (D.14), the number of $\bar{Q}$ evaluations only increases by a factor of two, providing an affordable change in terms of user computational load.

The benefits of the Multi Gaussian MHSS are even more interesting in the case of depleted scenarios. As illustrated in the lower plot of Figure 7.7, by using the baseline ISM design, VPL target of 35 m is exceeded during several hours leading to service unavailability. Conversely, MG options A and B guarantee that protection levels stay below the limits for almost the full period (100% and 99.75% correspondingly). One can also see that option B is a good compromise in case no modification in the ISM structure is wanted. Although having full flexibility (option A) to individually adjust σ^c_{ob}, σ^t_{ob}, and w_c is desired, the compromise solution by fixing w_c to 0.95 also provides excellent availability results. Both options A and B have a direct impact on the CSP performance commitments; for the same ARAIM service availability target, GNSS will be required to commit to more relaxed integrity bounds reducing the burden on the operations.

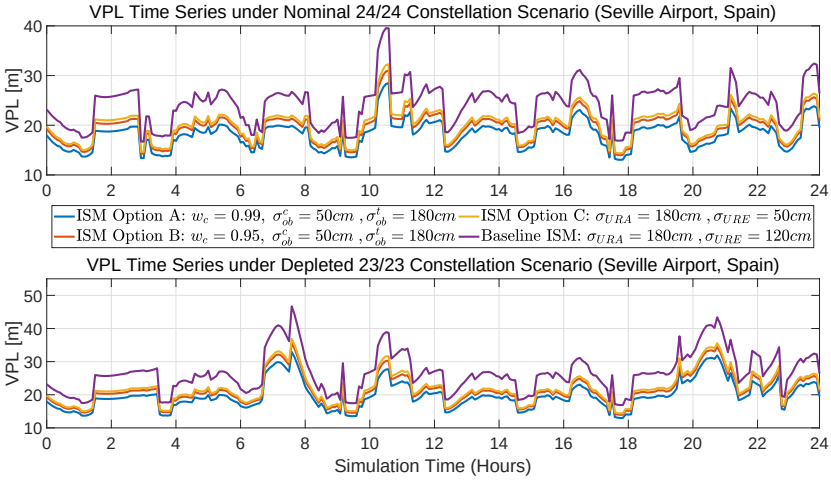

Figure 7.7: Vertical Protection Level time series at Seville Airport, Spain (37.42°N, 5.89°W) for the three proposed ISM design versus baseline ISM

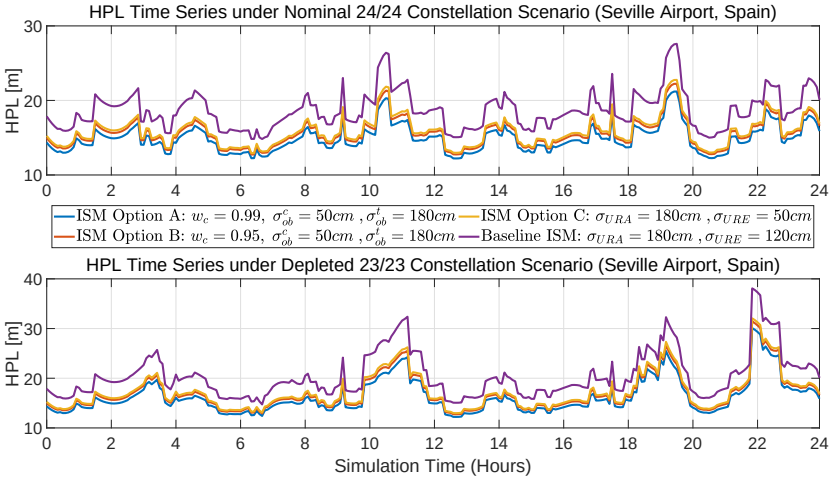

Figure 7.8: HPL time series at Seville Airport, Spain (37.42°N, 5.89°W) for the three proposed ISM design versus baseline ISM

8 Conclusions

Both the US Federal Aviation Administration and European Commission are investing large amounts of effort and resources to make ARAIM a reality in the coming years. The full deployment of Galileo along with the modernization of GPS will soon provide sufficient GNSS ranging measurements to enable ARAIM global coverage. In this context, constellation ground monitoring and Integrity Support Message generation acquire a paramount relevance for ARAIM operations. This dissertation has addressed key points related to performance characterization and error overbound which directly led to a new ISM design. By tailoring the bounds to an empirically suggested Multi Gaussian distribution, this new methodology provides tighter and equally safe protection levels. A small modification in the onboard MHSS user algorithm to accommodate this new ISM design significantly enhances ARAIM service availability for LPV-200 requirements with respect to the current model.

8.1 Summary of Achievements

This dissertation has covered three major aspects in the ISM generation. It has addressed the integrity and availability of service history data, the GPS and Galileo constellation performance characterization, and the temporal correlation of the range error. It all has been combined in the design of a new bounding methodology which led to a redefinition of the ISM structure along with a reshaped user algorithm. Areas of contributions are described in the following subsections.

8.1.1 Ephemeris and Clock Reference Products Monitor

By using a set of 29 ground monitor stations, this dissertation has designed a validation method to guarantee integrity and availability of the reference products used in the GNSS ephemeris and clock error characterization. One of the novelties that this method introduced is the satellite availability check based on ranging measurements. In the case of satellite outages, fictitious and largely degraded orbit and clock errors can be introduced in the distributions if the broadcast ephemeris are used independently of the observation measurements. Using code and phase observations collected by a global network of receivers, it is possible to internally generate continuous clock reference products. As shown, the accuracy of these clock estimates is on the order of 20 cm for GPS and 14 cm for Galileo satellites. In the case of data gaps in the sp3 repositories, this methodology allows the retrieval of satellite orbit and clock reference data by using ranging measurements. This validation method ensures two

essential aspects for integrity monitoring; first, it guarantees that no fabricated errors are introduced in the distributions, and second, that no integrity events are overlooked due to reference data unavailability.

8.1.2 GNSS Performance Assessment

This dissertation has carried out a detailed analysis of the unfaulted orbit and clock errors for both GPS and Galileo constellations. Orbit and clock components have been individually characterized showing that the onboard clock type is the main driver of the range error distribution. It was shown that the current Galileo SISRE nominal performance is twice as accurate as GPS. One of the novelties introduced in this study is the temporal breakdown into monthly, biannual and yearly datasets using folded CDF waterfall diagrams. It exposed that distributions are highly variable on a monthly basis, especially for Rb-equipped GPS satellites. As the monitoring period increases, the sample size grows, more independent data is collected and thus the variability observed among datasets decreases. This is an indicator of the high correlation among samples. We also showed that this correlation greatly depends on the onboard clock type. In this respect, the so-called *initialization period* has been identified. During the first weeks of operation, GPS satellites show abnormally large errors that are not representative of the satellite's performance after that period. Consequently, it is advised that ANSP waits a couple months after including new satellites for SoL use.

8.1.3 Correlation Analysis Methodology

An innovation brought by this dissertation is the error correlation study based on the variance of the estimator of the distribution mean and standard deviation. Unlike prior correlation analyses where only a qualitative assessment based on autocorrelation plots was carried out, this work provides an analytical method to quantitatively determine the time between effectively independent samples. As illustrated through this dissertation, this time varies between GPS and Galileo satellites being mostly driven by the onboard clock type. Range errors from GPS Rb-equipped satellites exhibit a time between independent samples of 50-60 hours, or in other words, only 16 independent samples per month. Conversely, Cs-equipped satellites present a decorrelation time of around 5-6 hours. As pointed out through this dissertation, Rb clock predictions are significantly more accurate than Cs ones but their errors are ten times longer correlated. This is due to the typically higher noise floor for Cs clocks that overshadows the orbit correlation effects. In the case of Galileo, due to the more frequent navigation data updates, correlation is significantly reduced to 2.5-3.5 hours for PHM clocks and 4-5 hours for RAFS-equipped satellites. In terms of number of independent error samples, it has been established that approximately 150-180 data points can be collected in a month of Galileo monitoring, depending on the clock type.

8.1.4 Impact of Sample Correlation on SISRE Overbound

This dissertation derives a methodology to compute error integrity bounds accounting for the limited number of independent samples for a given dataset. Based on Bayesian inference, this work derives an explicit expression of error CDF as a function of the number of independent data points and the sample standard deviation. It has been shown that in order for a Gaussian distribution to account for data independence, the sample standard deviation must be inflated by the so-called *uncertainty factor*. This factor is inversely proportional to the number of independent samples representing the higher confidence that can be placed in the estimation as more independent data are collected. It takes values below 1.1 as the dataset contains more than 150-180 independent data points. In terms of monitoring period, it implies that only 1.5 months of Galileo data is enough to characterize nominal range error mean and standard deviation. In the case of GPS Rb, due to the high correlation of the data, one would have to wait up to 10-12 months to confidently characterize the error nominal distribution. This Bayesian analysis has been corroborated by the GPS and Galileo service history data.

8.1.5 Multi Gaussian Distribution for Integrity Overbound

This work leverages the fact that empirical error CDFs have two distinctive parts; narrow quasi-Gaussian core and flat highly non-Gaussian tail distribution. In order to create tighter overbounds, this dissertation designs an integrity bound made up of two weighted Gaussian distributions. Current integrity bounds are driven by tail dispersion sacrificing the well-behaved core distribution. By choosing a proper weighting factor that ranges between 0.9 and 0.99, this work shows that a tighter and equally safe integrity bound can be applied. Correspondingly, the number of independent samples contained in each distribution is also accounted for in the determination of each individual bound. Typical sigma values for core bounds range between 30-40 cm for GPS and 15-25 cm for Galileo. In the case of tail overbounding, values show larger diversity across satellites. This is one of the advantages of this methodology; it allows flexibility between core and tail bounding.

8.1.6 Modification of the Baseline MHSS Algorithm

This dissertation proposes a modification of the baseline Multiple Hypothesis Solution Separation algorithm to accommodate the MG approach. The original URA sigma bound for integrity is now divided in two weighted distributions that individually bound each error partition. Respectively, it is been shown that the accuracy bound is determined by the core of the distribution. Availability results exposed the benefits of the MG MHSS in meeting LPV-200 requirements. Since each individual MG range bound is tailored to the actual behavior of the error, the convolution of the weighted Gaussians provide tighter protection levels and smaller fault-free accuracy values which

ultimately lead to better availability figures. This is particularly advantageous in the case of depleted constellation scenarios.

8.1.7 ISM Design for Optimal Integrity and Accuracy Bounds

This work proposes three prospective ISM designs to accommodate the three bounding parameters per satellite that MG MHSS needs. Option A, the ideal one, consists of the dissemination of these three parameters. In this case, the ISM generator would have full flexibility to optimize core and tail partitions depending on the actual distribution shape. Option B, the compromise solution, proposes a fixed weighting factor of 0.95 where only the individual one sigma bounds for core and tail are broadcast. This option would only imply a slight modification of the user ARAIM algorithm keeping the current ISM structure. Option C does not entail any changes in the user algorithm or ISM structure. It simply proposes a different setting of the accuracy bound based on empirical evidence. The options have been compared against the current baseline ISM showing that options A and B can decrease the VPL values up to 30% guaranteeing backwards compatibility to the current algorithm. Ultimately, without decreasing ARAIM service availability, the target URA value demanded from CSP can be significantly relaxed imposing less stringent requirements on GPS and Galileo ground segments.

8.2 Recommendations for Future Research Topics

A number of recommendations regarding data monitoring and ISM generations are provided in the following subsections.

8.2.1 Ground Stations Observation Model Refinements

The aim of the ground monitoring function is to validate reference orbit and clock products. With the current design this can be achieved down to the 20 cm level which is sufficient for our purpose. However, the observation model applied by the monitoring stations can be enhanced to obtain more accurate estimations of satellite clock biases. A more sophisticated tropospheric model can be applied keeping the residual tropospheric error as part of the state estimation. A second aspect to be improved is the inclusion of receiver-dependent biases within satellite and receiver clock estimation. MGEX analysis centers do account for the fact that each monitoring station introduces a receiver dependent code bias that can only be obviated if all stations have the same receiver configuration [89]. Accounting for these biases can significantly improve the accuracy of clock solutions at the expense of having a more complex estimation process.

8.2.2 Autoregressive Models for Ephemeris and Clock Error

This aspect acquires more relevance in the case of online ARAIM where the ISM is in charge of providing ephemeris and clock corrections for the navigation message. Analyzing the historical data with an AutoRegressive–Moving-Average (ARMA) model in order to predict the error behavior is a promising idea which has already been investigated in the field of SBAS [90]. One of the benefits of using ARMA models can be the relaxation of the online ISM dissemination latency.

8.2.3 Alternatives for Tail Bounding

The major difficulty that the Multi Gaussian bound faces is the determination of the tail overbound. The few available independent data points along with the unpredictability of the error magnitude itself makes it cumbersome. Previous work has analyzed the use of Extreme Value Theory (EVT) to overbound distributions tails [91][92] with no particular focus on the fact that data samples are highly correlated in time. Those analyses assumed that the observed error distribution is the actual one and hence no correlation effects are accounted for. The problem of the EVT is that more than one parameter would be needed to elaborate the tail integrity bound and hence further data capacity would be requested from the ISM. One of the open points for future research is the combination of the EVT for determining the SG tail bound that this dissertation proposes.

8.2.4 Optimization of Core and Tail Bounds and Nominal Bias

An open point that was left for future research is the optimization between the one sigma bound for integrity and the nominal bias. As analyzed by Blanch in [33], there is a trade-off between the σ_{URA} and b_{nom} that can be exploited in order to obtain more efficient integrity bounds. A more elaborated trade-off worth investigating is the optimization between w_c, σ^c_{ob}, σ^t_{ob}, and b_{nom}. The benefits of the core-tail partition can be further exploited by including the value of the nominal bias in the determination of MG bounds. By doing so, ISM provider would have a forth degree of freedom to optimize the MG pair bound. For this purpose, a further consolidation of a b_{nom} determination methodology is needed. Previous works have addressed bias budgeting and impact on the user performance in [83] and [93]. However an overbound determination methodology based on data monitoring still remains an open point for ISM generation.

8.3 Closing

The novel ISM design presented in this dissertation can significantly enhance ARAIM services availability with a slight modification of the current user algorithm. With a very small increase to computational load, the target LPV-200 global coverage can be achieved even in the case of depleted constellations.

A Ranging Error Models for Dual Frequency

This annex provides a mathematical model for the different ranging error sources detailed in Section 2.1.2. For a given pair of Ionosphere Free code and phase measurements from satellite i recorded by receiver j in frequencies, Section 2.1.3 defined the corresponding error terms as $\nu_{\varphi^{i}_{j,\mathrm{IF}}}$ and $\nu_{\rho^{i}_{j,\mathrm{IF}}}$. Models in this annex are particularized for frequencies L1/L2 and L1/L5 for GPS and E1/E5a for Galileo, respectively. They include orbit and clock error, residual tropospheric delay, receiver noise, and multipath error. In addition, the signal deformation error is accounted by the bias term. They are modeled as Gaussian distributions

$$\nu_{\rho^{i}_{j,\mathrm{IF}}} \sim \mathcal{N}\left(\mu_\rho, \left(\sigma^{i}_{\rho,j,\mathrm{AB}}\right)^2\right) \text{ and } \nu_{\varphi^{i}_{j,\mathrm{IF}}} \sim \mathcal{N}\left(\mu_\phi, \left(\sigma^{i}_{\varphi,j,\mathrm{AB}}\right)^2\right) \tag{A.1}$$

where the standard deviations account for each individual error contribution

$$\left(\sigma^{i}_{\rho,j,\mathrm{IF}}\right)^2 = \left(\sigma^{i}_{orb,clk}\right)^2 + \left(\sigma^{i}_{\mathrm{tropo},j}\right)^2 + \left(\sigma^{i}_{\rho,j,\mathrm{user,AB}}\right)^2 \tag{A.2}$$

$$\left(\sigma^{i}_{\varphi,j,\mathrm{IF}}\right)^2 = \left(\sigma^{i}_{orb,clk}\right)^2 + \left(\sigma^{i}_{\mathrm{tropo},j}\right)^2 + \left(\sigma^{i}_{\varphi,j,\mathrm{user,IF}}\right)^2. \tag{A.3}$$

The residual tropospheric uncertainty provided by the RTCA-MOPS-229D [39] is common to all frequencies and signals (non-dispersive media)

$$\sigma^{i}_{\mathrm{tropo},j}(\theta^{i}_{j}) = 0.12[m]\frac{1.001}{\sqrt{0.002001 + \sin(\theta^{i}_{j}[rad]^2)}} \tag{A.4}$$

where θ^{i}_{j} is the satellite i elevation with respect to receiver j.

Because code noise and multipath errors are typically two orders of magnitude larger than phase errors, for the applications in this dissertation only the first ones are given. Note that these errors highly depend on the environment and vary between GPS and Galileo. Chapter 3 utilizes L1/L2 and E1/E5a measurements from ground stations whereas Chapter 7 simulates L1/L5 and E1/E5a airborne measurements. Models for L1L5 GPS error overbound after carrier smoothing suggested by WGC are provided by

- GPS Airborne Receiver ([94] and [95])

$$\sigma^{i}_{\mathrm{noise},j}(\theta^{i}_{j}) = 0.15[m] + 0.43[m]\exp\left[-\frac{\theta^{i}_{j}[deg]}{6.9}\right] \tag{A.5}$$

$$\sigma^{i}_{\mathrm{mp},j}(\theta^{i}_{j}) = 0.13[m] + 0.53[m]\exp\left[-\frac{\theta^{i}_{j}[deg]}{10}\right] \tag{A.6}$$

$$\sigma^{i}_{\mathrm{user},j} = \sqrt{\frac{f_{L1}^4 + f_{L5}^4}{\left(f_{L1}^2 - f_{L5}^2\right)^2}}\sqrt{\left(\sigma^{i}_{\mathrm{noise},j}\right)^2 + \left(\sigma^{i}_{\mathrm{mp},j}\right)^2} \tag{A.7}$$

- Galileo Airborne Receiver [22]

Table A.1: Galileo elevation dependent SIS user error contribution

θ_j^i [deg]	$\sigma^i_{\text{user},j}$ [m]	θ_j^i [deg]	$\sigma^i_{\text{user},j}$ [m]
5	0.4529	50	0.2359
10	0.3553	55	0.2339
15	0.3063	60	0.2302
20	0.2638	65	0.2295
25	0.2593	70	0.2278
30	0.2555	75	0.2297
35	0.2504	80	0.231
40	0.2438	85	0.2274
45	0.2396	90	0.2277

This model has also been used for Galileo noise and multipath errors in Chapter 3 (subject to be updated when new Galileo error models become available).

- GPS and Galileo Ground Receiver [96]

$$\sigma^i_{\text{noise},j}(\theta_j^i) = 0.06[m] + 0.19[m] \exp\left[-\frac{\theta_j^i[deg]}{15}\right] \tag{A.8}$$

$$\sigma^i_{\text{mp},j}(\theta_j^i) = 0.12[m] + 0.52[m] \exp\left[-\frac{\theta_j^i[deg]}{30}\right] \tag{A.9}$$

$$\sigma^i_{\text{user},j} = \sqrt{\frac{f_{L1}^4 + f_{L2}^4}{\left(f_{L1}^2 - f_{L2}^2\right)^2}} \sqrt{\left(\sigma^i_{\text{noise},j}\right)^2 + \left(\sigma^i_{\text{mp},j}\right)^2} \tag{A.10}$$

A.1 Range Error Models for MHSS algorithm

The MHSS algorithm assumes two different error models, one for integrity and one for accuracy.

- Accuracy and Continuity: The orbit and clock error bounding is modeled by σ^i_{URE} and σ^i_{SISE} and the nominal bias for continuity is assumed zero.

$$\begin{cases} \mathcal{N}\left(\mu^i_{acc}, \left(\sigma^i_{acc,j}\right)^2\right) \\ (\sigma^i_{acc,j})^2 = (\sigma^i_{URE,SISE})^2 + (\sigma^i_{\text{tropo},j})^2 + (\sigma^i_{\rho,j,\text{user,IF}})^2 \\ \mu^i_{acc} = 0 \end{cases} \tag{A.11}$$

The covariance matrix for accuracy is defined as

$$\boldsymbol{C}_{acc}(i,i) = \left(\sigma^i_{acc,j}\right)^2. \tag{A.12}$$

- Integrity: The orbit and clock error bounding is modeled by σ^i_{URA} and σ^i_{SISA} and the nominal bias for integrity is assumed b_{nom}.

$$\begin{cases} \mathcal{N}\left(\mu^i_{int}, \left(\sigma^i_{int,j}\right)^2\right) \\ (\sigma^i_{int,j})^2 = (\sigma^i_{URA,SISA})^2 + (\sigma^i_{\mathrm{tropo},j})^2 + (\sigma^i_{\rho,j,\mathrm{user,IF}})^2 \\ \left|\mu^i_{int}\right| \leq b^i_{nom}. \end{cases} \tag{A.13}$$

  The covariance matrix for integrity is defined as

$$\boldsymbol{C}_{int}(i,i) = (\sigma^i_{int,j})^2. \tag{A.14}$$

The models for GPS and Galileo airborne receivers are detailed in (A.5)-(A.7) and Table A.1.

B Satellite attitude model

This annex defines the two coordinate transformation matrices $\boldsymbol{R}^{i,k}_{\text{ECEF,BF}}$ and $\boldsymbol{R}^{i,k}_{\text{ECEF,RAC}}$ needed in Section 3.6 to compute satellite orbit and clock error. The information here included has been extracted from [97]. For a given satellite i at an epoch k, CoM position and velocity vector expressed in ECEF can be rewritten as (let us drop the indexes in order to simplify the notation)

$$\boldsymbol{x}_{sv} = \boldsymbol{x}^{i,k,\text{BCE}}_{\text{CoM,ECEF}} \;\text{ and }\; \boldsymbol{v}_{sv} = \boldsymbol{v}^{i,k,\text{BCE}}_{\text{CoM,ECEF}} \tag{B.1}$$

A generic vector is defined as $\boldsymbol{e} = \left[e^{(1)},\ e^{(2)},\ e^{(3)}\right]^T$ and $\|\boldsymbol{e}\| = 1$.

ECEF to BF Rotation As shown in Figure 3.12, GNSS satellite attitude is governed by the position of Earth and Sun. Consequently, in order to transform from ECEF to BF (or vice-versa) the position of the Sun in the ECEF frame is needed. The description of the formulation to determine the Sun position as a function of time $\boldsymbol{x}_{sun} = f(t)$ is fully contained in Chapter 5 of [77] and has not been included in this annex for conciseness. Let us define the satellite-Sun euclidean vector as

$$\boldsymbol{x}^{sv}_{sun} = \boldsymbol{x}_{sun} - \boldsymbol{x}_{sv} \tag{B.2}$$

The row vectors of the rotation matrix are computed as

$$\begin{cases} \boldsymbol{e}_{z,BF} = \frac{\boldsymbol{x}_{sv}}{\|\boldsymbol{x}_{sv}\|} \\ \boldsymbol{e}_{y,BF} = \frac{\boldsymbol{x}^{sv}_{sun} \times \boldsymbol{x}_{sv}}{\left\|\boldsymbol{x}^{sv}_{sun} \times \boldsymbol{x}_{sv}\right\|} \\ \boldsymbol{e}_{x,BF} = \boldsymbol{e}_{y,BF} \times \boldsymbol{e}_{z,BF}. \end{cases} \tag{B.3}$$

Finally, the ECEF to BF rotation matrix is defined as

$$\boldsymbol{R}_{ECEF,BF} = \begin{bmatrix} e^{(1)}_{x,BF} & e^{(2)}_{x,BF} & e^{(3)}_{x,BF} \\ e^{(1)}_{y,BF} & e^{(2)}_{y,BF} & e^{(3)}_{y,BF} \\ e^{(1)}_{z,BF} & e^{(2)}_{z,BF} & e^{(3)}_{z,BF}. \end{bmatrix} \tag{B.4}$$

Because of the properties of the rotation matrices, it can be stated that $\boldsymbol{R}_{BF,ECEF} = [\boldsymbol{R}_{ECEF,BF}]^T$.

ECEF to RAC Rotation The Radial, Along-Track, Cross-Track frame is defined by Earth's position and satellite's velocity as

$$\begin{cases} \boldsymbol{e}_R = -\frac{\boldsymbol{x}_{sv}}{\|\boldsymbol{x}_{sv}\|} \\ \boldsymbol{e}_C = \frac{\boldsymbol{x}_{sv} \times \boldsymbol{v}_{sv}}{\|\boldsymbol{x}_{sv} \times \boldsymbol{v}_{sv}\|} \\ \boldsymbol{e}_A = \boldsymbol{e}_C \times \boldsymbol{e}_R \end{cases} \tag{B.5}$$

and the rotation matrix

$$\boldsymbol{R}_{ECEF,RAC} = \begin{bmatrix} e_R^{(1)} & e_R^{(2)} & e_R^{(3)} \\ e_A^{(1)} & e_A^{(2)} & e_A^{(3)} \\ e_C^{(1)} & e_C^{(2)} & e_C^{(3)}. \end{bmatrix} \tag{B.6}$$

Analogously, because of the properties of the rotation matrices, it can be stated that $\boldsymbol{R}_{RAC,ECEF} = [\boldsymbol{R}_{ECEF,RAC}]^T$.

C Methodologies for Gaussian Bounding

The CDF bounding, formalized by DeCleene in [31], is stated as follows. Let us define a random error variable $A(\mathrm{x})$ with an empirical PDF $f_A(\mathrm{x})$ and CDF $F_A(\mathrm{x})$. Let $O_A(\mathrm{x})$ be the bounding distribution with a PDF $f_{O_A}(\mathrm{x})$ and CDF $F_{O_A}(\mathrm{x})$. $A(\mathrm{x})$ is bounded by $O(\mathrm{x})$ if

$$\begin{aligned} F_{O_A}(\mathrm{x}) &\geq F_A(\mathrm{x}) \; \forall \; \mathrm{x} \leq 0 \\ F_{O_A}(\mathrm{x}) &< F_A(\mathrm{x}) \; \forall \; \mathrm{x} > 0. \end{aligned} \tag{C.1}$$

The previous expression only attends to the overbound of individual range measurements. Ultimately, augmentation systems need to provide safe overbounds in the position domain. For that purpose, it has to be proved that the convolution of individual ranging overbounds also delimits the convolution of individual range errors. Given a second random error variable $B(\mathrm{y})$ with an empirical PDF $f_B(\mathrm{y})$ and CDF $F_B(\mathrm{y})$, bounded by a distribution $O_B(\mathrm{y})$ with a PDF $f_{O_B}(\mathrm{y})$ and CDF $F_{O_B}(\mathrm{y})$, the convolution of $A(\mathrm{x})$ and $B(\mathrm{y})$ is defined as

$$f_{A+B}(\mathrm{z}) = \int_{-\infty}^{\infty} f_A(\mathrm{x}) f_B(\mathrm{z}-\mathrm{x}) d\mathrm{x} \tag{C.2}$$

and its corresponding CDF is defined as

$$F_{A+B}(\mathrm{z}) = \int_{-\infty}^{\mathrm{z}} \int_{-\infty}^{\infty} f_A(\mathrm{x}) f_B(\mathrm{z}-\mathrm{x}) d\mathrm{x} d\mathrm{z} \tag{C.3}$$

Analogously, the convolution of $O_A(\mathrm{x})$ and $O_B(\mathrm{y})$is defined as

$$f_{O_A+O_B}(\mathrm{z}) = \int_{-\infty}^{\infty} f_{O_A}(\mathrm{x}) f_{O_B}(\mathrm{z}-\mathrm{x}) d\mathrm{x} \tag{C.4}$$

and its corresponding CDF is defined as

$$F_{O_A+O_B}(\mathrm{z}) = \int_{-\infty}^{\mathrm{z}} \int_{-\infty}^{\infty} f_{O_A}(\mathrm{x}) f_{O_B}(\mathrm{z}-\mathrm{x}) d\mathrm{x} d\mathrm{z}. \tag{C.5}$$

DeCleene proved that the convolution of the individual range overbounds is also safe in the position domain

$$\begin{aligned} F_{O_A+O_B}(\mathrm{z}) &\geq F_{A+B}(\mathrm{z}) \; \forall \; \mathrm{z} \leq 0 \\ F_{O_A+O_B}(\mathrm{z}) &< F_{A+B}(\mathrm{z}) \; \forall \; \mathrm{z} > 0 \end{aligned} \tag{C.6}$$

under the following conditions:

- $A(\mathrm{x})$ is symmetric and unimodal

- $B(\mathrm{y})$ is symmetric and unimodal
- $O_A(\mathrm{x})$ is symmetric and unimodal
- $O_B(\mathrm{y})$ is symmetric and unimodal

The last two conditions can be met by simply choosing Gaussian distributions to create overbounds. However the two first points are quite restrictive in the case of signal deformation biases or other events that shift distribution median. In order to account for these effects, pair overbound [32] introduced the so-called nominal bias b_{nom}. Rife proposed a set of two symmetrically shifted distributions around the origin $L(\mathrm{x})$ and $R(\mathrm{x})$ so that the CDF of the bounding function $O(\mathrm{x})$ is defined as

$$F_O(\mathrm{x}) = \begin{cases} F_L(\mathrm{x}) \; \forall \; F_L < 1/2 \\ 1/2 \\ F_R(\mathrm{x}) \; \forall \; F_R > 1/2. \end{cases} \tag{C.7}$$

Given two arbitrary independent CDF functions $F_A(\mathrm{x})$ and $F_B(\mathrm{y})$ individually bounded by

$$\begin{matrix} F_{L_A}(\mathrm{x}) \geq F_A(\mathrm{x}) \; \forall \; \mathrm{x} \\ F_{R_A}(\mathrm{x}) \leq F_A(\mathrm{x}) \; \forall \; \mathrm{x} \end{matrix} \text{ and } \begin{matrix} F_{L_B}(\mathrm{y}) \geq F_B(\mathrm{y}) \; \forall \; \mathrm{y} \\ F_{R_B}(\mathrm{y}) \leq F_B(\mathrm{y}) \; \forall \; \mathrm{y} \end{matrix} \tag{C.8}$$

then, the convolution of $F_A(\mathrm{x})$ and $F_B(\mathrm{y})$ is bounded by the distributions $F_{L_A+L_B}(\mathrm{z})$ and $F_{R_A+R_B}(\mathrm{z})$

$$\begin{aligned} F_{L_A+L_B}(\mathrm{z}) &\geq F_{A+B}(\mathrm{z}) \; \forall \; \mathrm{z} \\ F_{R_A+R_B}(\mathrm{z}) &\leq F_{A+B}(\mathrm{z}) \; \forall \; \mathrm{z}. \end{aligned} \tag{C.9}$$

Unlike CDF-bounding, pair-bounding does not require the empirical distribution to be unimodal nor symmetric. As shown in [32], the pair overbounding requires F_L and F_R to be monotonic and fulfill conditions (C.8).

Proof of safety of Multi Gaussian pair bounding The Multi Gaussian pair bound is an extension of the MG bounding described in Chapter 6 with the addition of the b_{nom} term introduced by Rife. Note that in order to maintain the symmetry and unimodality of the bound, left and right distributions for core and tail are shifted by the same b_{nom} value. Individual MG range envelopes in (7.2) must guarantee the overbound of the error convolutions in the position domain as expressed in (C.9). As indicated in the above paragraph, $F_{O_{MG,L}}(\mathrm{x})$ and $F_{O_{MG,R}}$ must be monotonic and fulfill conditions (C.8) in order to ensure integrity in the position domain. The monotonic condition is straightforward to prove for MG bounds. $F_{O_{MG,L}}$ and $F_{O_{MG,R}}$ are defined as

$$F_{O_{MG,L}}(\mathrm{x}) = w_c \left[\frac{1}{2} + \frac{1}{2}\mathrm{erf}\left(\frac{\mathrm{x} + b_{nom}}{\sigma^c_{\mathrm{ob}}\sqrt{2}} \right) \right] + w_t \left[\frac{1}{2} + \frac{1}{2}\mathrm{erf}\left(\frac{\mathrm{x} + b_{nom}}{\sigma^t_{\mathrm{ob}}\sqrt{2}} \right) \right] \tag{C.10}$$

$$F_{O_{MG,R}}(\mathrm{x}) = w_c \left[\frac{1}{2} + \frac{1}{2}\mathrm{erf}\left(\frac{\mathrm{x} - b_{nom}}{\sigma^c_{\mathrm{ob}}\sqrt{2}} \right) \right] + w_t \left[\frac{1}{2} + \frac{1}{2}\mathrm{erf}\left(\frac{\mathrm{x} - b_{nom}}{\sigma^t_{\mathrm{ob}}\sqrt{2}} \right) \right] \tag{C.11}$$

where the error function $\mathrm{erf}(\mathrm{x}) = \frac{2}{\sqrt{\pi}} \int_0^{\mathrm{x}} e^{-v^2} dv$ is a monotonic function.

D Baseline Multiple Hypothesis Solution Separation Algorithm for Fault Detection

This annex provides a succinct (not full) description of the ARAIM reference airborne algorithm developed by the ARAIM Technical Subgroup of the WGC in [3]. An updated version of the algorithm was published by WGC in November 2017 [4] (latest version at the time of writing of this dissertation). Note that only the steps necessary to follow the Multi Gaussian derivation in Chapter 7 are given. Further details regarding the Multiple Hypothesis Solution Separation methodology can be found in Blanch's work in [18] and [10].

D.1 Definitions

The following definitions have been taken from the ARAIM algorithm definition in [4].

Q is the tail probability function of a zero mean unit normal distribution

$$Q(u) = \frac{1}{\sqrt{2\pi}} \int_u^{+\infty} e^{-\frac{t^2}{2}} dt. \tag{D.1}$$

$\bar{Q}$ is the modified tail probability function defined as

$$\bar{Q}(u) = \begin{cases} Q(u) \text{ for } u > 0 \\ 1 \text{ for } u \leq 0. \end{cases} \tag{D.2}$$

For a given geometry with N_{sat} number of satellites in view belonging to N_{const} constellations, the individual P_{sat} and P_{const} are provided thorough the Integrity Support Message (Table 7.4). Users shall determine the set of $N_f + 1$ complementary, mutually exclusive hypotheses H_k (including the fault-free hypothesis H_0). In addition they shall compute their associated *a priori* probability $p_{f,k}$ and the non-monitored probability P_{NM} as indicated in Annex A.VIII in [3] using the following expression

$$p_{f,k} = \prod_{i=1}^{N_{events}} P_{event,i}^{B_{i,k}} \left(1 - P_{event,i}\right)^{1-B_{i,k}}. \tag{D.3}$$

D.2 Definition of the test statistic and biases

The Multiple Hypothesis Solution Separation algorithm checks the consistency among different position solutions associated with each fault hypothesis $\hat{\boldsymbol{x}}^{(k)}$ and the all-in-view position solution $\hat{\boldsymbol{x}}^{(0)}$. Expressions (2.13)-(2.21) defined the state vector $\mathbf{x}$, geometry matrix $\boldsymbol{G}$, covariance matrix $\boldsymbol{C}$, weighting matrix $\boldsymbol{W}$ Least Square Estimator (LSE) matrices $\boldsymbol{S}$, and $\boldsymbol{P}$. The all-in-view state vector solution is defined as

$$\hat{\mathbf{x}}^{(0)} = \boldsymbol{S}^{(0)}\boldsymbol{z} \text{ where } \boldsymbol{S}^{(0)} = (\boldsymbol{G}^T\boldsymbol{W}^{(0)}\boldsymbol{G})^{-1}\boldsymbol{G}^T\boldsymbol{W}^{(0)}. \tag{D.4}$$

Under hypothesis h_k where s satellites are presumptively faulted, the fault-tolerant state vector solution is computed by excluding the measurements from those satellites as

$$\hat{\mathbf{x}}^{(k)} = \boldsymbol{S}^{(k)}\boldsymbol{z} \text{ where } {}^{(k)}(\boldsymbol{G}^T\boldsymbol{W}^{(k)}\boldsymbol{G})^{-1}\boldsymbol{G}^T\boldsymbol{W}^{(k)}. \tag{D.5}$$

where the fault tolerant weighting matrix is defined as (see A.1)

$$\boldsymbol{W}^{(k)}(i,i) = \begin{cases} 0 \text{ if } i \in h_k \\ \boldsymbol{C}_{int}^{-1}(i,i) \text{ otherwise.} \end{cases} \tag{D.6}$$

In the case of dual GPS-Galileo ARAIM, the East North Up selectors are $\boldsymbol{\alpha}_1 = [1\ 0\ 0\ 0\ 0]^T$, $\boldsymbol{\alpha}_2 = [0\ 1\ 0\ 0\ 0]^T$ and $\boldsymbol{\alpha}_3 = [0\ 0\ 1\ 0\ 0]^T$, and the individual coordinate position solution is obtained by $\hat{\mathrm{x}}_l^{(k)} = \boldsymbol{\alpha}_l\hat{\mathbf{x}}^{(k)}$. The corresponding covariance associated with each solution is given by

$$\left(\sigma_l^{(k)}\right)^2 = \boldsymbol{\alpha}_l^T\boldsymbol{P}\boldsymbol{\alpha}_l = (\boldsymbol{G}^T\boldsymbol{W}^{(k)}\boldsymbol{G})_{l,l}^{-1}. \tag{D.7}$$

The solution separation test statistic is then computed as the difference

$$q_l^{(k)} = \left|\hat{x}_l^{(k)} - \hat{x}_l^{(0)}\right| \tag{D.8}$$

and its corresponding variance is

$$\left(\sigma_{ss,l}^{(k)}\right)^2 = \boldsymbol{\alpha}_l^T\left(\boldsymbol{S}^{(k)} - \boldsymbol{S}^{(0)}\right)\boldsymbol{C}_{acc}\left(\boldsymbol{S}^{(k)} - \boldsymbol{S}^{(0)}\right)^T\boldsymbol{\alpha}_l. \tag{D.9}$$

The MHSS algorithm assumes the worst case combination of the nominal bias by projecting each $b_{nom,i}$ into the position domain through the absolute value of the LSE matrix. Under a given fault hypothesis h_k, the contribution of the nominal bias to each coordinate l is computed as

$$b_l^{(k)} = \sum_{i=1}^{N_{sat}} \left|\boldsymbol{S}_{l,i}^{(k)}\right| b_{nom,i}. \tag{D.10}$$

D.3 Solution Separation Detection Thresholds

The computation of the threshold (fault-free detection probabilities) is based on the continuity requirement. For each fault mode k and coordinate l

$$T_{k,l} = K_{fa,l}\sigma_{ss,l}^{(k)} \tag{D.11}$$

where

$$K_{fa,1} = K_{fa,2} = Q^{-1}\left(\frac{P_{FA,V}}{4N_f}\right) \text{ and } K_{fa,2} = Q^{-1}\left(\frac{P_{FA,H}}{2N_f}\right). \tag{D.12}$$

The vertical $P_{FA,V}$ and horizontal $P_{FA,H}$ probabilities of False Alarm are based on the continuity requirement from Table 1.1 and allocated according to Annex E.

D.4 Protection Level Equations

Using the law of total probability, the total PHMI can be used as criterion for availability of integrity as

$$P_{HMI} = \sum_{k=0}^{N_f} P(\mid \varepsilon \mid > AL, \mid q \mid < T | H_k) p_{f_k} \leq I_{REQ} - P_{NM} \tag{D.13}$$

where P_{H_k} is the prior probability of fault occurrence, H_k is set of hypothesis for $k = 0, .., .h$, P_{NM} is the prior probability of the unmonitored events ($P_{NM} \ll I_{REQ}$), and I_{REQ} is the navigation in integrity requirement from Table 1.1.

It is convenient to express (D.13) in terms of vertical and horizontal protection levels as

$$2\bar{Q}\left(\frac{VPL - b_3^{(0)}}{\sigma_3^{(0)}}\right) + \sum_{k=1}^{N_f} p_{f,k}\bar{Q}\left(\frac{VPL - T_{k,3} - b_3^{(k)}}{\sigma_3^{(k)}}\right) = I_{REQ,V}\left(1 - \frac{P_{NM}}{I_{REQ,V} + I_{REQ,H}}\right) \tag{D.14}$$

$$2\bar{Q}\left(\frac{HPL_l - b_l^{(0)}}{\sigma_l^{(0)}}\right) + \sum_{k=1}^{N_f} p_{f,k}\bar{Q}\left(\frac{HPL - T_{k,l} - b_l^{(k)}}{\sigma_l^{(k)}}\right) = \frac{1}{2} I_{REQ,H}\left(1 - \frac{P_{NM}}{I_{REQ,V} + I_{REQ,H}}\right). \tag{D.15}$$

The derivation of VPL and HPL equations is detailed in [18] and a method to solve them is presented in Appendix B of [10]. Note that the term I_{REQ} has been conveniently reassigned to vertical $I_{REQ,V}$ and horizontal $I_{REQ,H}$ components. The probability allocations are detailed in Annex E.

D.5 Accuracy and Effective Monitoring Threshold

The last two LPV-200 navigation requirements established by ICAO (Table 1.1) are evaluated through the computation of the following metrics

$$\sigma_{v,acc} = \sqrt{\boldsymbol{\alpha}_3^T \boldsymbol{S}^{(0)} \boldsymbol{C}_{acc} \boldsymbol{S}^{(0)^T} \boldsymbol{\alpha}_3} \tag{D.16}$$

$$EMT = max_{k|p_{k,f} \geq P_{EMT}} T_{k,3}. \tag{D.17}$$

More details regarding the interpretation of the accuracy and EMT requirements can be found in [10].

D.6 Simulation Tool

The implementation of the MHSS algorithm has followed the description given in latest version of the WGC document [4]. The MatLab Algorithm Availability Simulation Tool (MAAST), developed by the Stanford University GPS Lab and made freely available at [98], is the software utilized to elaborate the availability plots within WGC reports. Although in this dissertations the MHSS has been independently developed, three functions from this tool have been used: `determine_subsets_v4.m`, `compute_adjusted_position_1D.m`, and `compute_protection_level_v4.m`. The first one determines the set of monitored fault hypotheses (solution to Equation (D.3)); the second one provides an optimized subset for weak geometries (Section 4.11 of [4]); the third one finds a solution to the vertical and horizontal protection level equations (D.14) and (D.15).

E ARAIM Service Volume Simulation Parameters

This annex provides the necessary information regarding the ARAIM Service Volume Simulations (SVSs) in Chapter 7.

E.1 ARAIM Design Parameters

The allocation between horizontal and vertical coordinates of LPV-200 integrity and continuity requirements (Table 1.1) has taken the values recommended in the latest version of the ARAIM algorithm description published by WGC in [4]. The table below also includes some key parameters for the determination of the monitored subset, the solution of the protection level equations, and the computation of the EMT.

Table E.1: List of design parameters for ARAIM Simulations [4]

Parameter	Description	Value
$I_{REQ,V}$	integrity budget for the vertical component	9.8×10^{-8}
$I_{REQ,H}$	integrity budget for the horizontal component	2×10^{-9}
$P_{FA,V}$	continuity budget allocated to the vertical mode	3.9×10^{-6}
$P_{FA,H}$	continuity budget allocated to the horizontal mode	9×10^{-8}
P_{THRES}	threshold for the integrity risk coming from unmonitored faults	8×10^{-8}
N_{ITER}^{MAX}	maximum number of iterations to compute the PL	10
TOL_{PL}	tolerance for the computation of the Protection Level	5 cm
P_{EMT}	probability used for the calculation of the Effective Monitor Threshold	10^{-5}

E.2 Simulation Scenarios and Setup

Two scenarios have been selected for the SVS:

- Baseline Scenario: Nominal 24 GPS SV constellation distributed in 6 orbital planes and Nominal 24 Galileo satellites distributed in 3 orbital planes.
- Depleted Scenario: Nominal 24-1 GPS SV constellation distributed in 6 orbital planes and Nominal 24-1 Galileo satellites distributed in 3 orbital planes.

The almanacs for the above scenarios are available in *yuma* format in the Stanford GPS Lab repository [98].

Regarding grid, mask angle, and time for the simulations the following parameters have been chosen

- Rectangular grid of 5°
- 10 sidereal days
- 900 sec time step

Bibliography

[1] International Civil Aviation Organization, *Internatiomal Standards and Recommended Practices (SARPS), Annex 10 , Aeronautical Telecommunications, Volume 1 (Radio Navigation Aids)*, ICAO Std., July 2006.

[2] T. Walter and J. Blanch, "Charactrization of GPS Clock and Ephemeris Errors to support ARAIM," in *Proceedings of Pacific PNT Meeting, Honolulu, HI*, April 20-23.

[3] Working Group C, ARAIM Technical Subgroup, EU-US Cooperation in Satellite Navigation, "Milestone 3 report," Tech. Rep., March 2016.

[4] EU US Working Group C, "Advanced RAIM Technical Subgroup Reference Airborne Algorithm Description Document," Version 3.0, November 2017. [Online]. Available: http://web.stanford.edu/group/scpnt/gpslab/website_files/maast/ARAIM_TSG_Reference_ADD_v3.0.pdf

[5] T. Walter, P. Enge, J. Blanch, and B. Pervan, "Worldwide Vertical Guidance of Aircraft Based on Modernized GPS and New Integrity Augmentations," *Proceedings of the IEEE*, vol. 96, no. 12, pp. 1918–1935, Dec 2008.

[6] R. Braff, "Description of the FAA's Local Area Augmentation System (LAAS)," *Navigation*, vol. 44, no. 4, pp. 411–423. [Online]. Available: https://onlinelibrary.wiley.com/doi/abs/10.1002/j.2161-4296.1997.tb02357.x

[7] M. Felux, M.-S. Circiua, B. Belabbas, M. Meurer, M. Stanisak, C. Milner, Y. Jiang, A. Guilbert, and A. Lipp, "Concept for a Dual Frequency Dual Constellation GBAS," in *Proceedings of the 28th International Technical Meeting of The Satellite Division of the Institute of Navigation (ION GNSS+ 2015)*,, September 14 - 18, 2015, Tampa, Florida.

[8] P. J. Teunissen and O. Montenbruck, *Springer Handbook of Global Navigation Satellite Systems*, 1st ed., S. Verlag, Ed., 2017.

[9] ICAO, *Global Navigation Satellite System (GNSS) Manual, 2nd Edition*, June 2012.

[10] J. Blanch, T. Walter, P. Enge, Y. Lee, B. Pervan, M. Rippl, A. Spletter, and V. Kropp, "Baseline advanced raim user algorithm and possible improvements," *IEEE Transactions on Aerospace and Electronic Systems*, vol. 51, no. 1, pp. 713–732, January 2015.

[11] Y. C. Lee, "Analysis of Range and Position Comparison Methods as a Means to Provide GPS Integrity in the User Receiver," in *Proceedings of the 42nd Annual Meeting of The Institute of Navigation, Seattle, WA*, 1986, pp. 1–4.

[12] B. W. Parkinson and P. Axelrad, "Autonomous GPS Integrity Monitoring Using the Pseudorange Residual," *Navigation*, vol. 35, no. 2, pp. 255–274, 1988.

[13] M. Sturza, "Navigation System Integrity Monitoring Using Redundant Measurements," *NAVIGATION*, vol. 35, no. 483-501, 1988.

[14] M. Sturza and A. Brown, "Comparison of Fixed and Variable Threshold RAIM Algorithms," in *Proceedings of the 3rd International Technical Meeting of the Satellite Division of The Institute of Navigation (ION GPS 1990), Colorado Spring, CO*, September 1990, pp. 437–443.

[15] R. G. Brown, "A Baseline RAIM Scheme and a Note on the Equivalence of Three RAIM Methods," *Navigation*, vol. 39, no. 3, pp. 301–316, 1992.

[16] B. S. Pervan, S. P. Pullen, and J. R. Christie, "A Multiple Hypothesis Approach to Satellite Navigation Integrity," *Journal of the Institute of Navigation*, vol. 45, pp. 61–71, 1998.

[17] R. G. Brown and P. W. McBurney, "Self-Contained GPS Integrity Check Using Maximum Solution Separation," *Navigation*, vol. 35, no. 1, pp. 41–53. [Online]. Available: https://onlinelibrary.wiley.com/doi/abs/10.1002/j.2161-4296.1988.tb00939.x

[18] J. Blanch, T. Walter, and P. Enge, "RAIM with Optimal Integrity and Continuity Allocations Under Multiple Failures," *IEEE Transactions on Aerospace and Electronic Systems*, vol. 46, no. 3, pp. 1235–1247, July 2010.

[19] M. Joerger, F.-C. Chan, S. Langel, and B. Pervan, "RAIM Detector and Estimator Design to Minimize the Integrity Risk," in *25th International Technical Meeting of the Satellite Division of The Intitute of Navigation, Nashville TN*, September 17-21, 2012.

[20] M. Joerger, F.-C. Chan, and B. Pervan, "Solution Separation Versus Residual-Based RAIM," *Navigation*, vol. 61, no. 4, pp. 273–291. [Online]. Available: https://onlinelibrary.wiley.com/doi/abs/10.1002/navi.71

[21] Working Group C, ARAIM Technical Subgroup, EU-US Cooperation in Satellite Navigation, "Interim report, issue 1.0,," Tech. Rep., December 2012.

[22] Working Group C, ARAIM Technical Subgroup, EU-US Cooperation in Satellite Navigation, "Milestone 2 report," Tech. Rep., February 2015.

[23] T. Walter, K. Gunning, R. Eric Phelts, and J. Blanch, "Validation of the Unfaulted Error Bounds for ARAIM," *Navigation*, vol. 65, no. 1, pp. 117–133. [Online]. Available: https://onlinelibrary.wiley.com/doi/abs/10.1002/navi.214

[24] T. Walter, J. Blanch, B. Pervan, and M. Joerger, "Determination of Fault Probabilities for ARAIM," in *Proceedings of IEEE/ION Position, Location, and Navigation Symposium (PLANS 2016), Savannah, GA*, 2016.

[25] S. Perea, M. Meurer, I. Martini, M. Rippl, M. Joerger, and B. Pervan, "Nominal Range Error Analysis to Support ARAIM," in *Proceedings of the 29th International Technical Meeting of The Satellite Division of the Institute of Navigation (ION GNSS+ 2016), Portland, Oregon, September 2016, pp. 1726-1735.*

[26] S. Perea, M. Meurer, M. Rippl, B. Belabbas, and M. Joerger, "URA/SISA Analysis for GPS and Galileo to Support ARAIM," *Navigation*, vol. 64, no. 2, pp. 237–254. [Online]. Available: https://onlinelibrary.wiley.com/doi/abs/10.1002/navi.199

[27] L. Heng, G. Gao, T. Walter, and P. Enge, "GPS Signal-in-Space Integrity Performance Evolution in the Last Decade," *IEEE Transactions on Aerospace and Electronic Systems*, vol. 48, no. 4, pp. 2932–2946, October 2012.

[28] S. Perea, M. Meurer, I. Martini, M. Rippl, and B. Pervan, "ARAIM Ground Architecture Based on GNSS Monitoring Infrastructures," in *Proceedings of the 30th International Technical Meeting of The Satellite Division of the Institute of Navigation (ION GNSS+ 2017), Portland, OR, September 2017*, pp. 1008–1018.

[29] K. Gunning, T. Walter, and P. Enge, "Multi-GNSS Constellation Anomaly Detection and Performance Monitoring," in *Proceedings of the 30th International Technical Meeting of The Satellite Division of the Institute of Navigation (ION GNSS+ 2017), Portland, Oregon, September 2017*, pp. 1051–1062.

[30] Y. Zhai, S. Kiarash, M. Jamoom, M. Joerger, and B. Pervan, "A Dedicated ARAIM Ground Monitor to Validate the Integrity Support Message," in *Proceedings of the 30th International Technical Meeting of The Satellite Division of the Institute of Navigation (ION GNSS+ 2017), Portland, Oregon, September 2017*, pp. 1063–1076.

[31] B. DeCleene, "Defining Pseudorange Integrity Overbounding," in *Proceedings of the ION GPS 2000.* Salt Lake City, UT: Institute of Navigation, September 2000, pp. 1916 – 1924.

[32] J. Rife, S. Pullen, P. Enge, and B. Pervan, "Paired Overbounding for Nonideal LAAS and WAAS Error Distributions," *IEEE Tansactions on Aerospace and Electronic Systems*, vol. 42, pp. 1386–1395, 2006.

[33] J. Blanch, T. Walter, and P. Enge, "Gaussian Bounds of Sample Distributions for Integrity Analysis," *IEEE Transactions on Aerospace and Electronic Systems*, 2018. [Online]. Available: https://ieeexplore.ieee.org/document/8496835

[34] P. Misra and P. Enge, *Global Positioning System, Signals, Measurements, and Performance*, 2nd ed. Ganga-Jamuna Press, 2006.

[35] O. Montenbruck, P. Steigenberger, and A. Hauschild, "Broadcast versus precise ephemeris: a multi-GNSS perspective," *GPS Solutions*, June 2014.

[36] G. Galluzzo and et al., "Galileo System Status, Performance Metrics and Results," in *Proceedings of the 2018 International Technical Meeting of The Institute of Navigation, Reston, Virginia, January 2018*, pp. 790–809.

[37] J. A. Klobuchar, "Ionospheric Time-Delay Algorithm for Single-Frequency GPS Users," *IEEE Transactions on Aerospace and Electronic Systems*, vol. AES-23, no. 3, pp. 325–331, May 1987.

[38] European Comission, "European GNSS (Galileo) Open Service - Ionospheric Correction Algorithm for Galileo Single Frequency Users," Issue 1.2, September 2016.

[39] Radio Technical Commission for Aeronautics (RTCA), Special Committee 159, "RTCA/DO-229D: Minimum Operational Performance Standards for Global Positioning System/Wide Area Augmenation System Airborne Equipment," Tech. Rep., 2006.

[40] N. Vagle, A. Broumandan, A. Jafarnia-Jahromi, and G. Lachapelle, "Performance Analysis of GNSS Multipath Mitigation using Antenna Arrays," *The Journal of Global Positioning Systems*, vol. 14, no. 1, p. 4, Nov 2016. [Online]. Available: https://doi.org/10.1186/s41445-016-0004-6

[41] D. B. Thornberg, D. S. Thornberg, M. F. Dibenedetto, M. S. Braasch, F. Graas, and C. Bartone, "LAAS Integrated Multipath-Limiting Antenna," *Navigation*, vol. 50, no. 2, pp. 117–130. [Online]. Available: https://onlinelibrary.wiley.com/doi/abs/10.1002/j.2161-4296.2003.tb00323.x

[42] L. Lestarquit, Y. Gregoire, and P. Thevenon, "Characterising the GNSS correlation Function Using a High Gain Antenna and Long Coherent Integration - Application to Signal Quality Monitoring," in *Proceedings of the 2012 IEEE/ION Position, Location and Navigation Symposium*, April 2012, pp. 877–885.

[43] O. Montenbruck, A. Hauschild, and P. Steigenberger, "Differential Code Bias Estimation using Multi-GNSS Observations and Global Ionosphere Maps," *Navigation*, vol. 61, no. 3, pp. 191–201. [Online]. Available: https://onlinelibrary.wiley.com/doi/abs/10.1002/navi.64

[44] U.S. Department of Transportation Federal Aviation Administration, "Order 8110.57 - Gps as a Primary Means of Anvigation for Oceanic/remote Operations," July 1, 1995.

[45] U.S. Department of Defense, *GPS Interface Control Document ICD-GPS-200J: Navstar GPS Space Segment and Navigation User Interfaces.* Navtech Seminars & Navtech Book and Software Store, July 2018. [Online]. Available: https://books.google.de/books?id=FHjBnQEACAAJ

[46] *Global Positioning System Standard Positioning Service Performance Standard*, U.S. Department of Defence, 4th Ed. September 2008, pp A-22, Std.

[47] Radio Technical Commission for Aeronautics (RTCA), *DO-178C, Software Considerations in Airborne Systems and Equipment Certification*, RTCA Special Committee 159, RTCA/DO-245, 2004, Appendix D, Std., January 2012.

[48] O. Montenbruck, P. Steigenberger, L. Prange, Z. Deng, Q. Zhao, F. Perosanz, I. Romero, C. Noll, A. Stuerze, G. Weber, R. Schmid, K. MacLeod, and S. Schaer, "The Multi-GNSS Experiment (MGEX) of the International GNSS Service (IGS), Achievements, prospects and challenges," *Advances in Space Research*, 2017.

[49] International GNSS Service Station List, http://www.igs.org/network?network=multi-GNSS,mgex-experimental.

[50] J. Guo, G. Chen, Q. Zhao, J. Liu, and X. Liu, "Comparison of Solar Radiation Pressure Models for BDS IGSO and MEO Satellites with Emphasis on Improving Orbit Quality," *GPS Solutions*, vol. 21, no. 2, pp. 511–522, Apr 2017. [Online]. Available: https://doi.org/10.1007/s10291-016-0540-2

[51] International GNSS Service, "Data Repository." [Online]. Available: ftp://cddis.gsfc.nasa.gov/gps/data/

[52] P. Steigenberger, U. Hugentobler, S. Loyer, F. Perosanz, L. Prange, R. Dach, M. Uhlemann, G. Gendt, and O. Montenbruck, "Galileo Orbit and Clock Quality of the IGS Multi-GNSS Experiment," *Advances in Space Research*, vol. 55, no. 1, pp. 269 – 281, 2015.

[53] International GNSS Service, "RINEX, The Receiver Independent Exchange Format, version 3.03 ."

[54] Technical University of Munich / MGEX Repository. [Online]. Available: ftp://cddis.gsfc.nasa.gov/pub/gps

[55] Stanford University GPS Ephemeris Repository, "https://gps.stanford.edu/sugl-ephemeris-files."

[56] Centre National d'Etudes Spatiales, CNES, "Broadcast ephemeris data repository." [Online]. Available: ftp://serenad-public.cnes.fr/SERENAD0/FROM_NTMFV2/NAV/

[57] Crustal Dynamics Data Information System - Observation RINEX Repository, ftp://cddis.gsfc.nasa.gov/gnss/data/campaign/ mgex/daily/rinex3/.

[58] International GNSS Service, "SINEX, Solution (Software/technique) INdependent EXchange Format Version 2.10."

[59] US Naval Observatory, "Sinex tropo repository." [Online]. Available: ftp://cddis.gsfc.nasa.gov/pub/gps/products/troposphere/zpd/

[60] M. Rothacher and R. Schmid, "The Antenna Exchange Format, Version 1.4," September 2010.

[61] National Geospacial-Intelligence Agency, "GPS Antenna Phase Center Offset," http://earth-info.nga.mil/GandG/sathtml/gpsdoc2015˙04a.html, access on January 2018.

[62] European GNSS Agency, "Galileo metadata." [Online]. Available: https://www.gsc-europa.eu/support-to-developers/galileo-satellite-metadata

[63] International GNSS Service, "Antex files." [Online]. Available: ftp://ftp.igs.org/pub/station/general/pcv_archive/

[64] Multi-GNSS Experiment , "Data Repository." [Online]. Available: ftp://cddis.gsfc.nasa.gov/gnss/data/campaign/mgex

[65] Multi-GNSS Experiment Station List, http://www.igs.org/network?network=multi-GNSS.

[66] N. Ashby, "Relativity in the Global Positioning System," *Living Reviews in Relativity*, vol. 6, no. 1, p. 1, Jan 2003. [Online]. Available: https://doi.org/10.12942/lrr-2003-1

[67] Z. Dai, S. Knedlik, and O. Loffeld, "Real-time cycle-slip detection and determination for multiple frequency GNSS," in *2008 5th Workshop on Positioning, Navigation and Communication*, March 2008, pp. 37–43.

[68] M. Schenewerk, "A Brief Review of basic GPS Orbit Interpolation Strategies," *GPS Solutions*, vol. 6, no. 4, pp. 265–267, Mar 2003. [Online]. Available: https://doi.org/10.1007/s10291-002-0036-0

[69] M. Li, Y. Yuan, N. Wang, Z. Li, Y. Li, and X. Huo, "Estimation and Analysis of Galileo Differential Code Biases," *Journal of Geodesy*, vol. 91, no. 3, pp. 279–293, Mar 2017. [Online]. Available: https://doi.org/10.1007/s00190-016-0962-1

[70] C. Cohenour and F. Van Graas, "GPS Orbit and Clock Error Distributions," *NAVIGATION*, vol. 58, no. 1, Spring 2011.

[71] B. Wiley, D. Craig, D. Manning, J. Novak, R. Taylor, and L. Wiengarth, "NGA's Role in GPS," in *International Technical Meeting of the Satellite Division of the Institute of Navigation, Fort Worth, TX*, Sept. 26-29 2006.

[72] European GNSS Agency, "Galileo constellation status." [Online]. Available: https://www.gsc-europa.eu/system-status/Constellation-Information

[73] United States Coast Guards Navigation Center, "." [Online]. Available: http://www.navcen.uscg.gov/?pageName=gpsNanuInfo

[74] J. P. Boyero, I. Martini, E. Spinelli, S. Wallner, F. Cosson, F. Robert, P. Brieden, F. Luongo, and D. Laura, "Galileo Performance Characterization for Horizontal ARAIM," in *International Civil Aviation Organization (ICAO), Navigation System Panel (NSP), Fifth Meeting*, Montreal, 6 - 15 November 2018.

[75] D. C. Montgomery and G. C. Runger, *Applied Statistics and Probability for Engineers*, 3rd ed. John Wiley & Sons, Sept 2002.

[76] K. L. Monti, "Folded Empirical Distribution Function Curves-Mountain Plots," *The American Statistician*, vol. 49, no. 4, pp. 342–345, November 1995.

[77] O. Montenbruck and E. Gill, *Satellite Orbits*, 3rd ed. Springer-Verlag, 2005.

[78] R. Beard, "GNSS Clocks: Past and Present," in *Tutorials of the 2017 International Technical Meeting of The Institute of Navigation, Reston, Virginia, January 2018.*

[79] *Galileo Signal in Space Interface Control Document*, Issue 1.2, European Comission Std., November 2015.

[80] European GNSS Service Center, "Galileo Initial Service - Open Service - Quarterly Performance Report Jan-Mar 2018." [Online]. Available: https://www.gsc-europa.eu/system/files/galileo_documents/Galileo-IS-OS-Quarterly-Performance_Report-Q1-2018.pdf

[81] S. Perea, M. Meurer, and B. Pervan, "Impact of Sample Correlation on SISRE Overbound for ARAIM," in *31st International Technical Meeting of The Satellite Division of the Institute of Navigation (ION GNSS+ 2018)*, September 24 - 28, 2018, Miami, FL, pp. 2567 – 2582.

[82] J. S. Bendat and A. G. Piersol, *Random Data, Analysis and Measurements Procedures*, 4th ed., Wiley, Ed., 2010.

[83] T. Walter, K. Gunning, E. Phelts, and J. Blanch, "Validation of the Unfaulted Error Bounds for ARAIM," in *Proceedings of the ION 2017 Pacific PNT Meeting*, 2017.

[84] Boris Pervan and E. Sayim, "Sigma inflation for the local area augmentation of gps," *IEEE Transactions on Aerospace and Electronic Systems*, vol. 37, no. 4, pp. 1301–1311, Oct 2001.

[85] G. Box and G. Tiao, *Bayesian Inference in Statistical Analysis*, J. W. . Sons, Ed., 1992.

[86] E. W. Ng and M. Geller, "A Table of Integrals of the Error Functions," *Journal of Research of the National Bureau of Standards*, vol. 73B, no. 1, 1969.

[87] J. Blanch, A. Ene, T. Walter, and P. Enge, "An Optimized Multiple Hypothesis RAIM Algorithm for Vertical Guidance," in *ION Institute of Navigation Global Navigation Satellite Systems Conference, Fort Worth, TX*, September 2007.

[88] J. Blanch, T. Walter, P. Enge, J. Burns, M. Mabilleau, I. Martini, J. P. Boyero, and G. Berz, "A Proposed Concept of Operations for Advanced Receiver Autonomous Integrity Monitoring," in *Proceedings of the 31th International Technical Meeting of The Satellite Division of the Institute of Navigation (ION GNSS+ 2018)*, Miami, Florida, September 2018, pp. 1084–1090.

[89] O. Montenbruck, A. Hauschild, and P. Steigenberger, "Differential Code Bias Estimation Using Multi-GNSS Observations and Global Ionosphere Maps," in *Proceedings of the 2014 International Technical Meeting of The Institute of Navigation, San Diego, California*, January 2014, pp. 802–812.

[90] J. Kim and M. Kim, "ARMA Prediction of SBAS Ephemeris and Clock Corrections for Low Earth Orbiting Satellites," *International Journal of*

Aerospace Engineering, June 2015. [Online]. Available: http://dx.doi.org/10.1155/2015/165178

[91] P. B. Ober, D. Imparato, S. Verhagen, C. Tiberius, H. Veerman, A. Van Kleef, F. Wokke, A. Bos, and A. Mieremet, "Empirical Integrity Verification of GNSS and SBAS Based on the Extreme Value Theory," *Navigation*, vol. 61, no. 1, pp. 23–38. [Online]. Available: https://onlinelibrary.wiley.com/doi/abs/10.1002/navi.55

[92] J. Larson and D. Gebre-Egziabher, "Conservatism Assessment of Extreme Value Theory Overbounds," *IEEE Transactions on Aerospace and Electronic Systems*, vol. 53, no. 3, pp. 1295–1307, June 2017.

[93] C. Macabiau and C. Milner, "Impact of Nominal Bias Bounding Techniques on Final ARAIM User Performance," in *Proceedings of the 2014 International Technical Meeting of The Institute of Navigation*, San Diego, CA, January 2014, pp. 68–77.

[94] RTCA/SC-159, "CHANGE NO. 1 TO RTCA/DO-208," RTCA, Tech. Rep., 1993.

[95] G. A. McGraw, T. Murphy, M. Brenner, S. Pullen, and A. J. V. Dierendonck, "Development of the LAAS Accuracy Models," in *ION GPS*, 2000.

[96] J. P. Weiss, S. Anderson, and P. Axelrad, "Development of Multipath Error Budgets for JPALS Ground Station Receivers," *Navigation*, vol. 52, no. 3, pp. 145–154, 2005. [Online]. Available: http://dx.doi.org/10.1002/j.2161-4296.2005.tb01741.x

[97] O. Montenbruck, R. Schmid, F. Mercier, P. Steigenberger, C. Noll, R. Fatkulin, S. Kogure, and A. Ganeshan, "GNSS satellite Geometry and Attitude Models," *Advances in Space Research*, vol. 56, no. 6, pp. 1015–1029, September 2015.

[98] Stanford University GPS Lab, "MatLab Algorithm Availability Simulation Tool," Version 4, January 2018. [Online]. Available: https://gps.stanford.edu/resources/tools/maast